

2011-01-01

A Proposed Epithermal Model for the High Grade District, California

Michael Nicholas Feinstein

University of Texas at El Paso, mnfeinstein@gmail.com

Follow this and additional works at: https://digitalcommons.utep.edu/open_etd



Part of the [Geology Commons](#), and the [Statistics and Probability Commons](#)

Recommended Citation

Feinstein, Michael Nicholas, "A Proposed Epithermal Model for the High Grade District, California" (2011). *Open Access Theses & Dissertations*. 2280.

https://digitalcommons.utep.edu/open_etd/2280

This is brought to you for free and open access by DigitalCommons@UTEP. It has been accepted for inclusion in Open Access Theses & Dissertations by an authorized administrator of DigitalCommons@UTEP. For more information, please contact lweber@utep.edu.

A PROPOSED EPITHERMAL MODEL FOR THE HIGH GRADE DISTRICT, CALIFORNIA

MICHAEL NICHOLAS FEINSTEIN

Department of Geological Sciences

APPROVED:

Philip C. Goodell, Ph.D., Chair

Jose M. Hurtado, Ph.D.

David Borrok, Ph.D.

Jasper Konter, Ph.D.

Josiah M. Heyman, Ph.D.

Benjamin C. Flores, Ph.D.
Acting Dean of the Graduate School

Copyright ©

By

Michael N. Feinstein

2011

A PROPOSED EPITHERMAL MODEL FOR THE HIGH GRADE DISTRICT, CALIFORNIA

by

MICHAEL NICHOLAS FEINSTEIN, M.S., B.S.

DISSERTATION

Presented to the Faculty of the Graduate School of

The University of Texas at El Paso

in Partial Fulfillment

of the Requirements

for the Degree of

DOCTOR OF PHILOSOPHY

Department of Geological Sciences

THE UNIVERSITY OF TEXAS AT EL PASO

December 2011

ABSTRACT

A historic gold mining district in northeastern California has not been incorporated into the global knowledge base for precious metal vein deposits. This study collected various data types which are important characteristics in the classification and understanding of vein deposits. The High Grade District (HGD) is a gold mining site located in the northeast corner of Modoc County, California, in the Warner Mountains. The Warner Mountains are composed of Tertiary eruptive centers, cropping out between valleys formed through extensional tectonics. Mineralization of the HGD displays abundant silicification, adularia, and gold; these characteristics are sufficient to classify mineralization as low-sulfidation epithermal and warrants exploration activities to test models of this specific type. This study integrates local field mapping and hard-rock sampling with numerous laboratory methods to characterize the mineralizing system and test the classic epithermal model.

390 rock samples were collected and geologic maps were constructed. Rock samples are analyzed for elemental abundances, fluid inclusion studies, thin/polished section microscopy, and electron microprobe analyses were performed. Geochemical results were processed statistically with JMP software, surfaces modeled in Golden Software's Surfer, and visually interpreted in ArcGIS. This study constrains the timing of mineralization with $\text{Ar}^{40}/\text{Ar}^{39}$ dates and generates a data set of $\delta^{18}\text{O}$ values in the HGD. This new knowledge base can be used to guide later economic and scientific endeavors to better understand the mineralization encountered in the HGD. The addition of data from this study to the global knowledge base, surrounding epithermal vein deposits, makes our collective scientific understanding of this topic more complete.

TABLE OF CONTENTS

	Page
ABSTRACT	iv
LIST OF FIGURES	vii
LIST OF TABLES	xi
1. INTRODUCTION	1
1.1 Study Area Description	3
1.2 Production History	8
1.3 Exploration History	9
1.4 Previous Geologic Investigations	13
1.5 Regional Tectonics	14
2. STATEMENT OF THE PROBLEM	21
2.1 Methodology	23
2.2 Quality of Data	25
3. FIELD MAPPING	26
3.1 Stratigraphy	29
3.1.1 Basal Andesites (Ta & Tam)	32
3.1.2 Felsic Suite	36
3.1.3 Steens Basalt (Tb)	57
3.1.4 Mt. Bidwell Obsidian (Tbv & Tbvo)	59
3.2 Structure	60
3.3 Alteration	64
3.4 Sampling	70
4. DRILLING	71
5. GIS	75
6. GEOCHEMISTRY & STATISTICS	77
6.1 Univariant	79
6.2 Bivariant	84
6.3 Multi-variant	86
6.4 Factor Mapping	92
6.5 Outliers	98

6.6	Interpretation.....	101
7.	MINERALIZATION	102
7.1	Quartz Textures.....	104
7.2	Optical Microscopy.....	117
7.3	Electron Microprobe	120
7.3.1	Paragenesis.....	121
7.3.2	Quantitative Analysis.....	123
7.4	Interpretation.....	126
8.	HOMOGENIZATION AND FREEZING TEMPERATURES.....	128
8.1	Fluid Inclusion Studies	130
8.2	Discussion	134
8.3	Interpretation.....	137
9.	ABSOLUTE AGES	139
9.1	Ar ⁴⁰ /K ⁴⁰ – Whole Rock Ages.....	139
9.2	Ar ⁴⁰ /Ar ³⁹ - Adularia Ages	142
9.3	Discussion.....	148
10.	δ ¹⁸ O ISOTOPE VALUES.....	150
10.1	Interpretation - Fluid Transport and Mixing.....	153
11.	DISCUSSION	155
11.1	Integration of Methods.....	158
11.2	Epithermal Models by Mining Camp	162
11.3	HGD Integrated Conceptual Epithermal Model	171
11.4	District Synthesis	173
11.5	Mineral Resource Potential of the District.....	175
11.6	Future Work.....	178
11.7	Qualification of Observations	180
11.8	Related Areas	181
12.	CONCLUSIONS.....	187
13.	REFERENCES	189
14.	APPENDICES	194
14.1	Appendix 1.....	195
	CURRICULUM VITA	286

LIST OF FIGURES

	page
Figure 1. Shaded relief map of the Northwestern Great Basin from Google Earth.....	2
Figure 2. Portion of USGS 1:24,000 Quadrangle of Mt. Bidwell.	4
Figure 3. Digital elevation model (DEM) of the HGD.....	5
Figure 4. Aerial photography was flown over the HGD in summer 2008.....	6
Figure 5. This map shows the extent of surface sampling data points	7
Figure 6. Disseminated resource as calculated by Golden Phoenix Minerals in 1998	10
Figure 7. Alteration map from Nord Resources.....	11
Figure 8. Cenozoic tectonic evolution of western North America	14
Figure 9. The work of Egger and Colgan (2009) is 20 km south	15
Figure 10. Geologic cross-section of northern California	16
Figure 11. 1500m of the Warner Mountain horst block in drill hole LCSH-05	17
Figure 12. Two-stage spreading model of the Yellowstone mantle plume	18
Figure 13. Generalized estimates of percent extension	19
Figure 14. General kinematics of the northwestern Great Basin	20
Figure 15. General epithermal model	22
Figure 16. Field work photos.....	27
Figure 17. Observations made during regional mapping	28
Figure 18. Stratigraphic columns across the Warner Mountain horst block from West to East..	30
Figure 19. Geologic map from MS Thesis sponsored by Atlas Minerals. (Keats, 1985).....	31
Figure 20. Andesite outcrop.....	33
Figure 21. Yellow Mountain photos	37

Figure 22. Ttb - Brown Tuff	38
Figure 23. Tdmr - Discovery Mountain Rhyolite	39
Figure 24. Tcrf - Consolidated Rhyolite Flow	39
Figure 25. Tcrd - Consolidated Rhyolite Dome	40
Figure 26. Tlq - Lodgepole Aphyric Quartz Latite	40
Figure 27. Tmvp - Mt. Vida Peak Rhyolite	41
Figure 28. Tmpr - Moonlight Porphyry Rhyolite	41
Figure 29. Tkq - Klondyke Glassy Quartz Latite	42
Figure 30. Tkc - Kelly Creek Tuff	42
Figure 31. Tclt - Cave Lake Tuff	43
Figure 32. Tclv - Cave Lake Volcaniclastics	43
Figure 33. Tpl - Poison Lake Tuff	44
Figure 34. Tsp - Sugar Peak Rhyolite	44
Figure 35. Tbs - Bow Spring Rhyolite	45
Figure 36. Tai - Orange Ignimbrite	45
Figure 37. Tdc - Deep Creek Rhyolite	46
Figure 38. Tcrd - Cross-Roads Porphyritic Rhyolite Dome	46
Figure 39. Tbv - Mt. Bidwell Vent Rhyolite	47
Figure 40. Cave Lake Coarse Volcaniclastics (Tclv) in outcrop	51
Figure 42. Basalt flows	57
Figure 43. Three dimensional view of the northern Warner Mountains	61
Figure 44. Structure of the HGD	63
Figure 45. Silica bodies and tallus fields in the HGD	65

Figure 46. The rock piles along the Sunshine Vein and Modoc Mines.....	66
Figure 47. Andesite and hydrothermal breccias	67
Figure 48. Consolidated Silica Body (CSB) alteration.....	68
Figure 49. Alteration types observed in the study area. A) Silicic, B) Argillic, C) Propylitic...	68
Figure 50. Drilling photos.....	73
Figure 51. Core samples	74
Figure 52. ArcGIS layering method.....	76
Figure 53. Samples used in geochemical studies.....	78
Figure 54. The removal of outliers follows this flow-chart.....	81
Figure 55. Box plot explanation diagram.	81
Figure 56. Histograms from "outlier_removed" data	83
Figure 57. PC results of Factor 3, epithermal trace suite.....	88
Figure 58. Factor 3 map.....	93
Figure 59. Element concentration for representative samples of each factor (FS).....	96
Figure 60. Outlier data histograms.....	98
Figure 61. Map of Au outlier values.....	100
Figure 62. Diagram of Discovery Mountain.....	103
Figure 63. Vein material collected in the East Consolidated mines.	105
Figure 64. Vein material collected from the dumps of Consolidated West (CW/Con) camp. ..	107
Figure 65. Vein material observed in the Klondyke Camp segment of the study area.....	109
Figure 66. Vein and gouge material in the Lodgepole camp.....	111
Figure 67. Vein textures encountered on the Blue Bell dump.....	112
Figure 68. Vein textures encountered on the Sunshine dump.	114

Figure 69. Vein textures encountered on the Modoc Mines dump.....	116
Figure 70. Thin-section, LM-3a.....	118
Figure 71. Thin-section from the Moonlight Camp.....	119
Figure 72. Electron microprobe investigation: sample Con_6	122
Figure 73. Quantitative electron imaging	124
Figure 74. Quantitative imaging of Ag-nodules	125
Figure 75. Paragenetic observations	127
Figure 76. USGS heating stage.....	129
Figure 77. Some fluid inclusions observed.....	129
Figure 78. Some homogenization temperature charts.....	131
Figure 79. Reconnaissance of thick-sections.	132
Figure 81. All fluid inclusion data	135
Figure 82. Temperature data from the HGD is compared to studies by others	138
Figure 83. K-Ar ages returned for rocks from the silicic sequence (Keats, 1985).	141
Figure 84. Age spectrum and respective isochron	145
Figure 85. Bell plot of High Grade vein ages	146
Figure 86. This chart and table display all age data collected in the HGD.....	147
Figure 87. Age dates acquired in the HGD.....	149
Figure 88. Oxygen isotope values on map.....	151
Figure 89. $\delta^{18}\text{O}$ values from other ore deposits	152
Figure 90. Stratigraphic units of the study area with ages integrated.....	156
Figure 91. Hypothesis A for the relation of geochemical factors and paragenetic phases	159
Figure 92. Hypothesis B for the relation of geochemical factors and paragenetic phases	160

Figure 93. Legend for all epithermal models in chapter 11	163
Figure 94. Discovery Mountain epithermal model showing veining and stratigraphy.....	163
Figure 95. Discovery Mountain epithermal model showing veining and alteration.....	164
Figure 96. Discovery Mountain epithermal model showing temperature and $\delta^{18}\text{O}$ values.	164
Figure 97. Discovery Mountain epithermal model with the epithermal geochemistry.	165
Figure 98. Ruby Ridge - Klondyke epithermal model showing veining and stratigraphy.	166
Figure 99. Ruby Ridge - Klondyke epithermal model showing veining and alteration	166
Figure 100. Ruby Ridge - Klondyke epithermal model showing temperature and $\delta^{18}\text{O}$ values.	167
Figure 101. Ruby Ridge - Klondyke epithermal model with the epithermal geochemistry	167
Figure 102. Sunshine - Modoc epithermal model showing veining and stratigraphy.	168
Figure 103. Sunshine - Modoc epithermal model showing veining and alteration.	169
Figure 104. Sunshine - Modoc epithermal model showing temperature and $\delta^{18}\text{O}$ values.....	169
Figure 105. Sunshine-Modoc epithermal model with the epithermal geochemistry.	170
Figure 106. Conceptual epithermal model for HGD on general stratigraphy.....	171
Figure 107. Conceptual epithermal model for HGD on alteration pattern.	172
Figure 108. Conceptual model of the bimodal basalt-rhyolite assemblage	174
Figure 109. Priority targets for exploration drilling in the HGD.....	178
Figure 111. emplacement of volcanic domes in Bolivia and related deposits.....	182
Figure 112. Working genetic models from the Bodie District, California	183

LIST OF TABLES

Table 1. Record of previous operator activity and retained data.	9
Table 2. Methods used in this Dissertation were carried out in the time table	24

Table 3. Stratigraphic units of the study area.	29
Table 4. Silica body characteristics in the HGD.....	66
Table 5. Correlation Frequencies of the 48 elements included in processing.	85
Table 6. Factor score eigenvalues represent the prevalence of each factor in the data set.	86
Table 7. Table summarizing factor analysis	91
Table 8. Outlier cut-off values by element	99
Table 9. Results from $\text{Ar}^{40}/\text{Ar}^{39}$ dating of vein adularia. (Peters, 2009)	142
Table 10. Oxygen isotope data.....	150
Table 11. The total number of samples processed in each method.	155
Table 12. Compares HGD characteristics with general epithermal.....	186

1. INTRODUCTION

A yellow metal, malleable, resistant to corrosion, and magically lustrous has been prized since the dawn of civilization. It has driven civilizations and nations alike, currently it plays an important role in global currencies and economics. The last twenty years have seen a massive resurgence in gold production from the Great Basin of the Western U.S. Nevada accounts for 80% of all U.S. gold production, 5.64 million ounces in 2008 (George, M.W., 2008). The application of mineral deposit models to mining has had a profound impact on increasing efficiency of district exploration and reserve generation.

The High Grade District (HGD) is a gold property, located in northeastern California near the Oregon and Nevada borders (Fig.1), which displays sufficient evidence to be classified as a low-sulfidation epithermal system. This study has collected data from field mapping and sampling. A 130 sample dataset has been processed for geochemical analyses and statistical interpretation. Methods include optical microscopy, electron microprobe analyses, and fluid inclusion studies. This data set forms the control points in building an adaptive model, specific to the study area. Numerous studies (Romberger, 1993; Berger and Eimon, 1983; Buchanan, 1981) have focused on building genetic models for mineral deposits and this study creates a new model with respect to the mineralization encountered in the HGD (Fig. 1).

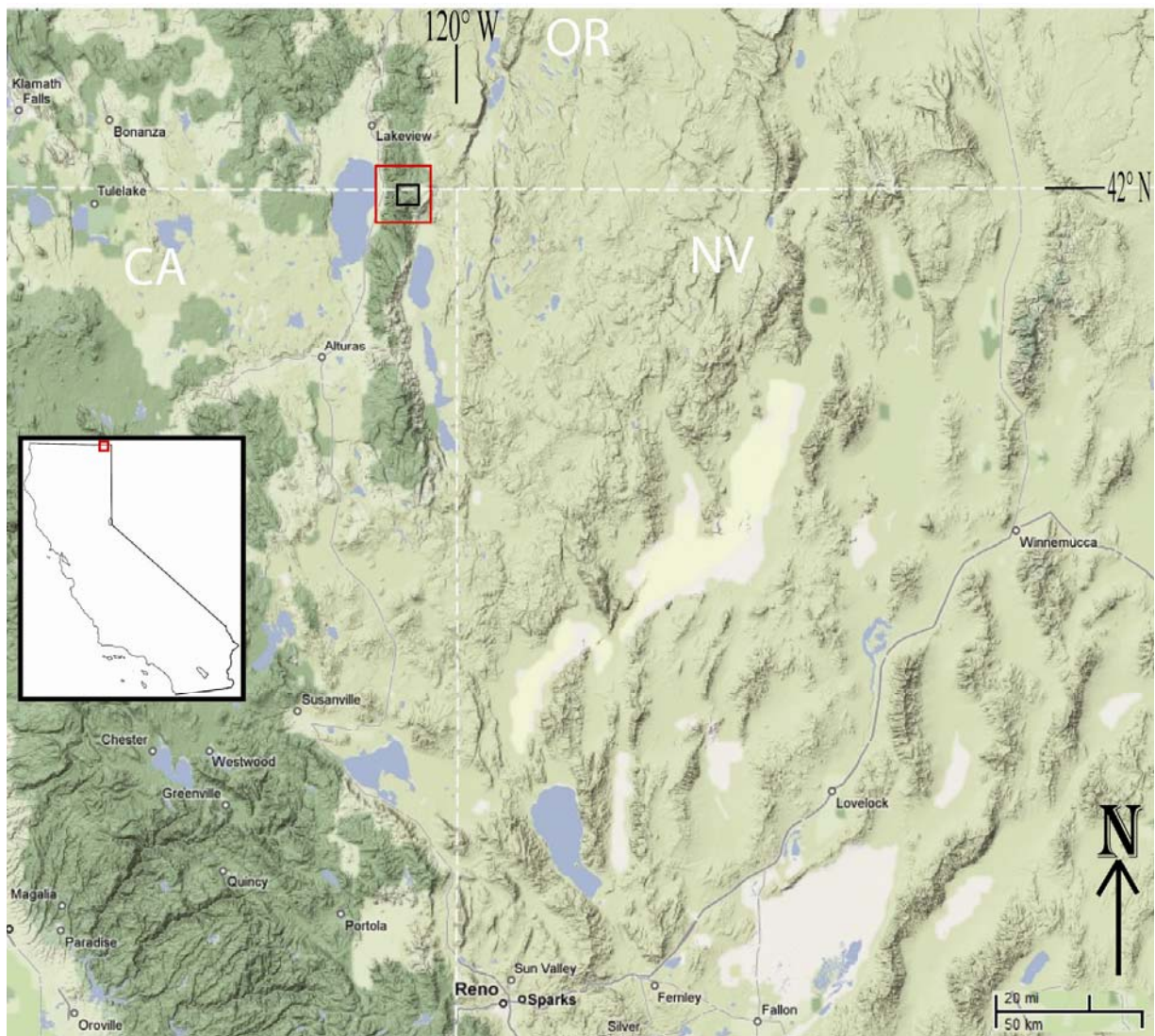


Figure 1. Shaded relief map of the Northwestern Great Basin from Google Earth. The study area is located on the California-Oregon border, regional map and district map locations are shown in red and black, respectively.

1.1 Study Area Description

The HGD is located in the northeast corner of Modoc County, California, in the Warner Mountains (Fig. 1). The Warner Range is a horst block extending ~150 km N-S and ranging from 10 to 20 km wide. The intermediate volcanics which make up the Warner Mountain Range, and host felsic units of the HGD, are similarly described to the south and dated (Egger and Colgan, 2009; Carmichael et al, 2006; Duffield and McKee, 1986; Martz, 1970). The interbedded andesite flows, mudflows, and pyroclastics are roughly correlative to the Soldier Creek volcanics and Cedar Pass volcanics in the central Warner Mountains. These units have age constraints between 30 and 20 Ma, and are composed of andesitic stratovolcanoes and related flows, and basaltic shield volcanoes and related flows (Egger and Colgan, 2009; Carmichael et al, 2006; Duffield and McKee, 1986). The horst and graben physiography observed in the study area is due to extension along the northwestern margin of the Basin and Range (Fig. 1) (Lerch, 2009; Colgan, 2005). The district lies within the northern part of the mountains in an area of complex early Tertiary volcanic rocks of intermediate composition, and younger Miocene-age bimodal eruptives of rhyolites and basalts (Matthewson, 2003; Vance and Shwertfeger, 2001; Taylor, 1997; Schuler, 1986; Keats, 1985; Cox, 1985).

The study area is located in the northwestern corner of the Great Basin Physiographic Province of the Western United States (Colgan, 2005; Wilkins, 1984). Elevations within the district are 7,000 to 8,000 feet above sea level. The district lies within the Modoc National Forest on land administered by the National Forest Service of the United States Department of Agriculture. Forest service studies recognize the mineral potential of the area and provide for multiple land use (Palmer, 1993; Asrow, 1991). Due to heavy snowfall, ground access is from

June to November. In conformance with Golden Predator Mines protocol, all measurements are taken in English units to correspond with State Plane coordinate systems.



Figure 2. Portion of USGS 1:24,000 Quadrangle of Mt. Bidwell, Modoc County, California. The numerous historic workings on the property are labeled: Consolidated (Con, east and west), North-Star Basin (NSB, NSRD), Ruby Ridge (RR), Klondyke (Klon, KAB), Lodgepole (LP), Blue Bell (BB), Moonlight (Moon), Sunshine (SS), Modoc Mines (MMS). Note the road trace in red, it will be used as a reference to district layout in all subsequent map figures. This map view is contained within the study area. This figure has the same geographic extent of figures 3, 4, and 5.

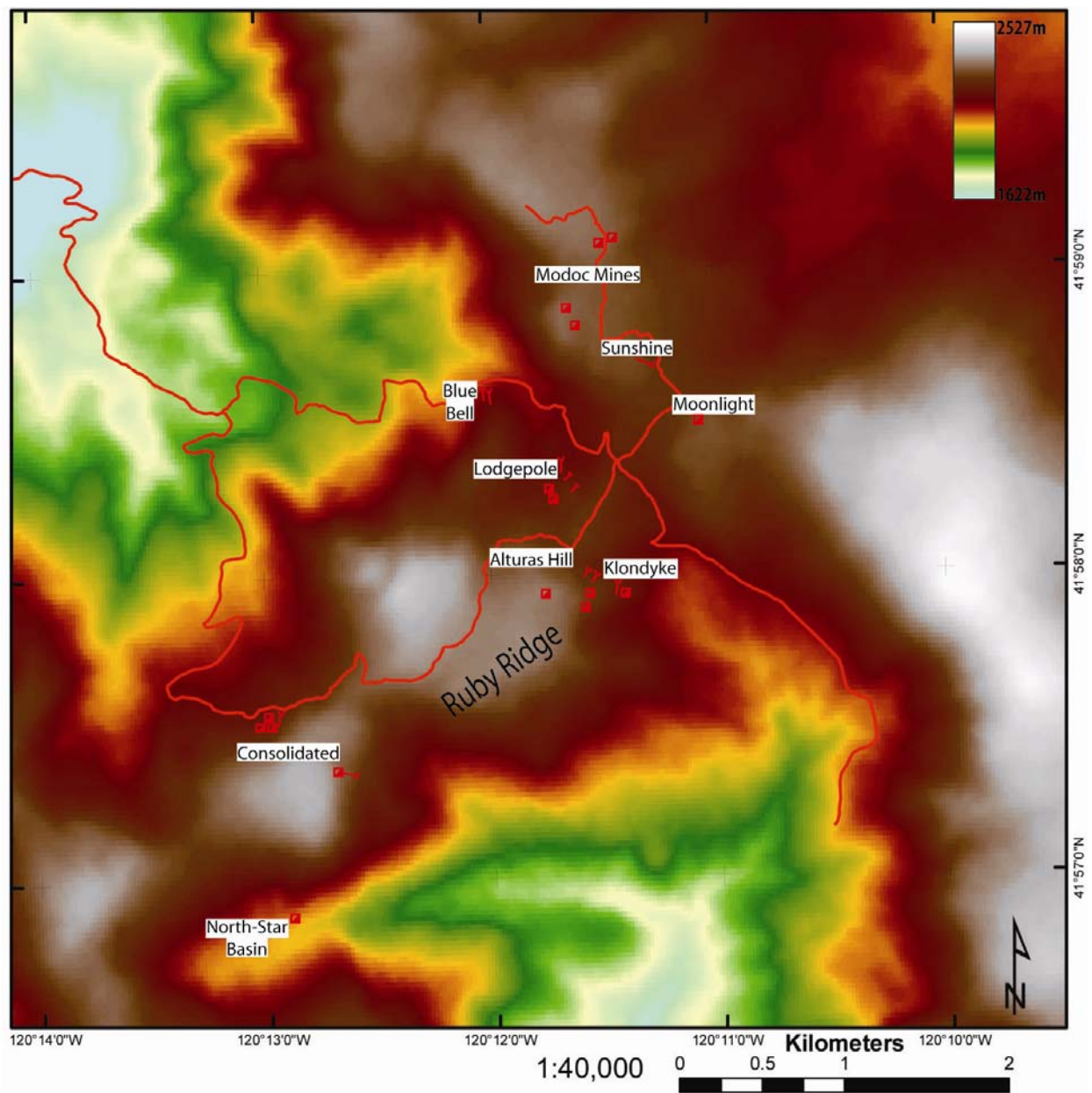


Figure 3. This digital elevation model (DEM) of the HGD shows the high northeast trending ridgeline that hosts mineralization. This figure has the same geographic extent of figures 2, 4, and 5.

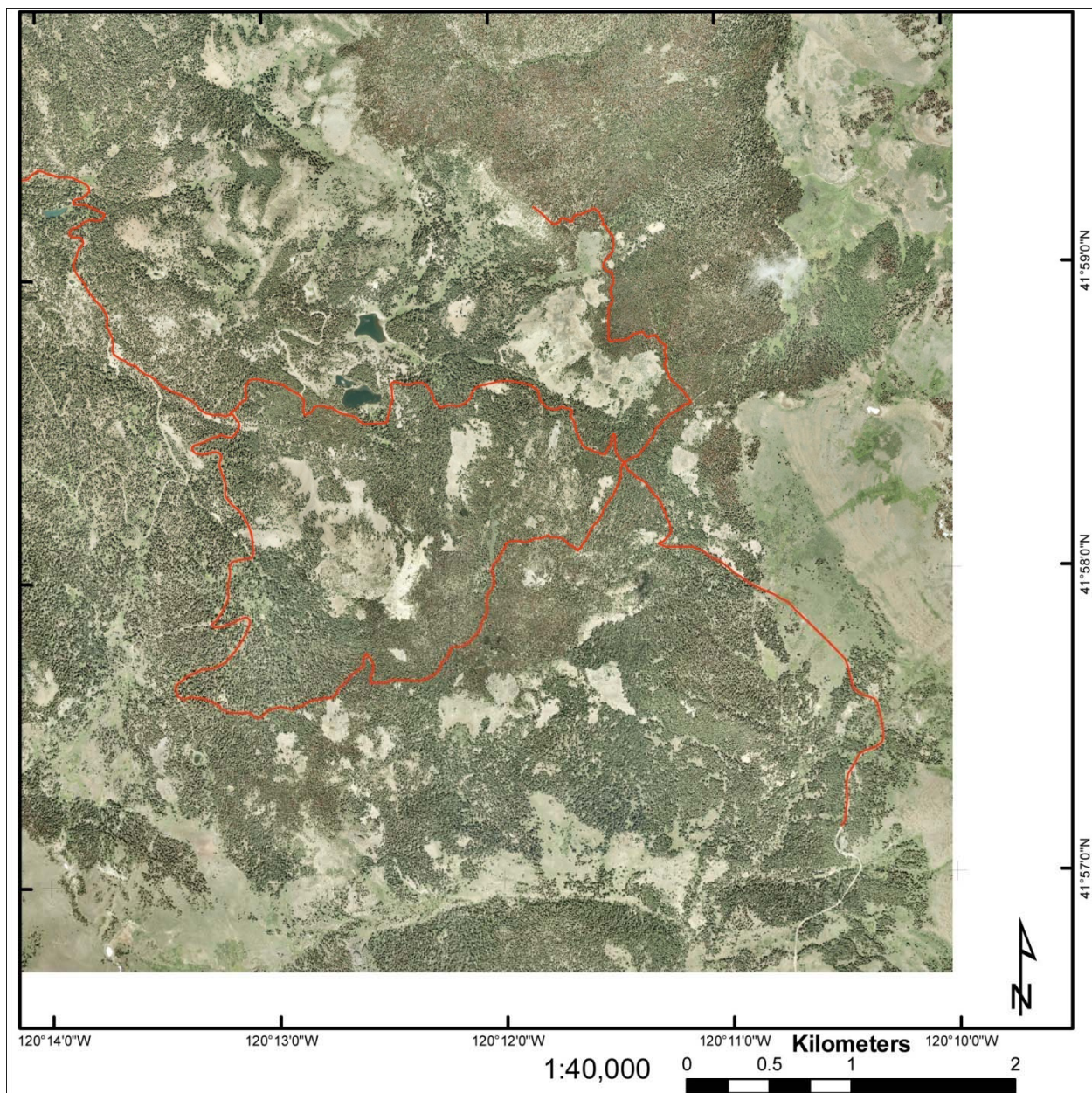


Figure 4. Aerial photography was flown over the HGD in summer 2008. This high resolution image aids in mapping and discerning linear features. Silica bodies and tallus are not vegetated. This figure has the same geographic extent of figures 2, 3, and 5.

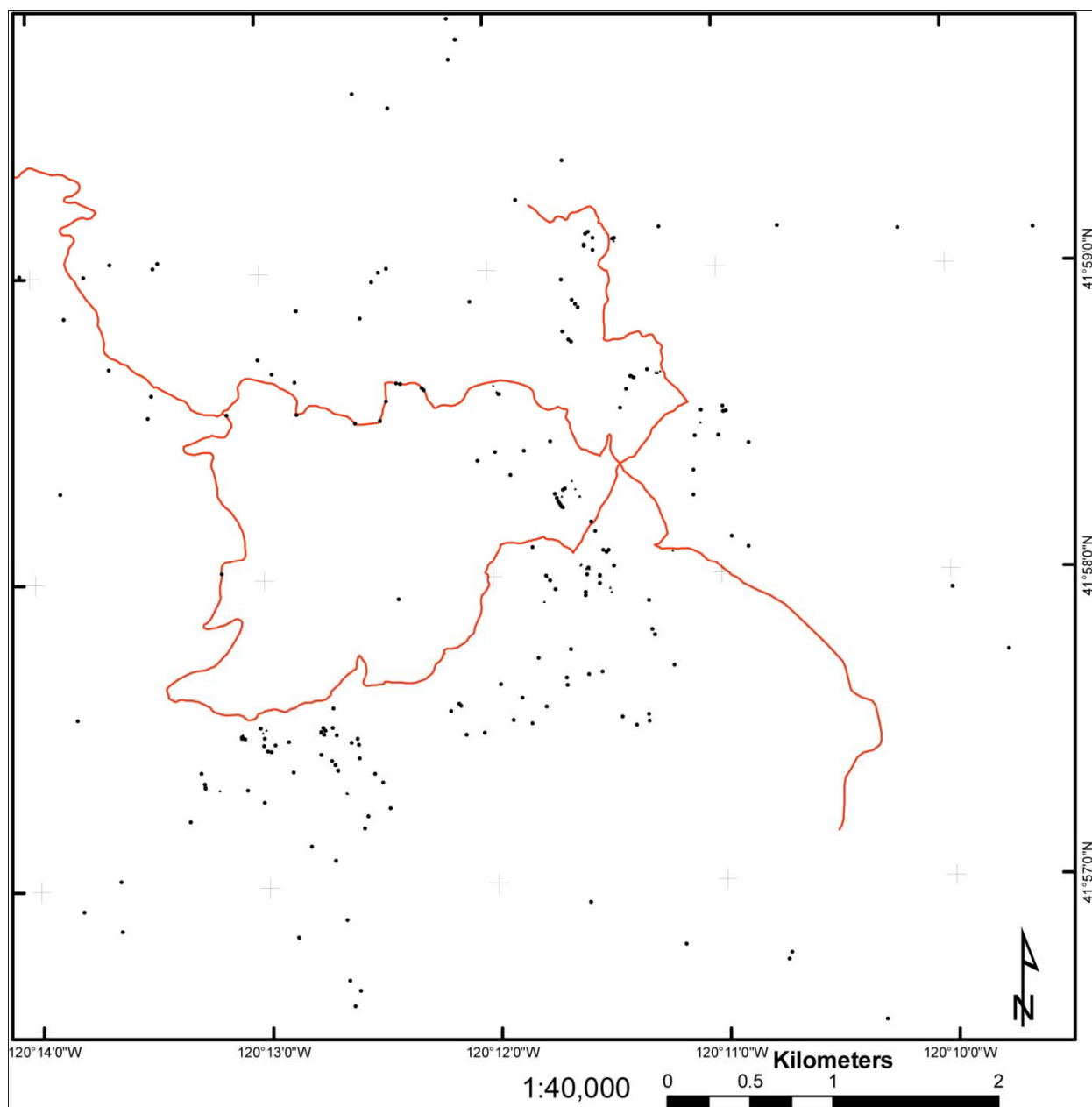


Figure 5. This map shows the extent of surface sampling data points in the immediate study area. This figure has the same geographic extent of figures 2, 3, and 4.

1.2 Production History

The discovery of gold in the district was reported by Hoag around 1880 (Hill, 1915). Gold was rediscovered by a sheepherder in 1905 and a small boom ensued in 1910. Several camps were inhabited by three hundred men in the first years. Production is reported to be \$75,000 in gold between 1910 and 1914 (Hill, 1915). A small resurgence was seen in the district during the Great Depression and production was reported to have been \$10,000 between 1931 and 1934 (Gay, 1966).

Most initial focus of early exploration was near the Consolidated camps (Fig. 2), in the southwestern portion of the district, where bonanza-grade (1+ ounce per ton) veins were exposed within this more deeply eroded portion of the district (Palmer, 1993; Cox, 1985; Keats, 1985; Hill, 1915).

The most notable historic workings in the district include a 212 foot shaft with multiple levels at the Modoc Mines camp (Fig. 2). In addition, three shafts and numerous tunnels were driven to intersect quartz veins and breccia zones at the Klondyke camp (Fig. 2). The large dump at the Consolidated West camp (Fig.2) is also indicative of extensive underground workings. The district is riddled with prospect pits and trenches, minor quartz stringers occur extensively.

1.3 Exploration History

Although numerous operators held claims within the district, no serious exploration utilizing modern day techniques occurred until the early 1980s when a renewed interest in the HGD developed (table 1). The project exploration goal was to identify a significant disseminated surface deposit (fig. 7), directed toward near-surface, bulk-mineable deposits; very much to the exclusion of underground mineable, bonanza deposits. When sufficient volumes of mineralization were not found; the property went dormant.

Drilling in the 1980s was focused on a large surface deposit, all holes drilled were vertical. Samples of Nord and FMC drill logs are provided in Appendix 1, figure 1-3 and 1-4. Kennecott examined the district several times in the 1980s. U.S. Borax briefly evaluated the Moonlight target (Fig.2) in 1988.

Table 1. Record of previous operator activity and retained data.

Operator	Data Type	Number of samples	Year	Integrity of data	Comments
Atlas Minerals	Rock Chip	68	'82	Good	
Atlas Minerals	Age Dates	3	'85	Good	
Nord	Drill Hole	67	'82, '83, '86	Fair	avg. depth- 125'
Nord	Drill Hole Log	11	'82	Fair	
Nord	Rock-Chip	1000+	'81, '82	N/A	
FMC	Drill Hole	34	'84, '85	Good	avg. depth- 100'
FMC	Drill Hole Log	32	'84, '85	Good	
FMC	Rock Chip	435	'84, '85	Fair	locations & Au assay
FMC	Soil Sample	152	'84, '85	N/A	
U.S. Borax	Rock Chip	129	'87, '88	N/A	

U.S. Borax	Grid Survey	339	'88	N/A	
Golden Phoenix	Drill Hole	13	'98	N/A	avg. depth- 600'
Golden Phoenix	Drill Hole Log	13	'98	Good	
Golden Phoenix	Rock Chip	108	'97, '98	Good	locations & Au assay
Newmont	Drill Hole	3	2000	N/A	avg. depth- 1,200'
Newmont	Drill Hole Log	2	2000	Good	
Newmont	Rock Chip	216	2000	Good	locations & Au assay
GAM	Rock Chip	124	2003	Fair	locations & Au assay
Golden Predator	Rock Chip	152	2008	Good	locations & Au+multi-elem assay

Golden Phoenix Minerals acquired High Grade in 1997; modern surveying was completed by Tri-State Surveying, Ltd. Golden Phoenix compiled and re-assessed the property based on 98 prior drill holes (fig. 7). The average depth of these was less than 200 feet, the deepest drill hole terminated at 445 feet. Golden Phoenix drilled an additional 13 holes to an average depth of 600 feet in 1998. Encouraging results are reported in the Klondyke camp. Their work culminated in a modern synthesis of historic drill-log data from which a resource was calculated (fig. 6) (Taylor, 1998).

High Grade Project – Resource Summary

0.010 opt Gold Cutoff Grade

Category	Tons	Grade	Ounces
Indicated Resource	810,700	0.036	29,430
Inferred Resource	422,600	0.036	15,210
Subtotal	1,233,300	0.036	44,640
Other Resource	1,661,500	0.033	54,690
Grand Total	2,894,800	0.034	99,330

Figure 6. Previous Drilling by FMC and Nord was compiled with 12 new holes to assemble a resource in the Ruby Ridge through Lodgepole area. Disseminated resource as calculated by Golden Phoenix Minerals in 1998. This resource was developed using the MedSystem M650AR program and a 0.01 opt Au cut-off grade. (Taylor, 1998)

A revived interest developed at High Grade in the late 1990s with interest focusing on defining the “high-grade roots” of the surface deposit (table 1). Newmont Mining evaluated the bonanza roots of the Ruby Ridge camp (fig. 2) in 2000 and 2001. Six lines of IP/resistivity were

completed in the central and northern portion of the district. Twenty two drill pads were permitted in 2000, and 3 holes were drilled to depth of ~1,200 feet. One promising hole deviated strongly along a NW structure. These drill pads are concentrated near the historic resource, in the Ruby Ridge, Klondyke, and Lodgepole camps (fig. 2 and 7).

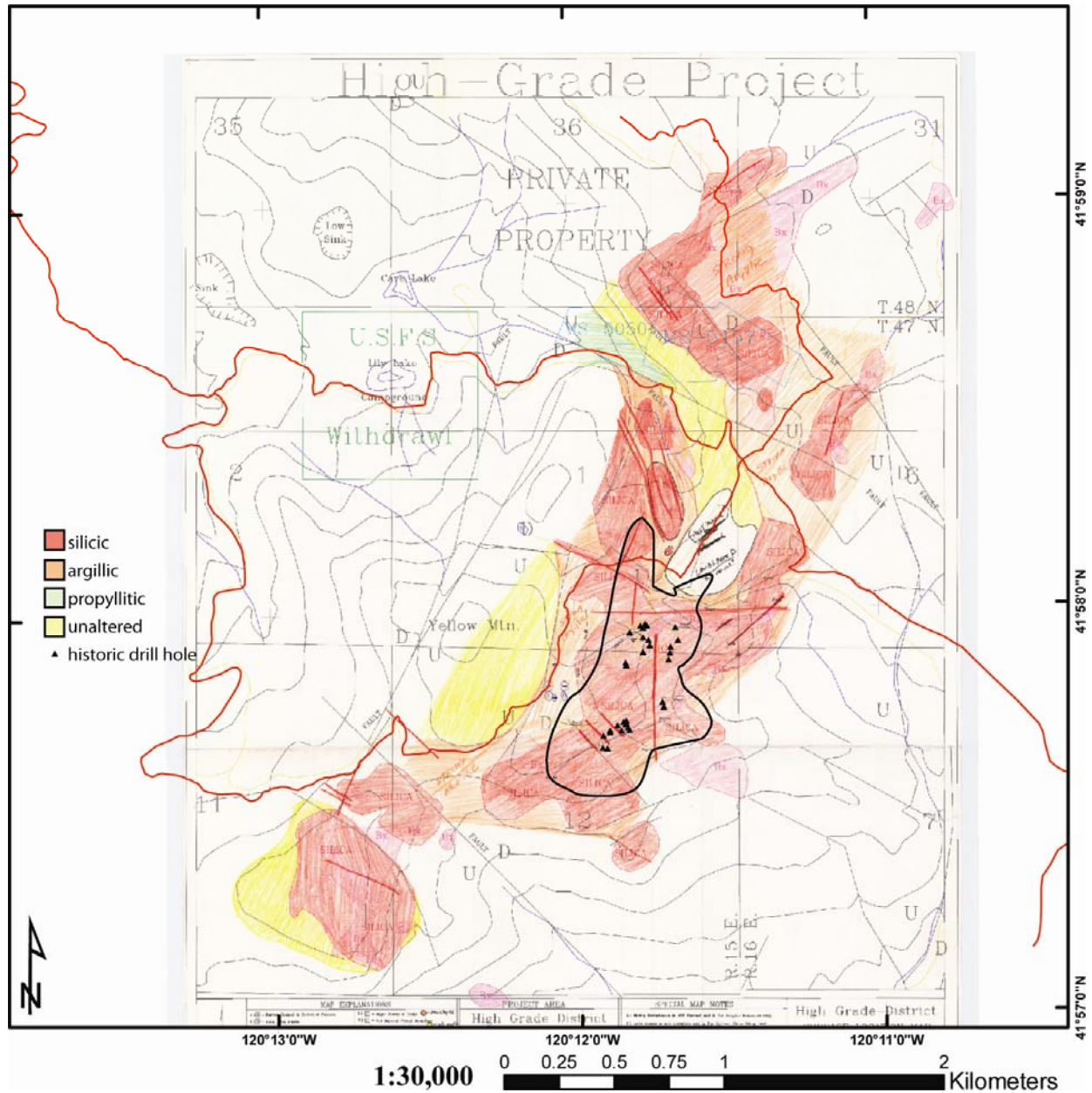


Figure 7. Alteration map from Nord Resources (Schuler, 1987). Historic drill holes are concentrated in the Ruby Ridge-Alturas Hill area. The surface deposit (fig. 6) is outlined in black.

Golden Predator Mines currently holds a district-wide claim position (www.goldenpredator.com/s/GoldenRidge.asp). In order to better understand the deposit Golden Predator financially sponsored this dissertation. The 2008 field season consisted of field mapping and sampling. Underground workings were examined where accessible. The 2009 field season involved 30 Reverse Circulation (RC) and 5 Core drill holes ranging in depth from 200 to 600 ft.

1.4 Previous Geologic Investigations

Donna Keats was commissioned by Atlas Precious Metals to conduct an M.S. study from 1982 to 1985 (fig. 19; Keats, 1985). Atlas drilled several holes in the northeastern portion of the district, but unfortunately no records of this activity have been retained. Nord Resources and Freeport McMoran Corp actively drilled, mapped, and sampled the central portion of the district, with work culminating in the development of a ~100,000 ounce resource estimate (fig. 7; Taylor, 1998; Schuler, 1986; Cox, 1985).

The rocks of the HGD can be divided into three stratigraphic suites on the basis of composition and chronology (table 3, figure 18; Vance and Shwertfeger, 2001; Schuler, 1986; Keats, 1985; Cox, 1984). These consist of a basal andesite, overlain by rhyolite and glassy rhyolite, which in turn is overlain by basalt flows (Matthewson, 2003; Vance and Shwertfeger, 2001; Keats, 1985; Cox, 1985; Hill, 1915). A felsic suite consists of a complex sequence of rhyolite flows, domes, and breccias. Alteration exists in all units except the basalt, and occurs both hydrothermally and deuterically. All of the rock units in the HGD are of Tertiary or Quaternary age (Egger and Colgan, 2009; Keats, 1985).

1.5 Regional Tectonics

The basement andesitic sequence was created in the terrestrial environment, inland from active subduction, along the paleo-Pacific coast (35-24 Ma) (fig. 8). Recent investigations by others, 20 miles south the study area, have been interpolated northwards where geologic correlations can be made with basement and mountain block tectonics (Egger and Colgan, 2009; Lerch, 2009; Ponce, 2009; Carmichael, 2006; Faulds, 2005; Camp and Ross, 2004). All rocks in the study area are of Tertiary or younger ages as constrained by vigorous age dating (Egger and Colgan, 2009). The evolution of the Warner Mountains, northeastern California, is presented in figure 9. The shift from compression to tension, approximately 15 Ma, corresponds with the onset of felsic volcanics. The work of Egger and Colgan, referenced here (fig. 9), is recognized as highly relevant in determining the temporal regional context of HGD mineralization, due to the close proximity (fig. 9) and modern methodology applied.

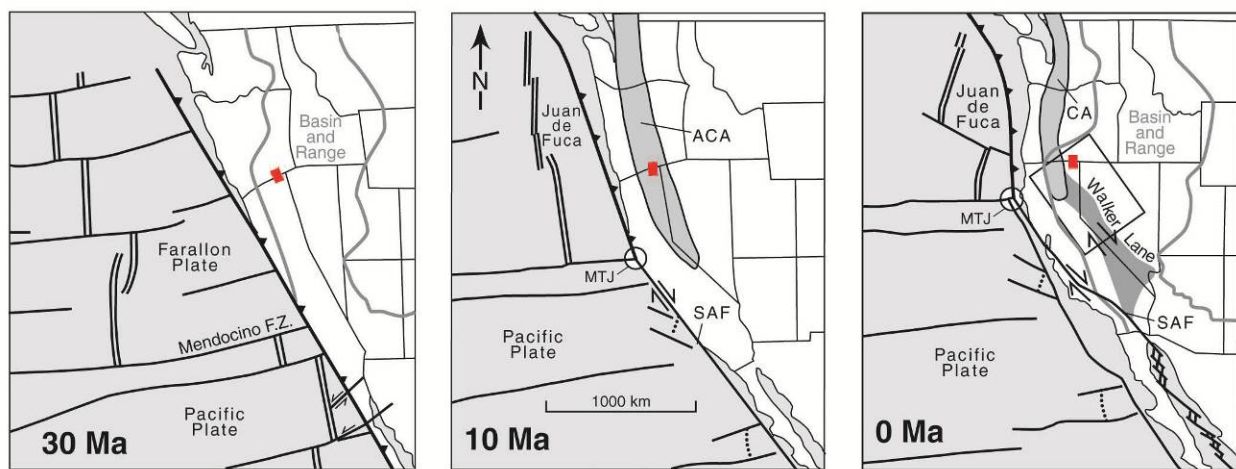


Figure 8. Cenozoic tectonic evolution of western North America, at 30, 10, 0 Ma (Faulds et al, 2005). The San Andreas fault has progressively lengthened over the past 20 Ma, as more of the Pacific plate has come into contact with North America. The evolution of this margin from convergent to transform is reflected within the continent as Walker Lane faulting, facilitating the extension of the Basin and Range. The red box indicates the study area.

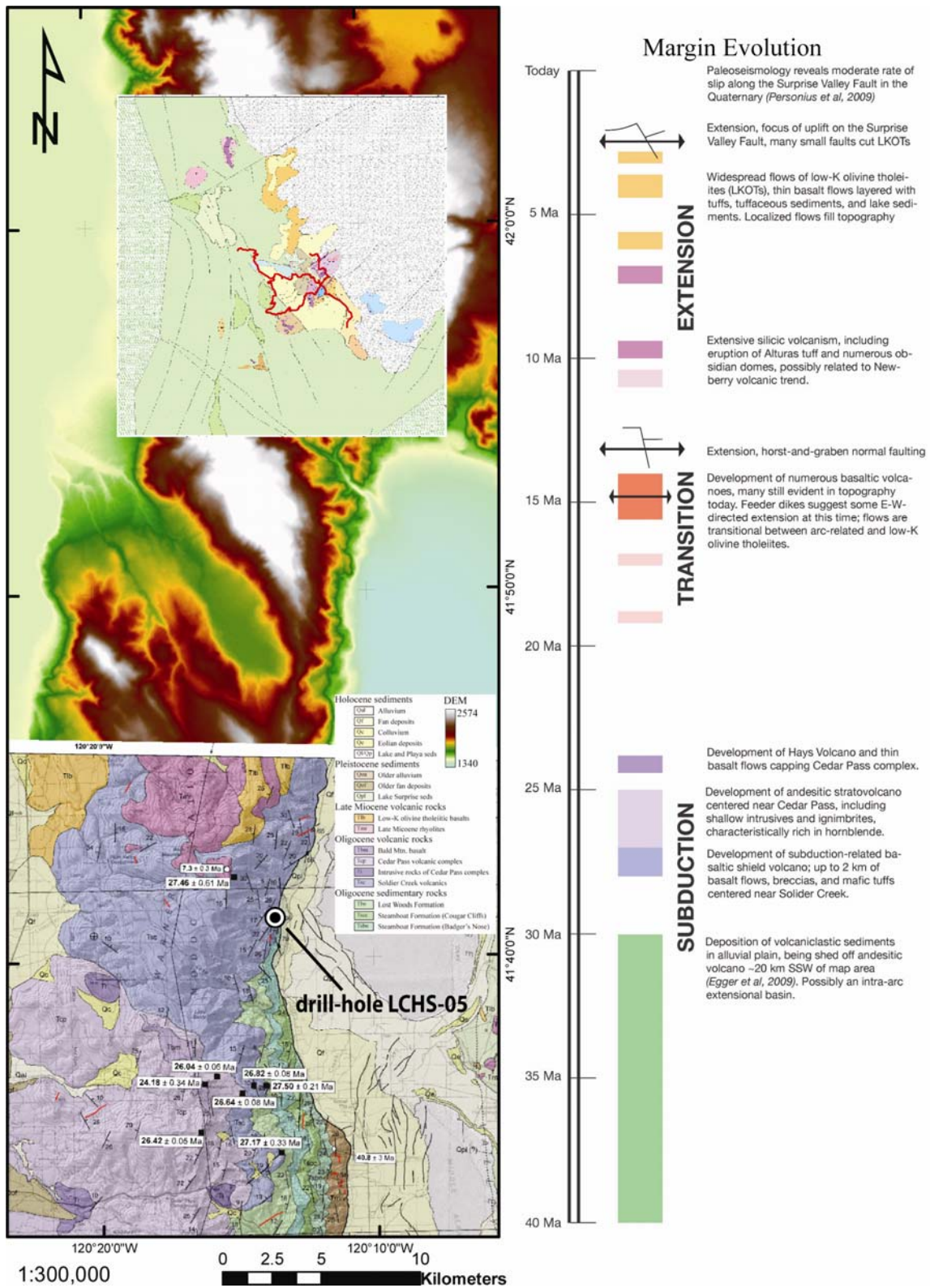


Figure 9. The work of Egger and Colgan (2009) is 20 km south of the extent of this study. A detailed margin evolution for the Warner Mountains is presented in the column at right.

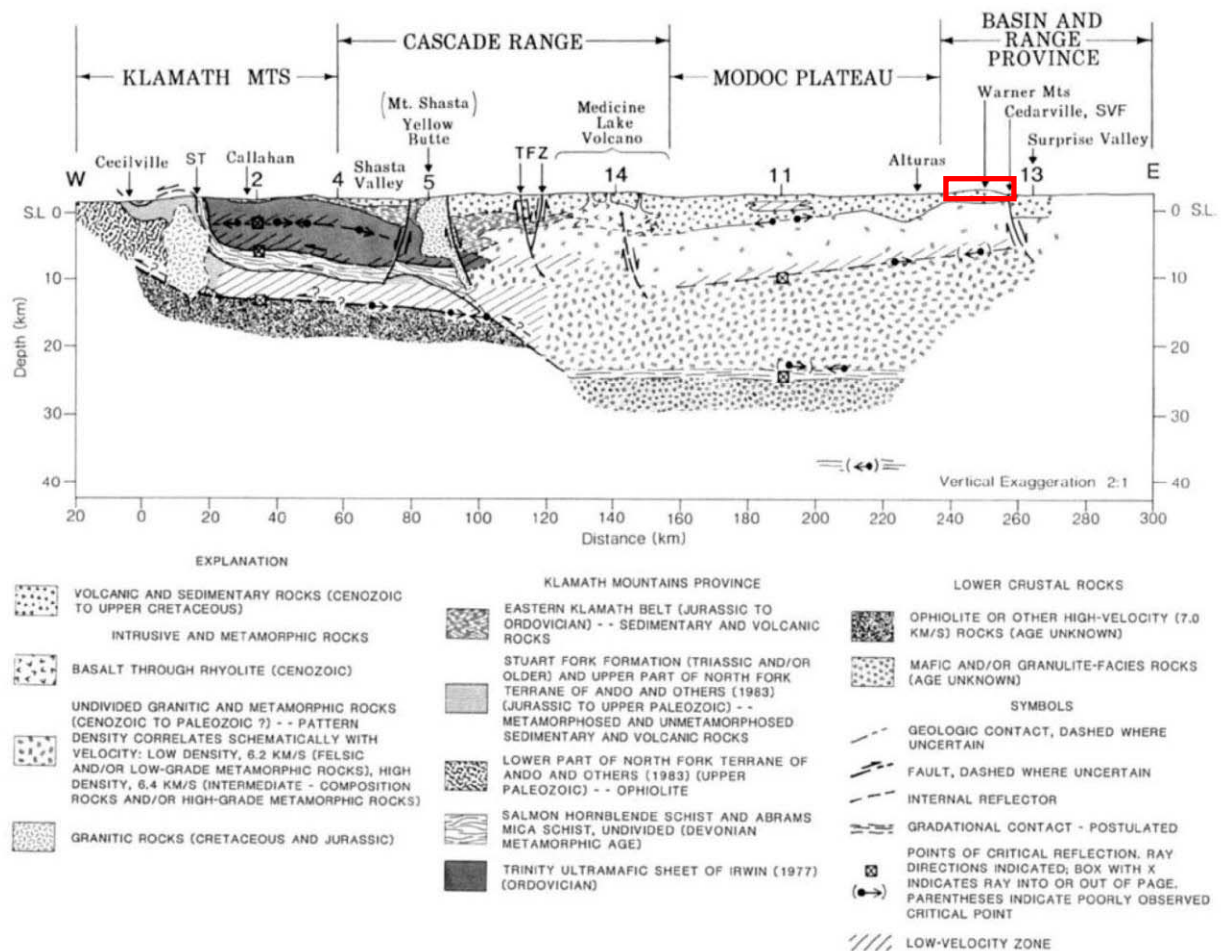


Figure 10. Geologic cross-section along west-east line from north-central California to northwestern Nevada (Fuis et al, 1987). The depth to moho for the Modoc Plateau is observed to be a minimum of 32km; the surficial volcanism and sedimentary package is underlain by roots of a magmatic arc (consisting of granitoid and metamorphic rocks). The study area is located in the red box.

The basal sequence of volcanic and sedimentary rocks, is underlain by crystalline igneous and metamorphic rocks constituting roots of magmatic arcs (Figure 10), interpreted from seismic-refraction results (Lerch, 2009; Fuis et al, 1987). A drill hole was completed to 1500m at location LCHS-05 (fig. 9) during geothermal exploration efforts in Surprise Valley. This drilling based stratigraphic column (fig. 11; Ponce et al, 2009) provides high resolution observations about the stratigraphic make-up of the Warner Mountain horst block.

Volcaniclastic units (sandstone, ash, portions of lahar) with a large glass component would allow preferential groundwater flow and dissolution of significant silica (fig. 11).

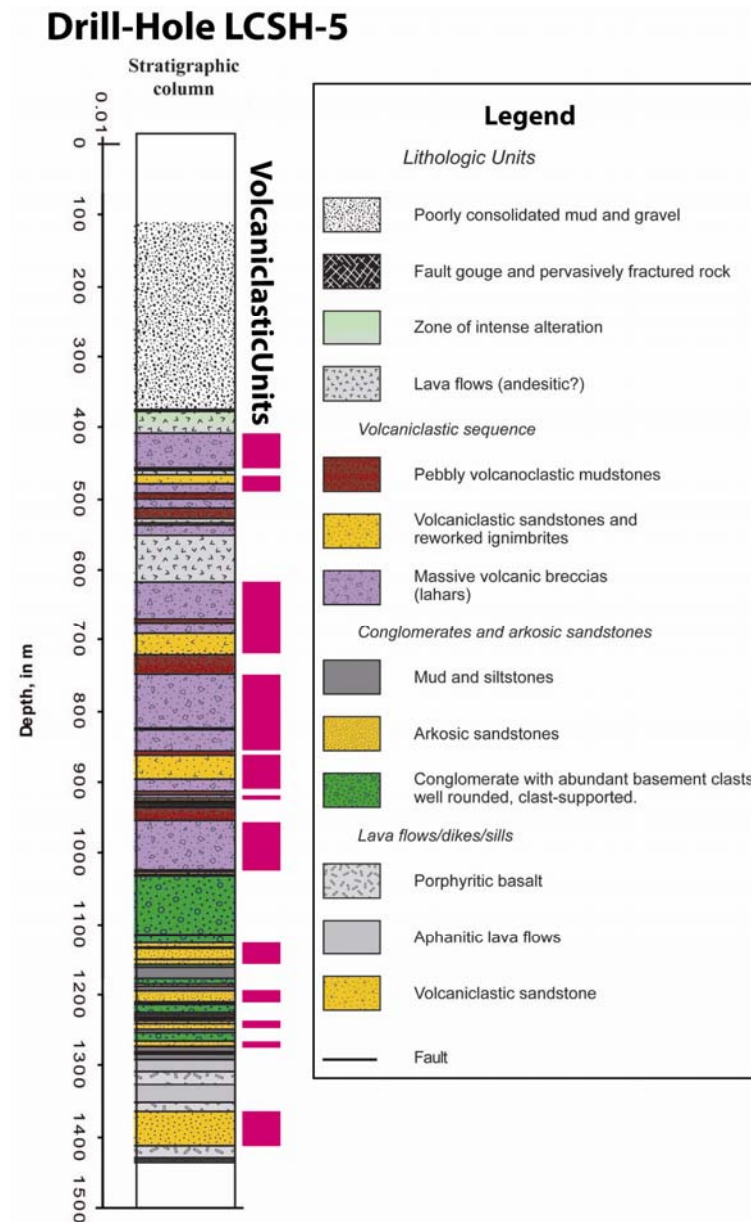


Figure 11. 1500m of the Warner Mountain horst block is represented in this stratigraphic column. This column was drilled in exploration of the geothermal prospect along the Surprise Valley fault. The LCSH-05 (Lake City slim hole) was drilled in conjunction with the

The change to a transitional environment began at approximately 16 Ma (fig. 9), and is age correlative with numerous late Miocene rhyolites south of the district (14.5Ma, south of

Cedarville; Egger and Colgan, 2009), as well as the host rhyolites within the district (14.6 Ma; Keats, 1985). This pulse of felsic magmatism occurs in conjunction with the influx of crustal heating related to the Yellowstone mantle plume (fig. 12; Camp and Ross, 2004). A speculated generative for the rhyolitic magmatism at HGD is superheating of a felsic magma chamber at depth by an impinging mafic intrusion.

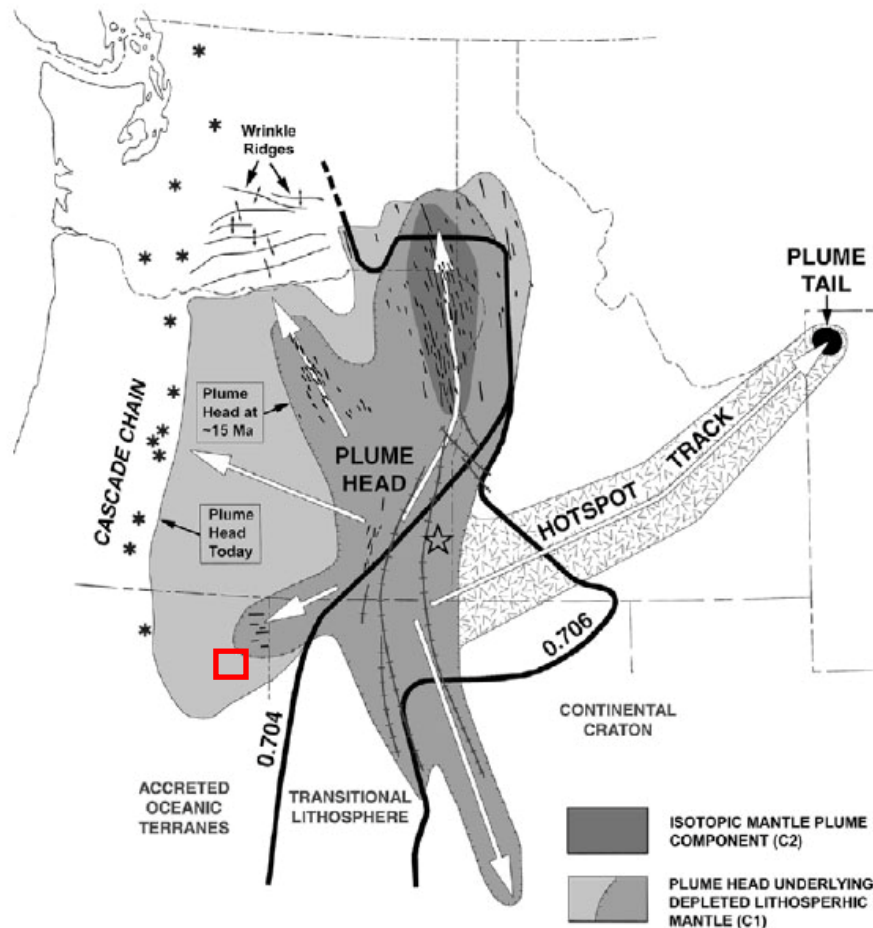


Figure 12. Two-stage spreading model of the Yellowstone mantle plume head, showing (1) approximate position of the plume head after impingement and rapid spreading (~15.0 Ma) and (2) its approximate position today after moderate rate spreading associated with asthenospheric drag and counter flow above the subducting plate (Camp and Ross, 2004). The red box indicates the location of the regional geologic map of this dissertation.

Basin and Range extension related to uplift of the Warner Mountain horst block has been constrained to 15 Ma through present (Egger and Colgan, 2009; Lerch, 2009; Colgan, 2005;

Duffield and McKee, 1986), with notable recent movement (<5 Ma) along the Surprise Valley Fault (Lerch, 2009). Extension within Western North America began approximately 50 Ma as a back-arc response to shallow subduction, this evolved into an isostatically-accelerated extensional environment as the undergoing plate floundered. As the plate margin evolved to accommodate Pacific motion, this trans-tensional environment evolved into the modern strike-slip configuration (fig. 8). Extension within the basin and range initiates in the southeast and moves northwestward through time and in magnitude. Those areas affected by both basin and range extension and walker lane transformation are reported to be extended more than 100%, however in the study are extension is estimated to be 5 – 10% (fig. 13, Van Buer, 2009).

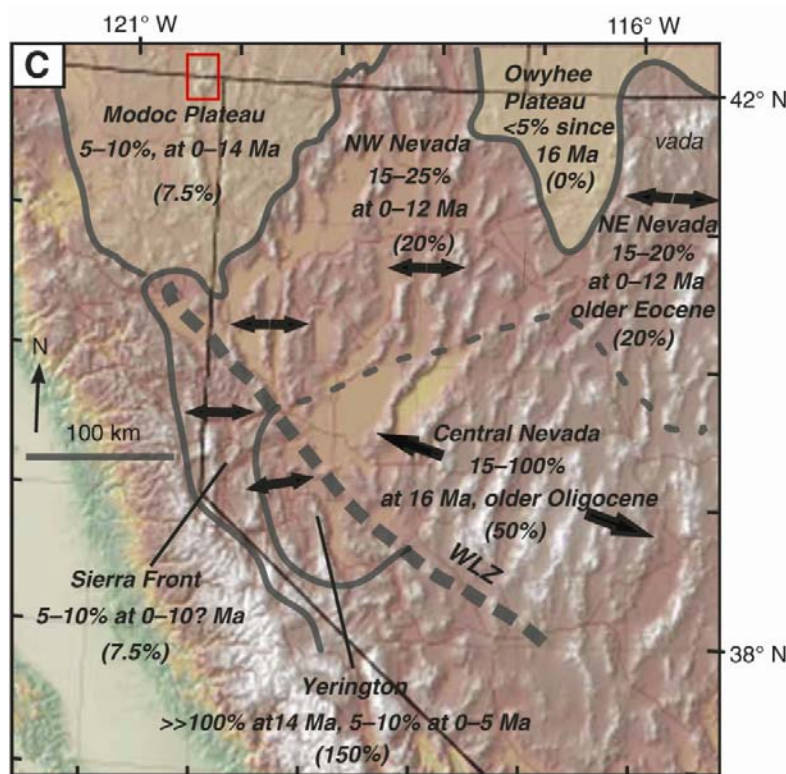


Figure 13. Generalized estimates of percent extension and its age east of Sierra Nevada, based on fault attitudes, tilt of Tertiary unconformity, and palinspastic restoration of cross sections. Northwestern Nevada from Colgan et al. (2006); Singatse-Wassuk Range from Surpless et al. (2002) and Profett and Dilles (1984); central Nevada from Smith et al. (1991); Modoc-Owyhee Plateau from Wells and Heller (1988); Actual values used for restoration are in parentheses. WLZ-Walker Lane zone. From Van Buer, 2009. Red box indicates study area, WLZ=Walker Lane zone.

The Walker Lane Transform Zone is mapped 200 miles south of the study area, and faulting through Fandango Pass (20 miles south) is likely subsidiary to Walker Lane movement (fig. 43, orange line). Walker Lane movement post-dates HGD magmatism and mineralization by 5 Ma. Extension in the study area has maximum tensile stress in the NW-SE direction (fig. 14); fractures trending NE experience maximum opening and host young (< 7 Ma) epithermal systems in Nevada fluids (Faulds et al, 2005).

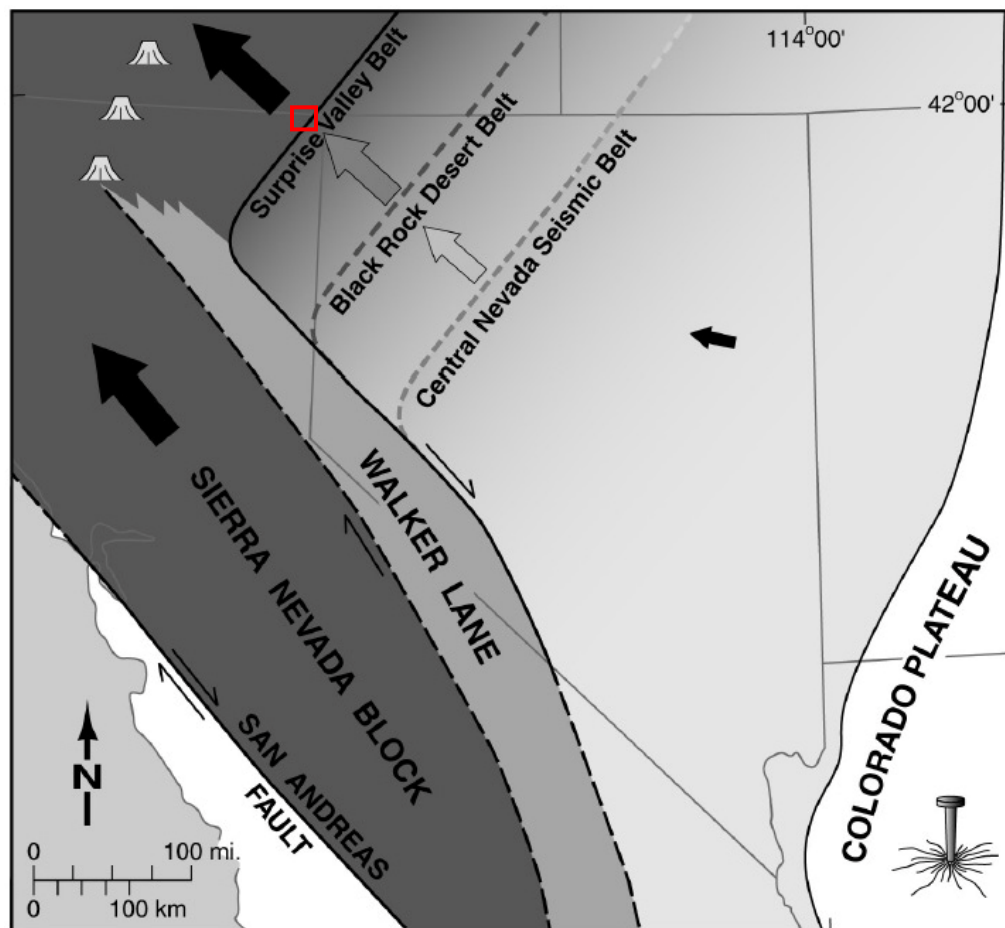


Figure 14. The figure, from Faulds et. al, 2005, depicts the general kinematics of the northwestern Great Basin. Dextral motion along Walker Lane accommodates the northwestward translation of the Sierra Nevada block relative to the Colorado Plateau. In the Great Basin, this northwestward movement is progressively disseminated among numerous north-northeast striking normal faults. The study area is shown in red.

2. STATEMENT OF THE PROBLEM

Mineralization of the HGD displays sufficient characteristics, namely abundant adularia, to classify mineralization as low-sulfidation epithermal and warrants exploration activities to test models of this type. The model to be tested (Fig. 7) is adapted from Buchanan and improvements suggested by others (Romberger, 1993; Berger and Eimon, 1983; Buchanan, 1981). An extensive knowledge base has been built through the study of exploited low-sulfidation epithermal vein deposits (John, 2001; Simmons and Browne, 2000; Ronde and Blattner; Hollister and Silberman, 1995; Herrera, 1993; Romberger, 1993; Cunnigham, 1991; Blaske et al., 1991; Berger and Henley, 1988; Heald et al., 1987; Berger and Silberman, 1985; Hayba et al., 1985; Silberman and Berger, 1985; Durning and Buchanan, 1984; Berger and Eimon, 1983; Buchanan, 1981). This study integrates field mapping and sampling with laboratory analyses to characterize mineralization and test the classic model at High Grade. In the study area, the presence of bonanza veins remains essentially untested, although their potential is recognized in well developed veining collected from dumps. Bonanza-grade gold mineralization (1+ opt) is reported in limited production records from camps in the more deeply eroded portions of the district (Hill, 1915). This company inspired project was undertaken in an attempt to better characterize and understand the mineralization encountered in the HGD.

The purpose of this study is to derive a site specific model based on data acquired by this research within the epithermal context. The integration of data collected over the district has produced a model for epithermal precious metal vein systems in the HGD (chapter 11). The problem to be solved is locating the high-grade gold mineralization. The application of this site-specific model will be used in targeting ore.

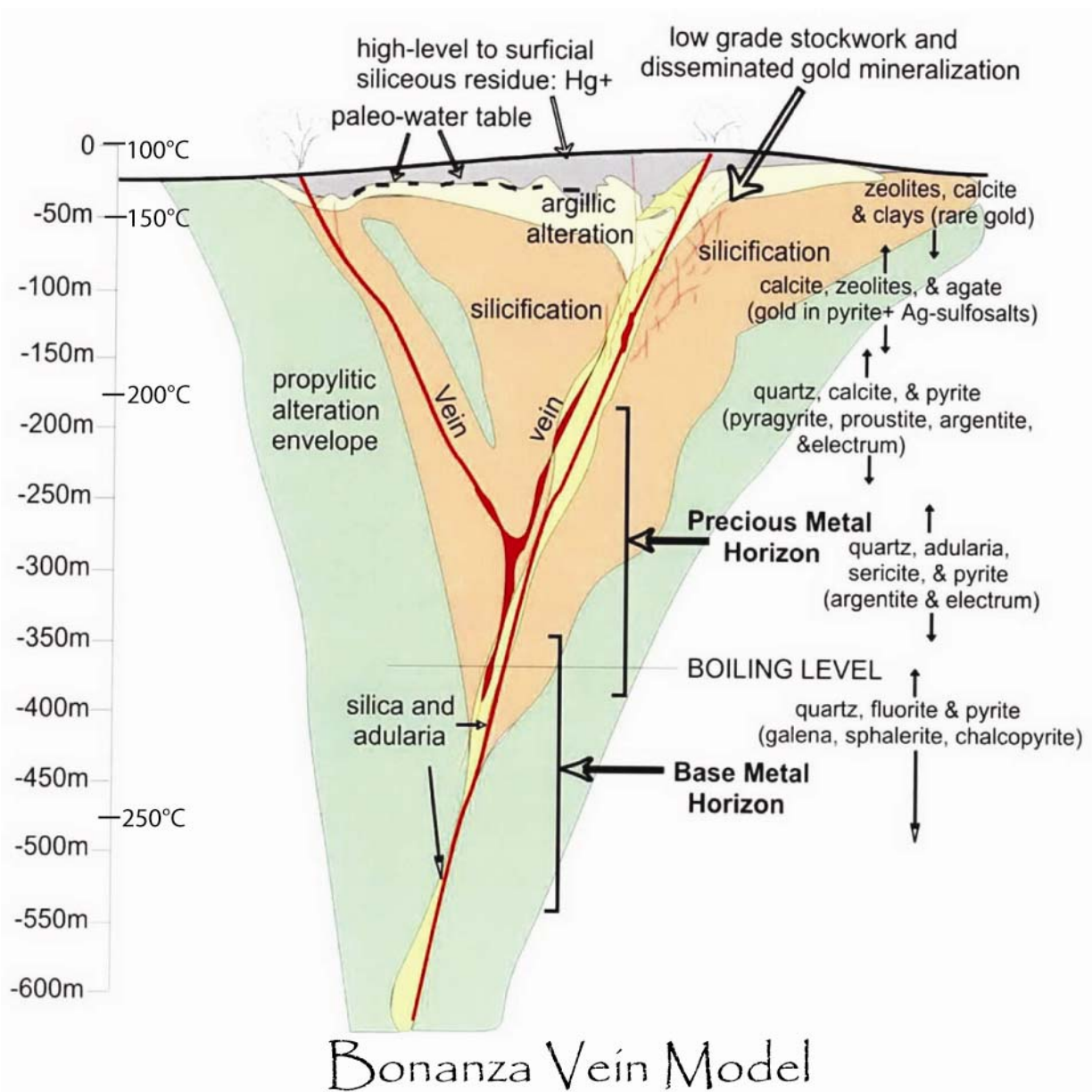


Figure 15. This general epithermal model takes mineralogy, textures, alteration, depth, temperature, and boiling into consideration. The vein seen above was sourced from depth and grew upward. Common minerals found are listed on the right with ore minerals listed in parenthesis. Alteration packages are seen in the colored portions of the figure; propylitic is green, silicic is orange, argillic is cream, the vein is red. Temperature and depth are represented along the left axis. This model has been adapted from Buchanan (1981).

2.1 Methodology

This section will discuss the methods used and provide brief descriptions, detailed descriptions of methodology are provided in chapter introductions. This study employs field mapping, sampling, drilling, and previous operator data to construct geologic maps and structural models in the study area. Analytical methods to be applied in this study include multi-element analyses, fluid inclusion studies, optical microscope and electron microprobe investigations, $\text{Ar}^{40}/\text{Ar}^{39}$ age dating, and oxygen isotope analyses.

Field mapping at both a local and regional scale have been performed. The study encompasses a 14 x 18 km region across the northern Warner Mountains with detail focusing in the 5 x 4 km HGD. Regional mapping is performed on enlarged 1:24,000 quadrangle maps, areas of significance are mapped on 1:1,000 topographic maps (generated in GIS) and aerial photography. Samples are collected and tagged with GPS locations. Data collected within the mining district was recorded in California State Plane Section 1 (NAD 1983 HARN) and differentially corrected for maximum accuracy. Regional observations and samples are located in UTM (Zone 10N and 11N) with average resolution of 10m WAAS. Acquiring samples of epithermal mineralization from bedrock was the primary focus, however float and dump samples account for ~60% of the 378 samples acquired. Silica body boulder fields were sampled on 50m spacing to investigate geochemical signatures and investigate zoning relationships.

Multi-element analyses provide a 130 sample, 48 element dataset. Homogenization and freezing temperatures are obtained for 45 thick-sections. Electron Microprobe analyses provide element maps and wavelength dispersive X-ray spectroscopy (WDS) scans, which can be interpreted to provide important paragenetic observations and identify metallic minerals. Three

ages from coarse adularia have been obtained from the three main vein systems, and 11 Oxygen isotope ($\delta^{18}\text{O}$) values have been obtained from hydrothermal quartz throughout the district.

Table 2. Methods used in this Dissertation were carried out in the time table below.

	May '08							Jan. '09										Jan. '10												Jan. '11						
	1	2	3	4	5	6	7	8	9	10	11	12	13	14	15	16	17	18	19	20	21	22	23	24	25	26	27	28	29	30	31	32	33	34	35	36
Field Mapping & Sampling	X	X	X	X									X	X	X	X	X																			
Drilling													X	X	X	X	X	X																		
Fluid Inclusion Studies									X	X	X	X						X	X	X	X	X	X	X	X			X	X	X						
Electron Microprobe								X	X	X	X	X								X	X	X	X	X	X	X										
Optical Microscope								X	X	X								X	X	X	X		X	X	X											
Geochemistry & Statistics					X	X				X	X	X	X						X	X	X	X	X	X	X					X	X	X				
Dissertation Writing												X	X					X	X	X	X	X	X	X	X	X	X	X	X	X	X	X	X	X	X	X

2.2 Quality of Data

This study has strived to maintain the highest level of data quality assurance and quality control (QA/QC). All samples collected were maintained in the supervision of the author and Golden Predator personnel. Sample submissions to ALS Chemex Laboratories (www.chemex.com) for geochemical analyses included 5% duplicates and blanks. All preparatory equipment was cleaned between samples to minimize cross-contamination. Calibration standards (pure CO₂ inclusions and ice) were used to validate the precision of fluid inclusion equipment; the electron microprobe was calibrated for Au and Ag during quantitative analysis. Isotopic data was professionally collected in conjunction with standards.

3. FIELD MAPPING

The 2008 field season focused on sample collection for target generation. Field work was carried out from a base camp to avoid time lost commuting to the property daily. Three months were spent hiking the district to produce field maps and sample collections. Each camp in the district was thoroughly walked and 278 samples of epithermal mineralization were collected. Orientation, mineralogy, texture, and physical observations (width, prevalence) were noted in the field, select samples were tagged for microscopic investigation.

The 2009 field season focused on detailed mapping of the northeast portion of the district to assist with interpretation of drilling in this area. An ATV was used to assist regional mapping that collected 160 data points, 100 samples, and produced a regional geologic map to situate the district in a regional context.

Local is geology is mapped on aerial photos at 1:1,000; this study produced a geologic map of the HGD at 1:7,500 (Appendix 2, plate 1). Regional Geology is mapped on USGS quads at 1:10,000; the regional geologic map (1:20,000) is provided in Appendix 2, plate 2.

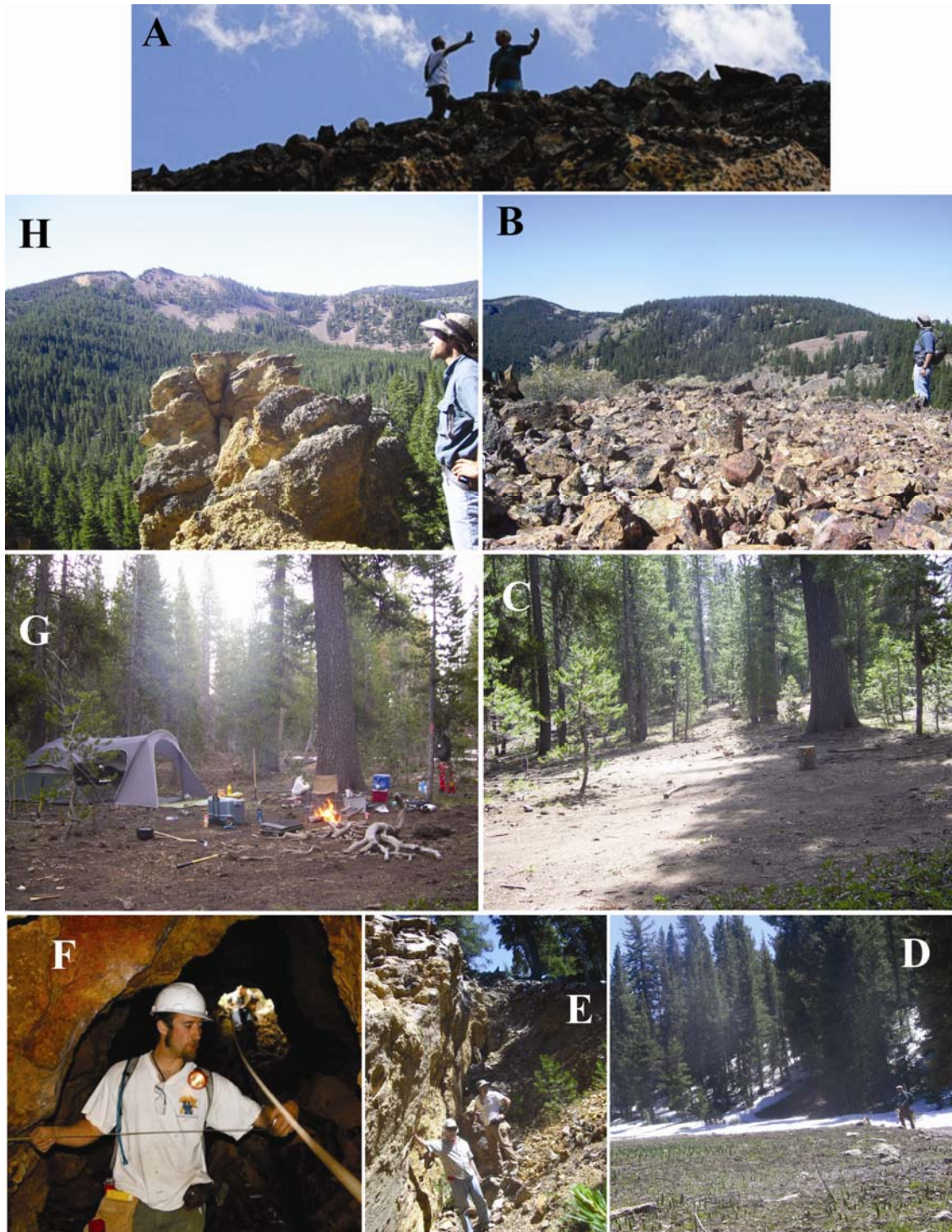


Figure 16. (A) The author and D. Hembree discussing structural features; (B) Discovery Mountain viewed from Ruby Ridge, looking southwest; (C) base camp site on departure; (D) hiking in Dismal Swamp; (E) the author and P. Goodell, PhD, stand alongside a stoped fracture zone in the Lodgepole camp; (F) underground mapping in the Klondyke camp; (G) base camp during 2008 field season; (H) viewing the Yellow Mountain normal faults, standing upon the Cave Lake Volcaniclastics (Tclv).

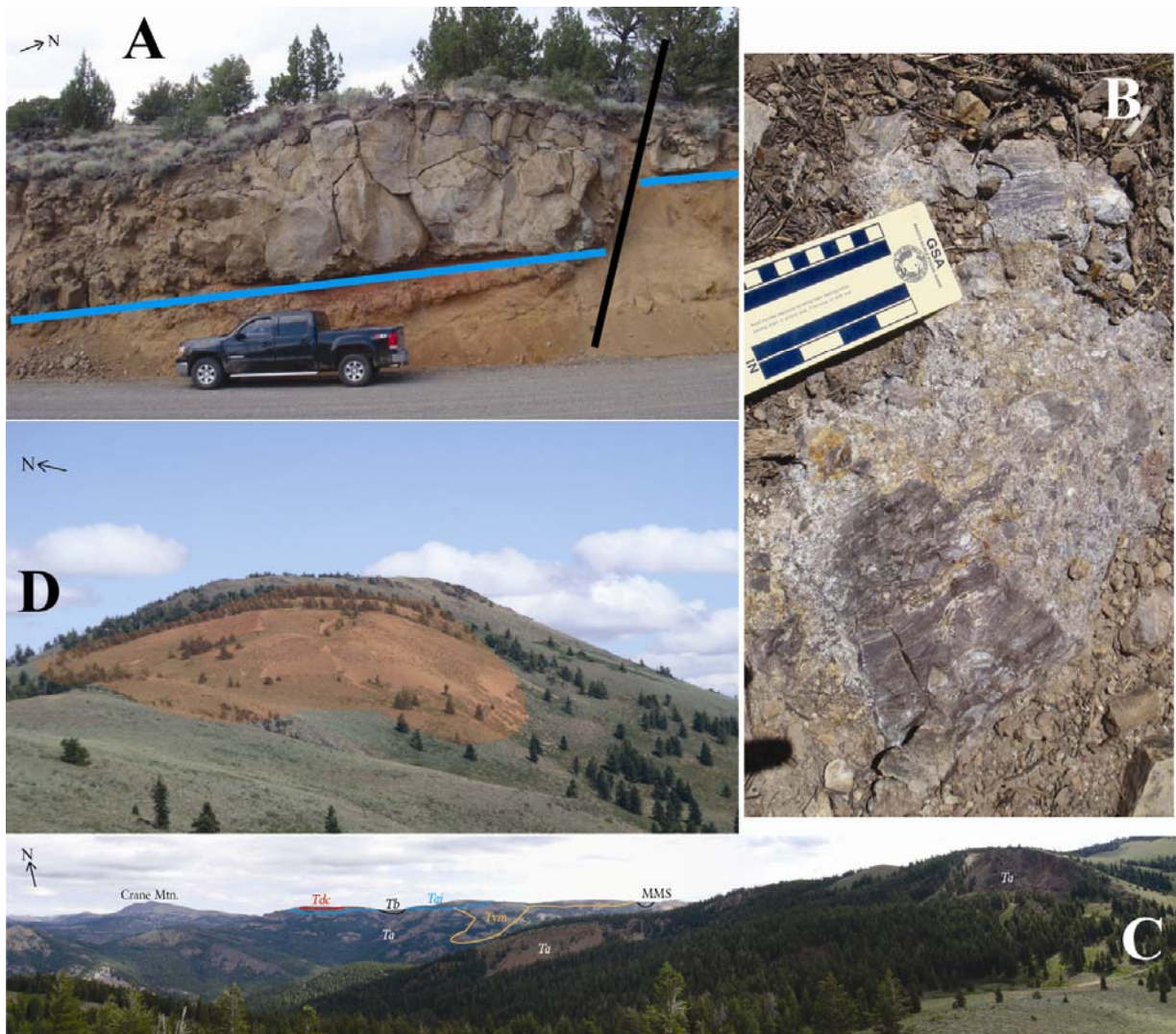


Figure 17. Observations made during regional mapping: (A) normal fault along the eastern flank of the Warner Mtn. Horst Block; (B) clasts up to 7 cm are recorded in multi-lithic breccia (Tmlb) occurring in the Bow Spring Rhyolite (Tbs); (C) Looking North from the Poison Lake Tuff with geology superimposed; (D) Mt. Vida Peak from the West (orange polygon indicates the extent of the Mt. Vida Porphyritic Rhyolite [Tmvp]).

3.1 Stratigraphy

Table 3. Stratigraphic units of the study area. Igneous phase is indicated (M=mafic, I=intermediate, F=felsic) along with geologic mapper (DK=D. Keats, MF=M. Feinstein) and whether a prospective unit displays silicic alteration. Geographic locations of units are provided in stratigraphic columns across the northern Warner Mountains in figure 9.

Phase	Map Symbol	Explanation	Host Silicification	Mapper
	Qt	Talus cover		
	Qs	Soil Cover		
F	Tbv	Bidwell vent/tuff		MF
F	Tbvo	Bidwell Obsidian		MF
M	Tb	Steen's Basalt		MF
F	Tcv	Vitrophyre		MF
F	Trvb	Pumiceous vent breccia		DK
F	Tdc	Deep Creek Rhyolite flow		MF
F	Tai	Andesine Ignimbrite		MF
F	Tct	O'Connor Blue Tuff		DK
F	Toi	O'Connor Ignimbrite		MF
F	Tcd	Crossroads Rhyolite Dome		DK
F	Tclt	Cave Lake Tuff		MF
F	Tclv	Cave Lake coarse volcanics		MF
F	Tkc	Kelly Creek Tuff		MF
F	Trd	Rhyolite porphyry flow dome	X	DK
F	Trt	Rhyolite porphyry vitric flow	X	DK
F	Trp	Vitric rhyolite porphyry		DK
F	Tym	Yellow Mtn. porphyritic rhyolite	X	DK
F	Tkq	Klondyke flow/dome; qtz latite porphyry	X	DK
F	Tbs	Bow Spring Rhyolite	X	MF
F	Tsp	Sugar Peak Rhyolite porphyry		MF
F	Tpl	Poison Lake Tuff		MF
F	Tmvp	Mt. Vida peak Rhyolite porphyry	X	MF
F	Tmlb	Hydrothermal Breccia	X	MF
F	Tlq	Lodgepole aphyric quartz latite flow/dome	X	MF
F	Ttss	Sunshine poorly welded silicified lithic tuff	X	MF
F	Tml	Modoc latite flow	X	MF
F	Tmpr	Moonlight pumiceous rhyolite	X	MF
F	Tfr	Flow banded aphyric flow domes	X	MF
F	Ttb	Poorly welded pumiceous brown tuff		MF
F	Tdmr	Discovery Mtn. rhyolite flow/dome	X	DK
F	Tcrr	Consolidated Mtn. rhyolite dome	X	DK
F	Tcrf	Consolidated Mtn. rhyolite flow	X	DK
I	Tam	Andesitic Mudflow		DK
I	Ta	Andesite		DK



30

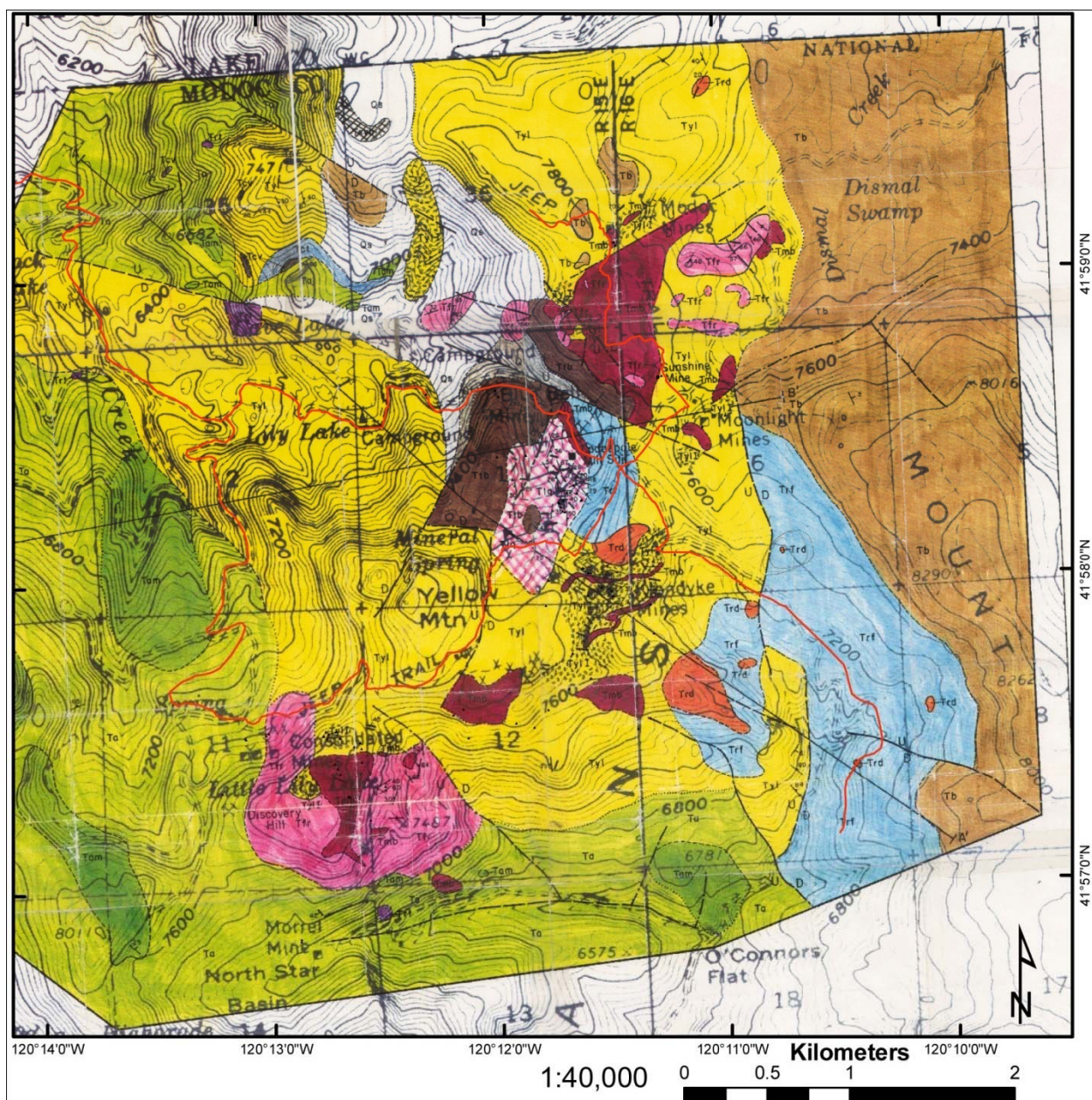


Figure 19. Geologic map from MS Thesis sponsored by Atlas Minerals. (Keats, 1985).

3.1.1 Basal Andesites (Ta & Tam)

The andesitic basement of the study area is similarly described to the south and thoroughly dated (fig. 9; Carmichael et al, 2006; Egger and Colgan, 2009; Martz, 1986). The interbedded andesite flows, mudflows, and pyroclastics are roughly correlative to the Soldier Creek volcanics and Cedar Pass volcanics in the central Warner Mountains, 30km South (Egger and Colgan, 2009; Martz, 1986). These units have age constraints between 30 and 20 Ma, and are composed of andesitic stratovolcanoes and related flows, and basaltic shield volcanoes and related flows. To interpret the basal intermediate sequence of the HGD, as a single rock package, it was formed by the same cycle of volcanism that deposited the Oligocene volcanic of the central Warner Mountains (fig. 9, 11). This basal sequence of volcanic and sedimentary rocks, is underlain by crystalline igneous and metamorphic rocks constituting roots of magmatic arcs (fig. 10), interpreted from seismic-refraction results (Fuis et al, 1987).

The andesite flows within the district are largely unaltered, except those surrounding Discovery Hill extending southwestward to Poison Lake (fig. 20-C). The aphanitic andesite flows have been argillized at their western contact with the aphanitic rhyolite dome which comprises the bulk of Discovery Hill (fig. 20-F, G). They have also been intensely propylitized near several of the shafts of the Consolidated Mines (fig. 47-C). The porphyritic andesite flows in the North Star Basin to the south of Discovery Hill have also been propylitized. Flows south of Morrel Mines are megascopically porphyritic (fig. 20-E), they contain 10 to 15% plagioclase feldspar phenocrysts, which range up to 3 cm in length, in an aphanitic, greenish grey groundmass. The flows are cut by veins of epidote, up to 2 cm, and epidote filling vesicles (fig. 20-D).

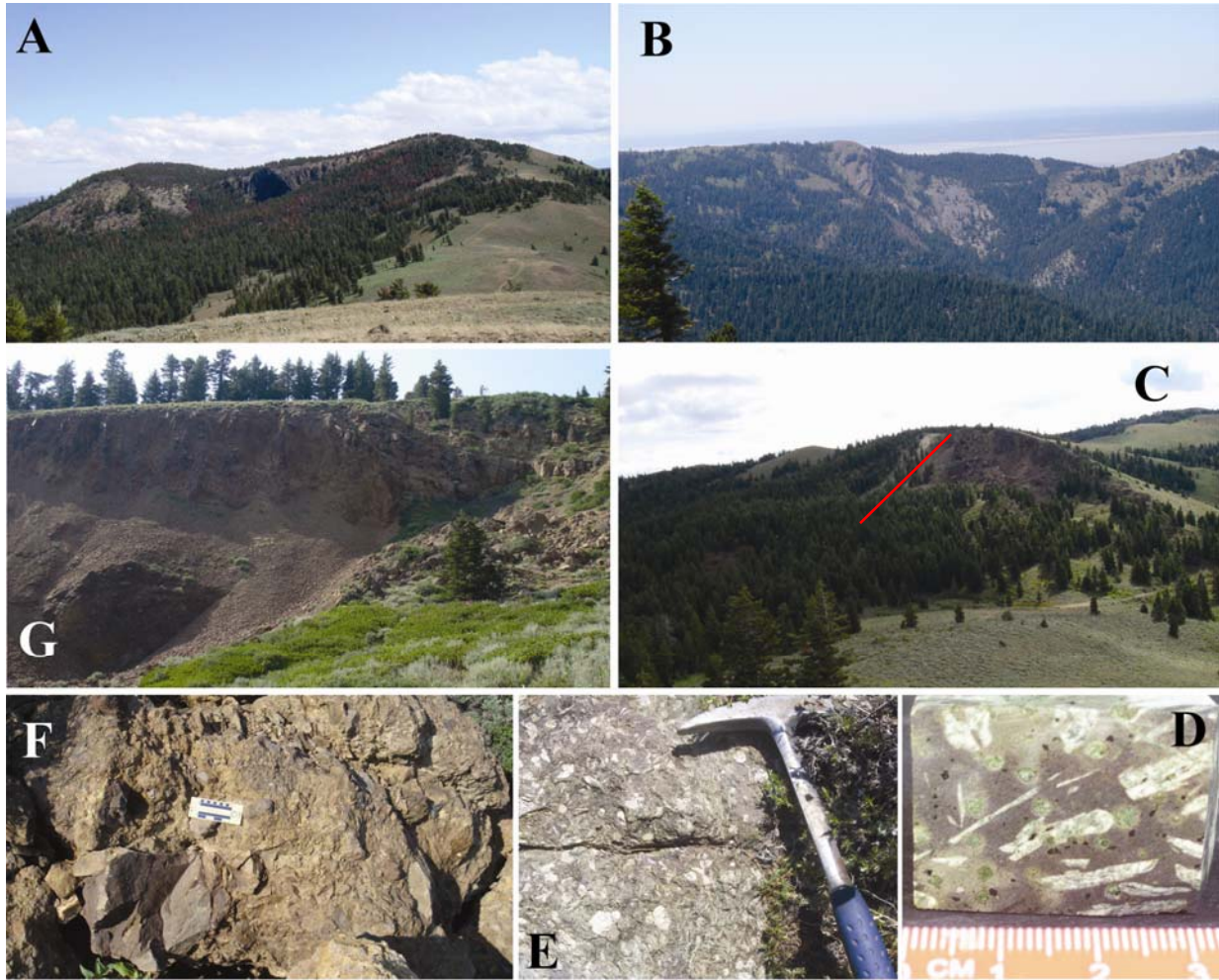


Figure 20. (A) Thick andesite flows dip east atop Mt. Vida. (B) Andesitic mudflows form the resistant peaks along the western front of the Warner Mountain horst block. (C) N-S normal fault cuts andesite near Poison Lake. (D) Altered andesite with plagioclase laths and vesicles filled with epidote and calcite. (E) Fresh andesite outcrop, south of North Star Basin, is 35% plagioclase. (F) Large boulders incorporated in andesite mudflow. (G) Fault scarp in andesite, southwest of Discovery Mountain.

Within the North Star Basin (fig. 3), along the southern boundary of the map area, the flows are strongly porphyritic with abundant phenocrysts of plagioclase feldspar (fig. 20-D, E). In this area, the porphyritic flows form prominent exposures, whereas the aphanitic flows are poorly exposed and occur primarily in drainages and road cuts. Microscopically, the dominant phenocryst phase is andesine (An 48), which is euhedral except where broken or altered along margins. Highly altered mafic minerals are present as a subordinate (58%), smaller (0.5-1.7 mm)

phenocryst phase. Relict subhedral forms of these phenocrysts commonly display an amphibole cross-section (fig. 20-D). Up to 15 percent magnetite is present as both primary euhedral (0.811) forms and secondary granular anhedral forms. The groundmass is composed of pilotaxitic, subhedral andesine (An 39-43) microlites which average 0.2 mm in length.

Alteration of these flows has yielded a mineral assemblage typical of a propylitically altered rock. Plagioclase feldspar phenocrysts show more pervasive alteration than do the microlites. Margins and interiors of the andesine phenocrysts have been altered to large amounts of calcite, lesser amounts of sericite and epidote. Relatively fresher parts of the feldspar phenocrysts contain a light dusting of kaolin clays. Amphibole (?) phenocrysts characteristically show complete alteration to an assemblage of epidote, Chlorite, and calcite. Relict amphibole rims and fractures are heavily coated by hematite. Epidote veinlets commonly crosscut larger phenocrysts and microlites of the groundmass, and contain localized parallel replacements of calcite. Calcite is especially abundant where the veins cut phenocrysts. Small amounts of zeolite are also present, predominantly as highly localized open-space fillings.

Outcrops of the andesitic mudflows are laterally discontinuous and occur as prominent ridge-forming knobs (fig. 20-A, B) or as smooth exposures of low relief in stream or road cuts. They are dark green to greenish brown in color, and highly variable with respect to fragment size, composition, and clast:matrix ratio. Clasts vary from angular to sub-round in a lithified muddy matrix (fig. 20-F). They are devoid of sorting, bedding, or grading. Fragment composition varies from abundant flow-banded, white to purple volcanic rocks, through moderate amounts of both aphanitic and porphyritic andesite, to rare occurrences of unidentified volcanic and sedimentary rocks. The poor sorting, angularity of clasts, variable fragment size

and composition, and localized distribution collectively suggest near-source deposition controlled by pre-existing topographic depressions.

The andesite flows comprise the lowermost and oldest rocks within the basal intermediate sequence (table 3, fig. 18), and contain other rock types of the sequence interbedded in their upper stratigraphic portions. They have been intruded by members of the silicic sequence, but intrusive contacts are rarely exposed. Andesite flows surrounding Discovery Hill and Sugar Peak are intruded by both the aphanitic rhyolite domes and the multi-lithologic intrusive breccia. The andesite is conformably overlain by flows of the Yellow Mountain rhyolite (Tym) and Cave Lake tuff (Tclt), although in most places this contact is not exposed. Andesite flows are conformably overlain by the Steens Basalt, observed at Crane Mountain (fig. 17-C).

3.1.2 Felsic Suite

The felsic suite within the district contains a series of intrusive and extrusive rocks whose emplacement and extrusion overlap in time and space. Rhyolitic magmatism began with the emplacement of several intrusive aphanitic rhyolite domes and multiple exogenous aphanitic rhyolite domes. This early phase was followed by the emplacement of the extrusive-intrusive Yellow Mountain porphyritic rhyolite complex, and by the younger multi-lithologic intrusive breccia. The waning phase of this cycle began with the deposition of porphyritic rhyolite flows, and ended with the emplacement of several porphyritic rhyolite domes. Metallization in the district is associated with rocks of the first two phases of magmatism, whereas those of the third phase are unmineralized (fig. 18), although locally altered.

Tym - Yellow Mountain Porphyritic Rhyolite

The Yellow Mountain Porphyritic Rhyolite (Tym) is the most expansive rhyolite in the study area. Faulting related to uplift, during extension is recorded in a series of listric faults (fig. 21-top) that display approximately 400 ft of movement (fig. 21-C). Lateral dimensions are estimated at 11 km², taking cover into consideration and expanding the flow accordingly. This unit is largely un-mineralized; the silica body of Ruby Ridge may be hosted by an additional rhyolite dome within this unit.



Figure 21. Yellow Mountain, located in the center of the HGD, has experienced slump faulting related to uplift and extension (top; looking south-southwest). Massive yellow mountain rhyolite displays near columnar jointing and possibly vertical flow foliation at peaks seen in A and B, respectively. The main fault scarp (bottom, looking east) along the west side of Yellow Mountain displays approximately 400 ft. of movement.

Felsic units encountered outside of the HGD have not been previously described. Thin-sections were prepared from each unit and are presented below. Captions accompany full-section photos taken under cross-polarized light and cover general features, detailed petrographic

descriptions follow thin-section photos. Sample labels appear as dark etching in the right of some sections.

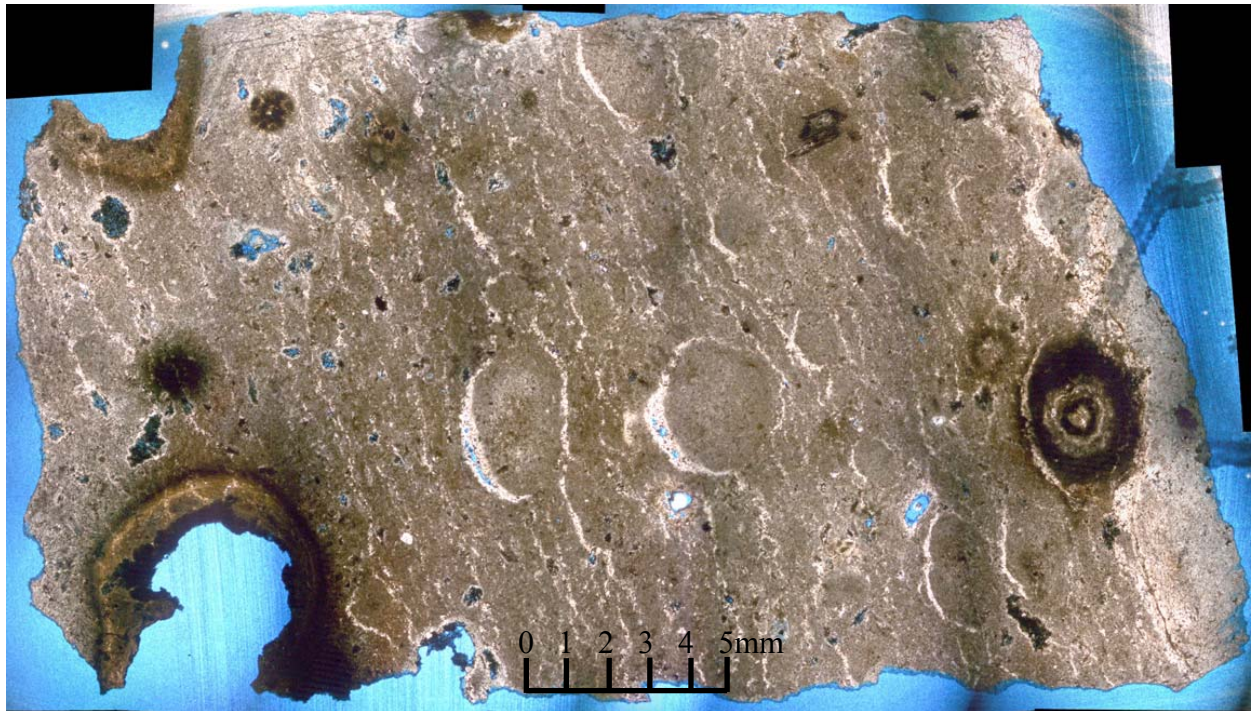


Figure 22. Ttb – Brown Tuff: This unit is encountered in the central part of the HGD, within the depression of Cave Lake, and extends eastward underneath the Yellow Mtn. Latite (Tym). This unit has a mappable extent of 1.3 km², drilling has confirmed this unit beneath Alturas Hill and MMS. Lateral thickness variations have not been measured. Color is light pink. To the writer's knowledge, this unit has not been described before and the attempt to correlate this unit regionally has not been made. This unit is of lesser importance.

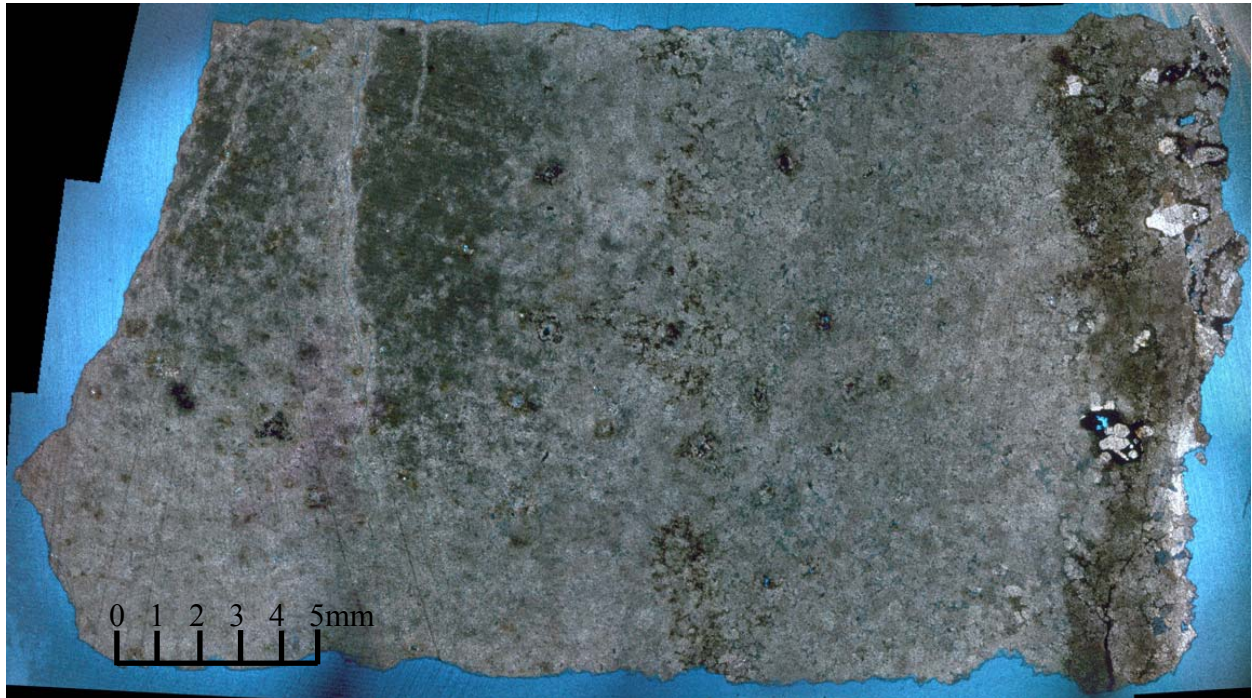


Figure 23. Tdmr – Discovery Mountain Rhyolite: This unit is encountered to the SW portion of the HGD and contains a multi-lithic breccia. This unit is approximately 1.2 km². No structural measurements were possible. Its origin or source is not known. Lateral thickness variations have not been measured. Color is pink. To the writer's knowledge, this unit has not been described before and the attempt to correlate this unit regionally has not been made. This unit has been mineralized (fig. 48, 63, 64).

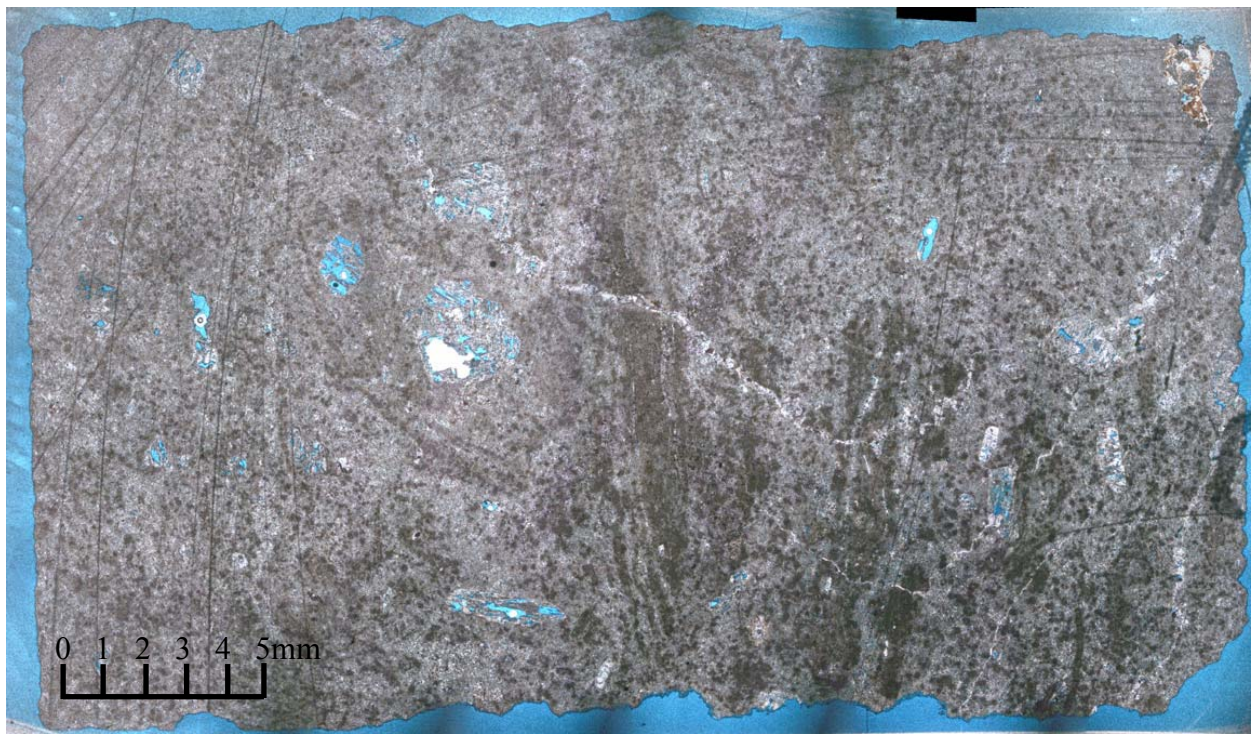


Figure 24. Terf – Consolidated Rhyolite Flow: This unit is encountered to the SW portion of the HGD and contains a multi-lithic breccia. This unit is approximately 0.3 km². Its origin or source is not known. Lateral thickness

variations have not been measured. Color is light pink. To the writer's knowledge, this unit has not been described before and the attempt to correlate this unit regionally has not been made. This unit has been mineralized (fig. 63).

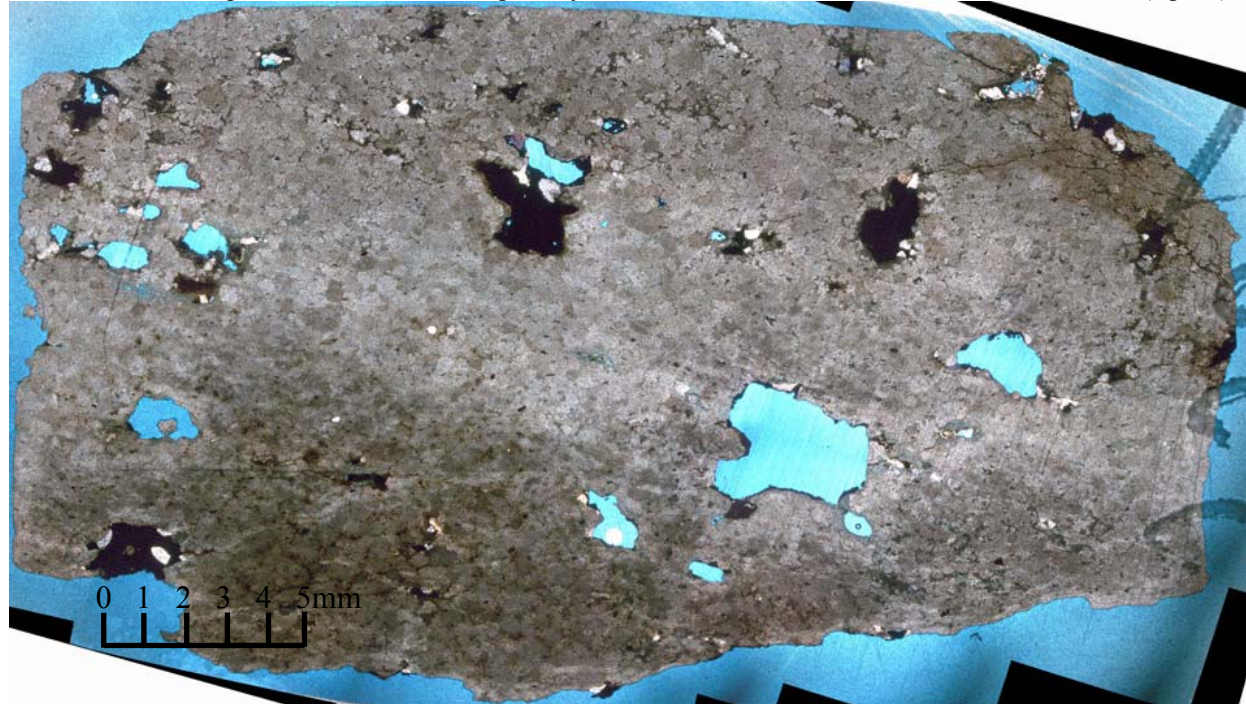


Figure 25. Consolidated Rhyolite Dome: This unit is encountered to the SW portion of the HGD and contains a multi-lithic breccia. This unit is approximately 0.07 km². Its origin or source is not known. No structural measurements were possible. Lateral thickness variations have not been measured. Color is light pink. To the writer's knowledge, this unit has not been described before and the attempt to correlate this unit regionally has not been made. This unit has been mineralized (fig. 64).

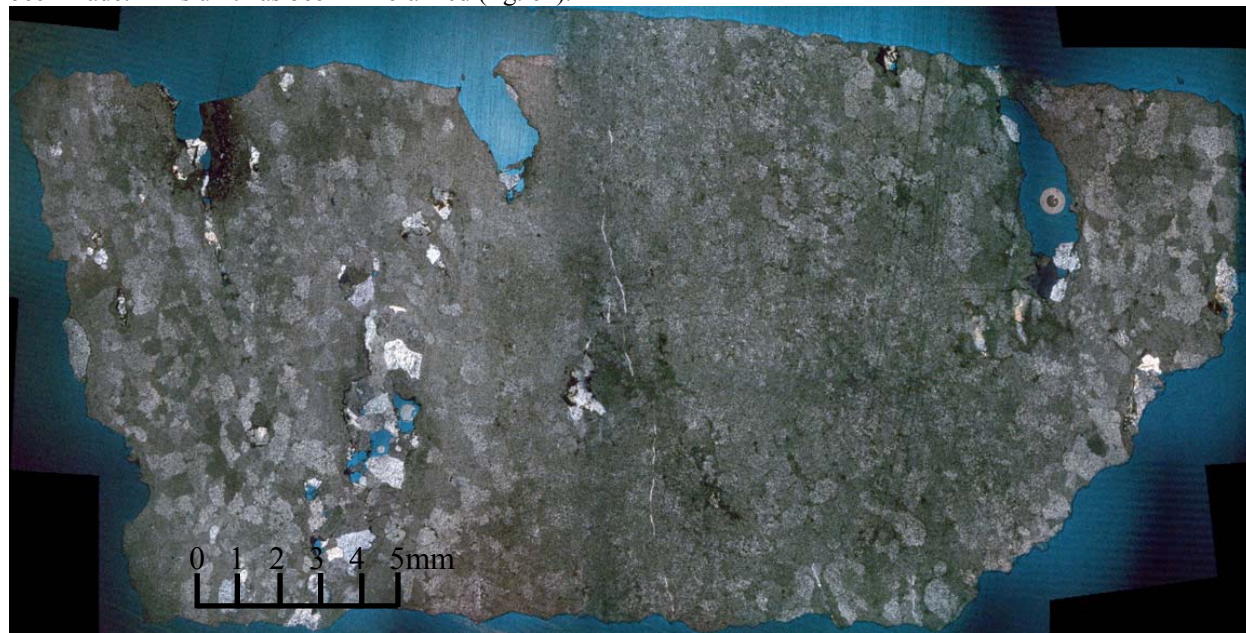


Figure 26. Tlq – Lodgepole Aphyric Quartz Latite: This unit is found in the north-central part of the HGD. This unit is approximately 0.5 km². Its origin or source is not known. Lateral thickness variations have not been measured. Color is light pink/gray. To the writer's knowledge, this unit has not been described before and the attempt to correlate this unit regionally has not been made. This unit hosts mineralization (fig. 66).

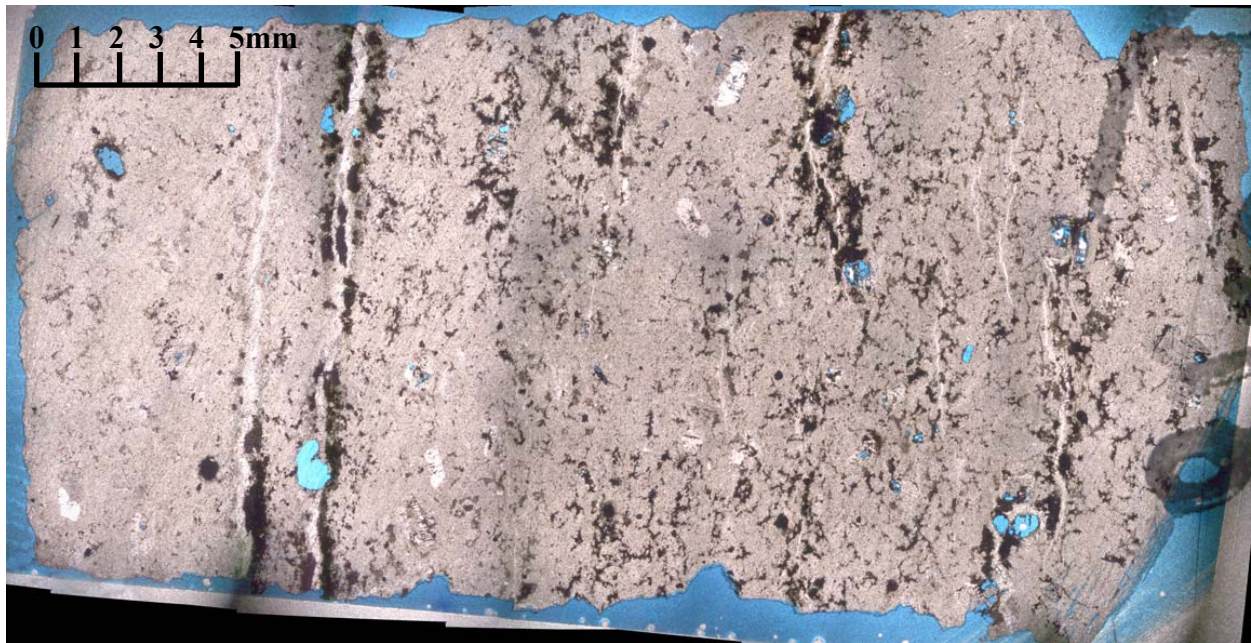


Figure 27. Tmvp – Mt. Vida Peak Rhyolite: This unit is found 2.5 km south-southwest of Discovery Mtn. This unit is approximately 0.35 km². Its origin or source is not known. Lateral thickness variations have not been measured. Color is pink. To the writer's knowledge, this unit has not been described before and the attempt to correlate this unit regionally has not been made. This unit is of lesser importance.

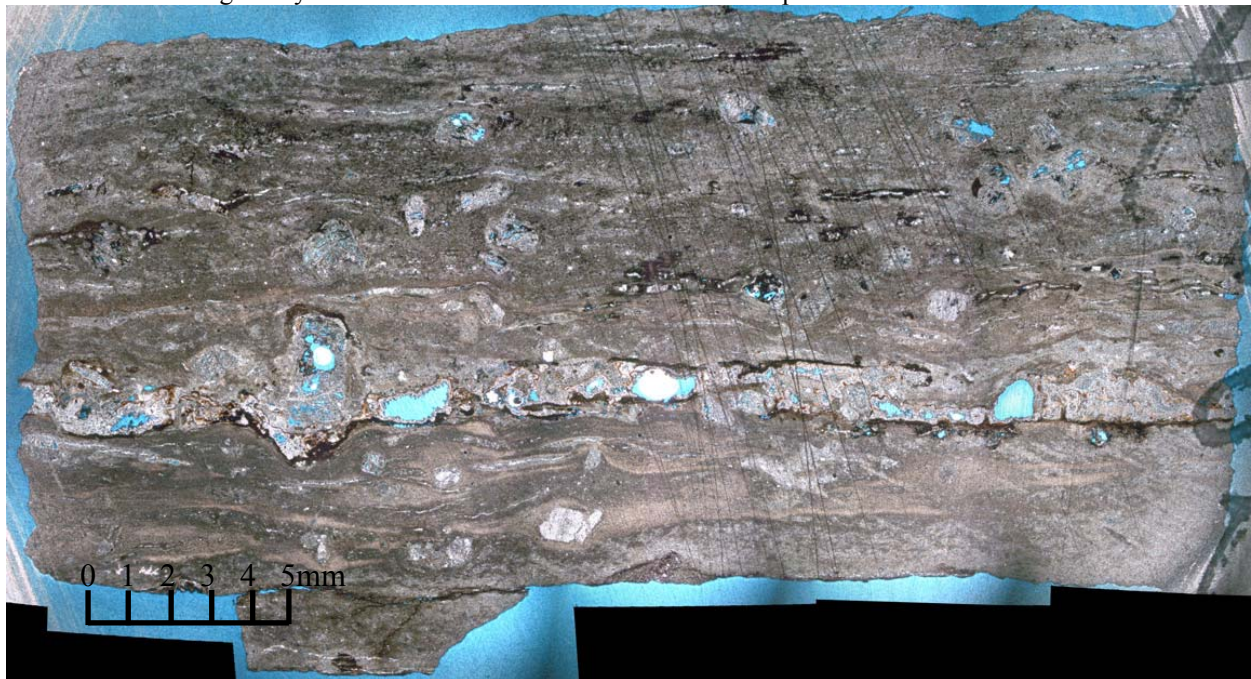


Figure 28. Tmpr – Moonlight Porphyry Rhyolite: This unit is found in the central eastern part of the HGD. This unit is approximately 0.5 km². Its origin or source is not known. Lateral thickness variations have not been measured. Color is dark pink. To the writer's knowledge, this unit has not been described before and the attempt to correlate this unit regionally has not been made. This unit hosts the easternmost camp of the district.



Figure 29. Tkq – Klondyke Glassy Quartz Latite: This unit is found in the east-central part of the HGD. This unit is approximately 0.35 km². Its origin or source is not known. Lateral thickness variations have not been measured. Color is light pink. To the writer's knowledge, this unit has not been described before and the attempt to correlate this unit regionally has not been made. This unit hosts mineralization (fig. 65).



Figure 30. Tkc – Kelly Creek Tuff: This unit occurs immediately south of the Sugar Peak Rhyolite (Tsp). The unit is approximately 3 km². Color is light gray. To the writer's knowledge, this unit has not been described before and the attempt to correlate this unit regionally has not been made. This unit is of lesser importance.

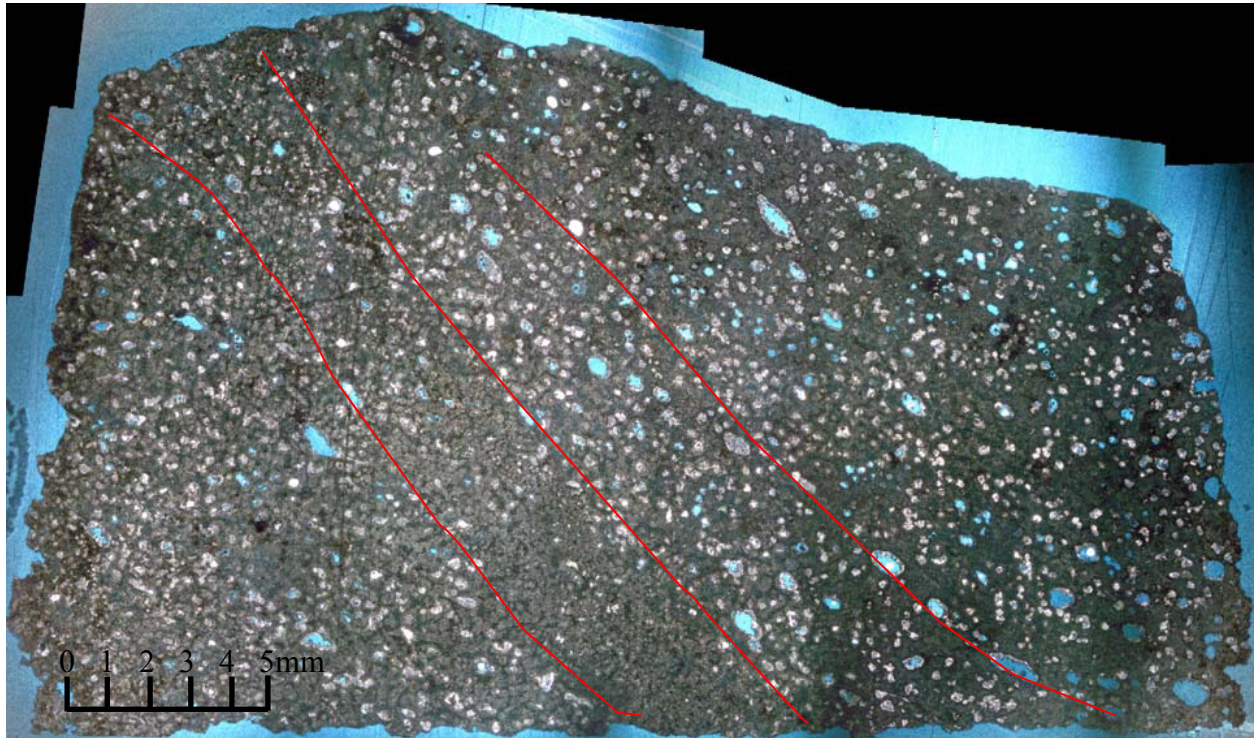


Figure 31. Tcvt – Cave Lake Tuff: This unit is encountered at Cave Lake, and extends westward. This unit is approximately 0.7 km²; lateral thickness variations have not been measured. Color is light blue. To the writer's knowledge, this unit has not been described before and the attempt to correlate this unit regionally has not been made. This unit is of lesser importance.

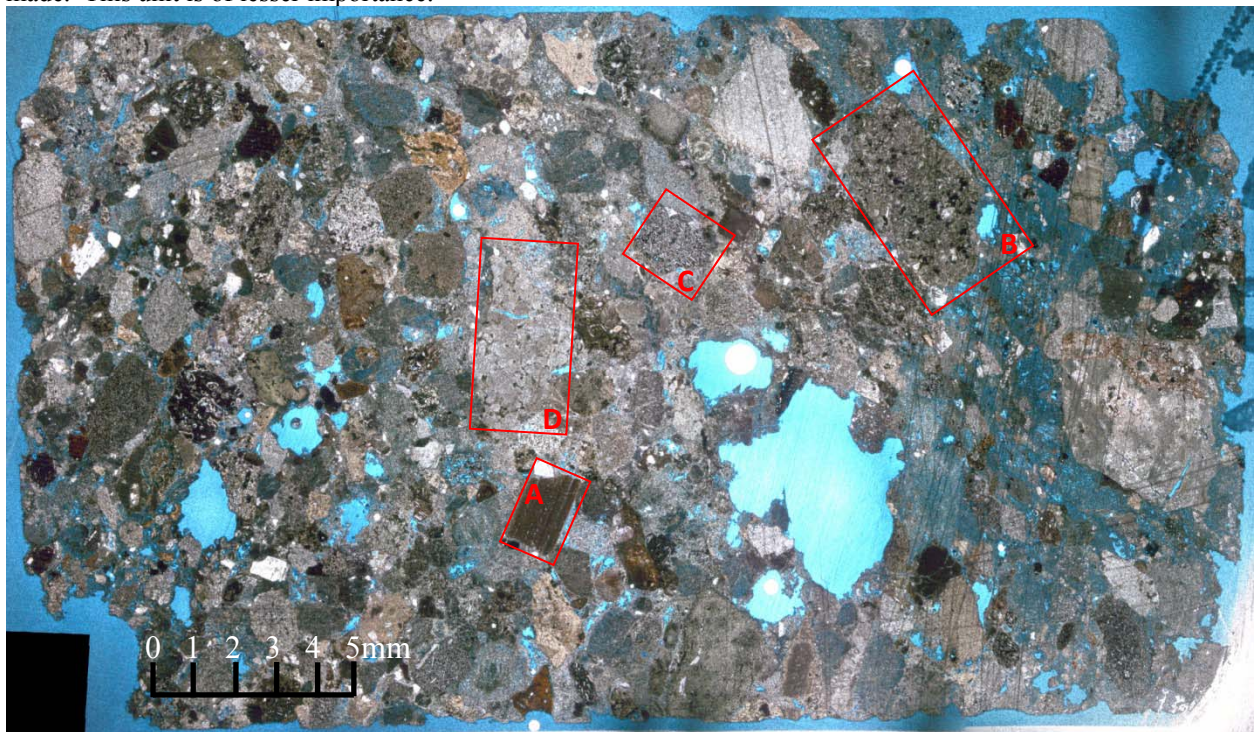


Figure 32. Tcvt – Cave Lake Volcaniclastics: This unit is encountered 200 m north of Cave Lake. This unit is approximately 0.03 km²; lateral thickness variations have not been measured. Color is light green to tan. To the

writer's knowledge, this unit has not been described before and the attempt to correlate this unit regionally has not been made. This unit is of lesser importance.



Figure 33. Tpl – Poison Lake Tuff: This unit is found 3 km west of Discovery Mtn. This unit is approximately 0.22 km². Its origin or source is not known. Lateral thickness variations have not been measured. Color is light pink. To the writer's knowledge, this unit has not been described before and the attempt to correlate this unit regionally has not been made. This unit is of lesser importance, and the westernmost felsic unit.

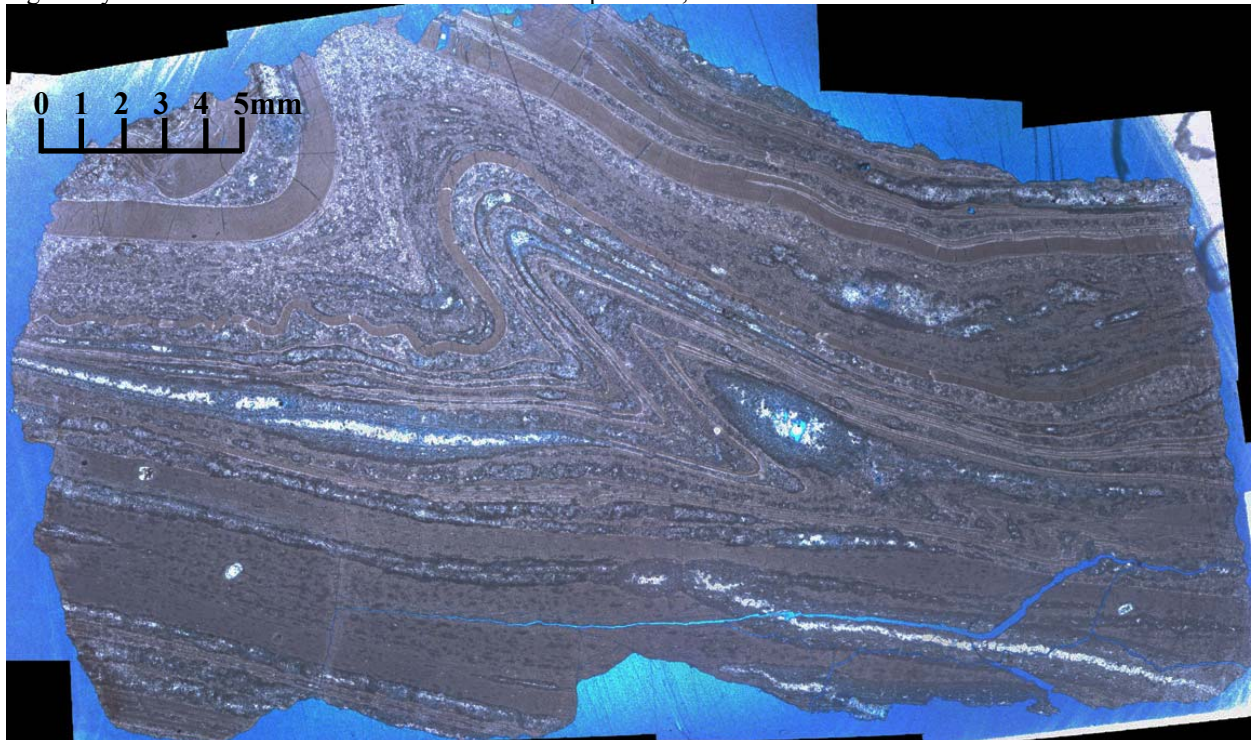


Figure 34. Tsp – Sugar Peak Rhyolite: This unit is found 7.5 km northwest of the HGD. This unit is approximately 0.9 km². Color is dark pink. To the writer's knowledge, this unit has not been described before and the attempt to correlate unit regionally has not been made. This unit is of lesser importance.

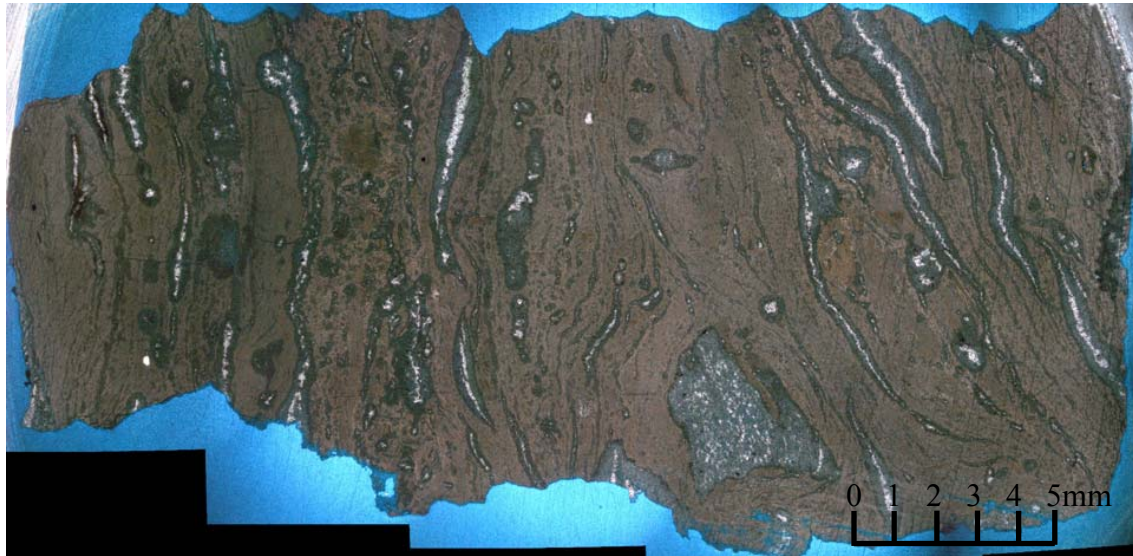


Figure 35. Tbs – Bow Spring Rhyolite: This unit is encountered to the 6.6 km NW of the MMS and contains a multi-lithic breccia, it is present as a layered, sub-horizontal unit. This unit is approximately 0.8 km², and lies far to the NW of the HGD, 7.3 km NW from MMS. Its origin or source is not known. Lateral thickness variations have not been measured. Color is pink. To the writer's knowledge, this unit has not been described before and the attempt to correlate this unit regionally has not been made. This unit has been mineralized; preliminary sampling returns anomalous Au values (0.1 ppm).



Figure 36. Tai – Orange Ignimbrite: This unit is encountered 1km west-northwest of MMS, and extends northward for 5km. This unit is approximately 5 km², lateral thickness variations have not been measured. Color is light blue with orange phenocrysts. To the writer's knowledge, this unit has not been described before and the attempt to correlate this unit regionally has not been made. This unit is of lesser importance.

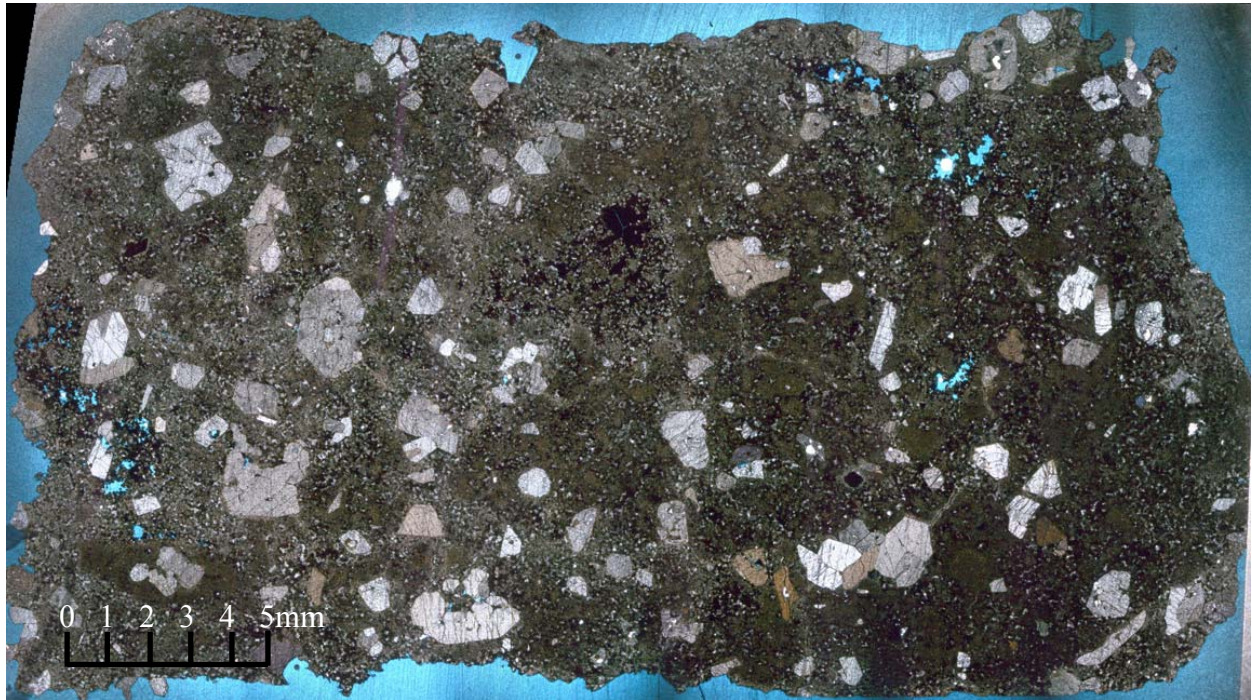


Figure 37. Tdc – Deep Creek Rhyolite: This unit is encountered 4 km northwest of MMS, overlying the Orange Ignimbrite (App. 2, Map 1). This unit is approximately 1 km², lateral thickness variations have not been measured. Color is dark pink/red. To the writer's knowledge, this unit has not been described before and the attempt to correlate this unit regionally has not been made. This unit is of lesser importance.

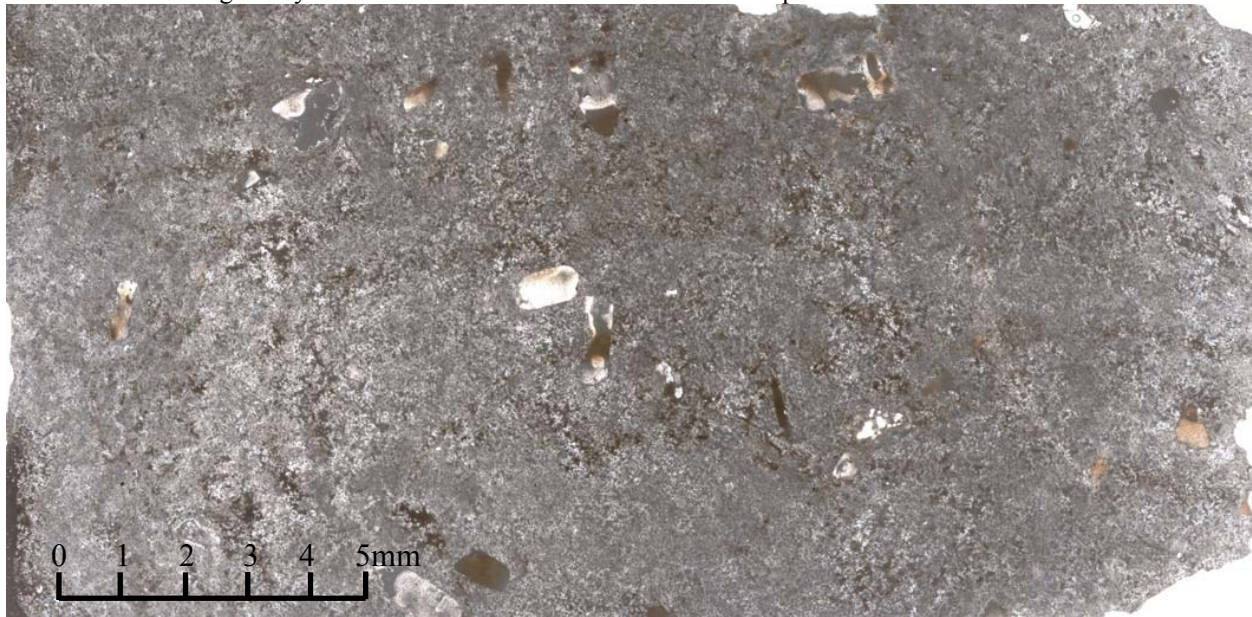


Figure 38. Tcrd - Cross-Roads Porphyritic Rhyolite Dome: This unit occurs in the center of the district; immediately east of the Lodgepole camp. The unit is approximately 0.4 km². Color is light tan. To the writer's knowledge, this unit has not been described before and the attempt to correlate this unit regionally has not been made. This unit has been dated as post-mineralization phase (Keats, 1985) and it is epithermally unaltered.

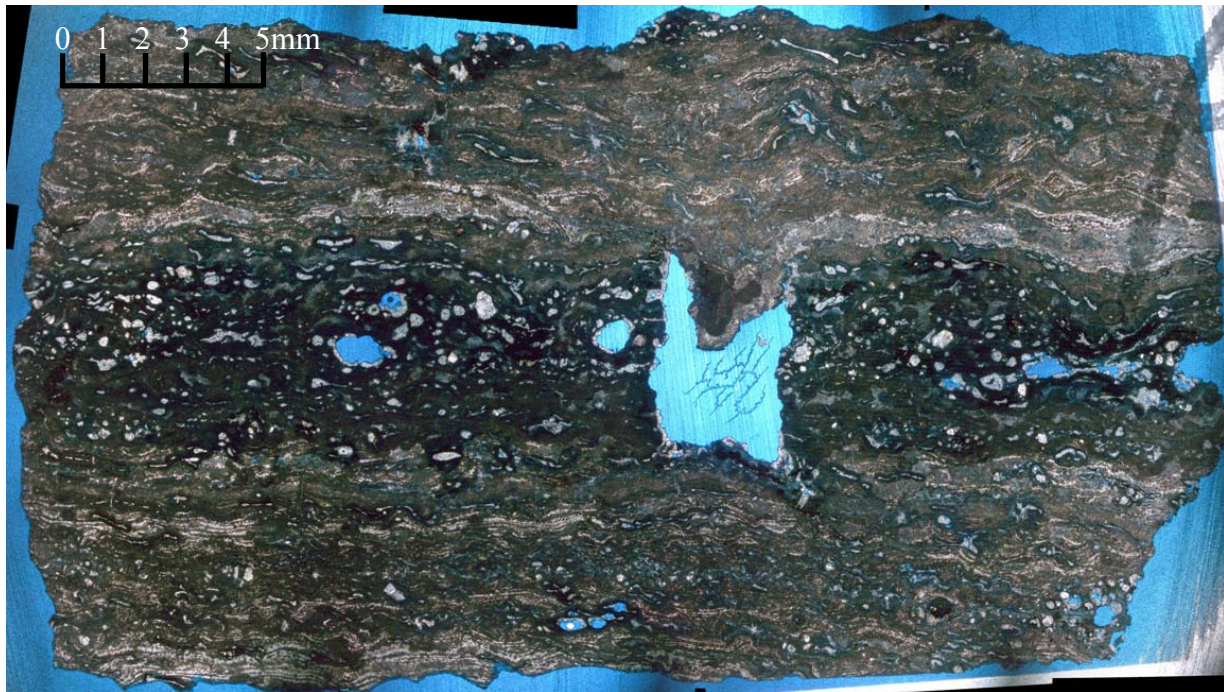


Figure 39. Tbv - Mt. Bidwell Vent Rhyolite: This unit is encountered along the highest points of Mt. Bidwell and a vertically-flow-foliated vent (fig. 41) is present along the eastern flank of Mt. Bidwell. Mt. Bidwell is in the far east of the regional map (app. 2, fig 1) where this vent occurs at the highest point, elevation 8,239 ft. This unit has a lateral extent of 0.2 km², but may underlie a large portion of the related obsidian flow (2.3 km²). Lateral thickness variations have not been measured. Color is light blue. To the writer's knowledge, this unit has not been described before and the attempt to correlate this unit regionally has not been made. This unit is of lesser importance.

Ttb – Brown Tuff

This unit is a moderately welded rhyolite tuff. As seen in figure 22, lithophissle cavities and leached feldspar holes occur throughout this section. The cavity on the far right has been agatized. Yet unexplained phenomena appear in the left (top and bottom), curvo-linear features surround some prior, unknown object, the exsolution of iron into the surrounding host-rock is yet unexplained.

Tdmr – Discovery Mountain Rhyolite

Discovery Mountain is a massive silica body hosting the initial gold shows reported for the district. This aphyric flow (Tdmr) is completely replaced by silica and displays textural

gradation from crypto- (left) to micro-, and macro-crystalline quartz prograding toward cooling planes (fig. 23). Black color due to opaque/sulphide mineralogy. Background replaced rock, areas of more silicification are lighter colored. The Tdmr is the largest felsic eruptive unit on Discovery Mountain, which entirely hosts mineralization of the Consolidated camps. The Tcrf and Tccr are hosted within this unit.

Tcrf – Consolidate Rhyolite Flow Dome

The Consolidated rhyolite flow dome (Tcrf) of Discovery Mtn. has an aphyric texture that is completely replaced by silica. Some remnant holes remain from leached feldspar phenocrysts and pumice fragments. Phenocryst orientation is N-S (fig. 24) which may indicate original flow foliation. This unit is not welded, but as it underwent crystallization. Later crack displays micro-crystalline quartz, possibly fissures escaping along gas phase, may be cristobalite (high-quartz; gas-phase precipitate).

Tccr – Consolidated Rhyolite Dome

The Consolidated rhyolite dome (Tccr) is aphyric, vesicular, and contains 3% hematite in a microcrystalline quartz matrix. Some cavities have been precipitated with hematite and subhedral quartz (fig. 25). This unit is mapped separately due to the massive, columnar nature of these domal features (Append. 2, fig. 2). Aphyric quartz + feldspar groundmass. Holes (up to 4mm) deserve further investigation, possibly lithic fragments. Hypothesis 1: holes have been leached out from lithic fragments and later precipitated with hematite and clay. Hypothesis 2: holes have been leached out from feldspar phenocrysts and later precipitate. Hypothesis 3: holes have been leached from pumice fragments..... Some of these questions have been left

unanswered due to their low priority. Prior to hematite precipitation in holes, they were leached out of the host during silicification.

Tlq – Lodgepole Aphyric Rhyolite Flow Dome

The aphyric flow-dome (Tlq) of the Lodgepole camp is highly silicified (stock works and silicified fractures), but does not contain a multi-lithic breccia. Holes have been slightly compressed along the vertical axis of fig. 26. There are small objects, difference in grayness, does not appear oriented, gray ghost objects. Hypothesis 1: This aphyric flow texture has been preferentially replaced by silicification, these may not be remnant grains. Hypothesis 2: This porphyritic flow has been entirely replaced by quartz.

This aphyric texture is notable comparatively to the flows of Consolidated/Discover Mtn [the three previously mentioned units].

Tmvp – Mt. Vida Peak Rhyolite

Moderately silicified rhyolite (Tmvp) is encountered on the peak of Mt. Vida (fig. 17), 2.5 km S-SW of Discovery Mtn. This ignimbrite contains 3% orthoclase phenocrysts, remnant grains are dissolved along pumaceous zones along with hematite enrichment (fig. 27). Holes are dissolved phenocrysts. Pumice fragments have been squished 10:1.

Tmpr – Moonlight Porphyry Rhyolite Flow

The rhyolite dome of the Moonlight mines camp (Tmpr) is a glassy, highly viscous, porphyritic flow (5% orthoclase [replaced by quartz]) (fig. 28). A quartz veinlet cuts the sample

(fig. 26) along a cooling boundary. This flow-dome hosts a multi-lithologic breccia and quartz-sulfide veining;

Tkq – Klondyke Rhyolite Flow Dome

Layered rhyolite flow (Tkq) of the Klondyke camp is dominantly glass with a moderate viscosity. The right portion of fig. 29 displays moderate welding and a low level of flow banding irregularity. The sample chosen to represent this unit displays a glassy (quartz +feldspar) matrix with 3% pumice cavities that have been leached. A coarse crystalline quartz vein is seen cutting the rhyolite in the upper portion of this thin-section. The Klondyke camp hosts notable (1-2m thick, barren massive quartz) veins but no related multi-lithic breccias.

Tkc – Kelly Creek Tuff

This light gray/cream colored tuff is unwelded and has a significant pumice component. Pumice grains are largely un-leached (0.5 mm, 15% of unit) and biotite phenocrysts (0.05mm, 2% of unit) are fresh, subhedral metallic minerals account for 1%. The matrix is silicic ash (fig. 30).

Tclt – Cave Lake Tuff

This light-blue tuff (Tclt) outcrops along an east-west trend, extending westward from Cave Lake. This ash-fall tuff contains 30% pumice and is un-welded. Figure 31 shows numerous leached pumice grains and dark areas of hematite enrichment. A minor cooling layer trend is recognized and indicated by red lines (fig.31).

Tclv – Cave Lake Volcaniclastic

Directly North of Cave Lake this volcani-clastic unit (Tclv) forms green-tan outcrop (fig. 40). Matrix has been largely argillized. Several rock types are distinguishable in thin section (fig. 32): A) layered tuff, B) hornblende andesite, C) plagioclase andesite, D) aphyric rhyolite. Large holes are a notable feature of this unit (in outcrop this unit displays strong argillic [clay] alteration) and may be the result of leached feldspar-rich clasts.



Figure 40. Cave Lake Coarse Volcaniclastics (Tclv) in outcrop (A), north of Cave Lake. Layered ashy mudflows (B) with angular clasts (C). Layering is very poorly developed and clast size ranges from 0.2 to 7cm in length.

Tpl – Poison Lake Tuff

The western-most rhyolite dome, associated to HGD magmatism, is found along a NW trend of Mt. Vida and the nearby multi-lithic breccia (App. 2, fig.1). This rhyolite flow dome consists of layered glass and ash-tuff. As seen in figure 33, the glassy sections display a high level of irregular flow banding and are welded. Dark zones are due to hematite enrichment. A

0.7 mm feldspar is seen in the lower part of fig. 33, porphyritic zones may be present as cooling units shift from pumaceous to glassy. This unit has a centrally located vertical flow foliation (2m x 10m).

Tsp – Sugar Peak Rhyolite Dome

This unit occurs as a geomorphic pinnacle, protruding from the surrounding andesite (App. 2, Map 1). This unit displays a high level of internal variability. The rhyolite in thin-section (fig. 34) displays two phases of eruptive material, shifting from pumaceous (top-middle) to glassy (bottom). In the pumaceous zone, alternating layers (0.2-0.8 mm thick) of glass and pumice display a high level of irregular flow banding. Glassy layers (up to 2mm thick) in the bottom portion of this section display minor feldspar phenocrysts (<2%, 0.4mm).

Tbs – Bow Spring Rhyolite

The northern-most extension of HGD epithermal mineralization (as currently known) manifests in the Bow Spring Rhyolite. A multi-lithic breccia (Tmlb, fig. 9, 17-B) cuts (N-S) through this flow unit and is accompanied by silicification and stockworks. The rhyolite contains 10% pumice and 2% phenocrysts (not compacted) in a glassy flow matrix (fig. 35). Extreme welding has compressed most pumice grains by a 15:1 ratio. Phenocrysts and pumice have been leached and commonly replaced by quartz during silicification. The glass is composed of quartz + feldspar.

Tai – Orange Ignimbrite

The Orange Ignimbrite (Tai) overlies the Yellow Mountain Latite (Tym) to the north of the HGD (fig. 17). As seen in figure 36, this unit contains 5-10% orthoclase phenocrysts (Carlsbad twinning, up to 1cm, orange in hand-sample) in a glassy-tuff matrix. Two size populations (1.0 cm and 0.2 mm) exist, and occur as subhedral to euhedral crystals, elongate crystals. Color is micro-granular dark green-black; periodic fracturing and dissolution has caused partial oxidation to limonite. Potential mafic phenocrysts are the same size as the smaller phenocryst population. The feldspars are fresh, but groundmass shows dueteric alteration (hematite enrichment along fractures). This unit is encountered just across the Oregon border, and contains several small prospect pits on opaline quartz showing. Nearby these diggings a subtle exposure of vertical flow foliation (fig. 41, Tai) is recognized within this unit.

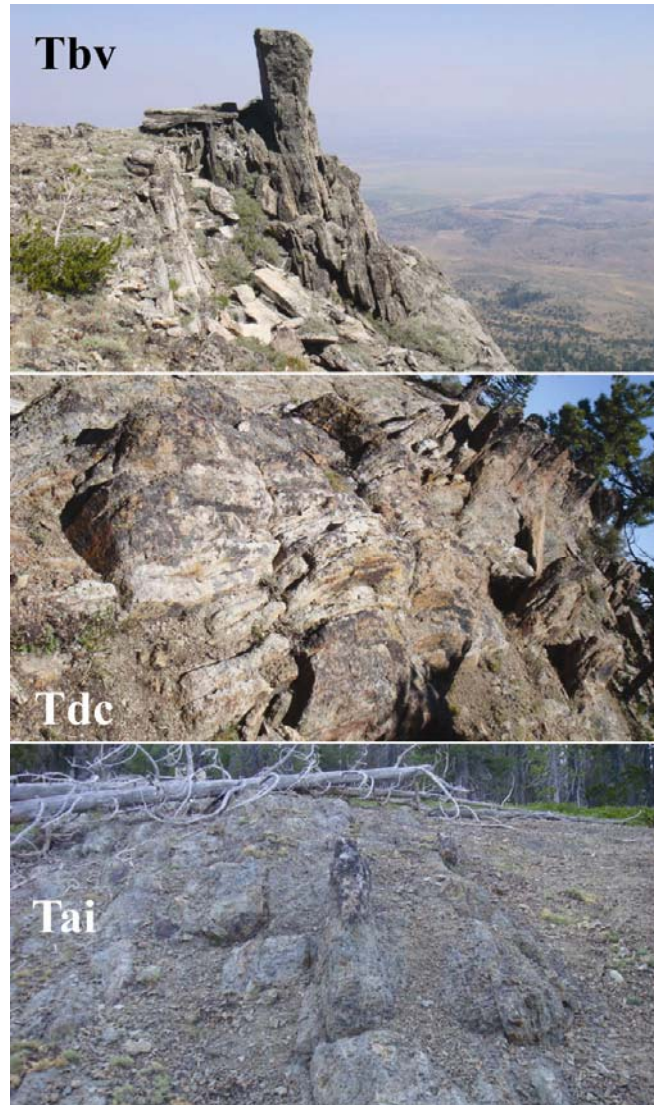


Figure 41. Vertical flow foliation is limited to a small (10 x 25m) ellipsoidal area in each one of these flow units pictured above.

Tdc – Deep Creek Rhyolite

The Deep Creek Rhyolite (Tdc) (fig. 17) overlies the Tai (Orange Ignimbrite), 5km north-northwest of the MMS, (Appendix 2, map 1). This unit has a vent area of 30 x 100m (fig. 41, Tdc) with very strong vertical flow foliation and alternating layers of glassy and pumaceous rhyolite. This porphyritic flow contains 10% sanidine phenocrysts (up to 0.5cm) (fig. 37). Hematite is concentrated in pumaceous zones. Two feldspar populations exist, one of small

ehedral phenocrysts and another of clustered fragments/growth clusters (Potassic feldspar + Plagioclase). Chloritic (drusy chlorite) alteration gives a green color to the sample.

Tcrd – Cross-Roads Porphyritic Rhyolite

The cross-roads rhyolite occurs in the center of the HGD and is a post-mineralization unit. This poorly welded unit is 95% glass which has been weathered and moderately stained with FeOx (fig. 38). Feldspar phenocrysts to 1mm have been deuterically altered and destroyed, replacement by FeOx and minor silica is observed, although not all casts have been filled.

Tbv – Mt. Bidwell Vent Rhyolite

This scoraceous material underlies an associated obsidian flow (Tbvo) and is stratigraphically above the Steen's Basalt. The vent (fig. 41, Tbv) is 10-15m thick and consists of similar layers occurring repeatedly. This scoraceous rhyolite displays alternating bands of glass (with 10% pumice, ~2 cm thick) and pumice layers (displaying numerous voids, ~1 cm thick). Figure 39 illustrates the vertical flow-foliation in three distinct layers [top to bottom]: A) grey pumaceous glassy layer, B) red pumaceous phenocryst rich layer, and C) pink glassy pumaceous layer.

Tfr - Aphanitic Rhyolite Domes

A cognate series of aphanitic rhyolite domes are found in the central portion of the district. The largest of these domes hosts the multi-lithic breccias and silicification of the Sunshine Vein. Although the individual domes are limited in lateral extent, they are lithologically inseparable by field criteria and probably are related at depth. These rocks are

generally pink in color although many have been locally iron-stained to shades of medium purple or bleached to an off-white or pinkish-gray. Rhyolites comprising the domes are ubiquitously flow-banded and large portions of each exhibit a fissility imparted by flowage.

Megascopically, the rhyolites are dense, lithoidal aphanites. They exhibit a well developed trachytic texture in thin section. Microlites of alkali feldspar average between 0.1 and 0.3 mm in size, but may be as small as 0.02 mm. They commonly comprise as much as 65% of the rock. Material interstitial to the microlites is composed primarily of Quartz (30%) and randomly distributed cryptocrystalline iron oxides (2-3%). The interstitial Quartz causes a patchy or mosaic extinction pattern in which relatively large, sub-rounded, and mutually interfering areas, ranging from 0.3 to 2.0 mm in diameter, exhibit uniform extinction. A similar texture has been described by Lofgren (1971) as a micropoikilitic Quartz surrounding spherulites. It is likely that the aphanitic rhyolite domes exhibit the same phenomena with respect to microlites rather than spherulites. It has been suggested that the presence of micropoikilitic quartz may represent the initial sub-solidus formation of silicate crystals or glass. The presence of poikilitic quartz, together with high concentrations of microlites and the lack of devitrification textures, indicate that these rhyolites were not quenched to glass during or after emplacement. Instead, they were probably emplaced as a slowly cooling crystal mush, which allowed crystallization to continue to completion at sub-solidus temperatures.

3.1.3 Steens Basalt (Tb)

The basalt flows that dominate the Warner Mountains conformably overly the northeastern extent of the district and emplacement closely followed the felsic suite. The massive basalts flows of the northern Warner Mountains have been mapped as part of the Steens Mountain Group (Camp and Ross, 2004). The 650m thick sequence, observed 30 km north of the district, thins in exposure to the south and is limited to a 100m thick sequence clearly observed on the western flank of Mt. Bidwell (fig. 42-A). The basalts are fresh, dense, porphyritic flows which weather to a dull brown color.



Figure 42. (A) Mt. Bidwell as viewed from Discovery Mountain, with geology overlain. (B) Looking south into Surprise Valley, from atop Mt. Bidwell. (C) Two basalt dikes outcropping near Modoc Mines.

Near Modoc Mines (fig. 42-C), these basalt flows are weakly porphyritic rocks whose dominant textural types include pilotaxitic, sub-ophitic, and occasionally diabasic. Phenocrysts

of andesine (An₄₂) are subhedral to euhedral and range from 1.6 to 3.3 mm in length. They comprise approximately 3 percent of the rock, and commonly display albite twins. Carlsbad twins are less common, and both pericline twins and zoning are rare. The phenocrysts of plagioclase feldspar contain small inclusions of clinopyroxene, apatite, and magnetite. Both clinopyroxene and olivine are present in the groundmass, with olivine less abundant than clinopyroxene. Augite comprises 25 percent of the rock, and is present as sub-ophitic grains (1.0-1.5 mm) and as smaller (0.6 mm) anhedral that are interstitial to crystals of plagioclase feldspar. Anhedral grains of olivine range from 0.1 to 0.5 mm in diameter and comprise approximately 10 percent of the groundmass. Magnetite is found in concentrations of up to 5 percent in the groundmass, and has an average diameter of 0.1 mm. Crystal shape varies from euhedral to disseminated anhedral that are interstitial to microlites of the groundmass. All of the magnetite is primary. The groundmass is composed of microlites of pilotaxitic plagioclase feldspar. These microlites consist of labradorite (An₆₅) laths which are characteristically subhedral and range from approximately 0.2 to 0.8 mm in length.

3.1.4 Mt. Bidwell Obsidian (Tbv & Tbvo)

The youngest unit encountered in the study area lies above the Steen's Basalt and is limited to the southeastern portion of the regional mapping area. A light-blue tuff (Tbv, fig. 39) is encountered which grades to the east into a light-blue scoraceous rhyolite, displaying 10% sanidine phenocrysts. Vertical flow foliations are observed on the eastern peaks of Mt. Bidwell (fig. 41) and these extend downwards, although talus cover begins approximately 100m down. This rhyolitic unit is overlain by an expansive, glassy, obsidian flow (Tbvo). Obsidian is largely jet black, but pieces of rainbow, and orange flame are also observed. The extent of the obsidian flow is limited to the highest parts of Mt. Bidwell.

3.2 Structure

The horst and graben physiography of the Warner Mountain block is a product of the extensional tectonic regime in the Basin and Range province of the western United States (Lerch, 2009; Colgan, 2005). Linear mountain ranges, bounded by normal faults, have a general trend of N-S (fig. 1) and typify an extensional regime. The Surprise Valley Fault, eastern bounding fault of the Warner Mountain horst block (fig. 43, red line), makes a northeastward bend at Ft. Bidwell and then continues under young volcanic cover into Adel Valley. A major NNW fault zone (fig. 43; teal line, parallel to Fandango Pass [orange]) cuts the Warner Range within the HGD and intersects the Surprise Valley Fault at Ft. Bidwell.

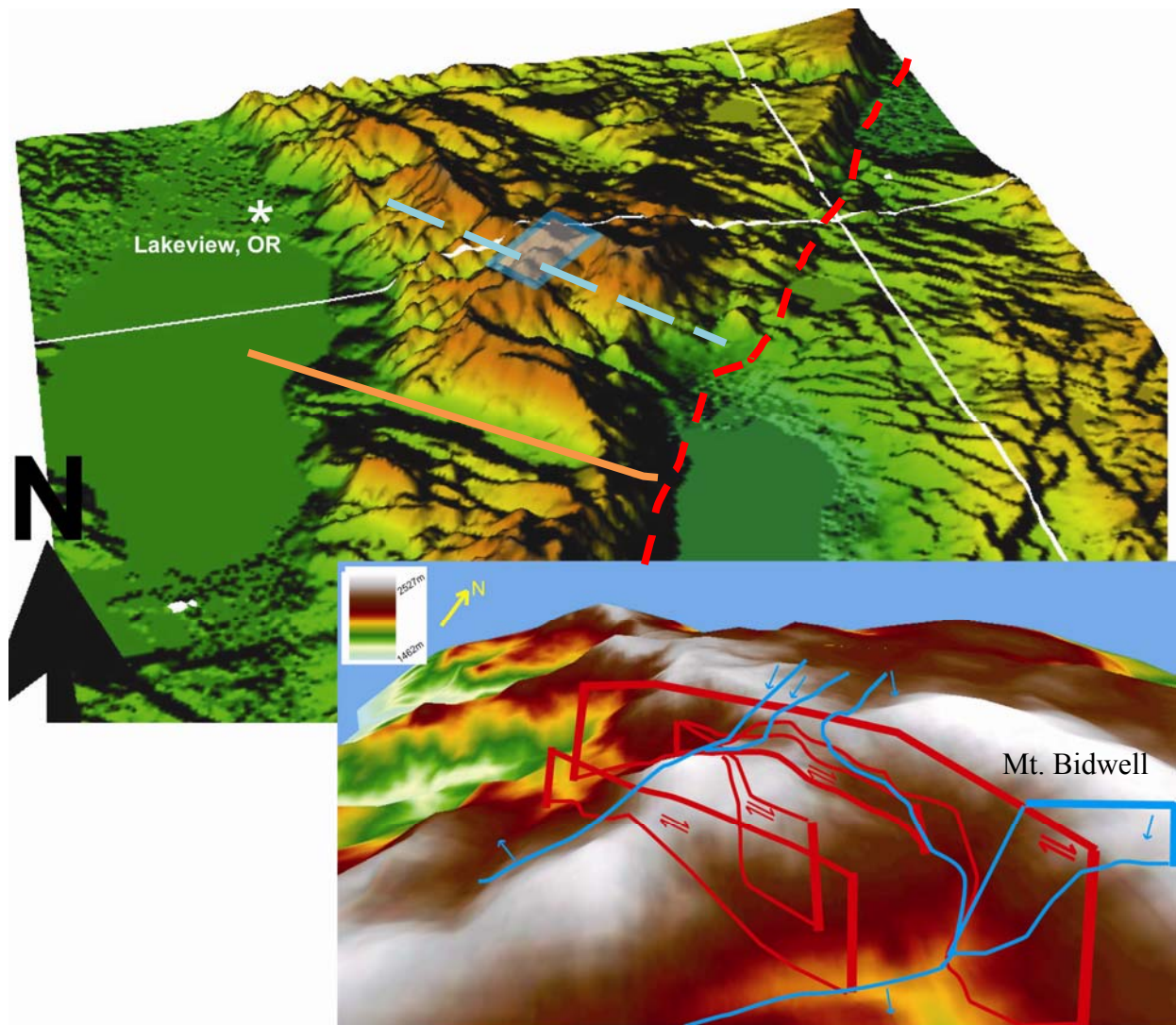


Figure 43. Three dimensional view of the northern Warner Mountains, and a detailed view of the HGD and local tectonics. On the regional photo, Fandango Pass records major NW-trending strike-slip movement 10 km South of the HGD, peach line; the area of zoom is indicated by the blue box. These 3D images were created in the GRASS open source GIS platform.

The rhyolitic magmatism in the study area appears to play an important role in present topography. Felsic units are locally resistant to weathering, forming the high ridges and related talus fields. Intrusive stocks related to eruptive felsic units are a likely component to increase the tenacity of the immediately surrounding horst block and create topographic highs.

The felsic rock units in the study area have a general dip of 20° to the east-northeast. Within the felsic sequence, strikes and dips of all flows and tuffs are highly variable (Matthewson, 2003; Vance and Shwertfeger, 2001; Reighard, 1988; Schuler, 1986; Cox, 1985; Keats, 1985). An older group of N-S striking faults are reported in historic reports (Cox, 1986; Schuler, 1985). These faults have been cut into small strike lengths by later faulting

The accommodation of extensional and transform motion, within the study area, dominate the surface structure. Two main sets of faulting are recognized from present geomorphology in the study area (fig. 44): A) Large normal faults trending NE-SW to ENE-WSW (Fig. 44; red lines), and B) Right-lateral (dextral) strike-slip faulting which trends NW (Fig. 44; blue lines).

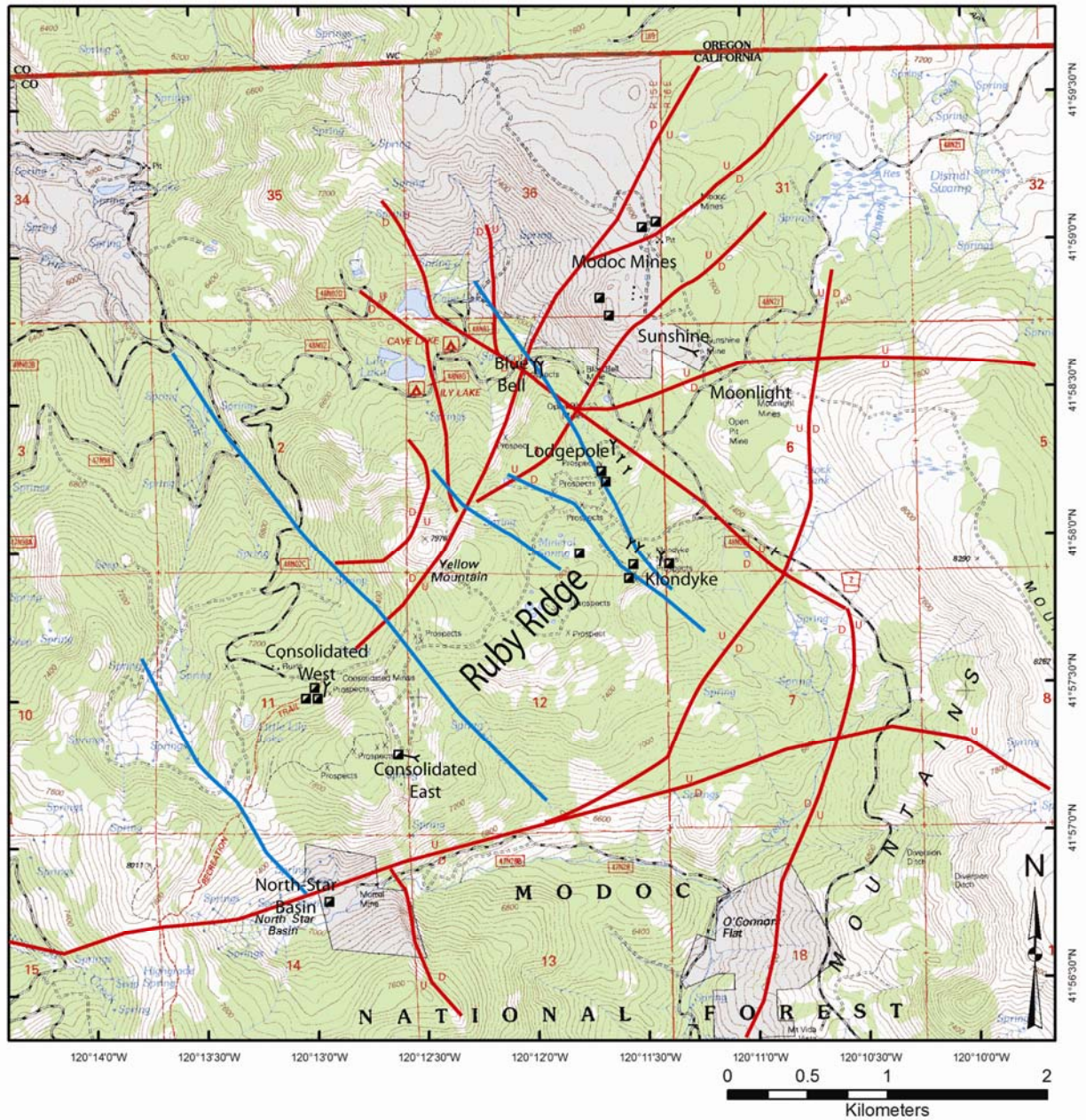


Figure 44. Structure of the HGD is shown on a topographic basemap with camp names for reference. Red lines indicate normal faults; blue lines represent dextral strike-slip fault zones.

3.3 Alteration

The defining features of the HGD are 14 massive silica bodies which crop out as bedrock and boulder fields adjacent to the mining camps (fig. 45). Silica bodies are elongate with a length:width ratio of 4:1 to 2:1. These silica bodies protrude above surrounding vegetated areas by approximately 50 feet (fig. 46), dimensions are in excess of 1,000 feet² (table 4). Eruptive multi-lithic breccia units (fig. 47) occur coincidentally within silica bodies. Alteration in the study area has been effectively mapped (fig. 7) and a typical epithermal zoning signature is represented with a silicic core, minor argillic halo, and prominent propylitization at depth.

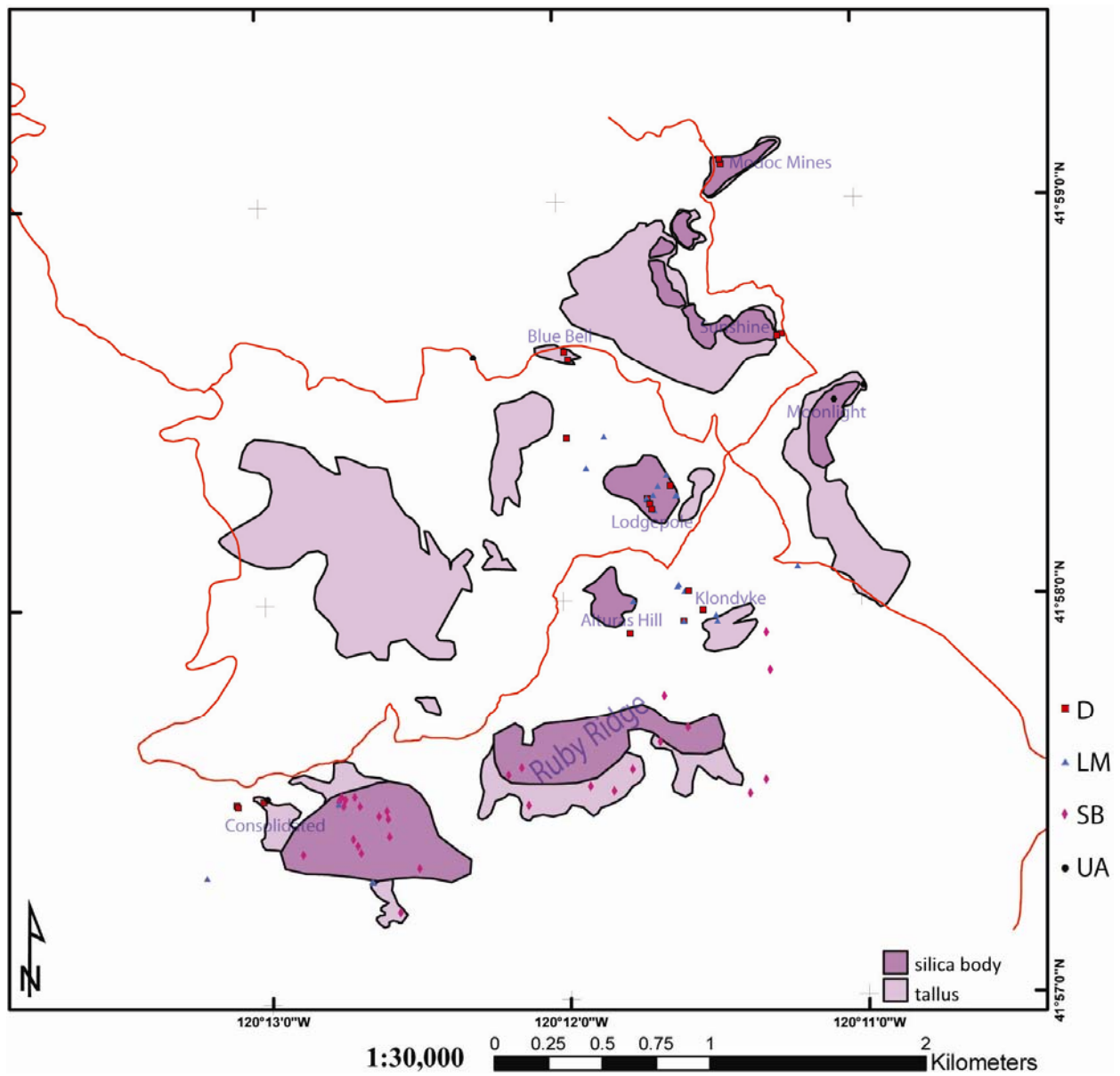


Figure 45. Silica bodies and tallus fields in the HGD are shown along with locations of samples used in geostatistics.

Table 4. Silica body characteristics in the HGD.

Silica Body	Area (acres)	Elongate	Structure	Exposure	Qtz Occurrence	Workings	Dump Mineralogy
Modoc Mines	6.2	NE-SW		Tallus	colloform, drusy, sugary, pyritized & silicified, primary and secondary replacement textures	Shafts, huge dump	Qtz, pyrite, minor adularia
N Modoc Mass	20.4	NE-SW		Tallus, Minor Knobs	silicified, cocks-comb, opal	shafts, stopes	qtz, chaledonic crusts, hematite
S Modoc Mass	23.62	no		Tallus, Minor Knobs			
Sunshine Adit	29.11	no		Rhyolite Flow Domes, Tallus	colloform, drusy, vuggy	Tunnel ~200'	Qtz, electrum
Moonlight Mines	33.03	NNW-SSE		Tallus		Open Pit	Qtz
BlueBell Mines	3.32	E-W		Tallus	platy calcite pseudomorphs, coarsely crystalline vein, barite replacement	2 collapsed portals	Qtz, platy calcite pseudomorphs
Lodgepole Group	3.66	NNE-SSW		Tallus, Silicified Flows	drusy, sugary, chalcedony, cocks-comb,	8 portals, stopes	Qtz, vuggy / sugary, Adularia, Barite replacement
N Klondyke	3.95	E-W		Felsic Vent, Silicified Flow	colloform veining 2 feet wide		
S Klondyke	7.24	ENE-WSW		Silicified Flow		6 portals, 3 shafts, stopes	Qtz, Colloform banding, barite pseudomorphs
Yellow Mountain	141.55	no	NE listric faults	Tallus, Columnar Knobs	none	No	
Ruby Ridge	71.73	E-W		Tallus (Major Silicification)	chalcedonic growth, drusy, crystalline growth, limonite, jarosite	defined surface deposit	Qtz, Jarosite, Limonite
Consolidated Ridge	30.64	NW-SE	Oblique SS fault just NE	Rhyolite Domes, Silicified Tallus, Silified Flow	qtz veining 3 feet wide, drusy, cocks-comb, chalcedonic growths, drusy, crystals up to 1cm, long,	4 portals, 5 shafts	opal, qtz, VG, amethyst, adularia, hematite, pyrite, chalcopryrite, turqite, chrysocolla, plagioclase, epidote
East Consolidated Plug	14.11	NNW-SSE		Rhyolite Dome		No	
West Consolidated Plug	21.75	no		Rhyolite Dome		No	



Figure 46. The rock piles along the Sunshine Vein and Modoc Mines vein trends, these rhyolites and multi-lithic breccias are entirely replaced by silica. Looking northeast.

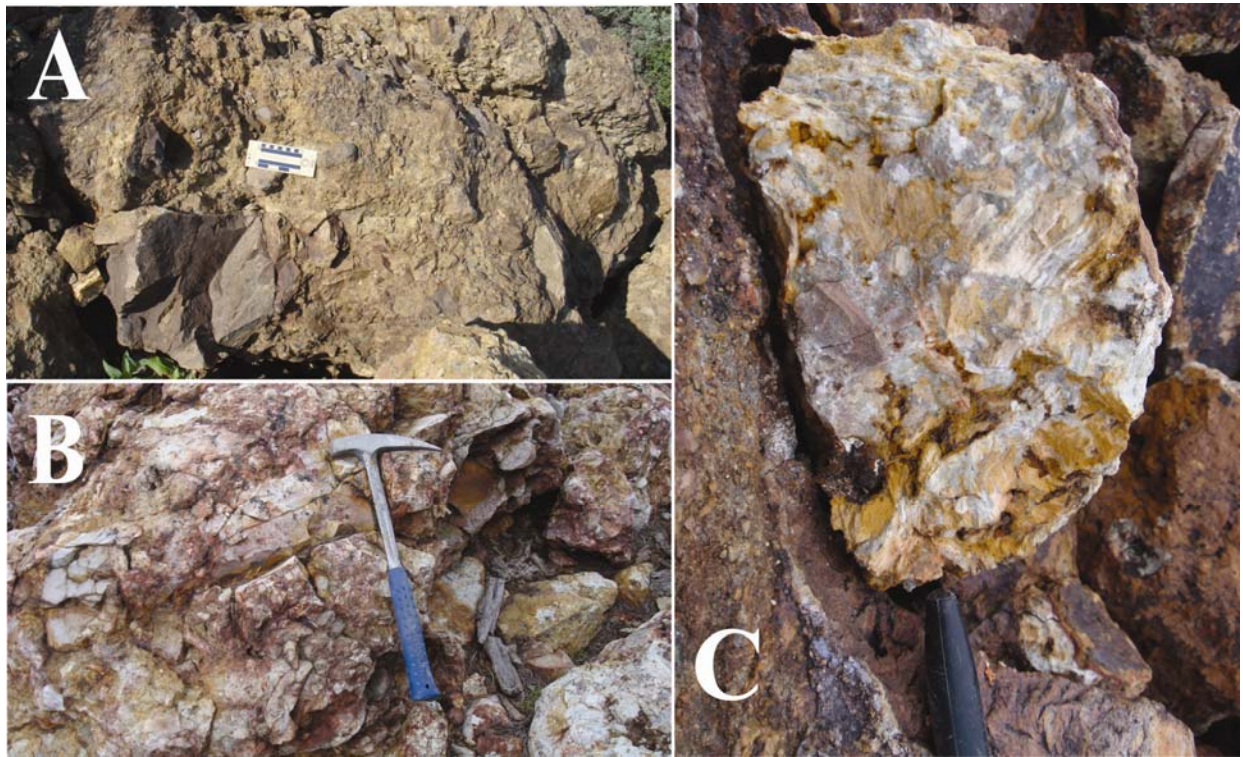


Figure 47. Andesite breccias (A) are massive and do not accompany mineralization. Hydrothermal breccias (B, C) are intensely silicified and are integrally related with mineralization.

Silicic alteration (fig. 46, 47-C, 48, 49-A) is generally expressed as abundant chalcedony, opal, cockscomb quartz and occurs as veinlets, stockworks (fig. 48-A), and breccia matrix (fig. 47-C). Pyrite, hematite, and goethite commonly accompany the silicification (fig. 48). Silicification is followed by faulting/brecciation, then a quartz/adularia stockwork phase, then a later period of faulting and barren silicification. This paragenetic observation, from a high grade zone in the Alturas Hill area, is based on cross-cutting relationships in drill-core (fig. 51; Hembree, D.R., pers. comm.) Some silicified units have been overprinted by supergene argillization and regional propylitization by hydrous deuteric processes (Keats, 1985).

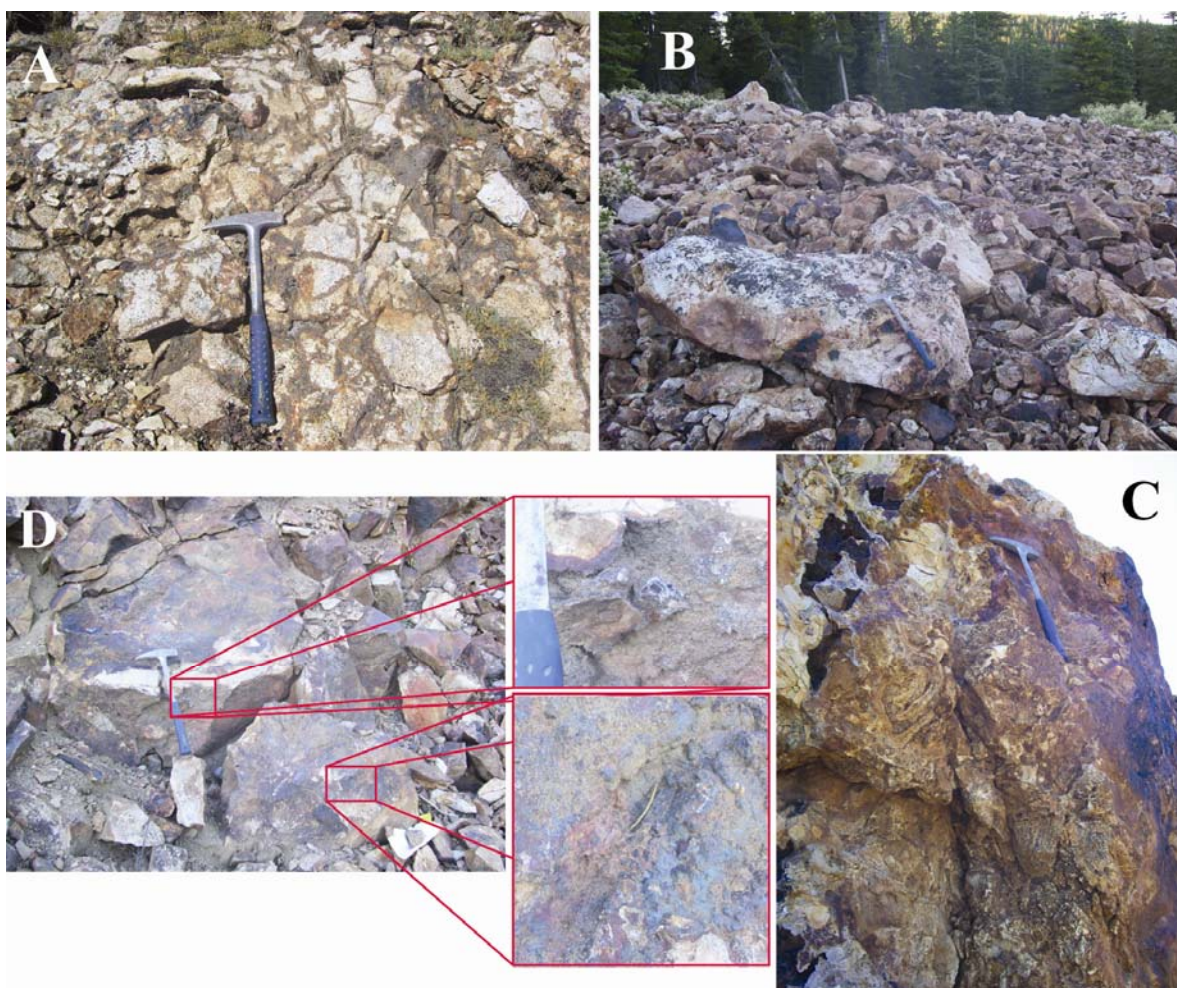


Figure 48. This compilation of figures is compiled from the Consolidated Silica Body (CSB). Silicification is accompanied by hematitic staining (A, B) and less abundant goethite/jarosite (D) in fractures. (C) Trenching atop Discovery Mountain samples this silicic breccia vein.

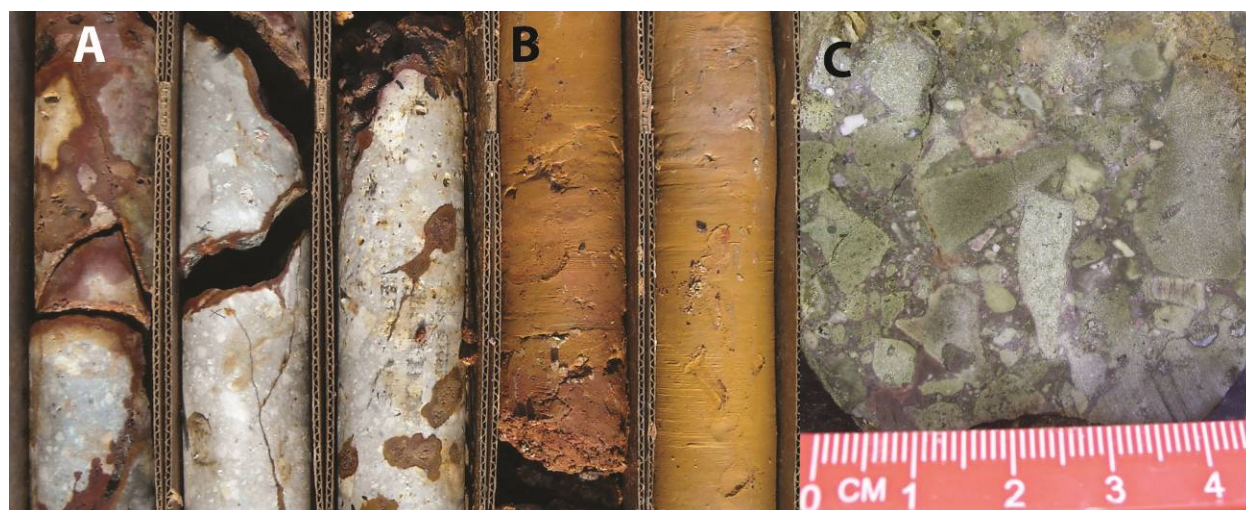


Figure 49. Alteration types observed in the study area. A) Silicic, B) Argillic, C) Propylitic

Argillic alteration is observed in the district as bleaching and clay alteration. Zones of advanced argillic alteration, to massive clay (fig. 49-B; tan to battleship-gray in color), are encountered along faults contained within silica bodies and in 20 to 40 feet thick zones along the periphery of some silica bodies, as observed at the Sunshine camp (fig. 104). This advanced alteration appears to be the result of superheating the country rock during rhyolite dome emplacement. Argillization is commonly encountered along the host rock contact with the overlying rhyolite flow dome and related epithermal mineralization (models presented in chapter 11.2 and 11.3 illustrate this). In the Ruby Ridge area, argillization is encountered where drilling penetrates the underlying tuff, below this contact alteration sharply decreases (Schuler, 1986). Bogs in the Rudy Ridge area are brown/gray clay and may represent the advanced argillic cap to veining.

Propylitic alteration (fig. 49-C) is prominent in the deeper portions of the district (Blue Bell, West Consolidated, and North-Star Basin), and it is best developed in the andesitic sequence. The characteristic green color is due to chloritic alteration of mafic minerals, epidote and calcite veinlets are observed in zones of maximum propylitization. Where the host andesite is vuggy, fillings of drusy epidote and acicular zeolites are observed (Keats, 1985; Schuler, 1986).

3.4 Sampling

Sampling goals included: characterizing the mineralization of each camp, collecting channel samples, systematic sampling of silica bodies, defining each felsic unit, finding hydrothermal quartz in bedrock, grab sampling mineralization in tallus. All samples used in this study were personally collected by the author.

Two GPS units were employed in the course of this study. District mapping, sampling, and drilling were directed with the assistance of a Trimble GeoXT handheld unit. Data collected with the GeoXT was post-processed using Trimble Pathfinder Office version 2.9 software. Post-processing entailed a differential correction using 5 CORS (Continuously Operating Reference Station). Data collected with the Trimble unit was acquired in a State Plane reference grid and after correction accuracy was typically sub-meter.

Regional mapping was done with the assistance of a Magellan Explorer 200. This unit uses WAAS (Wide Area Augmentation System), which incorporates a real-time correction embedded in the satellite broadcast. Data was collected in UTM format and typical accuracy was 10 meters (33 feet).

4. DRILLING

A reverse circulation (RC) drilling program of 30 holes was undertaken during the second summer field season of this study (fig. 50). Silica bodies in the district occur coincidentally with multi-lithic breccias and host all veining investigated by this study. The drilling program focused on extending mineralized structures along strike. Five core holes were drilled to further investigate significant intercepts. An example log and constructed profile from RC drilling in the 2009 season are provided in appendix 1, fig. 1-5 and 1-6.

The Sunshine-Yellowjacket veining was the first target assessed by the drilling program, with 18 angled holes. Multiple parallel vein zones were encountered, these are interpreted to be auxiliary structures related to the epithermal veining event. These veins trend from N70W to N50W, the bend zone is not accompanied by any surficial outcrop of hydrothermal quartz. Fractures present in the bend zone are iron stained and on trend with anticipated veining.

Five holes were drilled to test the veining encountered in the working of Modoc Mines, where bulk dump samples returned multiple ppm Au values. The system at Modoc mines included numerous parallel zones of quartz and quartz-sulfide veining/veinlets and stockworks in a ~N80E trend. Interpretation of historic records leads to the interpretation that good ore (colloform banded quartz vein 2+ft wide; 0.5 – 1+ opt Au) exists along a N-S cross-structure to the west of the shaft (Dave Hembree, Personal Communication).

Five holes were drilled to test mineralization within the sulfide breccias of Alturas Hill. Numerous phases of brecciation were encountered and a high grade zone was discovered.

One hole tested veining in the Moonlight camp, several small (<6") quartz veins were encountered.

One hole attempted to intercept the massive quartz veining in the Klondyke camp. A 70ft zone (true width) of gray clay was encountered in flow-banded rhyolite. The 550 ft hole did not intersect significant veining.

5 core holes were drilled to further test the presence of a high-grade zone in the Altura's Hill area. Numerous phases of brecciation are observed in the samples recovered (fig. 51). The highly brecciated oxide zone (fig. 51-A) contained the high-grade zone of interest and is encountered down hole from a slightly auriferous sulfide breccia (fig. 51-B).

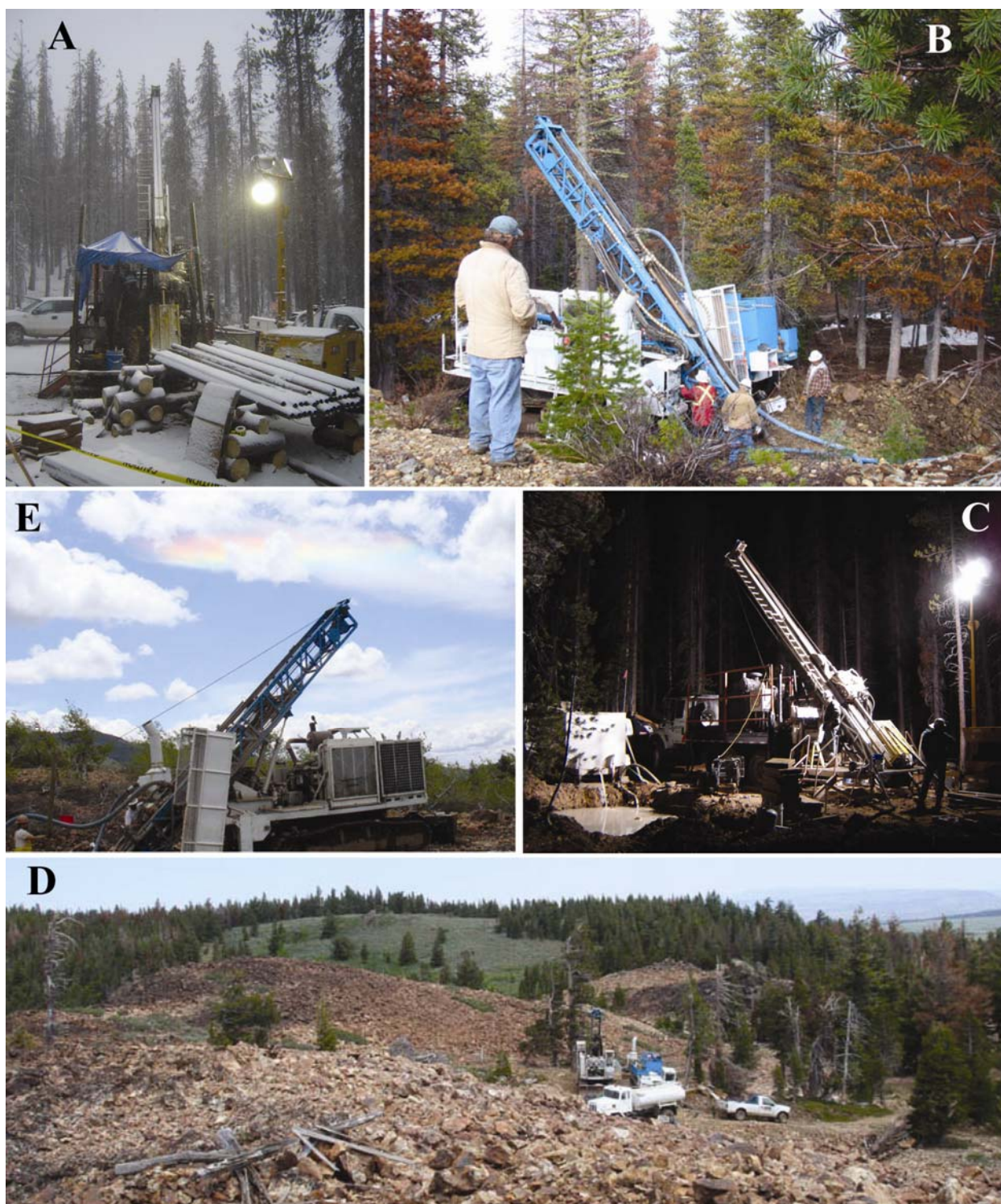


Figure 50. (A) Core drilling in the Alturas Hill zone. (B) Dave Hembree oversees RC hole 1, testing the Sunshine Vein. (C) Night drilling in Alturas Hill zone. (D) Probing veins within the Northwest Group silica body. (E) RC drilling to test the Sunshine vein trend.

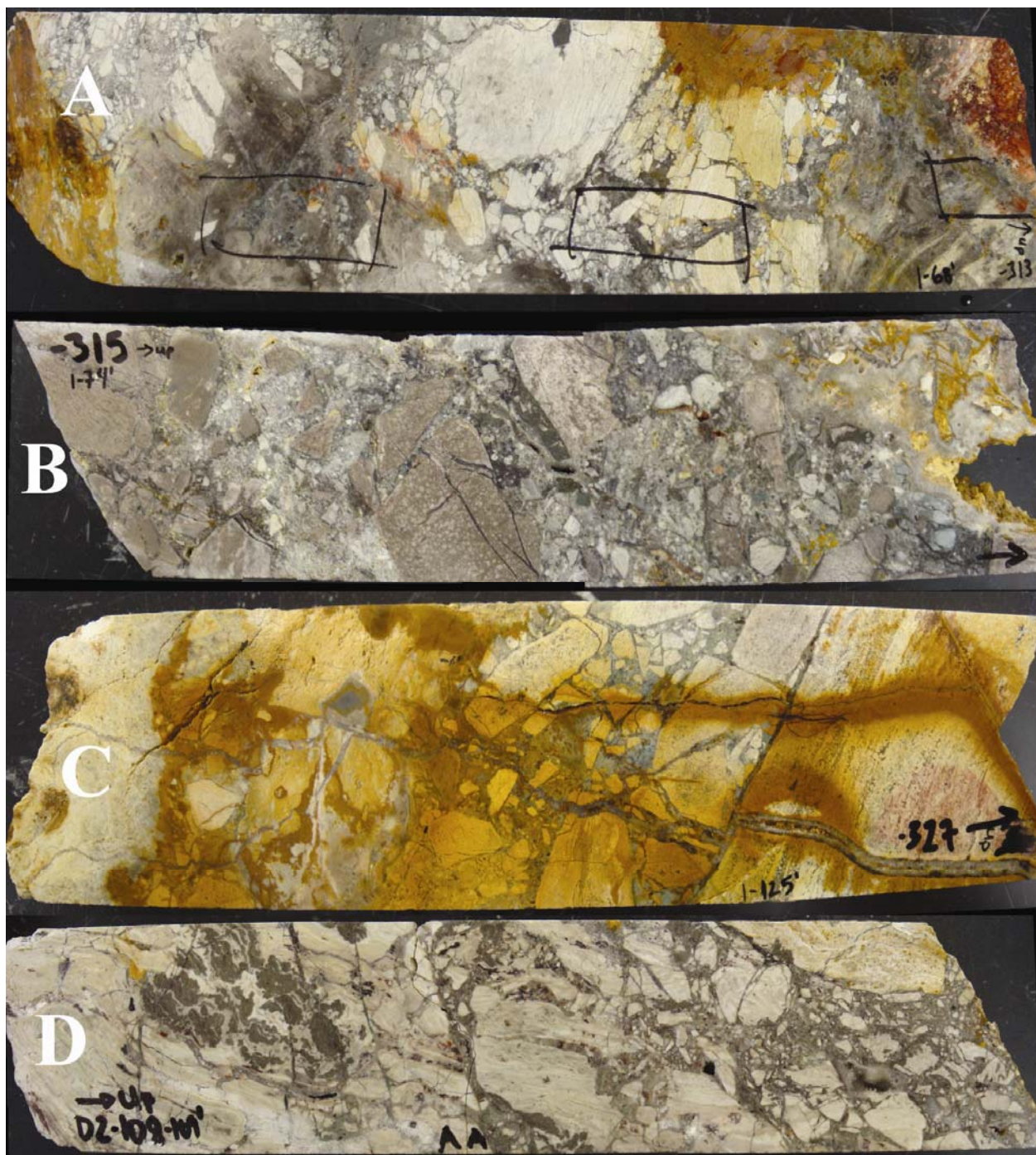


Figure 51. Core drilling in the Alturas Hill provides a detailed view of multiple stages of brecciation: A) heterolithic breccia displaying bleached clasts and iron-staining. B) homolithic breccia is dominantly quartz-pyrite phase and barren of precious metals, later quartz phase (cockscomb with Fe-ox) is auriferous. C) epithermal breccia vein occurs along contact with rhyolite tuff, cross-cutting quartz and Fe-Ox veinlets are observed in the right of photo. D) homolithic breccia within strongly laminated flow unit, bright red hematite grains have developed in numerous small vugs.

5. GIS

Using a Geographic Information System to integrate multiple data types within one reference frame has been an important part of this study. Numerous detailed maps were retained from previous operators and having the capability to geo-reference data in different reference frames was an integral feature of ESRI ArcGIS 9.3. This study has used GIS to incorporate the simultaneous consideration of multiple types of spatial data, such as: geology, geochemistry, structure, alteration, temperature of mineralization, fluid flow, and timing of mineralization. Data sets are digitized and brought into the GIS (layers are stacked as shown in fig. 52) where positive and negative correlations are visually made by the author.

USGS Quadrangle maps are integrated with California State orthophotos and a subset from the NASA Global Digital Elevation Model (DEM) Database. The accompaniment of sub-meter resolution aerial photography, flown in July 2008, plays an important role in verifying ground observations. Slight color variations are perceptible on the massive silica bodies and ground-truth will be an essential part of any remote-sensing investigation. The digital elevation model available from the NASA Shuttle Radar Topography Mission (SRTM) is a powerful tool in discerning regional structural features (fig. 43).

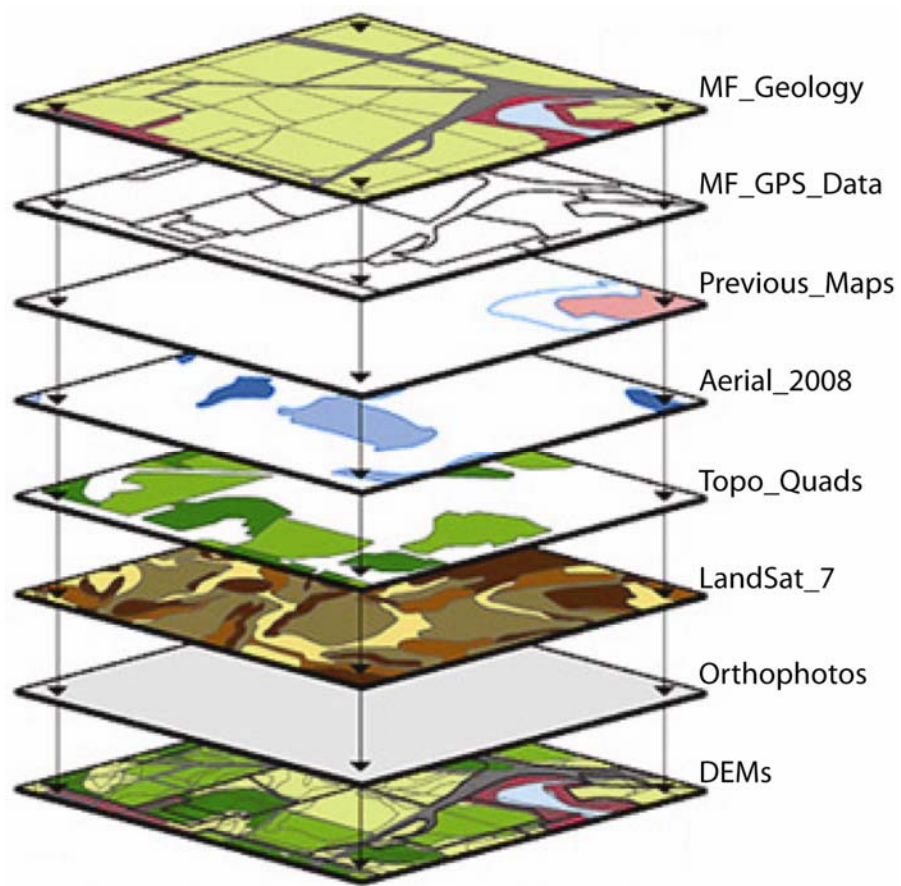


Figure 52. The main layers used in the study are overlain, in the above fashion, in ArcMap and integrated.

6. GEOCHEMISTRY & STATISTICS

The following chapter will discuss the geochemistry of the HGD from a univariant, bivariate, and multi-variant perspective. Univariant statistics analyze the distribution of values for a single element. Bivariate statistics are used to analyze the direct correlation between two elements. Multi-variant statistics take the entire dataset into account; correlating elements are grouped together generating a geochemical signature of a geologic process. Statistical processing of geochemical data is an essential tool in extrapolating the maximum amount of significant elemental correlations.

Geochemical analyses have been made for 129 samples (fig. 53) by ALS Chemex Laboratories (www.alsglobal.com) in Vancouver, B.C., Canada; Samples have been analyzed by ALS Chemex laboratories by acid-digestion ICPMS for 48 elements. Quality control is maintained with 5% submission of duplicates and/or blanks. Quality Assurance is maintained for drill results with the additional submission of standards. Samples are distinguished as being from mineralized structure, silica bodies, dump samples, or unaltered country rock (fig. 53).

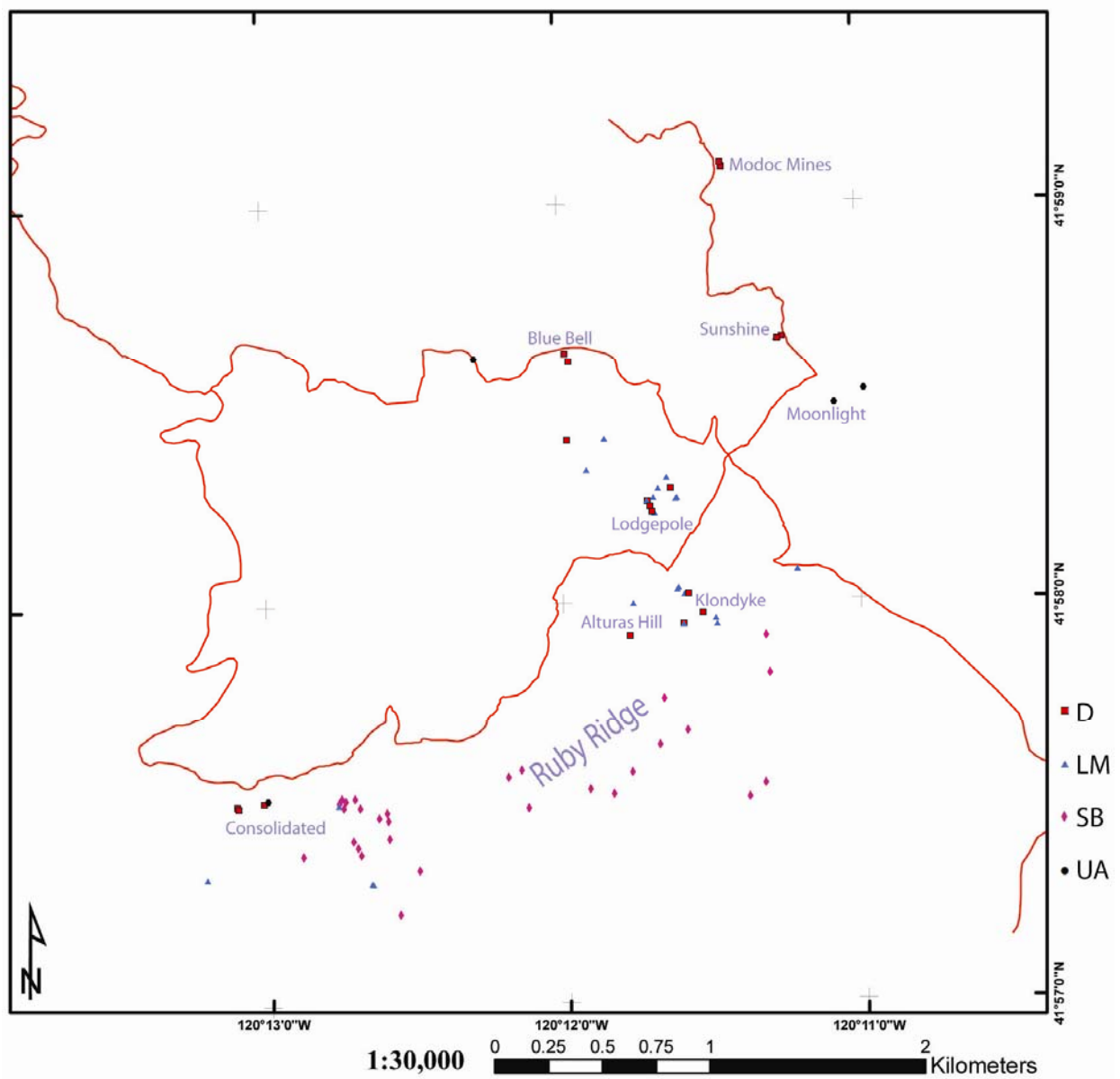


Figure 53. Samples used in geochemical studies are represented by sample type; corresponding sample numbers are provided in Appendix 2, plate 2. This map is a base for all natural neighbor factor maps. Symbols represent each sampling type: (D) dump, (LM) located mineralization, (SB) silica body, (UA) unaltered country rock.

6.1 Univariant

Microsoft Excel and JMPin ver. 4.0.4 statistical software package were used to manipulate database files. Initial Excel processing repairs missing values and those beyond detection limit. If the sample returned a concentration below the detection limit, this was replaced with a value half that of the detection limit. Refinement of data led to the removal of B, Re, and Ta because these elements did not return any values for 95% of the samples, and values returned did not exceed twice the detection limit. The entire original dataset is provided in appendix 3, plate 1. Standards statistics (including average, median, mode, skewness, and kurtosis) are calculated for the initial dataset and are presented in appendix 3, plate 3. Skewness is a measure of the asymmetry of data portrayed on the histogram, and kurtosis is the measure of the multi-peaked nature of histogram.

Processing of multi-element data was completed as seen in the provided flow-chart (fig. 54). Data is imported from Excel to JMP software where outliers are identified. Box-Plot whiskers extend to confinable data, the remaining dots, left floating above represent the outliers. These dots are selected and their respective samples are exported to a separate file. Outliers are collected for all elements and retained for later use. The minimum outlier value is retained for each element (table 8) and used in principal component analysis (chapter 6.3).

After outlier values have been attained, the original excel file is processed to remove all outlying values with blank spaces, this file is saved “outliers_removed”. When all the outliers are removed the data is exported to JMP for more histogram analysis (fig. 56; Appendix 1, fig. 1-7 through 1-13). Outliers were analyzed for the remaining 45 elements. Outlier histograms are provided, figure 60 and appendix 1-14 through 1-21, and discussed in chapter 6.5.

After removing outliers many of the elements show a much more normal distribution, other elements could use a further outlier removal. Histograms are much more open to familial interpretations, which are indicated by secondary bells and change in slope of the normal quantile (Q-Q) plot.

Univariant analyses for this study include histograms, box plots, normal quantile diagrams, and outlier analyses. Descriptive statistics such as the mean, median, mode, and standard deviation are returned in Excel (appendix 3, plate 3). A histogram, box plot and normal quantile plot is provided for each element in figure 56 and appendix 1, fig. 1-7 to 1-13. The values represented in the histograms have been processed for 1st order outliers as shown in figure 54. A histogram helps to visualize the population of numerical values, columns represent how many occurrences of a given ppm value are returned. The box plot (fig. 55), provided in the center of the diagram, shows a visual representation of the mean, quartiles, and outliers. A normal quantile plot is seen to the right of each histogram and box plot (figure 56). The normal quantile diagram is a unique graph for each variable, which is useful for visualizing the extent to which the variable is normally distributed. If a variable is normal, the normal quantile diagram is a diagonal straight line. This diagram is also referred to as a theoretical quantile-quantile diagram or Q-Q diagram. Normal quantile-quantile (Q-Q) diagrams are created by plotting observed values of a variable against the corresponding normal quantiles. Display of data is done by plotting the normal quantiles (or scores) of the standard normal distribution on the x-axis with values usually between -4 to 4, and the variable under study on the y-axis. In this study, the observed values (in ppm or %) are plotted on the x-axis, and values for a normal distribution are plotted on the y-axis. If the samples represent a normal distribution, points will cluster along a straight line.

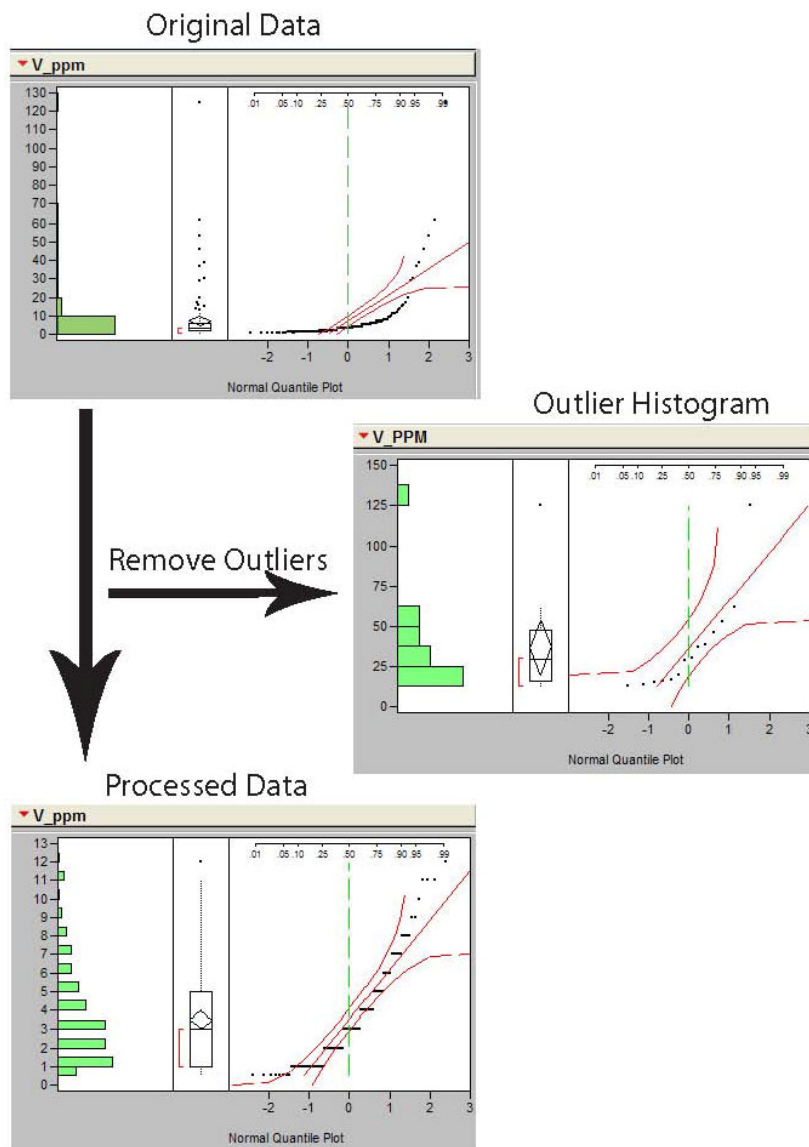


Figure 54. The removal of outliers was performed on each element. The box plot, center, is explained in Figure 54.

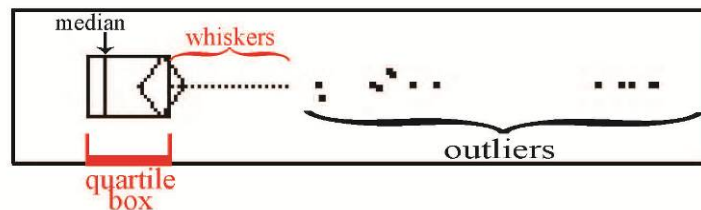


Figure 55. Box plot explanation diagram. Box plots appear to the right of each histogram and describe the data as shown.

“outlier_removed” data is processed in JMP to create histogram, box plot, and Q-Q diagram for each element. Ag, As, and Au are all elevated (fig. 56) with respect to the granitic average (indicated by red line, fig. 56). Q-Q diagrams show that As values occur with a normal distribution, while Ag and Au both have a distribution indicative of a high concentration of low values (Q-Q plot pulls to bottom right). Another notable observation from Q-Q diagrams is that the three mentioned elements all display multiple changes in slope (fig. 56). Ag has one notable inflection, where Au and As have two inflections with similar spacing. Additional histograms are provided for the remaining elements in appendix 1 (fig. 1-7 through 1-13).

The original dataset (before correction) returns very strong standard statistics for precious metals (appendix 3, plate 3). Au has a mean of 5.13, median of 0.4, and mode of 0.01 (all values in ppm). Ag has a mean of 7.25, median of 0.96, and mode of 6.0. As has a mean of 132.01, median of 61.7, and mode of 5.7. These elements also return kurtosis values above 10, and on their respective histograms (fig. 56) two peaks are noticed, indicating an enriched family. Average values for the three discussed elements are strong indications of the possibility for significant precious metal mineralization within the HGD. There are abundant precious metals recognized in the geochemical signature.

Standard statistics from “outlier_removed” data are subdued by removing extraneously high values (appendix 3, plate 3). Au has a mean of 1.34, median of 0.3, and mode of 0.01 (all values in ppm). Ag has a mean of 2.99, median of 0.67, and mode of 6.0. As has a mean of 74.51, median of 55.3, and mode of 5.7. These values are proof of an auriferous system in the study area.

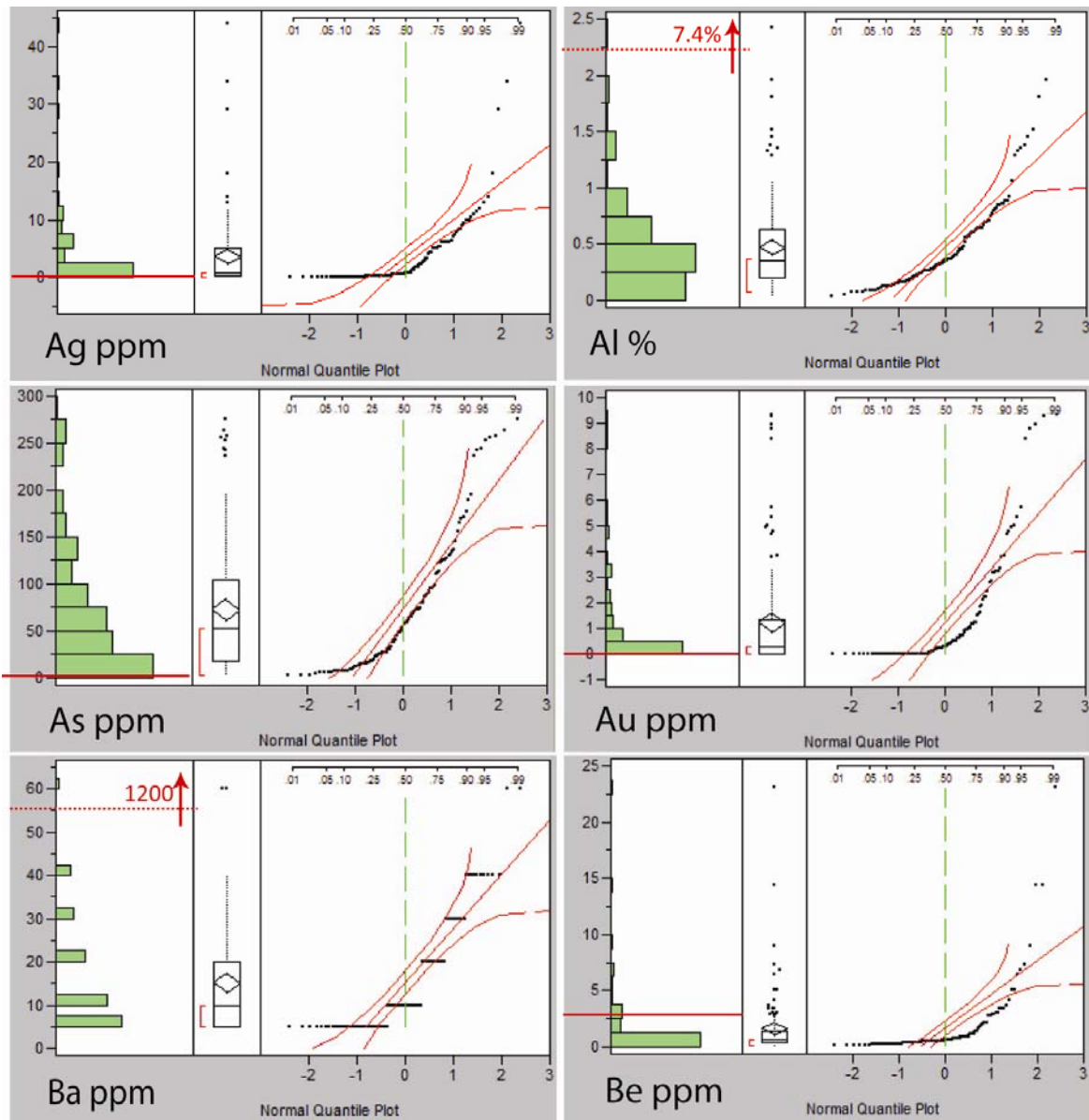


Figure 56. Histograms, box plots, and normal quantile plots from "outlier_removed" data. Elements are labeled in the upper left along with value (values of y-axis are ppm, unless indicated %). Average granitic composition for each element is indicated by the red line. Additional figures from the "outlier_removed" data are provided in appendix 1, fig. 1-7 to 1-13.

6.2 Bivariant

Bivariant analyses in this study are correlation coefficients, pairwise correlation, and correlation scatter diagrams. A logarithmic transformation of the (outlier-removed) data set brings values closer to normality conditions, this is recommended for the statistical analysis of natural datasets, such as rock geochemistry. A base 10 logarithmic transformation is applied to the outlier-removed dataset (appendix 3, plate 2); this modified dataset is used in bivariant and multi-variant analyses.

Correlation coefficients are presented in matrix form (appendix 3, plate 3) which shows the Pearson product-moment correlation coefficients. All correlation coefficients larger than $|0.3|$ are added to arrive at the correlation frequency for the given element. The matrix contains 48 variables, and summarizes the strength of the linear relationships between each pair of variables. If there is an exact linear relationship between two variables then the correlation is 1 or -1 depending on whether the variables are positively or negatively related. If there is no linear relationship the correlation tends toward zero. A detailed analysis of the correlation matrix exhibits some elements standing out as having high correlation frequencies, meaning that they correlate with 20+ elements, and have a correlation coefficient of ≥ 0.3 . The numbers of correlations per element are provided in table 5.

Elements displaying 21 or more correlations on table 5 are analyzed and noticed to be strongly depleted in the rocks of the study area. These elements are discounted in their importance to the geologic system. These elements of lesser importance include a resistate suite (Ce, Ge, La, Sc, Y, Hf, and P), major rock forming elements (Al%, Fe%, Mg%, and Ti%), and a poorly understood group (Ga, Zn, Ba, Bi, Cd, Co, Cu, In, Sn, Th, U, V, and Zr).

Moderate frequency elements (table 5, 10 to 20 correlations) appear to be more relevant in the geochemical signature of epithermal mineralization at High Grade.

Table 5. Correlation Frequencies of the 48 elements included in processing.

Number of Correlations	Elements
26 or more	Al%, Ce, Fe%, Ga, Ge, La, Sc, Y, Zn
21 - 25	Ba, Bi, Cd, Co, Cu, Hf, In, Mg%, P, Sn, Ti%, Th, U, V, Zr
16 - 20	Ag, Ca%, Nb, Te, Tl
11 - 15	Au, As, Cs, K%, Na%, Rb, Sb, Se, Sr,
10 or less	Be, Cr, Hg, Mo, S%, W

6.3 Multi-variant

This study tests the idea of the presence of geochemical families. By reducing outlier values to the minimum outlier value, no samples are removed from multi-variant analysis. The “outlier_reduced” dataset is processed in excel to return log-base 10 values. This log normalization is important when working with any dataset derived from the earth, or nature. This outlier corrected, log-normalized dataset is then imported to JMP where multi-variant analysis on all elements are performed. Principal components are extracted from the correlation matrix into a separate data table. Final output is listed by Factor, giving element coefficients within each factor. These factors are then plotted on bar graphs in excel for analysis.

Factor Analysis allows an empirical analysis and simplification of the inter-relations of many variables. In many cases, a group of elements correlate with each other and reflect the operation of a single process, geochemical characteristic, or master variable. The information contained in large datasets can be expressed by a smaller number of variables that combine elements into groups with close correlation. Principal Component Analysis (PC) is performed to reduce a large number of variables into a smaller number, and for further investigation of the relationships between the elements.

Table 6. Factor score eigenvalues represent the prevalence of each factor in the data set.

Factor	1	2	3	4	5	6	7	8
Variance	29.1	18.3	10.5	5.6	4.4	3.1	2.9	2.6

The principal components (PCs) with eigenvalues larger than 2.5 are extracted with the PC loadings rotated for the maximum variance. A total of eight PCs are extracted, which account

for 76.71% of the total variance. Factor three is presented in figure 57, and represents the epithermal suite. The remaining seven factor score loading bar graphs are presented in appendix 1 (fig. 1-22 through 1-28). A summary table of these factors has been broken down into geologic families for integration with geologic observations reported other places in this work; table 7 is provided at the end of this sub-chapter.

Factor 3, figure 57, is strongly representative of the epithermal event in the study area. Au, Ag, As, Bi, Hg, Mo, S, Sb, Se, Te and Tl are all either part of the epithermal indicator suite or hydrothermal ore components (Simmons and Brown, 2000; Romberger, 1993; Herrera et al, 1993; Heald et al, 1987; Silberman and Berger, 1985; Buchanan, 1981). These elements are also chalcophile and are likely concentrated in pyrite and associated sulfides. Be and Fe are not epithermal indicator minerals and their presence in this factor is poorly understood. This factor is depleted of all the major rock forming elements, Al, Ca, Na, Mg, probably due to the pervasive silicification related to the epithermal event of this factor.

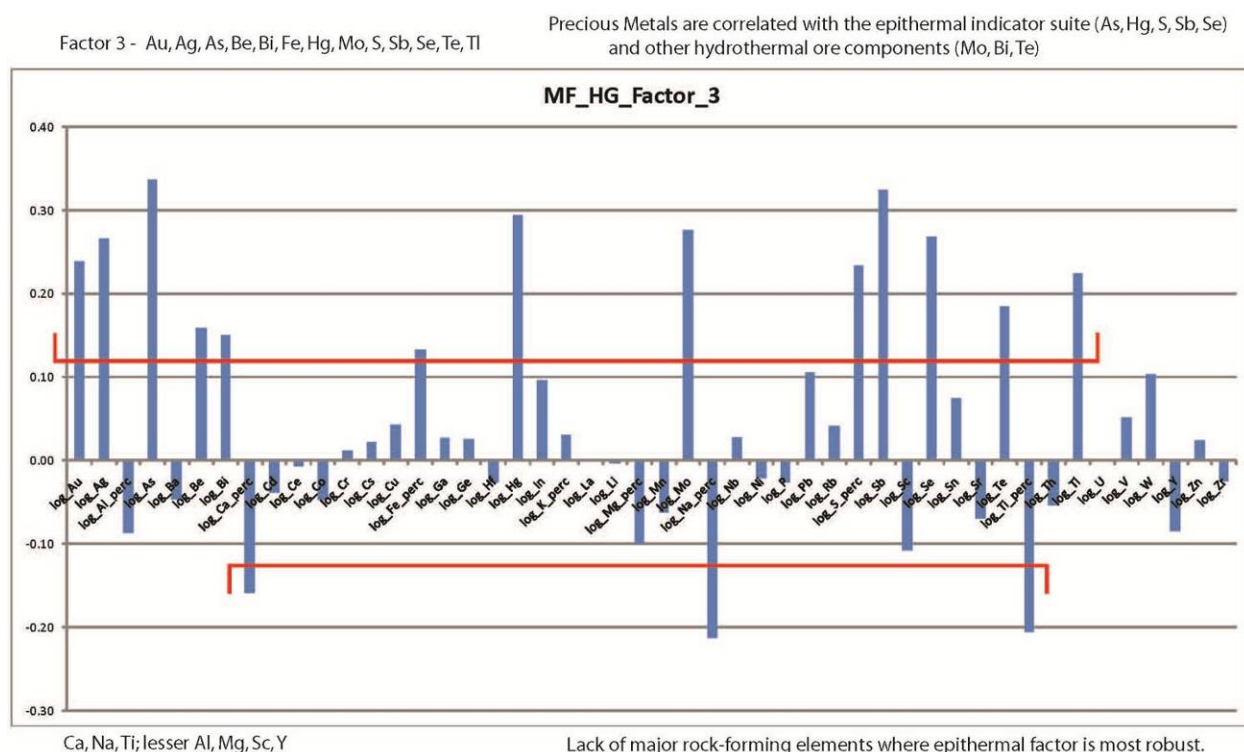


Figure 57. PC results of Factor 3, epithermal trace suite.

Factor 1 (appendix 1, fig. 1-22) has many components and can be broken down into at least seven groups based on minerals. The strong rare earth manifestation of the elemental group, Ce, La, P, Sc, Th, U, and Y is seen in phosphate minerals, namely monazite (appendix 1, fig. 1-54, 1-55, 1-56, 1-64, 1-66, 1-72). Al and Ga are indicative of clay minerals. Zn, Ge and In are chalcophile and may be related to a sphalerite phase. Bi, Cd, Pb and Sn are part of the base metal group in the study area. Ba, Mg, Ti and V are the manifestation of mafic basement materials. The remaining elements, Fe, Mn, K, Zr, are not immediately distinguishable to an event. Factor 1 is possibly made up of multiple other factors. 24 elements are actively associating in this factor, too many dissociative elements are teamed up and this reduces the interpretative strength of this factor.

Factor 2 (appendix 1, fig. 1-23) shows Cu actively correlating and making familial relationships. Cu, Co, Mg, and Ni represent a mafic base metal component. Au, Ag, and Mn are present for the precious metal family. Ca, Te, Li are present and point toward a minimal sulfide capacity for Factor 2. Zr, Hf, Sn, Th, and Nb all have negative factor score loadings in this factor.

Factor 4 (appendix 1, fig. 1-24) shows the epithermal event with a distinctively different mineralogy to factor 3 (fig. 57). Bi, Pb, and Te are representative of epithermal mineralization. Na, Be, Zr, Hf, Nb, and W are indicative of alkaline hydrothermal environments, much like the rhyolite domes of the study area.

Factor 5 (appendix 1, fig. 1-25) appears to represent a phase of precious metal deposition. Li, Be, Cs, and Rb are indicative of alkaline hydrothermal environments. Paragenetic observations, section 7.4, indicate that significant precious metal mineralization is associated with the adularia-rich phase. Au, Al, Ga, K, and Te may represent the gold in adularia observed in multiple sections. The V is not understood at this point. It is also notable that the negatively correlated elements, Hg, Na, S, and Se, may show that this factor indicates a deeper phase of epithermal activity (Hg and Se are reportedly elevated in the upper portions of epithermal systems [Simmons and Brown, 2000; Buchanan, 1981]), possibly accompanied by sodic leaching.

Factor 6 (appendix 1, fig. 1-26) may represent the basement component of the study area. Ba, Co, Cr, Mn, and Ni are all strongly mafic, whereas Mo, Nb, and W are strongly felsic. This opposition between mafic and felsic may be explained by a bimodal factor. Another notable feature of factor 6 is the depletion of alkalis.

Factor 7 (appendix 1, fig. 1-27) may again be a representative of the epithermal phase of activity. Mn, Cd, Hg, S, and Zn are indicative of an epithermal environ. Li, Cs, Na, Rb are alkali/alkali-earth and may represent a more intermediate (andesitic) composition. The Cr and Ni are strongly mafic and combined with the alkali/alkali-earths this factor may represent the host stratigraphy for rhyolite/hydrothermal emplacement.

Factor 8 (appendix 1, fig. 1-28) has elemental components that indicate minor Bi and S. Cr and Ni are strongly mafic, possibly representative of basement. Ba, K, Ca, Sr, and Rb are alkali-earth elements and may indicate andesitic basement.

Table 7. Table summarizing factor analysis of 129-sample, 48 element data set, outlier_removed.

	Active Elements	Geochemical Associations
Factor 1	Ce, La, P, Sc, Th, U, Y	1.1 REE-Phosphate (monazite)
	Al, Ga	1.2 adularia phase
	Zn, Ge, In	1.3 sphalerite phase
	Bi, Cd, Pb, Sn	1.4 trace hydrothermal
	Ba, Mg, Ti, V	1.5 mafic
Factor 2	Cu, Co, Mg, Ni	2.1 mafic base metal
	Au , Ag, Mn	2.2 precious metal family
	Ca, Te, Li	2.3 anti-sulphide
Factor 3	Au , Ag, As, Be, Bi, Fe, Hg, Mo, S, Sb, Se, Te, Tl	3.1 Epithermal precious metal indicator suite with hydrothermal ore components
	neg Ca, Na, Ti, Al, Mg	3.2 lack of rock-forming elements
Factor 4	Bi, Pb, Te	4.1 epithermal
	Na, Be, Zr, Hf, Nb, W	4.2 high field strength
Factor 5	Li, Be, Cs, Rb	5.1 felsic alkalic
	Au , Te, Al, Ga, K	5.2 Au-telluride phase with adularia
Factor 6	Ba, Co, Cr, Mn, Ni	6.1 mafic
	Mo, Nb, W	6.2 high field strength
	As, Be, Cd, Li, U	6.3 epithermal + alkali-earth
Factor 7	Mn, Cd, Hg, S, Zn	7.1 epithermal
	Li, Cs, Na, Rb	7.2 felsic alkalic
	Cr, Ni	7.3 mafic
Factor 8	Ba, Cr, Ni	8.1 mafic
	K, Ca, Sr, Rb	8.2 alkali/alkali-earth

6.4 Factor Mapping

After calculating the Principal Component Analysis to determine factors 1 through 8, JMP software extrapolates factor scores to each sample for factor mapping. Factor scores are given to each sample and provided in appendix 3, plate 3. Factor scores are mapped in Surfer using a natural neighbor model to create a contour map, a blue-yellow-red (low to high) color scale is used. A natural neighbor modeling method was preferred for this dataset due to the samples having a poor spatial distribution.

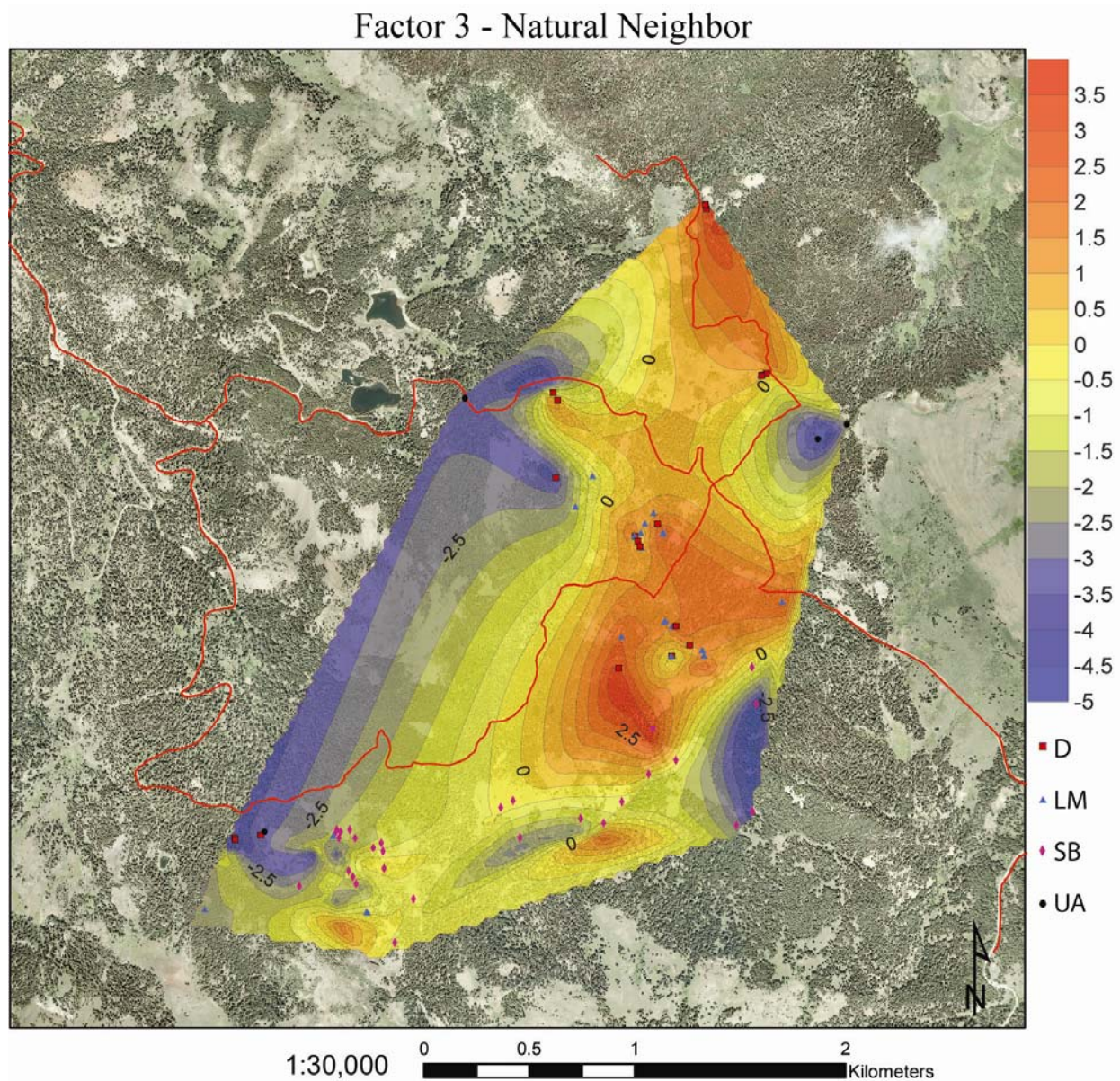


Figure 58. A natural neighbor method was used to model geochemical factor scores in a geographic format. Additional Factor Maps are provided in Appendix 1, fig. 1-27 to 1-33.

Factor 1 (appendix 1, fig. 1-29) is strongly represented in the western Consolidated mines and to the east through the CSB. There is also an anomalous area in the Lodgepole camp, as well as to the east and south of the Klondyke. Rare earths manifest as monazite (chapter 7.5) in samples from these camps.

Factor 2 (appendix 1, fig. 1-30) is encountered in the vein samples obtained from camps that displayed well developed veining. Colloform and banded vein samples were obtained in these positive anomaly areas, whereas the large blue areas were typically hydrothermal quartz (minor veining/stockworks/breccia) with variable pyrite. Quartz veining from positive areas commonly displayed boiling textures and such samples were submitted; the strong precious metal family presence in this factor should be anticipated from texture, but the background mafic signature is less common.

Factor 3 is mapped in figure 58, the area in red includes the disseminated surface deposit (fig. 7) and extends NE along trend through the multi-lithologic breccias (Tmlb; appendix 2, plate 2) of the Sunshine and Modoc Mines camps. Blue Bell and Klondyke are strong as well. The negative anomalies of Moonlight and Consolidated may indicate their not experiencing the epithermal phase represented by factor 3.

Factor 4 (appendix 1, fig. 1-31) is very strong in the Sunshine and Moonlight Camps, also notable highs are encountered in the silica body along Ruby Ridge, extending in an east-west trend stopping at the western extent of the Consolidated silica body. This factor may indicate a later stage (more evolved felsic component) of epithermal activity expressed in the semi-linear (E-W) trend of silica bodies (fig. 46) in the southern half of the HGD.

Factor 5 (appendix 1, fig. 1-32) is concentrated along the northwestern shear zone trend that is constrained immediately West of the Klondyke and extends through Lodgepole and Blue Bell. The positive anomaly of the Sunshine and Moonlight camps may be due to their proximity and inherent influence from the regional normal fault zone that is the western boundary fault of Mt. Bidwell (appendix 2, plate 1, 2). Hypothesis 1: Negative values are returned from West Consolidated, this felsic factor should not be strong in the andesite hosted vein; it is not

understood why the rhyolite hosted vein of Modoc Mines is negative as well. Hypothesis 2: Modoc Mines and Consolidated display the thickest colloform banded veining encountered in the HGD (up to 0.3 m)(massive quartz veins in the Klondyke reach 1.5 m, and also return lower values). Positive areas seem to be along fault zones which were mined for variable precious metal in silicified gouge.

Factor 6 (appendix 1, fig. 1-33) is strongest in the Sunshine and West Consolidated camps. A minor positive trend is seen in samples from Klondyke through Blue Bell. This factor indicates a poorly understood, bimodal (felsic + mafic), possibly epithermal phase of alteration.

Factor 7 is indicative of a unique epithermal phase. The isolated nature of anomalies, observed in appendix 1, figure 1-34, and concentration within silica bodies (fig. 45) indicate a limited lateral extent to this phase. Anomalies are encountered at Alturas Hill, Sunshine, Modoc Mines, and the Consolidated Silica Body.

Factor 8 (appendix 1, figure 1-35) is strongest around the Blue Bell camp. This factor is poorly understood and of lesser importance.

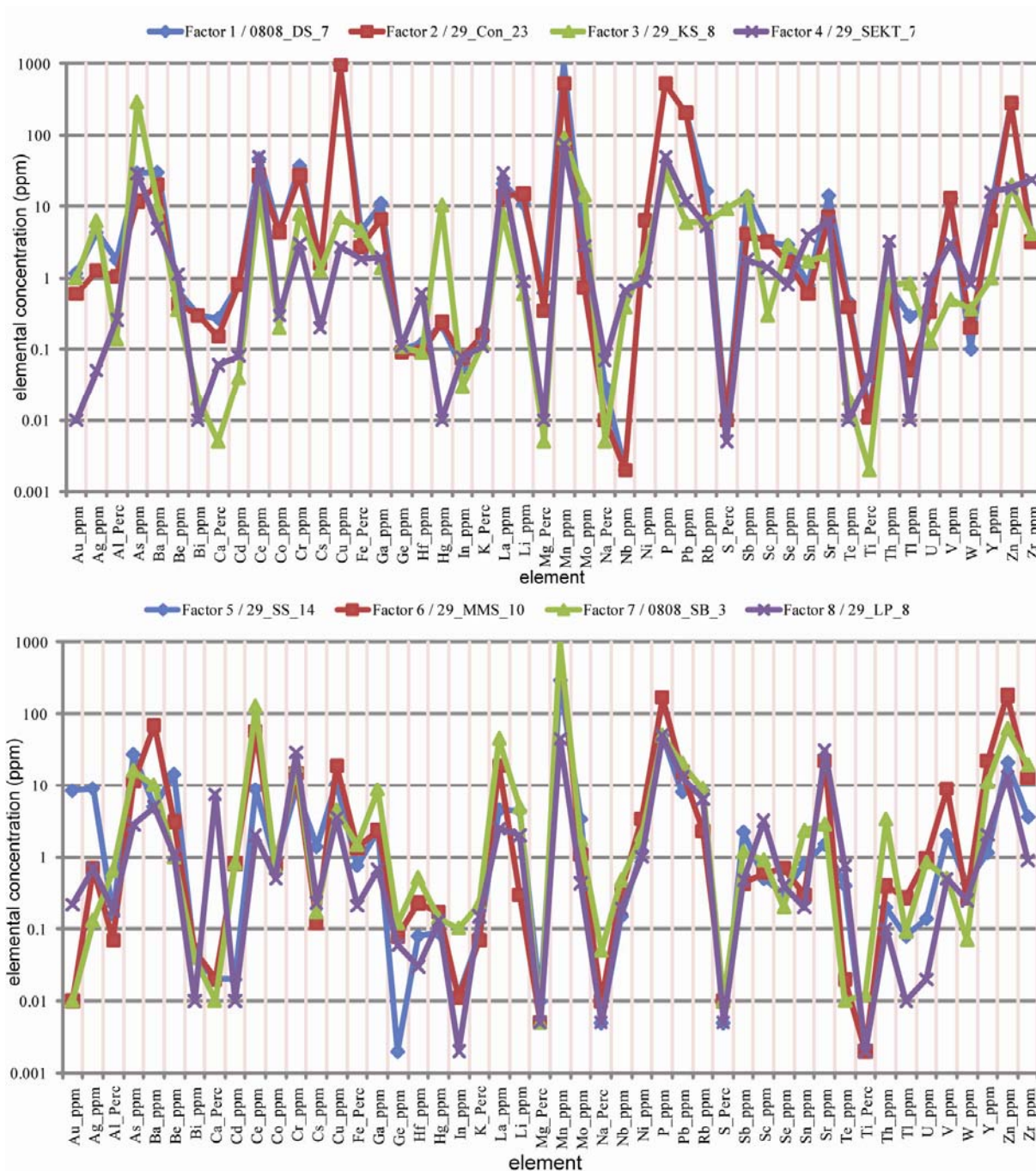


Figure 59. Forty eight element concentration, presented in spider diagram format, for representative samples of each factor (FS).

The sample displaying the highest value from figure 58 is chosen to represent this group (named Factor Sample {FS}) in figure 59 as factor 3. Each sample chosen to represent the factor in figure 59 is chosen in this manner. Figure 59 focuses on the ppm values returned for the FS,

sample names are provided in the top-centered legends. Geochemistry for each factor sample is also provided in chart form (appendix 3, plate 3).

6.5 Outliers

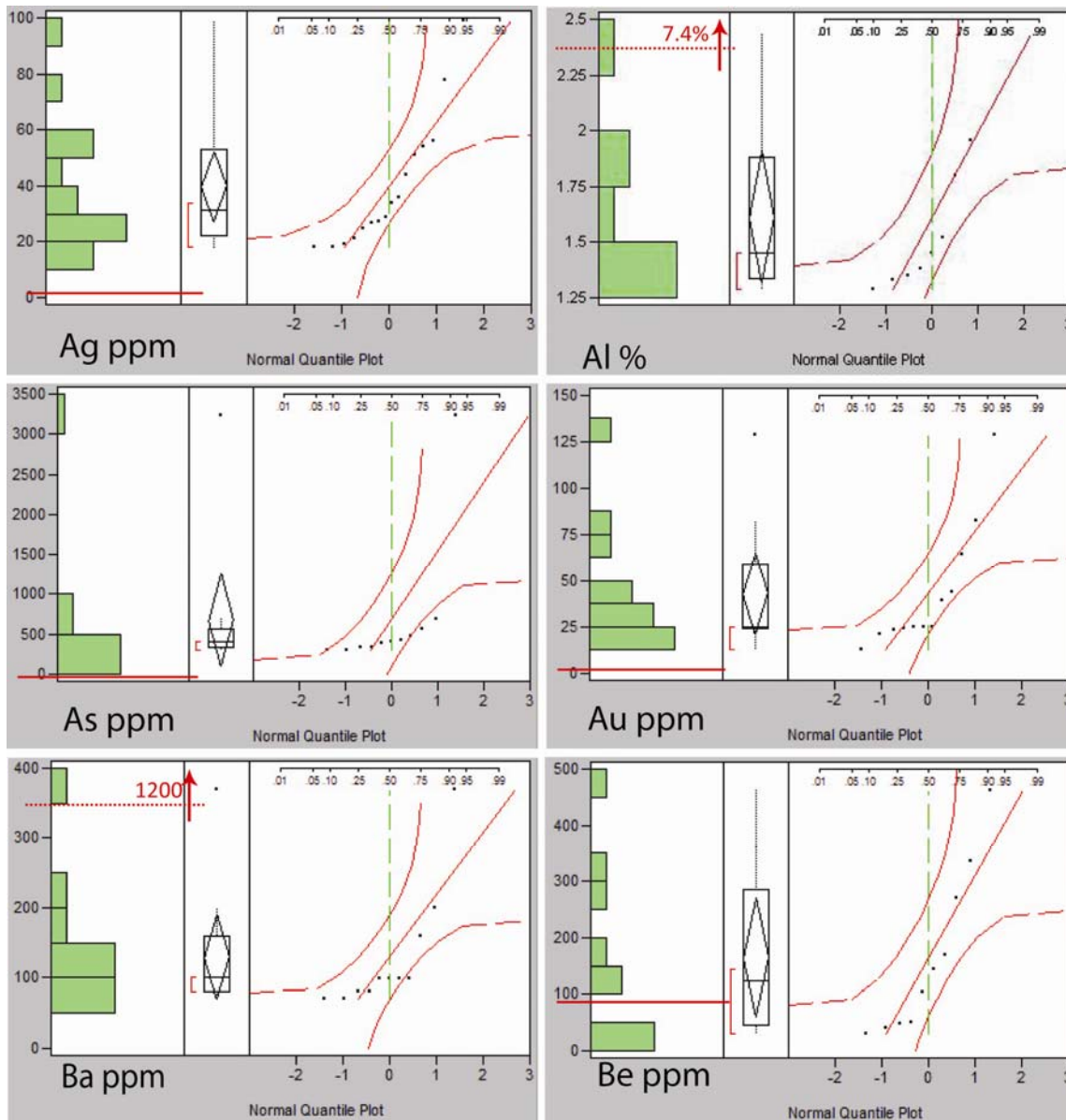


Figure 60. Outlier data is extracted and presented here. Outlier histograms, box plots and normal quantile diagrams are provided for the indicated elements (Ag, Al, As, Au, Ba, Be). Additional outlier histograms are provided in appendix 1, fig. 1-14 to 1-21.

The outliers values for precious metals (Au, Ag) within the study area reach a maximum around 100 ppm (fig. 60), sampling aimed to acquire maximum values. Au returns 12 outlier values which range from 12.5 to 129 ppm. Ag returns 16 outlier values which range from 18 to 99 ppm. As returns 11 outlier values which range from 297 to 3,240 ppm. Au and Ag outliers

(fig. 61; appendix 1, fig. 1-36) are concentrated at the Sunshine camp with, some single highs from other camps. As outliers (appendix 1, fig. 1-38) are concentrated in the area of the surface deposit (fig. 7)

Histograms for each element's outliers are provided in fig. 60, and appendix 1, fig. 1-14 through 1-21. Outlier cut-off values are provided in table 8. These anomalous, outlier values are some impressive indicators of the localized elemental concentrations encountered over the study. Outlier values are geographically plotted in ArcGIS using graduated circles which correspond to the indicated values in the bottom-right legend, as seen for Au in figure 61 (outlier maps for Ag, Al, As, Ba, Bi, Co, Fe, Li, Mn, P, Sb, Se, Te, and Tl are provided in appendix 1, fig. 1-36 through 1-49). Hg, Pb, Zn, Cu, and U are displayed together (appendix 1, fig. 1-50). There are no outliers to report for Indium.

Table 8. Outlier cut-off values by element, values presented are in ppm unless indicated percentage.

Au – 12.75	Ag – 18	As – 294	Ba – 70	Be – 29.5	Bi – 0.3
Cd – 0.81	Ce – 134	Co – 4.4	Cr – 62	Cs – 1.6	Cu – 955
Ga – 17.85	Ge – 0.22	Hf – 0.61	Hg – 10.5	La – 80.7	Li – 10.9
Mn – 1035	Mo – 41.4	Nb – 0.67	Ni – 6.5	P – 530	Pb – 205
Rb – 23.5	Sb – 14	Sc – 3.2	Se – 2.9	Sn – 3.9	Sr – 22.1
Te – 0.76	Th – 3.3	Tl – 0.84	U – 0.95	V – 13	W – 0.79
Y – 15.9	Zn – 280	Zr – 23.6			
Fe% - 4.64	Al% - 1.33	Ca% - 0.37	K% - 0.42	Na% - 0.02	S% - 1

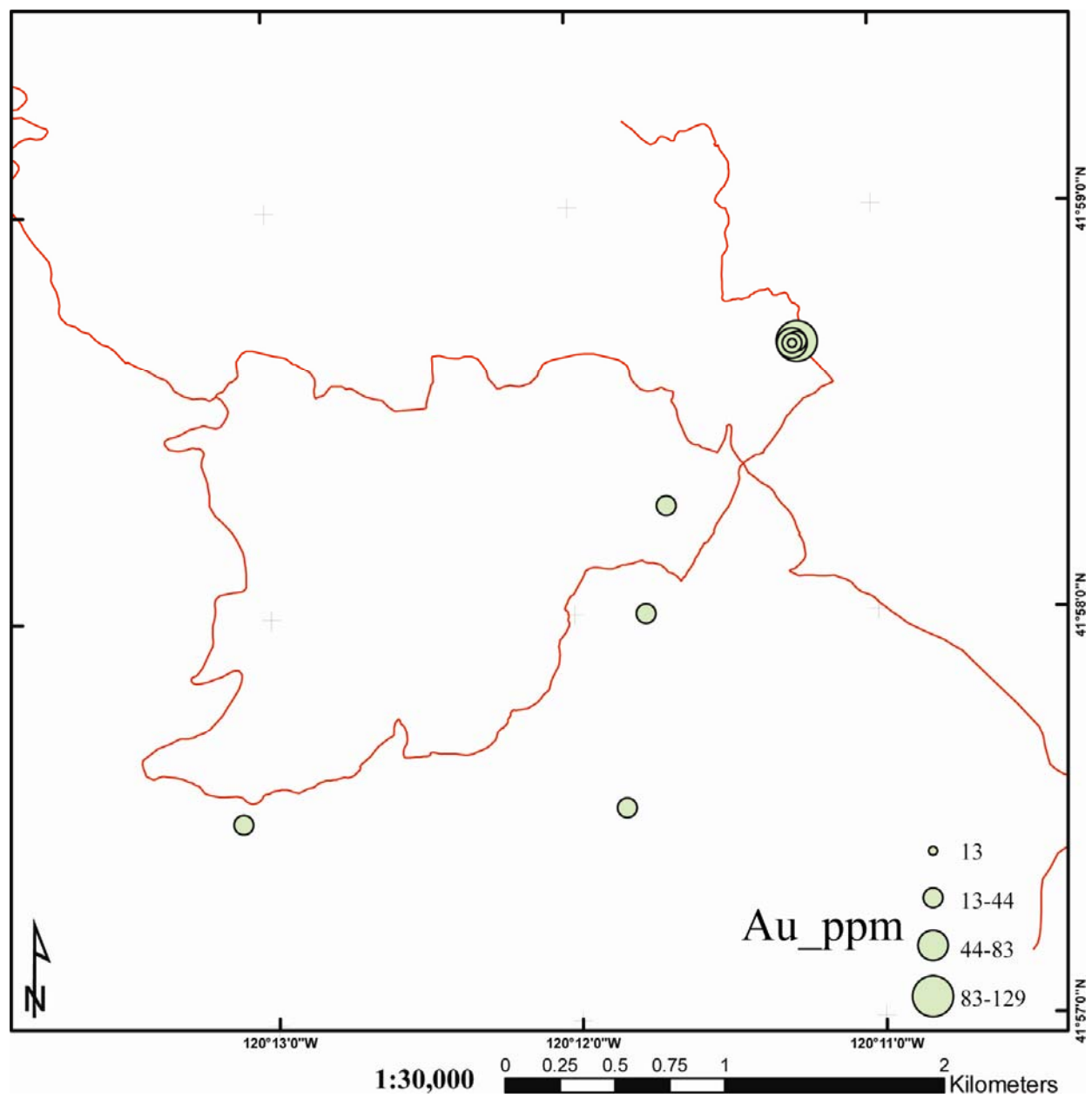


Figure 61. Map of Au outlier values. The stacking of multiple values from the sunshine vein is striking.

6.6 Interpretation

The geochemical signature of the HGD follows typical epithermal chemistry from literature, with some modification. Au, Ag, As, Hg, Li, In, Sb, and Se are all enriched in the epithermal system of the HGD. Factor analysis has proved highly useful in the geochemical classification of multiple phases and parts of the epithermal mineralization system.

Of the eight factors interpreted, five represent epithermal phases of mineralization. Factor 3.1 contains precious metals and every epithermal element mentioned in literature (Simmons and Brown, 2000; Romberger, 1993; Herrera et al, 1993; Heald et al, 1987; Silberman and Berger, 1985; Buchanan, 1981); this strong epithermal signature is accompanied by a depletion of all major rock-forming elements and indicates a silica concentration nearing 100%. Factor 4.1 is an epithermal subset of 3.1 (also similar to 1.4). Hydrothermal monazite \pm rutile (appendix 1, fig. 1-54, 1-55, 1-56, 1-64, 1-66, 1-72) are present in the quartz/adularia phase. All chalcophile elements will concentrate in pyrite.

There is a mafic theme to 5 of the factors (Table 7: 1.5, 2.1, 6.1, 7.3, 8.1), this is likely due to the prevalence of mafic and intermediate rocks in the study area, contributing to the system through melt incorporation and meteoric fluids circulating in these units.

The felsic alkalic and high field strength elements show up actively in factors 4, 5, 6, and 7; they combine with epithermalphile and/or chalcophile elements to create these factors. Factor 4 and 5 (without mafic/chalcophile) are almost inverse to one another when mapped (appendix 1, fig. 1-31, 1-32), significant lows (factor 4) along the Klondyke-Blue Bell trend abruptly shift to highs (factor 5). Lows in West Consolidated and Modoc Mines persist in both factors. Factors 6 and 7 have similar highs and lows, significant highs in both of these factors are seen in the Sunshine, Blue Bell, and West Consolidated.

7. MINERALIZATION

The study collected 264 mineralized samples throughout the district, displaying a wide variety of hydrothermal quartz. Field descriptions include a visual description of observed quartz textures. This study analyzes 30 thin-sections and 60 thick-sections of hydrothermal mineralization. Samples have been studied by optical microscope for textural description and to prioritize opaque identification. Electron Microprobe analyses provide element maps which are interpreted to determine mineralogy and make paragenetic observations. A visual breakdown of mineralization encountered on Discovery Mountain is provided in figure 62.

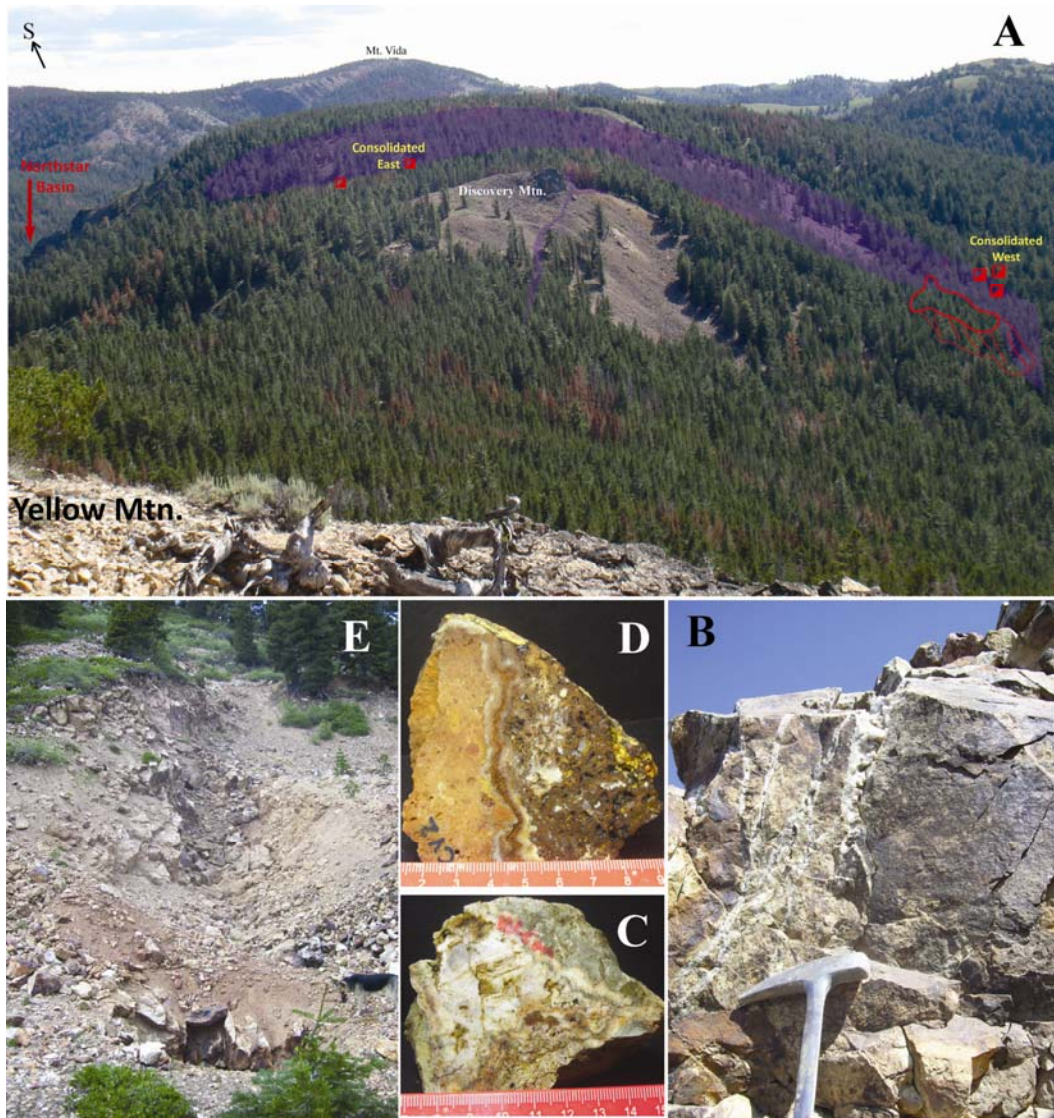


Figure 62. Northwest trending vein/shear zone cutting across Discovery Mountain, the Consolidated Mines Camps are on both sides of the mountain. Taken from Yellow Mtn., looking southwest. The purple indicates epithermal veining.

7.1 Quartz Textures

Historic mine dumps were thoroughly picked for all available mineralization. The quartz textures observed are organized by camp and described below, with respective photos in accompanying figure.

East Consolidated (ECon/Con) – This dump occurs on the SE slope of Discovery Mountain (fig. 62) and workings include three tunnel levels along vein. Vein material (fig. 63) displays opaline quartz with hematite, limonite (A), jarosite, and goethite (B). Hematite-cemented intrusive breccias occur in close proximity and breccias display multiple stages (C). The highly silicified and locally argillized Consolidated Silica Body yields multiple silica forms: host rhyolites are pervasively bleached and display colloform banding followed by crystalline quartz (D), conversely Fe-oxide stained rhyolites are located in proximity to shear zones and their hematite-cemented breccias display a later phase of cocks-comb quartz within vugs (E).

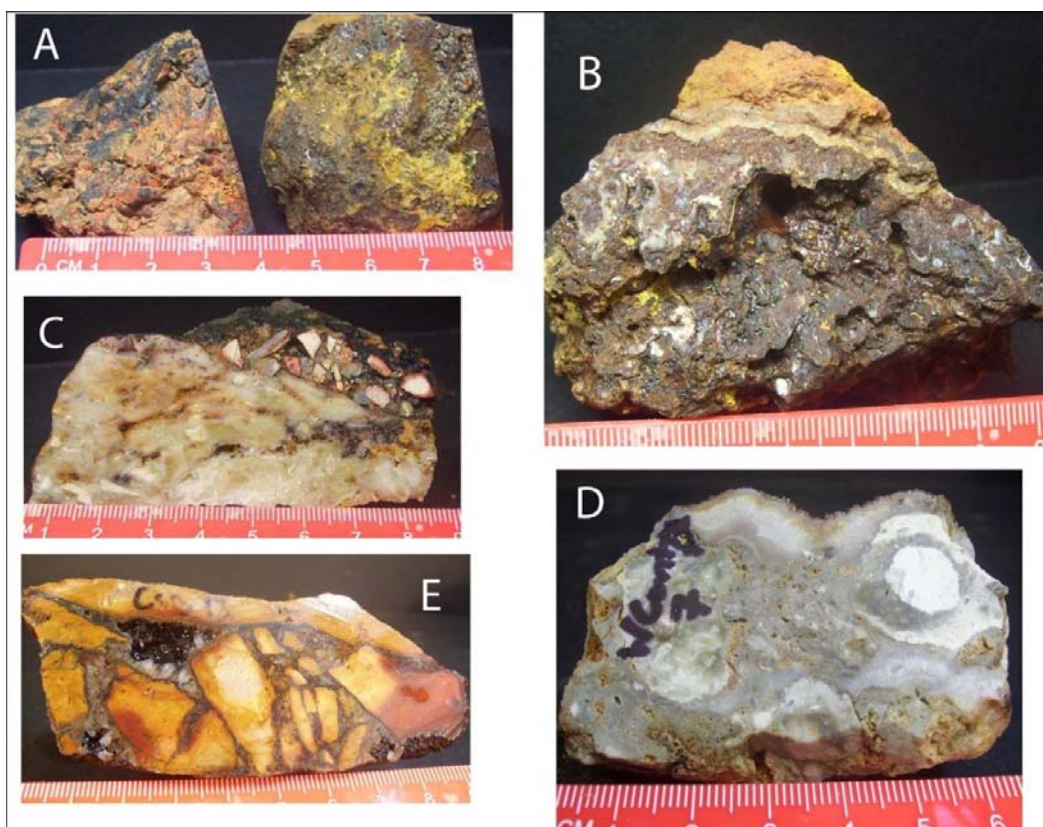


Figure 63. Vein material collected in the East Consolidated mines.

West Consolidated (WCon/Con) - The main workings of the Consolidated Mines display a wide variety of textures and pulses of mineralization (fig. 64). Most vein material encountered on the western portion of Discovery mountain (fig. 62) is hosted by the andesitic sequence, however the upper portion is hosted in silicified rhyolite (A) this example displaying some siliceous sinter. Andesite hosts (B) banded veins of waxy green quartz, crumbly white adularia, and vuggy orange pockets. (C) displays the andesitic wall rock contact and the minimal pervasive silicification, the competence of the green quartz is enhanced when the Fe-rich zone is encountered at the wall contact. An initial layer of pink adularia is seen on the wall rock contact in D, E, and H; each of the samples then proceeds into: bladed calcite which is replaced by quartz, sample Con-6, fig. 72, 74; appendix 1, fig. 1-51 through 1-53) (D), cloudy crystalline

white quartz (E), and coarsely crystalline, translucent amethystine zones (H). White, crystalline adularia occupies minor veinlets (G-right) while vugs are precipitated with micro-crystalline quartz (G-left). Coarse, crystalline amethystine quartz after waxy, vuggy quartz/adularia (J). Deep purple quartz is found in conjunction with the basal precious metal horizon and the lower base metal zone (I), the presence of adularia abruptly stops and is accompanied by Fe enrichment along the wall contact. Chalcopyrite is observed in variable abundance, along with some secondary copper oxides (K). The base metal zone is accompanied by a higher level of wall rock propylitization, visible pyrite and epidote druses within vesicles are observed (F). Barren, plagioclase-cemented breccias (L) are interpreted to be the roots of the system in this portion of the district (Simmons and Brown, 2000; Buchanan, 1981).

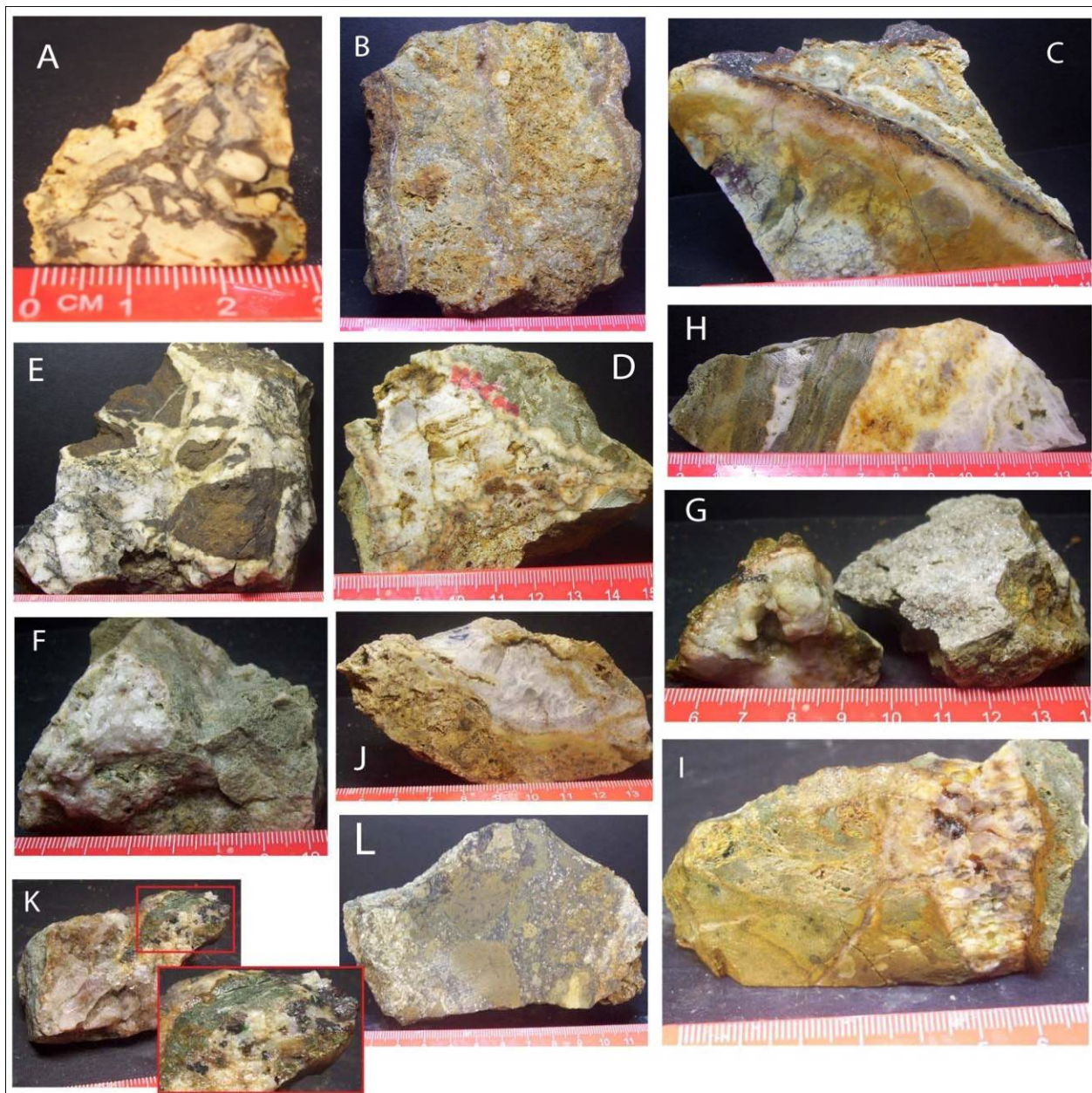


Figure 64. Vein material collected from the dumps of Consolidated West (CW/Con) camp.

Klondyke (K) - Mudcracks (A) have been preserved by silica and bubbly box works (B) represent the paleo-surface (fig. 65). Quartz veins within the Klondyke camp are the thickest observed in the HGD; massive barren quartz accompanied by vuggy zones (C) are encountered, up to 2 m wide and striking NE. There are at least 5 veins and 3 fault zones that dissect this

camp (Appendix 2, Plate 2). White massive quartz also proceeds into vuggy zones that display increased iron content and also coarse grained quartz crystals (D). Large blades, 5+ cm, are interpreted to be barite replacements (F), whereas the smaller blades (G) were calcite. A large sample was collected of the pictured vein, it displays a highly vuggy texture (E) along with “stringer” sprays of colored oxides. Quartz veining is cut perpendicularly by shear zones, consisting of hematite cemented breccias (H). The uppermost levels of a hot springs system are observed along Ruby Ridge, near the intersection with the Klondyke camp.

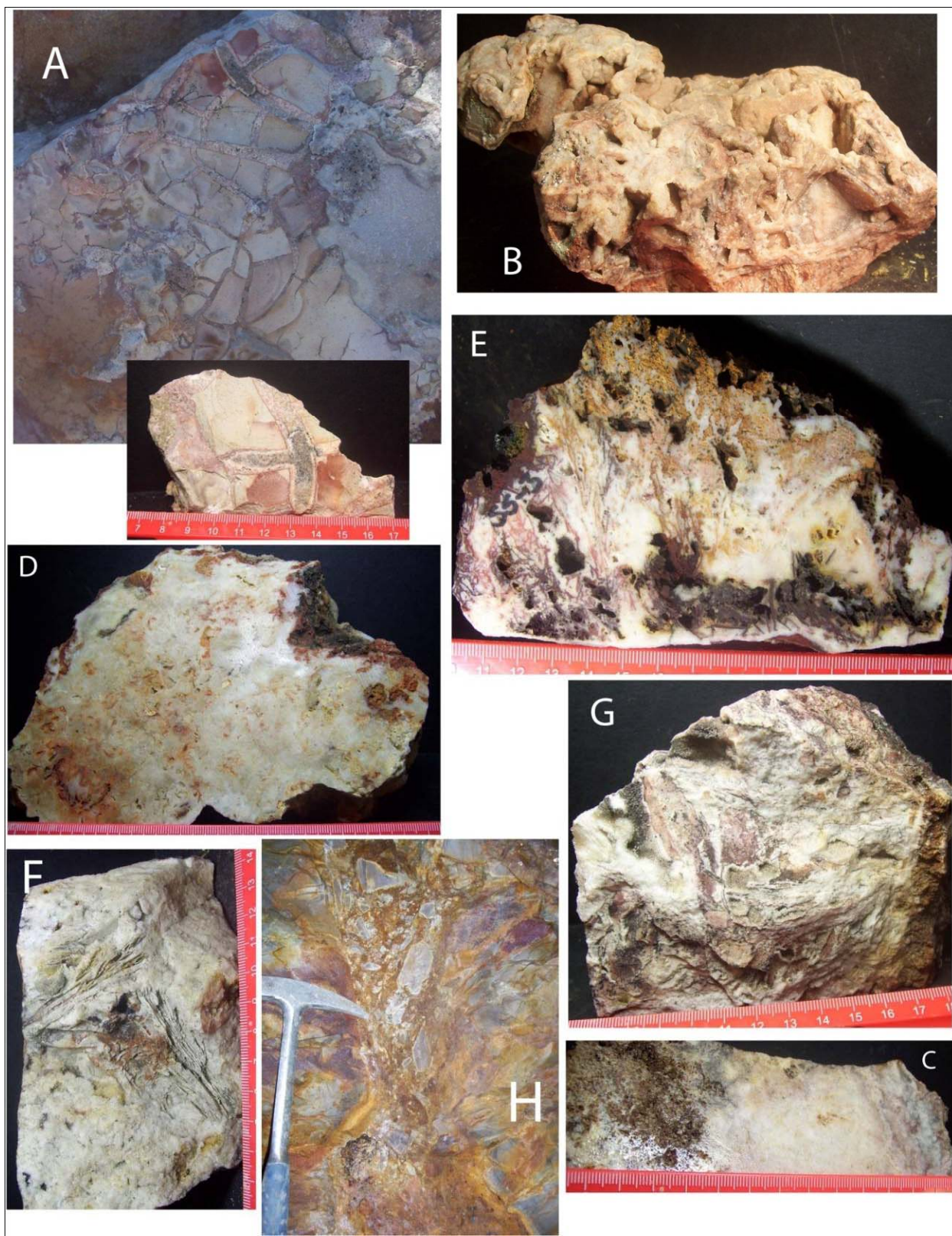


Figure 65. Vein material observed in the Klondyke Camp segment of the study area.

Lodgepole (LP) - There are two main mineralized features in the Lodgepole camp, both striking NNW and dipping towards each other at $\sim 80^\circ$. The eastern, vein-type structure (A) is typified by opaline to colloform banding and prominent iron-oxide staining. Along the western fault/fracture-zone there are gouge zones that have been silicified (D), two clast groups are recognized. The gouge silicification varies from opaline (D) to a layered vuggy nature (B) as a traverse up-section is made. Minor veining of coarsely crystalline (C) quartz is observed in abundance between these two structures. Goodell and Feinstein stand along a stoped gouge zone (fig. 66).

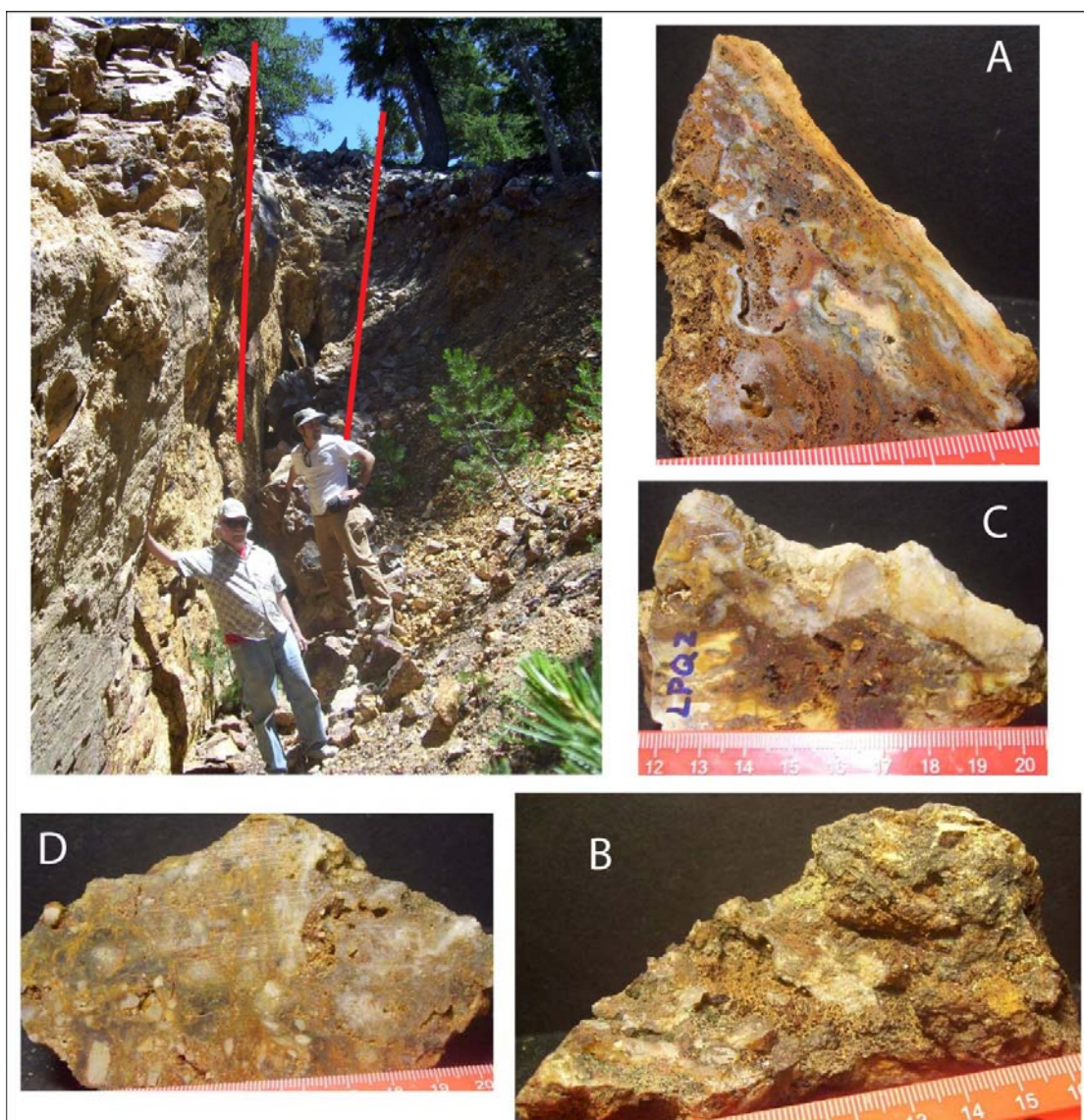


Figure 66. Vein and gouge material in the Lodgepole camp.

Blue Bell (BB) - To the NW of the Lodgepole, along strike, lays the Bluebell adit and dump. A 5 foot wide chip-channel sample along the prospective gouge zone returned 5.3ppmAu. The mineralization here (fig. 67) displays quartz replacement of platy (C) and bladed (A) calcite. These quartz pseudomorphs are followed by a later phase of .5mm clear, terminated quartz crystals (B). Also encountered are large crusts of white crystalline adularia

with the apparent lack of quartz (D). Minor smoky quartz crystals up to 1 cm are also encountered on the Bluebell dump.

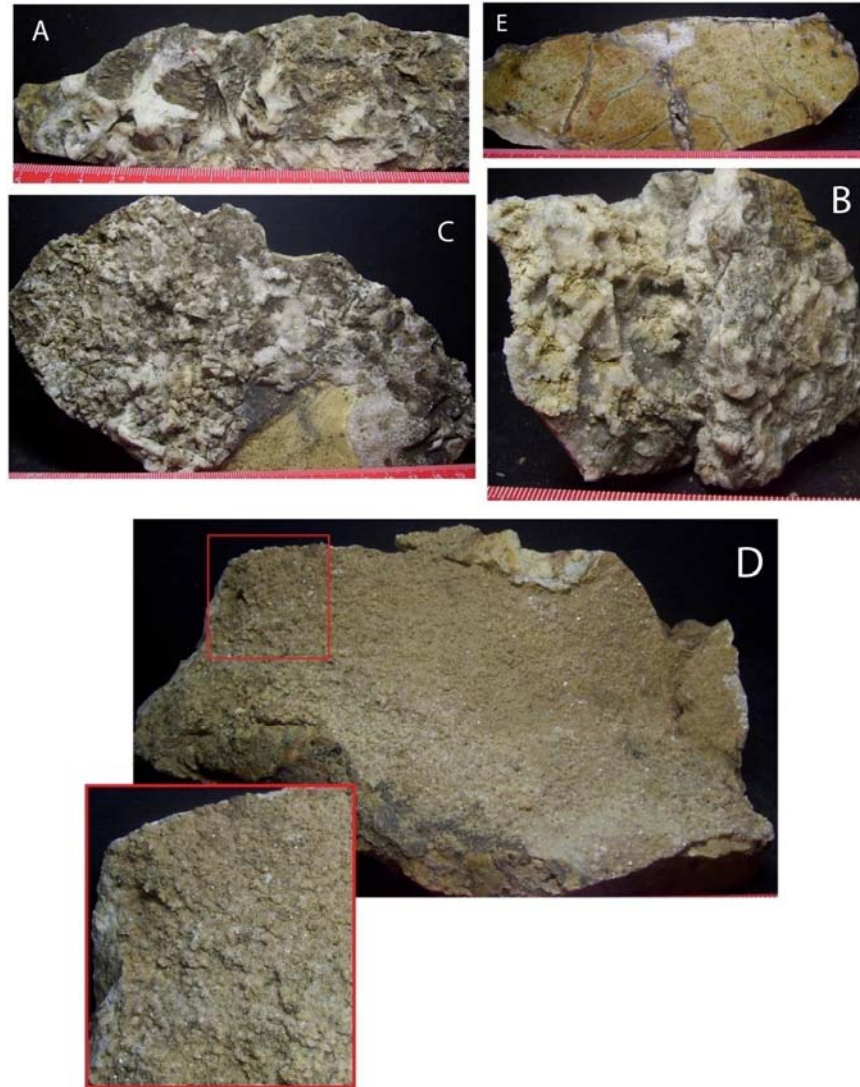


Figure 67. Vein textures encountered on the Blue Bell dump.

Sunshine (SS) - The Sunshine Vein yielded multiple samples with 20+ ppm Au values returned along the surficial trace (Golden Predator, private doc.). Visible flakes of electrum are seen in multiple hand-samples (fig. 68). This high-grade portion (F) of the vein is characterized by iron-oxide stained vuggy texture. The vuggy zones are separated by micro-fingers of milky

quartz (F). Vein textures appear to be highly dependent on their host rock consistency; flow banded rhyolite (C), and multi-lithologic breccia (A), and rhyolite tuff (F). The iron-oxide stained wall-rock contact (A, C, D, F) is likely the result of pyrite oxidation, although in A and F the variable amount of penetration into the host from vein may be due the leaching and replacement of host rocks. Banding is very thin (~1mm) and poorly developed with small vuggy pockets (E) throughout in some samples. (B) Large vuggy zones display blade replacement followed by the inward growth of cloudy, terminated quartz.

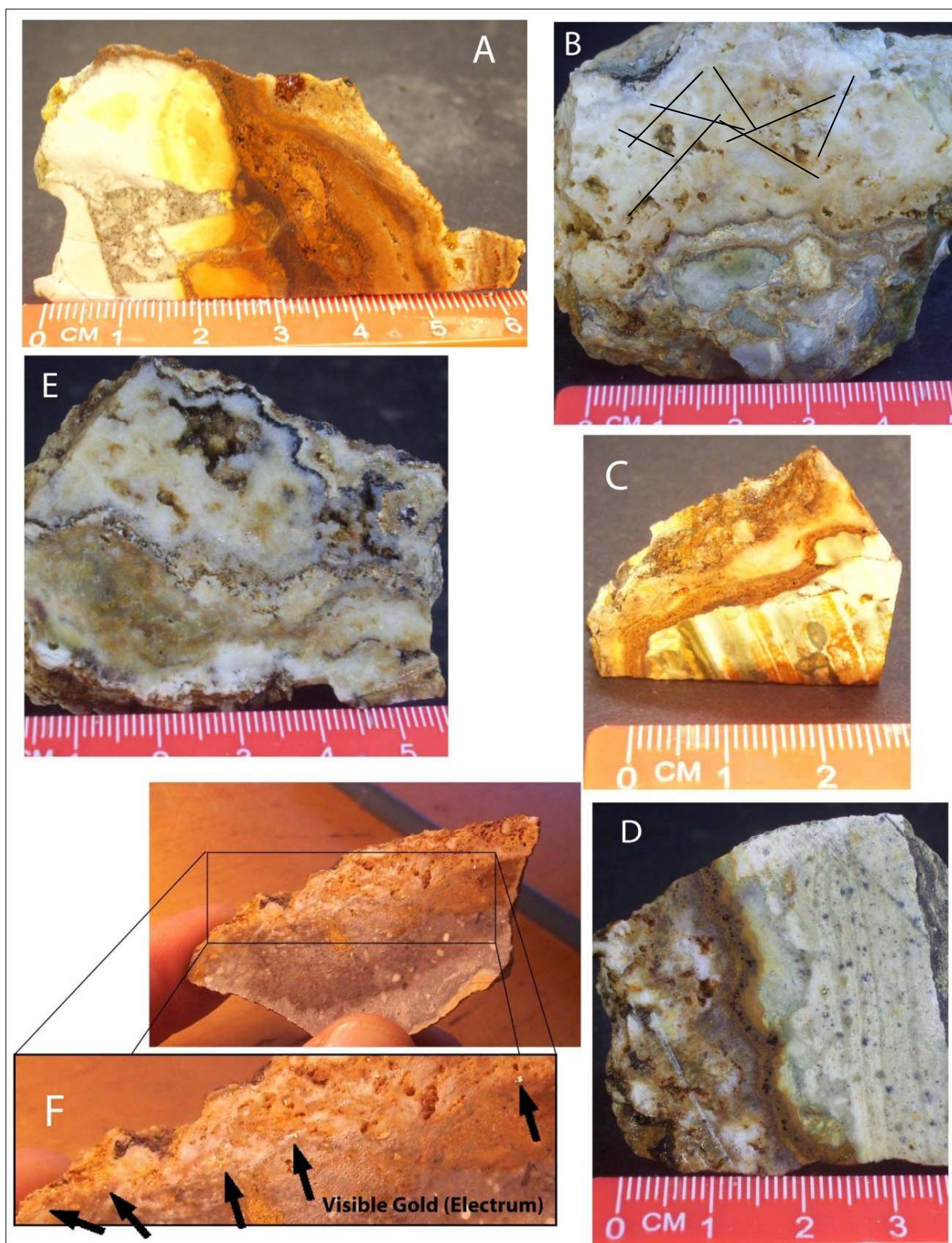


Figure 68. Vein textures encountered on the Sunshine dump.

Modoc Mines (MMS) - The shaft and dump that accompany the NE trending vein in this area are the largest encountered throughout the district. Operations at this location include a 100+ foot shaft and multiple tunnel levels. The quartz vein mineralization here is well developed (fig. 69). Colloform banding shows a variety of colors (A, D, G), and is commonly interspersed with sections of platy calcite replacement (A, E). A bubbly silica-ooze (A, C, D) precipitates to form irregular layers of colloform banding. A phase of coarsely crystalline amethystine quartz follows colloform banding, followed by a later coating of small, terminated quartz crystals (B). Colloform banded vein is fractured, mobilized, and re-cemented by hematite in a fault zone (H); a fault-fracture event post-dates mineralization.

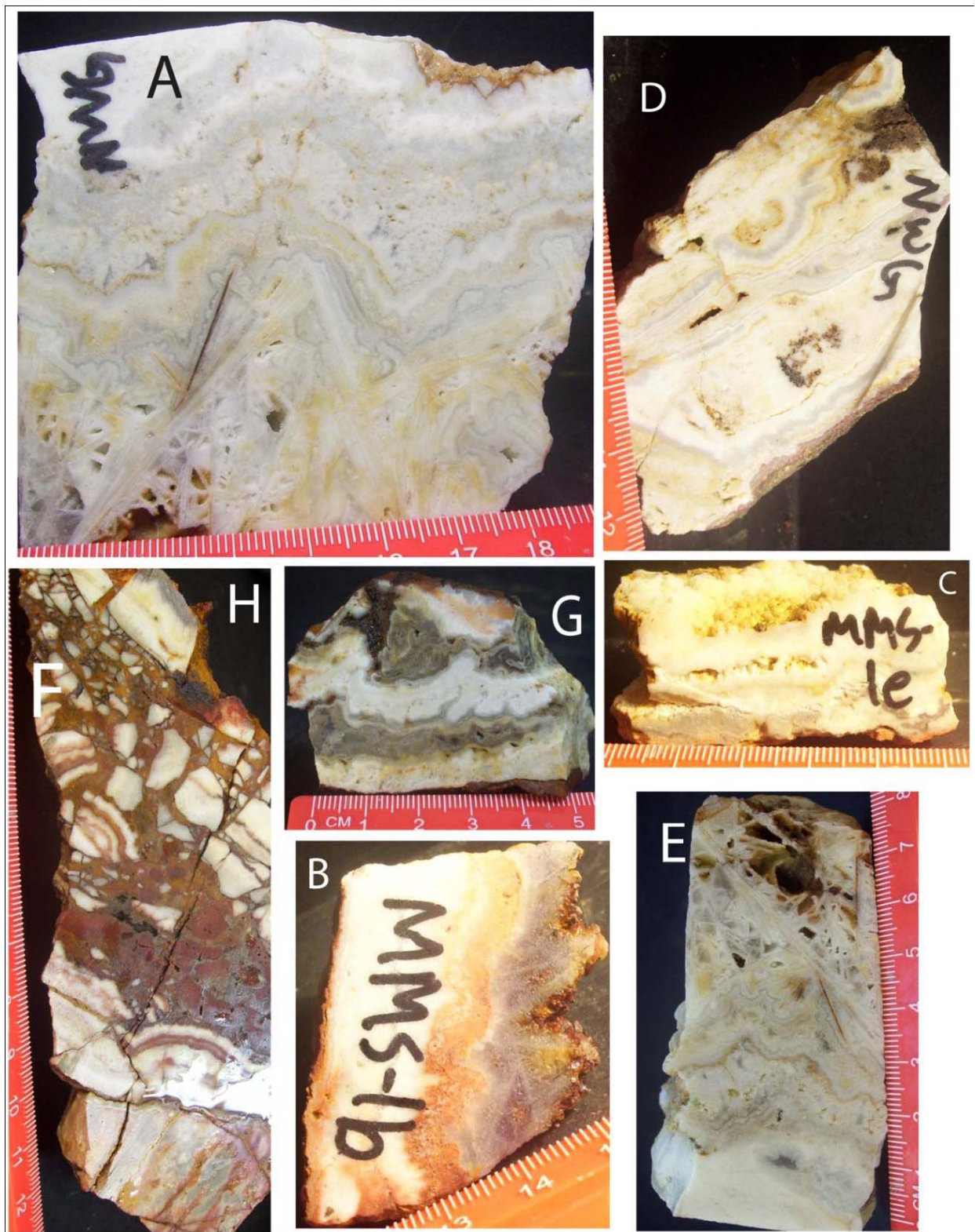


Figure 69. Vein textures encountered on the Modoc Mines dump.

7.2 Optical Microscopy

The optical microscope was employed to further distinguish quartz textures and provide an estimate of the percentage of opaque minerals present. Samples were processed as seen in figures 70 and 71. Quartz is the dominant mineral and occurs in numerous crystalline forms of variable dimensions. No calcite was observed although textural features (blades and plates) indicate the presence of this mineral; quartz and quartz-adularia mineralization have completely replaced calcite in veins throughout the district. Quartz-adularia zones display strongly elevated proportions of opaque minerals to the quartz only zones. An optical reconnaissance was completed on each sample to aid in later microprobe investigations (Chapter 7.3).

LM-3a

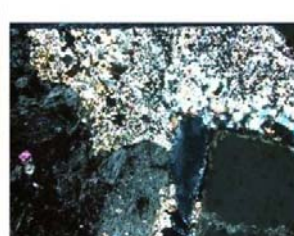
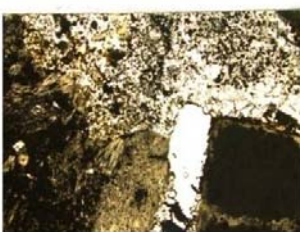
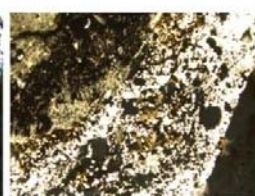
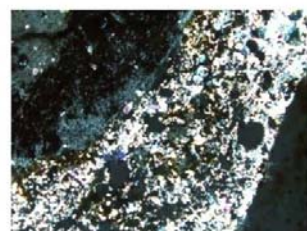
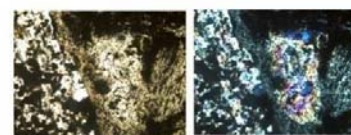
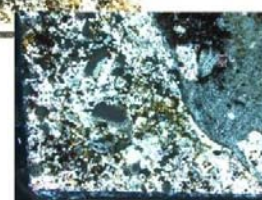
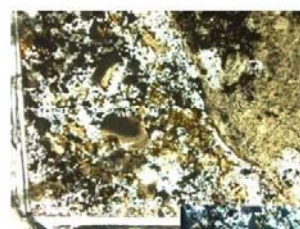
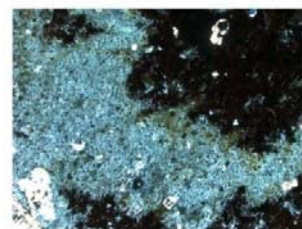
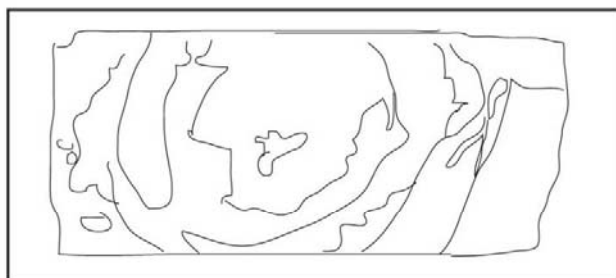


Figure 70. Thin-section, LM-3a, was collected from outcropping structure in the Blue Bell camp.

Moon-3

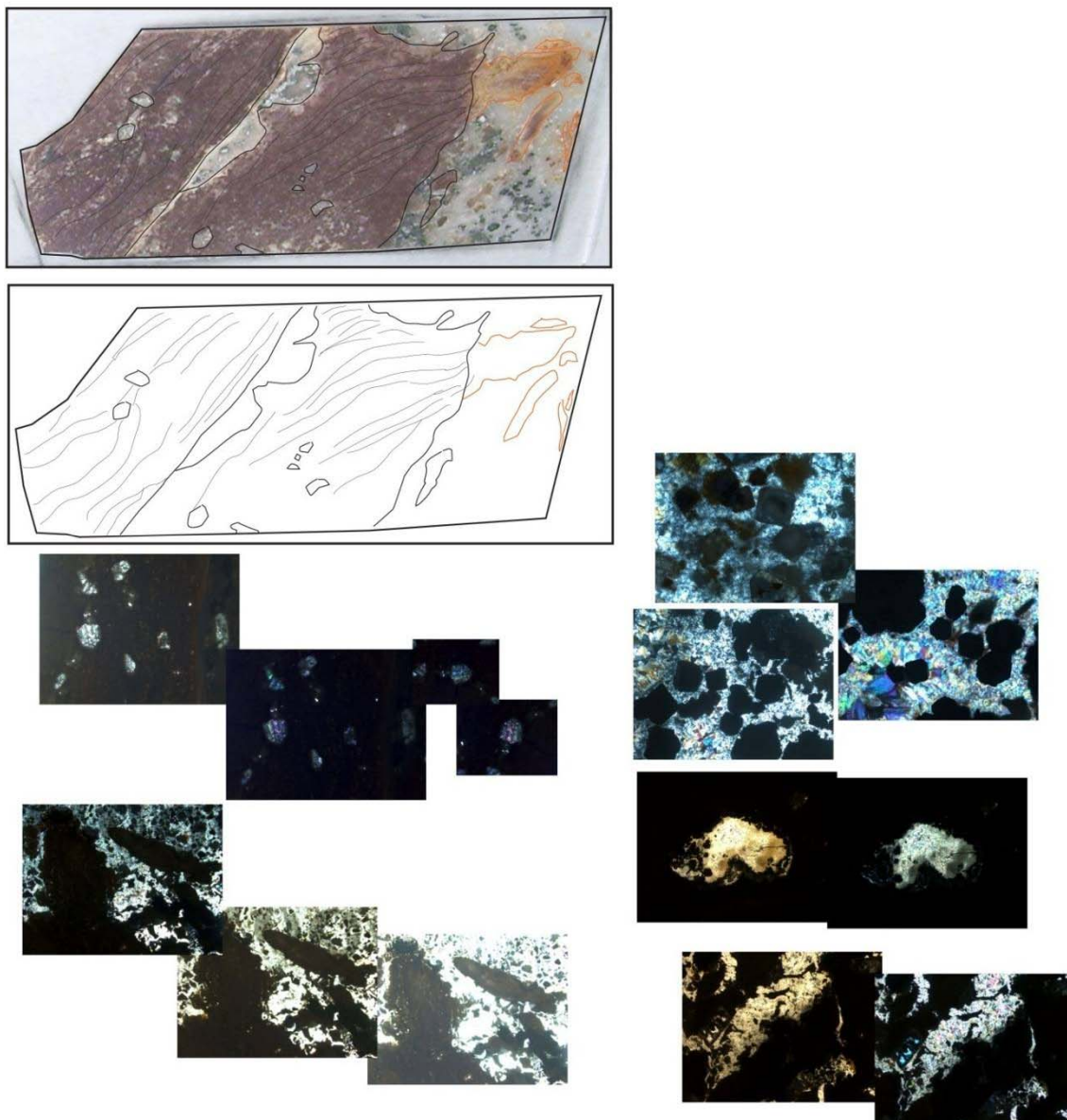


Figure 71. Thin-section from the Moonlight Camp. Flow-banded rhyolite phenocrysts are totally replaced by quartz. Vein quartz displays incorporation of rhyolite and zones of pyrite => hematite enrichment are observed.

7.3 Electron Microprobe

Thin-sections collected over the district were analyzed on the electron microprobe to identify metallic and high density grains. A complete reconnaissance of the section is made in which areas of interest are identified and given textural context within the sample. The areas of interest are returned to for image capture, element mapping, and wavelength dispersive X-ray spectroscopy (WDS). The above steps are performed in a single session on the electron microprobe.

List of abbreviations:

qtz = quartz	adl = adularia	pyr = pyrite
hem = hematite	rut = rutile	mon = monazite
ng = native gold	Ag = native silver	elct = electrum (amalgum)
fract = fracture event	dissol. = dissolution	

7.3.1 Paragenesis

Minerals of interest in this study to be investigated by the microprobe include precious metal bearing varieties and associated metallic minerals. Gangue textures are noted, along with prevalence, size, and species observed. Paragenetic context is given to auriferous and indicative minerals, as shown in figure 72; 46 additional microprobe figures are provided in appendix 1 and account for six camps of the HGD.

Figure 72 provides two locations in section Con_6, from the western consolidated camp. The paragenetic column, provided in the top right (bottom is first event), has been constructed from the following observation. metallic precipitates are encountered near the late part of crystalline adularia growth and are contained within euhedral crystals; crystal growth continues, incorporating the metallic grain within adularia. This observation is deconstructed to explain the process by stating which minerals were actively precipitating: an initial adularia phase is followed by adularia + metallic phase, then pure adularia, this is followed by quartz (A) and/or pyrite (B) filling open space.

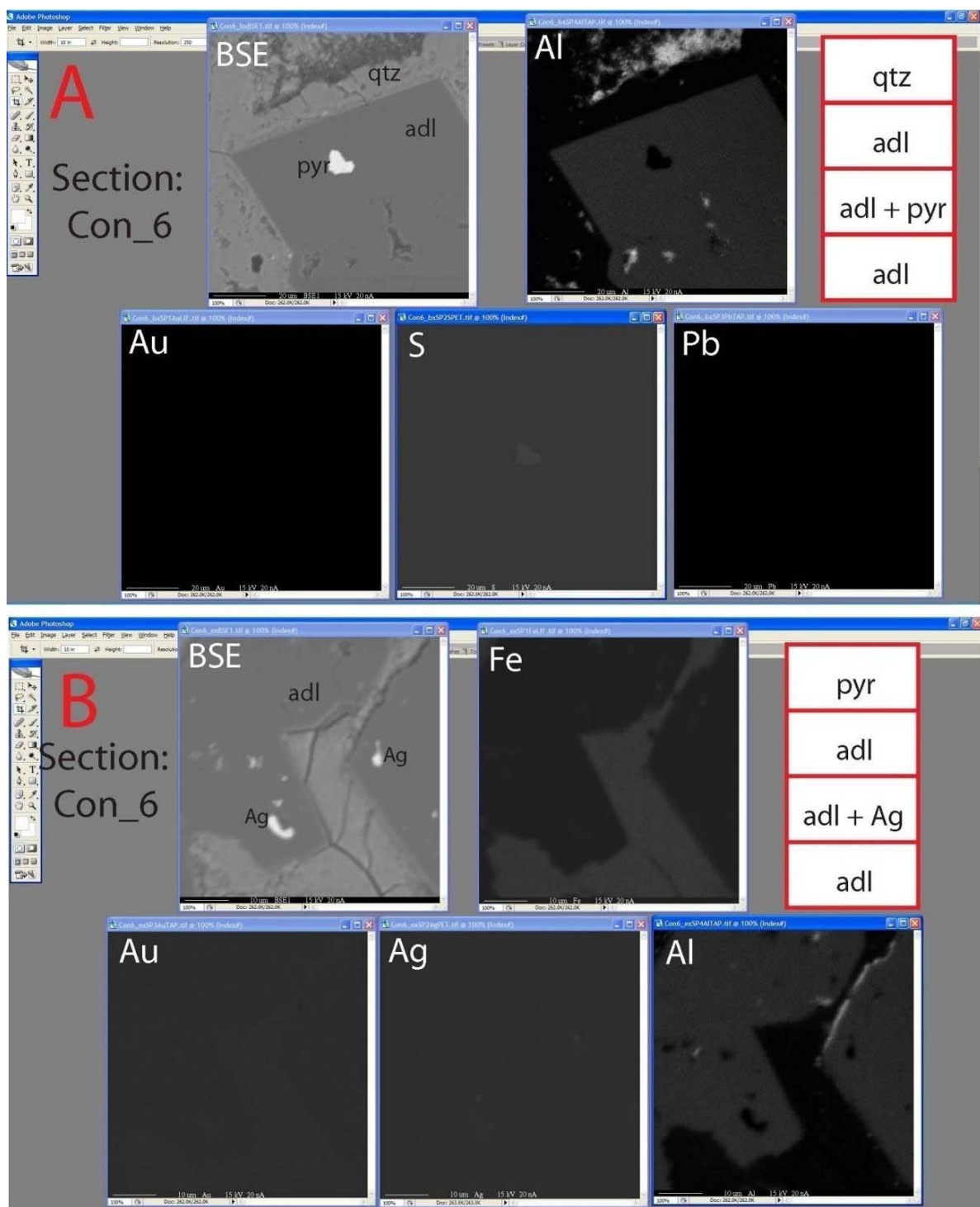
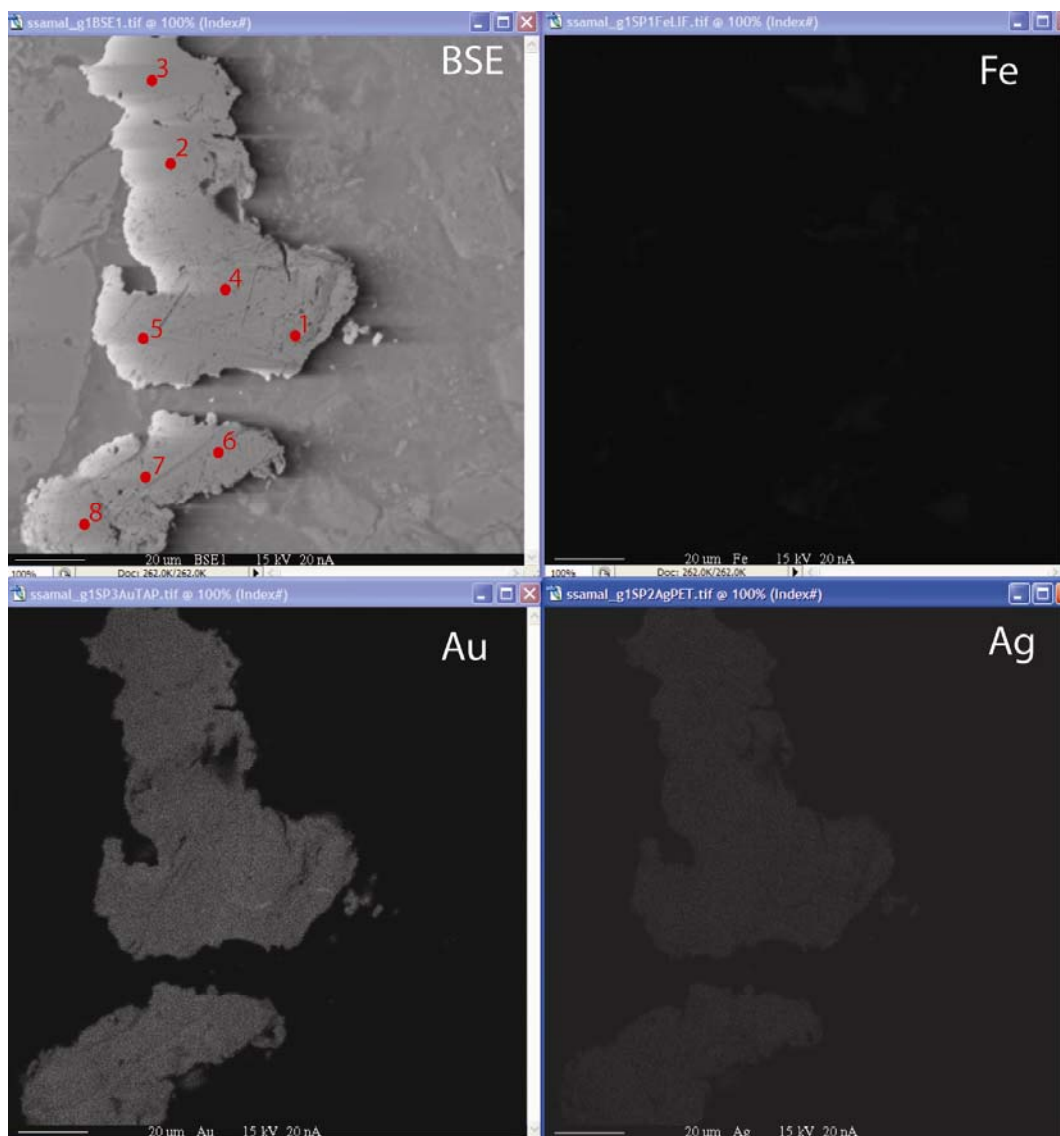


Figure 72. Electron microprobe investigation of mineralization encountered in section Con_6. A BSE image is provided along with 4 labeled element maps. Paragenetic observations are made in the white boxes (bottom is 1st).

7.3.2 Quantitative Analysis

Precious metal grains of 20+μ were encountered in samples from the Sunshine vein and Consolidated camp. These grains were processed quantitatively with Au and Ag standards.

Electrum grains from the Sunshine vein yield consistent values (65% Au, 35% Ag) and do not display any compositional zoning. Figure 73 provides a BSE image to the top left, and labeled element maps. Values returned from indicated points are reflected in the table below, data is summarized to the right. It may be assumed that these electrum grains were all generated from the same precipitation event. Additional grain analyses from the Sunshine Vein are presented in appendix 1 (fig. 1-73 through 1-76). Chalcedony nodules from the Consolidated camp contain considerable Ag (fig. 74) which inversely correlates with Fe and S.



point	Au%	Ag%
1	67	38.5
2	64.5	38.2
3	64.7	37.8
4	63.5	40
5	61.8	41.2
6	61.9	38.5
7	64.6	34.2
8	60.5	36

	Au%	Ag%
average	63.56	38.05
std. dev.	2.08	2.18

Figure 73. This large (60 μ) grain of electrum was analyzed for any compositional zoning. 8 point scans yield results of roughly 66% Au & 33%Ag with a low deviation.

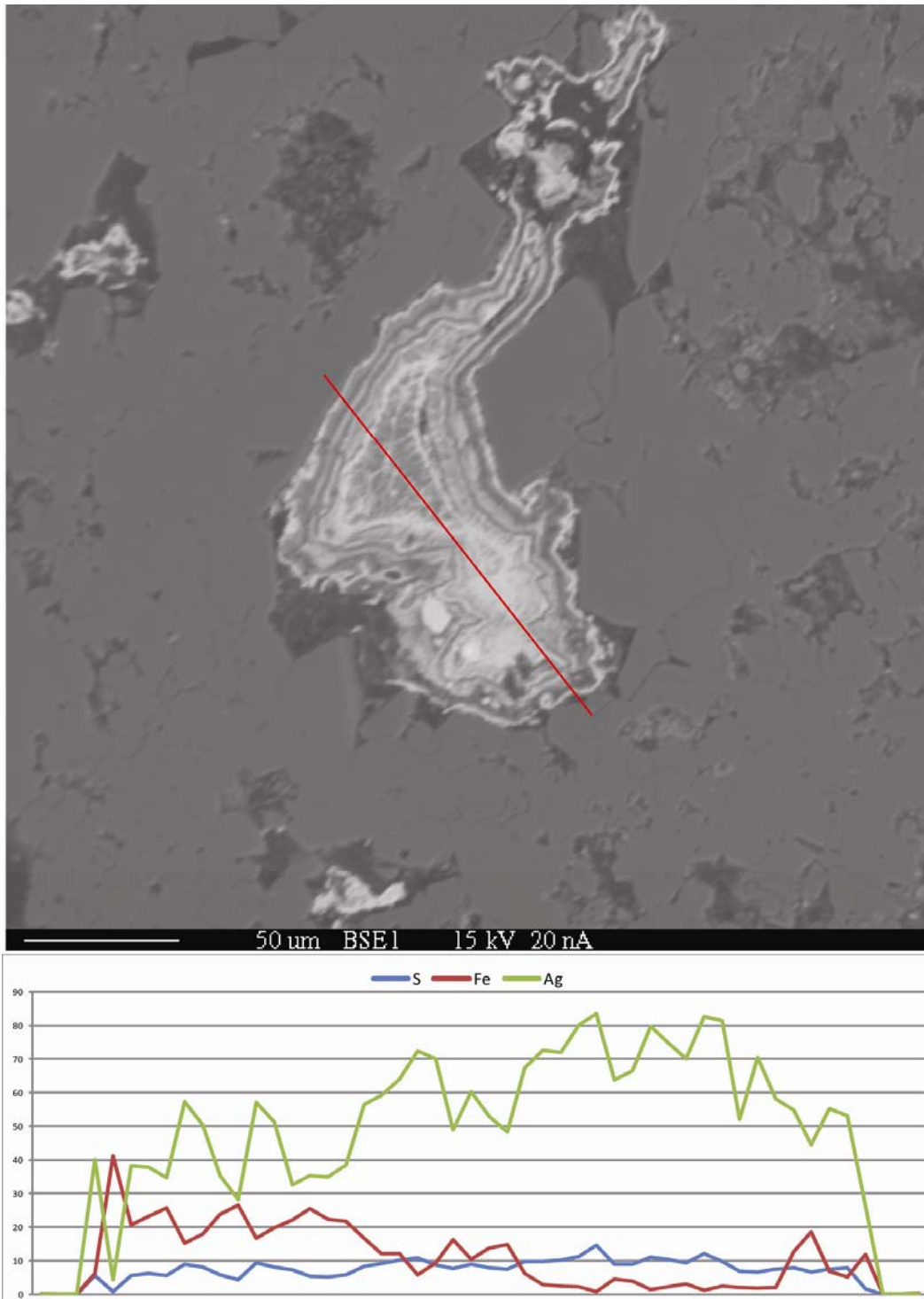


Figure 74. This BSE of an Ag nodule is overlain with a traverse line, which corresponds to the quantitative plot of grain chemistry below.

7.4 Interpretation

By compiling all the paragenetic observations observed under the microprobe it is possible to create a pattern of mineralization, paragenetic summary, for each camp. Figure 75, has compiled all the paragenetic observations made in the interpretation of figure 72 and appendix 1, fig. 1-51 through 1-72.

A common thread to each camp sequence is a fracture/dissolution event/series of events that accompany the precious metal phase of deposition. This should be expected within the precious metal horizon of an epithermal system; as the system rapidly depressurizes from surface, fracturing along pre-existing structures provides pathways for rapidly expanding hot fluids to boil downwards (as ~surficial pressures move downward, calcite is precipitated). The column of hot water is now expanding (boiling) upwards, as it experiences phase change to gas. Quartz rapidly replaces calcite (boiling texture, blades) and this is the point where precious metals will precipitate with adularia. Points of inflection (horizontal and vertical bends) within the vein systems should be considered strong targets for high grade mineralization. The dominant vein minerals of HGD are quartz, adularia, and pyrite; hydrothermal monazite and rutile are common accessory minerals. Trace chalcopyrite, sphalerite, Ag-sulfosalts, rhodochrosite, and arsenopyrite have been identified by electron microprobe. Precious metals occur almost exclusively as native gold or electrum (variable amalgam of Au & Ag).

Native gold is the dominant ore in the Modoc Mines vein material (appendix 1, fig. 1-67 through 1-69), grains are $<10\mu$. Chalcedony nodules from the Consolidated Camp (fig. 74) display periodic Ag-sulfide mineralization (also a 7μ native gold grain [appendix 1, fig. 1-53] is included within the nodule), but are not fully understood at this point. Hydrothermal monazite of the West Consolidated is enriched in Au (appendix 1, fig. 1-54, 1-56), and Au occurs with

monazite in the Blue Bell and Sunshine (appendix 1-54, 1-66, 1-72). Pyrite in the Sunshine Vein shows enrichment in Au and contains anomalous Ag-grains (appendix 1, fig.1-58, 1-60, 1-72). Electrum is encountered abundantly in select Sunshine vein material, grains reach maximum size of 100 μ and are ~66% Au (appendix 1; fig. 1-71, 1-73 through 1-76).

MMS		SS	
hem		hem	
fracture event		fracture along dissol.	
qtz		adl + pyr \pm Ag	
qtz + hem + ng		major dissol.	
qtz + pyr \pm ng		qtz + adl \pm mon/elct	
qtz + adl + pyr \pm ng		qtz	
minor dissol.			
qtz \pm adl + pyr			
qtz			

BB	Klon-LP	West Con
hem	qtz \pm pyr	qtz + pyr
fracture event	dissol.	qtz + adl
mon \pm ng	pyr \pm rut	qtz + adl + pyr \pm Ag
adl + pyr	qtz + pyr	adl + rut + mon
minor dissol.	qtz	fract + dissol
qtz + adl \pm pyr		qtz + adl \pm elct
qtz		

Figure 75. Paragenetic observations from electron microprobe investigations are summarized by camp.

8. HOMOGENIZATION AND FREEZING TEMPERATURES

Each cubic centimeter of white quartz may contain a billion fluid inclusions, each a self-contained recording geothermometer, preserving the moment of sealing for each inclusion (Sampson, 2003; Sander and Black, 1988; Roedder, 1984). Samples are processed into 120 and 240 micron thick-sections which are polished on both sides using a soluble epoxy (contracted to Texas Petrographic). In UTEP laboratories, the epoxy is dissolved and samples are inserted into the USGS heating stage (Fig. 76), which is housed in a high temperature plaster-board. Forty five samples were processed in UTEP facilities, accepted methods of analyses were carried out (Sampson, 2003; Roedder, 1984). Analyses produce temperature and salinity data, along with noting observable boiling conditions, growth planes, and inclusion families. Fluid inclusion studies can help establish relative levels within mineral deposits and illuminate the transport of fluids (Sampson, 2003; Brathwaithe and Faure, 2002; Simpson, 2001; Matsuhisa and Aoki, 1993; Goldfarb et al., 1988; Seward, 1988). Forty Samples collected from dumps, and outcropping hydrothermal quartz have been analyzed for fluid inclusion data (fig. 78; appendix 1, fig. 1-80 through 83). Seven samples of quartz veining from RC-drilling were also processed (fig. 80).

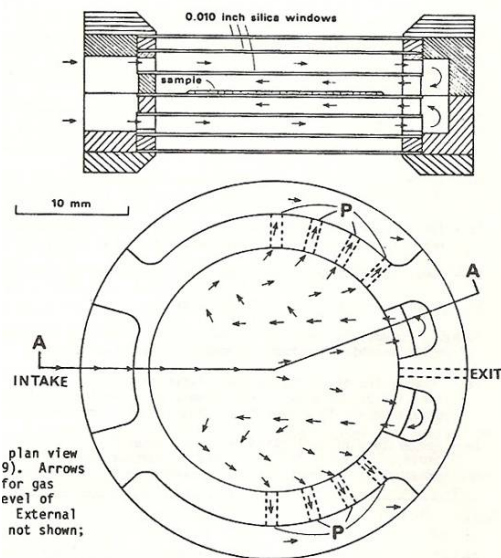


Figure 76. Cross-section(top) and plane view of a USGS heating stage, arrows indicate gas flow paths. External N-12 Pyrotherm Dense Board is not shown, but houses the sample receptacle, above. This equipment is used at UTEP to microscopically monitor fluid inclusions at temperatures ranging from -80° to 600°C.

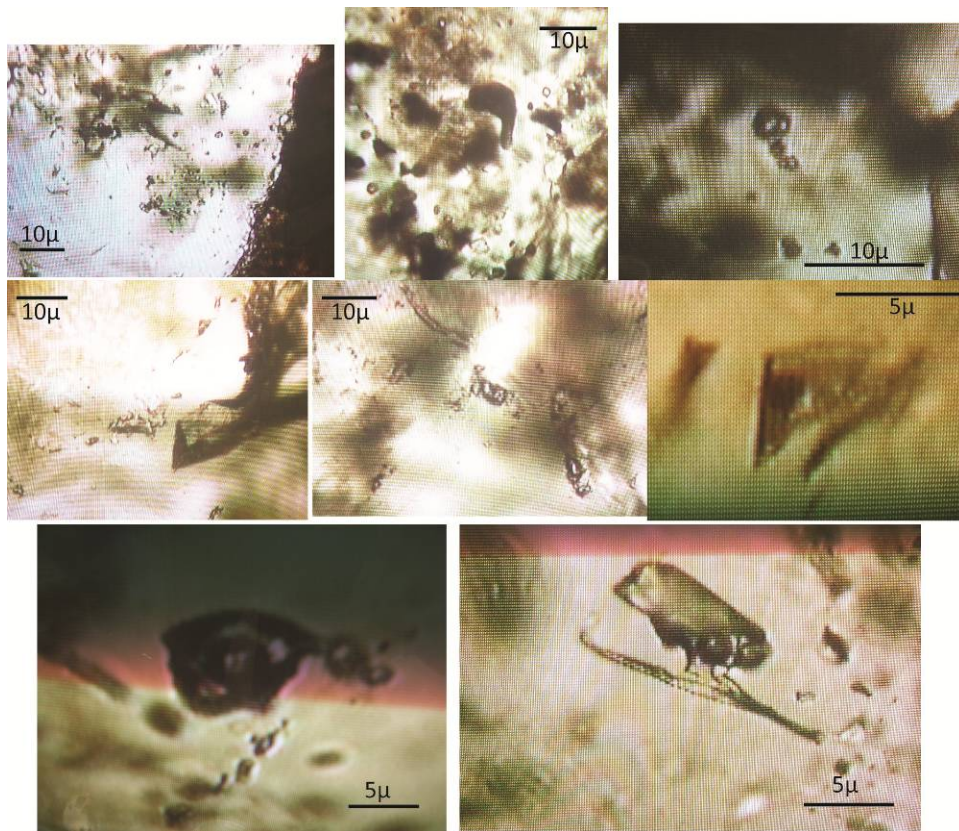


Figure 77. Some fluid inclusions observed and recorded in this study. Inclusions were dominantly two-phase, liquid-rich.

8.1 Fluid Inclusion Studies

Initial reconnaissance of each section generates a map which includes mineralogy and fluid inclusion location (fig. 79; appendix, fig. 1-84 through 1-87). Heating is performed at a steady rate of 4°C/min, cooling occurs much more rapidly at 1°C/10sec. The temperature at which the gas and liquid components of each inclusion recombine is known as the point of homogenization and records the condition of formation. Inclusions are watched under the microscope during heating to observe this visual change, temperatures are recorded.

Dissolved NaCl^2 in solution has an effect on the physical properties of water and depresses the freezing point. The amount of depression to the freezing point can be correlated with a salinity percentage, based on a standardized curve (Sampson, 2003; Roedder, 1984). The temperature at which the liquid component within an inclusion freezes and spontaneously expands is known as the freezing point. The phase change observed during freezing/melting is much more subtle, than that of homogenization, resulting in poor results from samples containing inclusions smaller than 3 μ (fig. 77).

A target, of seven inclusions to be measured in each section, was set to constrain data collection. Freezing was performed at a separate time than heating. Optical magnification used during analyses is 320x (fluid inclusions below 3 μ are difficult to observe under the available magnification). Many of the samples processed included colloform banded vein material, this material hosts inclusions with dimensions of <1 μ , making data collection impossible.

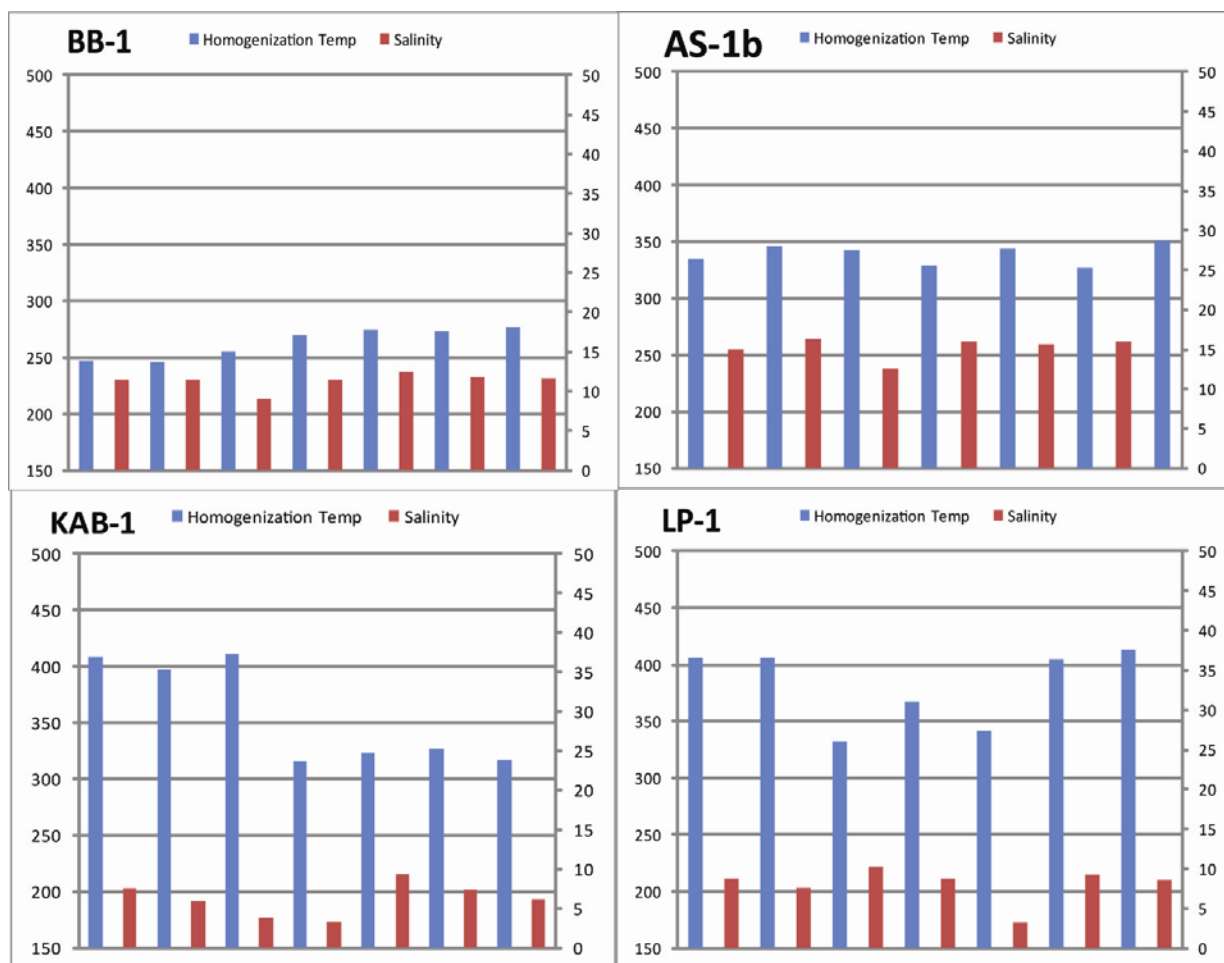


Figure 78. Each bar graph represents the fluid inclusion data obtained from the indicated sample. This group of samples is from the central part of the HGD. All temperature data is presented, this format, in appendix . The left axis charts homogenization temperature from 150 to 500 °C, the right axis charts salinity from 0 to 50%; blue bars are homogenization, red bars are salinity.

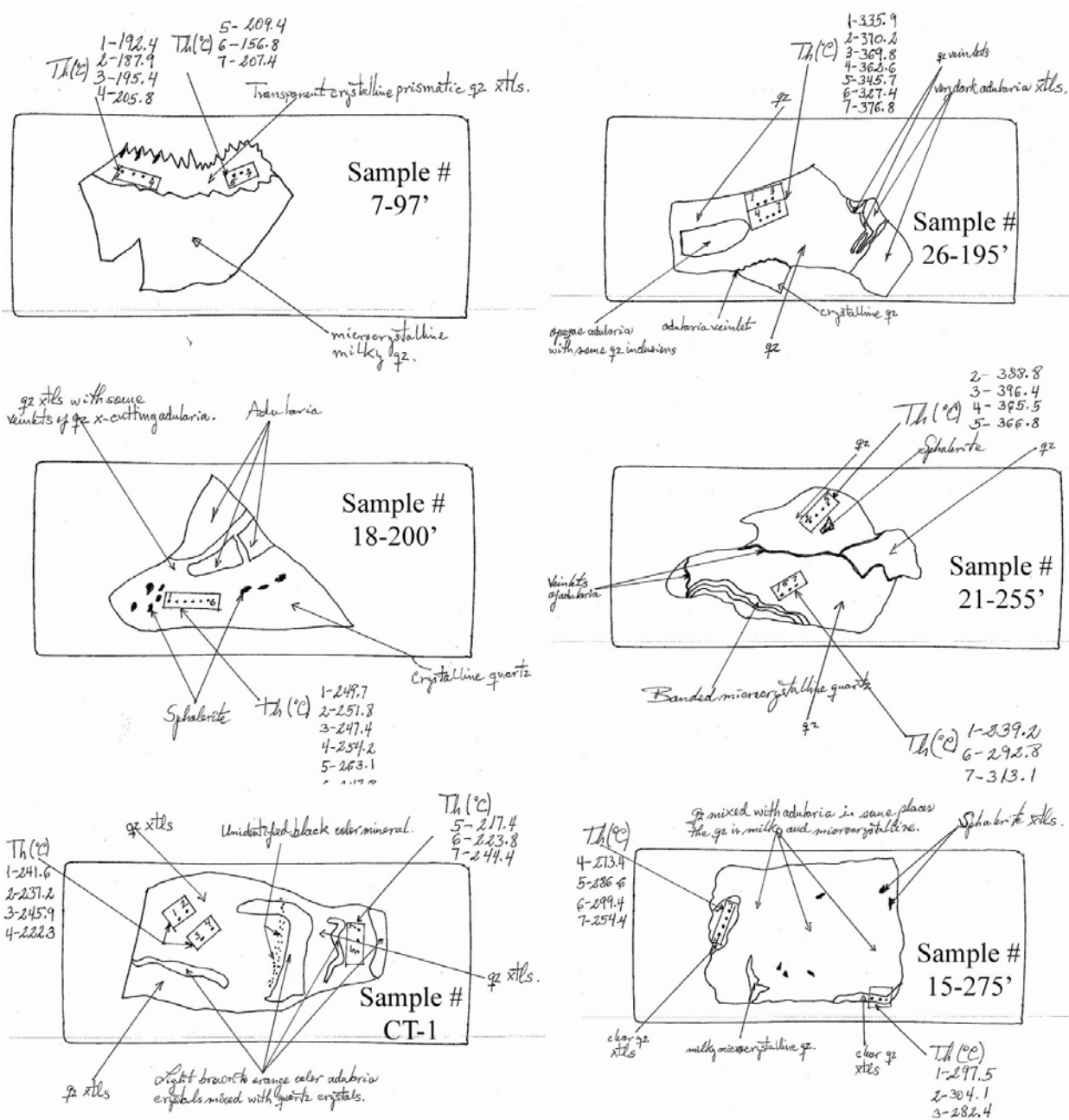


Figure 79. Reconnaissance of thick-sections was performed in the above manner for each sample. Inclusion families, growth planes, and mineralogy are noted. Temperatures measured are indicated and correlate to charted temperature data.



Figure 80. Samples were recovered, on site, during the RC drilling of the study area in summer of 2009, and processed into fluid inclusion sections. Each bar graph represents the fluid inclusion data obtained from the indicated RC interval. The left axis charts homogenization temperature from 150 to 500 °C. The right axis charts salinity from 0 to 50%. The blue bars are homogenization, red bars are salinity.

8.2 Discussion

The Consolidated Camp (appendix 1, fig. 1-80) has a temperature range from 190° to 325°C, salinity values are 5 to 15%. CT-1 was taken from a trench atop Discovery Mountain, the five other samples are from the West Consolidated dumps. Con-5 records anomalously high temperatures (from 350° to 400°C) and significantly elevated salinity values (13 to 21%). Quartz veining from a rhyolite dike in North Star Basin (NSRD-1; appendix 1, fig. 1-83) records temperatures from 170° to 220°C, with salinity values from 3 to 11%.

Located mineralization (LM) samples are collected from bedrock, availability of these samples is limited to the accessible workings. Sunshine (LM-1), Blue Bell (LM-3), Lodgepole (LM-4) and Klondyke (LM-10, 12, 13) are represented in this group. Temperatures recorded in these samples (appendix 1, fig. 1-81) can be divided into high and low groups. The low temperature group has homogenization temperatures between 180° and 270°C; high temperature group ranges from 350 ° to 500°+C. Salinity values range from 4 to 12%, and 10 to 20% in the low-temp and high-temp groups, respectively. This anomalous high temperature group exceeds the limitations for classification of an epithermal system. Most samples collected from dumps in this part of the district (appendix 1, fig. 1-81) show similar temperature characteristics (fig. 81). Klondyke (KAB-1) and Lodgepole (LP-1) record temperatures ranging from 300° to 400°C, Alturas Hill is slightly cooler with an average of 342°C. Blue Bell (BB-1) sample yields temperature average of 255°C and 10% salinity, which closely correlates with LM-3.

Samples from the dump of the Modoc Mines Shaft (MMS) are generally colloform banded vein and inclusion dimensions rarely exceed 4 μ . Homogenization temperatures of MMS samples (appendix 1, fig. 1-82) vary from 240° to 340°C; the three samples display internal

consistency with average temperatures of 240°C, 300°C, and 330°C. Salinity values range from 2 to 8%.

Samples from the Moonlight Camp (Moon-3, 4; append. 1, fig. 1-82) record an inclusion group at ~250°C and 400°C. Salinity values for the 250°C group are consistent with an average of 12%. This high-temperature group is limited to secondary inclusions (~1μ) along growth planes.

Three samples from the Sunshine (SS) dump (append. 1, fig. 1-83) have been processed and each displays internal consistency. SS-2a and SS-2b have a temperature range from 230° to 260°C; Salinity values range from 8 to 17%, high salinities correlate with high temperatures. Sample SS-1 and LM-1 (append.1, fig. 1-81) both record anomalous (~350°C) temperatures and lower salinity values (4 to 10%) than the lower temperature inclusion family.

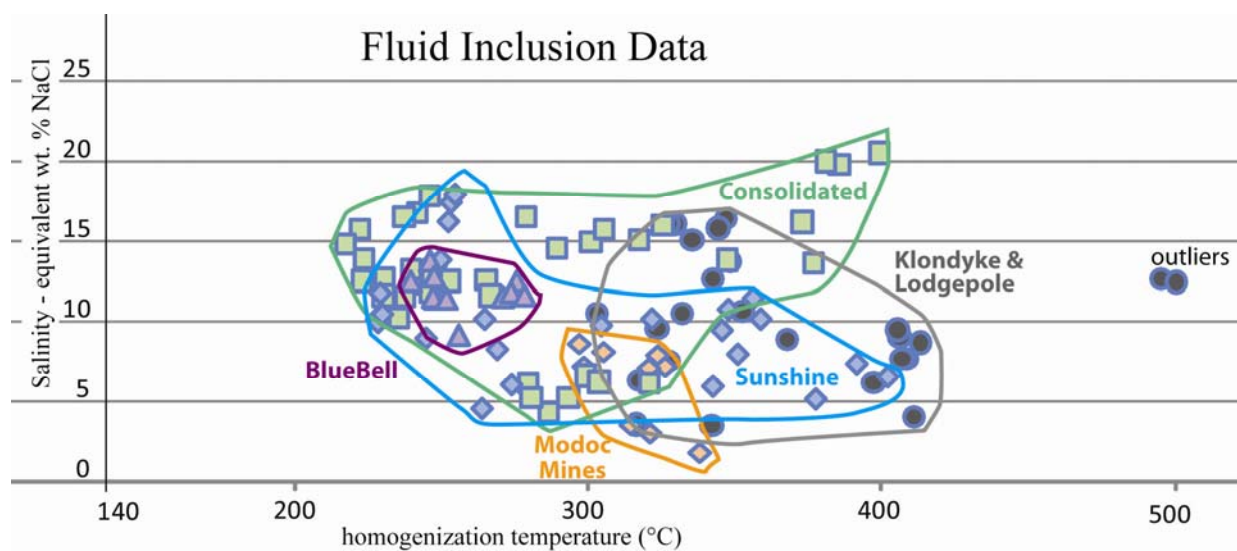


Figure 81. All fluid inclusion data, represented by points. Camp groups have been divided by color-coded polygons.

The seven samples from RC-drilling (fig. 79, 80) are from the Sunshine camp (7_97', 11_47', 14_242', 15_275'), Modoc Mines (18_200', 21_255'), and Moonlight camp (26_195'). Each sample name is derived from drill-hole number and depth. Samples 7_97' and 11_47' are

from intercepts of veining in multi-lithic breccias (Tmlb) directly uphill of the Sunshine portal. Sample 7_97' has an average temperature of 200°C, while sample 11_47' records an average of 285°C; this increase of 85°C is encountered across the Sunshine adit fault (NW-trend), from the foot wall to hanging wall (to SW). Salinity values in both samples are 15+%. Samples 14_242' and 15_275' are from intercepts of Yellowjacket/subsidiary vein intercepts. These samples record homogenization temperatures from 260° to 340°C, and salinity value average of 17%. Sample 18_200' and 21_255' are collected from vein intercepts on the N and S side, respectively, of the E-W vein of Modoc Mines. 18_200' records homogenization at a steady 250°C, with salinity values of 17%. 21_255' display high internal variability, ranging from 290° to 390°C, salinity value is 14%. The vein intercept in the Moonlight camp (26_195') yielded homogenization temperature from 330° to 370°C, and salinity values of 13%.

8.3 Interpretation

The homogenization temperatures in the study area are on the high-end (Simpson, 2001; Heald, 1987; Buchanan, 1981), but generally within range of epithermal systems (fig. 82; table 11). Epithermal temperatures measured range from 170° to 400°C (fig. 81). There are several samples (LM-1, LM-4, LM-10, Moon-4) that yield anomalously high (~500°C) temperatures. These samples are all in close geographic proximity to the Cross-Roads Rhyolite (Tcr; dated at $12.1 \pm 0.6\text{my}$ [fig. 83]). It is hypothesized that this young unmineralized rhyolite is a possible source for the extremely high temperatures recorded in secondary inclusions from nearby epithermal quartz.

There is a temperature gradient across mineralization-controlling faults, evidenced by RC-sample data from Sunshine and Modoc Mines. Variation of ~100°C is observed across the structure controlling mineralization.

Data trends from fluid inclusion analyses are provided in figure 82. Four of the five groups have a negative linear trend, three of which display very similar slope. The Consolidated group has a positive linear trend, and carries a high relative salinity.

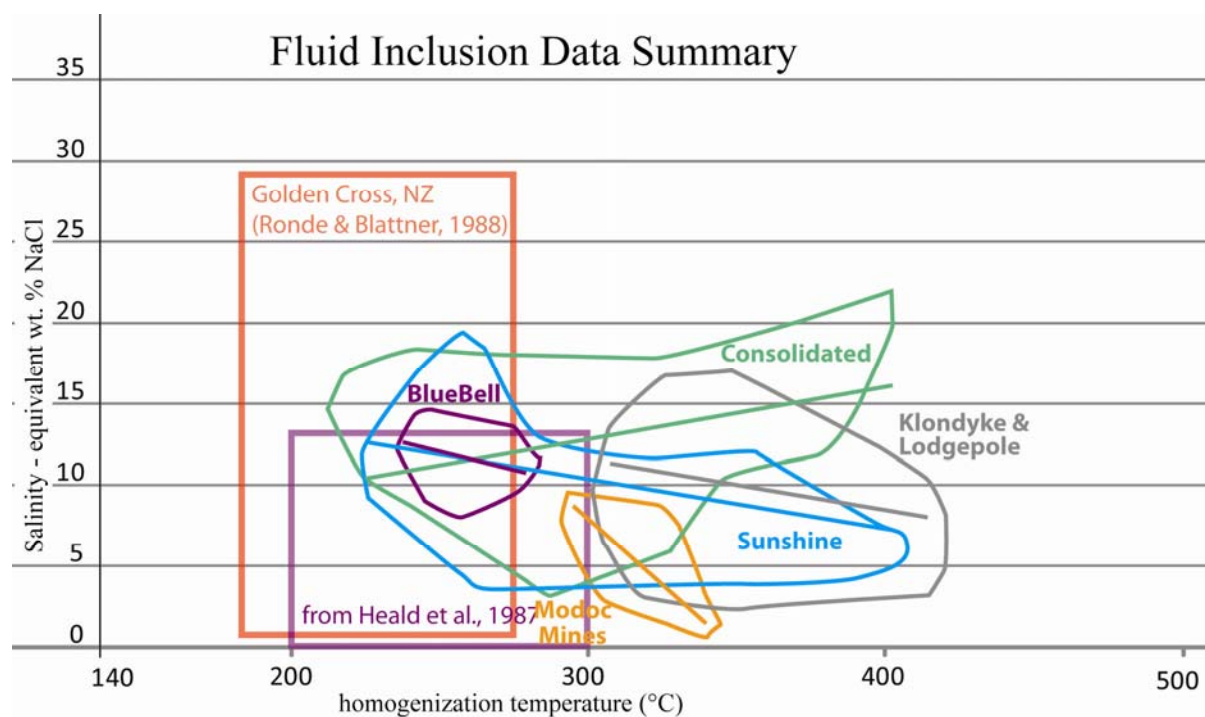


Figure 82. Temperature data from the HGD is displayed in polygons with trend lines. Studies by others and general characteristics of epithermal systems are shown by the purple and red rectangles, respectively.

9. ABSOLUTE AGES

9.1 $\text{Ar}^{40}/\text{K}^{40}$ – Whole Rock Ages

Potassium-argon age determinations were obtained from whole rock analyses performed on three distinctive rock units of the silicic sequence. Analyses were performed by Krueger Enterprises, Inc. in Cambridge, Massachusetts. The following sample descriptions have been provided by Keats (1985).

The youngest age is 12.1 ± 0.6 Ma for a sanidine concentrate from sample KAR-1 of the porphyritic rhyolite dome, also known as the Tcrd (Cross-Roads rhyolite dome). Partial major oxide analyses of this sample, as whole rock, are listed in Table 2 (no. 883) in the following section. The sample is chemically anomalous as defined by the high SiO_2 (81.50%), low Al_2O_3 (8.80%), and low K_2O (3.40%). Although petrographic analysis shows that the phenocrysts of quartz and sanidine are slightly embayed and have reacted with the groundmass, the feldspar is unaltered except along crystal margins and has not been replaced by clay minerals. The groundmass, however, has been texturally and mineralogically altered to a cryptocrystalline, granular mosaic consisting primarily of quartz. Thus, the alteration which produced the anomalous oxide concentrations appears to be confined to the groundmass. Consequently this age, as determined from phenocryst concentrates, is considered valid in spite of the alteration indicated by oxide analyses of the whole rock sample. (Keats, 1985)

An intermediate age of 13.6 ± 0.6 Ma was obtained for a sanidine concentrate from sample KAR-2 of the extrusive Yellow Mountain porphyritic rhyolite, referred to in this work as the Yellow Mountain latite (Tym). The corresponding whole rock oxide analysis is listed in the

table below. Neither chemical nor petrographic analyses indicate alteration in this sample, and the age determination is considered valid. (Keats, 1985)

The oldest age is 14.4 ± 0.6 Ma, for the aphanitic rhyolite domes, and was obtained by a whole rock analysis. However, hydrothermal or dueteric alteration is indicated in the partial major oxide analysis of the whole rock sample by the high K_2O (7.3%) and low Na_2O (1.9%) concentrations. Although petrographic analysis reveals the presence of wispy, secondary quartz (vapor phase?) and an increase in iron oxide relative to other samples of this unit, the microlites of potassium feldspar have not been obviously altered and clay minerals are not present. The high K_2O content may reflect a hydrothermal addition of potassium, in which case the reported age may be too young. Alternatively, the K_2O content may be unchanged and reflect the removal of other constituents (as Na_2O) rather than an addition of potassium. In this case the age may be valid, provided radiogenic argon was not released during alteration. In the absence of evidence to the contrary, the reported date must be considered a minimum age of the aphanitic rhyolite domes. (Keats, 1985)

Rock Type	K-Ar Sample #	Oxide Analysis ¹ #	Material ² Analyzed	Age m.y.	Error ± m.y.	Ar ⁴⁰ * ppm	K ⁴⁰ ppm	Ar ⁴⁰ */K ⁴⁰
porphyritic rhyolite dome	1	883	sanidine concentrate	12.1	0.6	.003154	4.436	.000711
Yellow Mtn. porphyritic rhyolite	2	887	sanidine concentrate	13.6	0.6	.005182	6.506	.000797
aphanitic rhyolite domes	3	888	whole rock	14.4	0.6	.007080	8.380	.000845

Constants used: $\lambda_B = 4.72 \times 10^{-10}$ /year

$\lambda_e = 0.585 \times 10^{-10}$ /year

$K^{40}/K = 1.22 \times 10^{-4}$ g./g.

¹oxide analyses listed in Table 2; sample locations plotted on Plate 3.

²treated with dilute HF and HNO₃ to remove alterations.
All analyses done by Krueger Enterprises, Inc., Cambridge, MA.

Figure 83. K-Ar ages returned for rocks from the silicic sequence (Keats, 1985).

9.2 $\text{Ar}^{40}/\text{Ar}^{39}$ - Adularia Ages

This study has obtained three adularia ages from samples obtained from West Consolidated, Blue Bell, and Modoc Mines (table 9, figure 84). Purified mineral separates were prepared at UTEP facilities from vein samples containing abundant adularia. Samples were given a coarse crush, then handpicked for finer crushing. Finely crushed samples were sorted to remove both a coarse and dust component. The remaining grains were then subjected to heavy liquid separation, during which the heavier quartz (2.65) sank to the bottom, leaving the lighter adularia (2.57) floating. After repeated flushing with de-ionized water the concentrates were deemed clean and allowed to dry. The adularia concentrate was hand-picked for pure, clean grains under a 30X reflected light microscope by the author. Separates were then sent to be analyzed with the $\text{Ar}^{40}/\text{Ar}^{39}$ method at the New Mexico Geochronology Research Laboratory at New Mexico Tech.

Table 9. Results from $\text{Ar}^{40}/\text{Ar}^{39}$ dating of vein adularia. (Peters, 2009)

Sample	Phase	Age $\pm 2\sigma$ (Ma)	Comments
Con	Adularia	14.37 \pm 0.03	Well-behaved
BB	Adularia	14.44 \pm 0.05	Fairly well-behaved
MM	Adularia	14.40 \pm 0.16	somewhat disturbed

The adularia concentrates prepared by the author were processed in the following manner, provided by Lisa Peters. The mineral separates and monitors (Fish Canyon tuff sanidine, 28.02, Renne et al., 1998) were loaded into aluminum discs and irradiated for 5 hours in C.T. position at the USGS TRIGA reactor in Denver, Colorado. Quartz contained in the MM mineral separate darkened during irradiation; this enabled purification of the sample by hand-

picking before analysis. This resulted in a smaller aliquot for the MM analysis than for samples BB or Con. (Peters, 2009)

The monitors were analyzed by the single crystal laser fusion method. The adularia were analyzed with the furnace incremental heating age spectrum method. The adularia samples yielded fairly well-behaved age spectra (fig. 84). Primarily because of the purer mineral separate and greater sample weight, BB and Con yielded flatter and more precise age spectra. It is noted that the K_2O values for BB and Con are 13.17 and 13.46, respectively, while the K_2O for MM is 8.42. The first few percent of the Con and BB age spectra reveal lower radiogenic yields, less precise ages and slightly lower apparent ages. The remainder of the Con age spectrum was used to calculate a weighted mean age of 14.37 ± 0.03 Ma from 88.1% of the ^{39}Ar released. The nearly concordant mid-portion of the BB age spectrum, that contains 60.7% of the ^{39}Ar released, was used to calculate a weighted mean age of 14.44 ± 0.05 Ma. Radiogenic yields increase rapidly over the initial 10-20% of the spectra from 0.1% for BB and 2.5% for Con to over 90% and then gradually decrease to 75.7% for BB and 69.6% for Con over the remainder of the age spectra. The K/Ca values for BB vary between 46.3 to 3970, and overall increase across the spectrum. K/Ca for Con varies between 28.7 to 5960, with an overall decrease from the early steps to the late ones. BB and Con were evaluated with the inverse isochron technique (fig. 84) and found to yield atmospheric intercepts with isochron ages that agree within error to the weighted mean ages calculated from the age spectra (14.46 ± 0.04 Ma and 14.35 ± 0.04 Ma, respectively). A weighted mean age of 14.40 ± 0.16 Ma was calculated from the most concordant mid-portion of the MM age spectrum (contains 68.8% of the ^{39}Ar released). The spectrum is more discordant than either the BB or Con and thus the error of the weighted mean age is an order of magnitude

larger. Both the K/Ca values and radiogenic yields are highest and most consistent over this portion of the age spectrum (between 80.5% and 95.7% radiogenic with K/Ca values of between 306.3 and 161.9). The radiogenic yields decrease to 54.9% and less over the remaining 12.8% of the spectrum and K/Ca values drop to 55.0 and below. As with the other two samples, the inverse isochron analysis reveals an atmospheric intercept (291.3 ± 6.3) and an isochron age of 14.41 ± 0.15 Ma that agrees within error compared to the weighted mean. (Peters, 2009)

The goal of this method was to evaluate the longevity of epithermal mineralization within the HGD, by determining if the adularia formed in the one mineralizing period or if they represent multiple periods. The age spectra for samples BB and Con provide precise and reliable ages for mineralization of 14.44 ± 0.05 and 14.37 ± 0.03 Ma and agree at the 2σ confidence level (fig. 84). MM adularia dated at 14.40 ± 0.16 Ma is also within statistical agreement compared to BB and Con but has a notably higher uncertainty. These three adularia dates display an approximately normal distribution (fig. 85) and provide a weighted mean age for mineralization of 14.39 ± 0.04 Ma and indicate that a one epithermal period was responsible for adularia mineralization. The results cannot resolve events separated in time by less than about 40 ka and thus within the data resolution indicate a single mineralizing event at the HGD, NE Modoc County (fig. 86). (Peters, 2009)

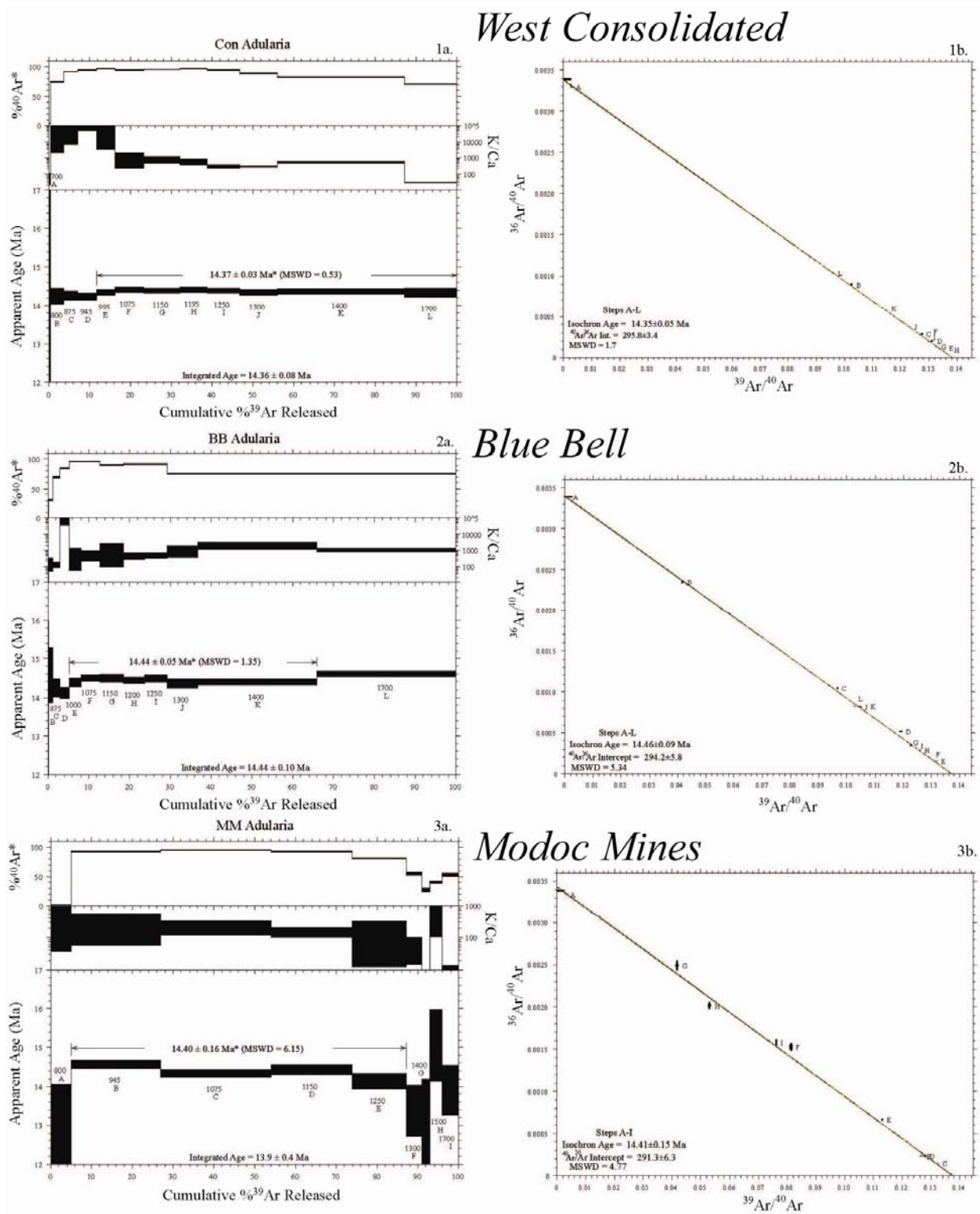


Figure 84. Age spectrum and respective isochron. The step heating method provides the indicated plateau ages. Isochron plotting, to right, shows that Con and BB fit very well, while MM shows a higher level of error. (Peters, 2009)

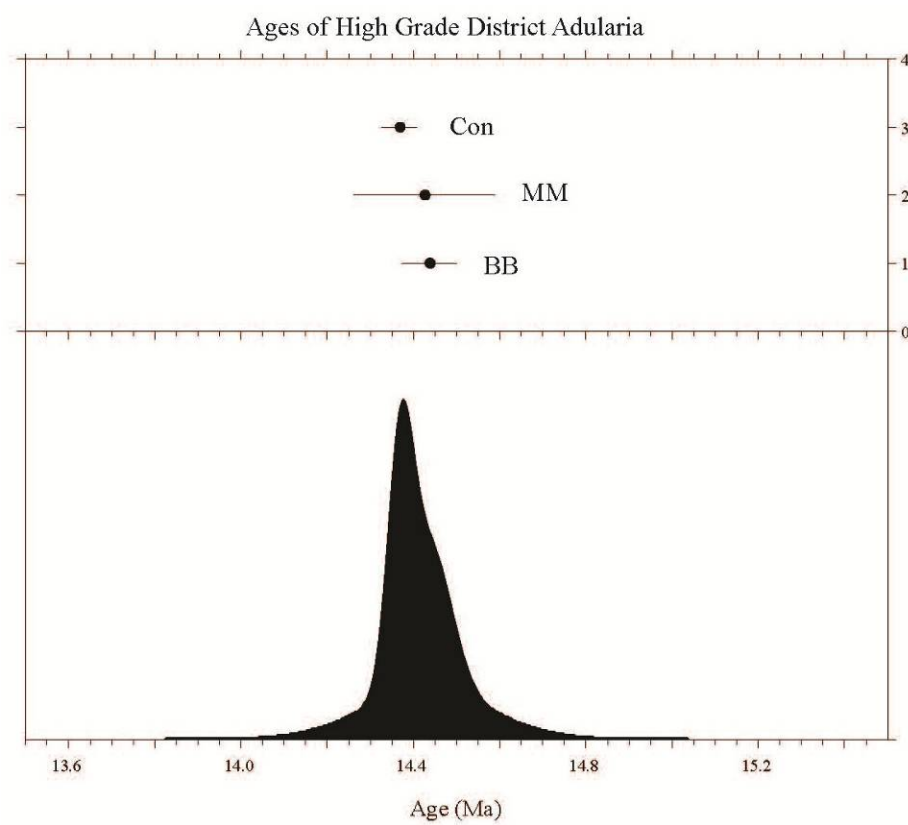


Figure 85. Bell plot of High Grade vein ages, average age of 14.39 Ma is derived from the peak. (Peters, 2009)

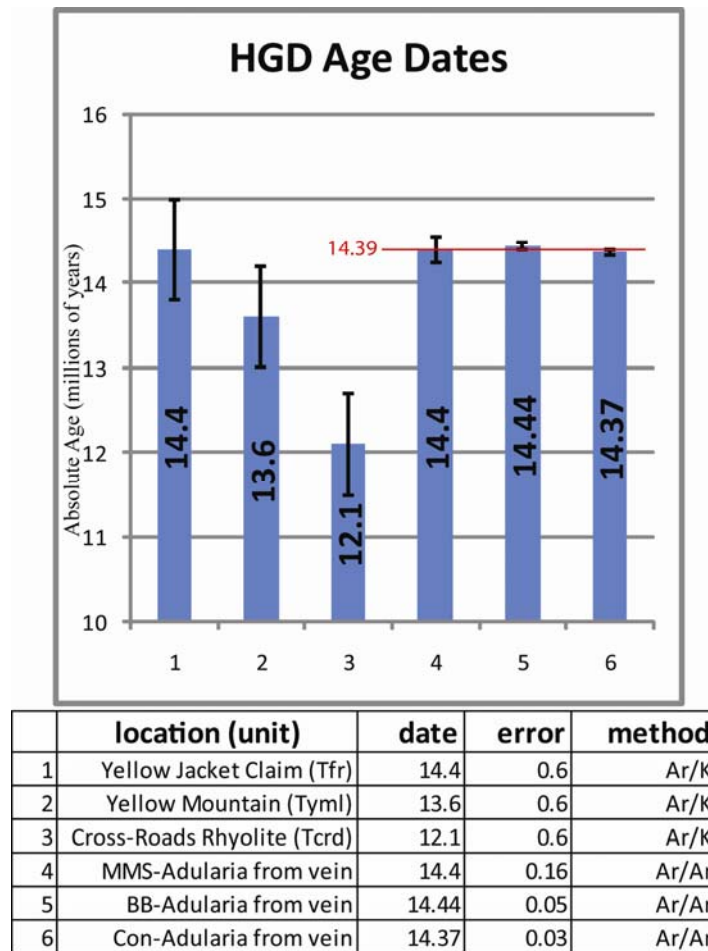


Figure 86. This chart and table display all age data collected in the HGD. Average timing of mineralization is shown by red line and correlates with emplacement of aphanitic rhyolite domes (Tfr).

9.3 Discussion

Epithermal systems are typically short-lived geologically, having an average age of 100,000 years. The average life-cycle of an epithermal system is based upon observations made in the Basin and Range and New Zealand (John, 2001; Simmons and Browne, 2000). Did multiple epithermal periods of activity occur progressively over the district, or did one period of activity cause HGD mineralization? This question poses the conclusion that a singular period of epithermal activity will have a consistent generative depth, excluding influence from paleotopography. The three ages obtained are within sufficient range to constrain quartz-adularia mineralization to a single period of epithermal activity occurring at 14.39 ± 0.04 Ma (fig. 86). Ages collected by this study have high reliability and confine epithermal veining to a single event. Thus, it is reasonable to assume that the three vein trends have a similar generative point and vertical correlations (accounting for any later faulting) can be made across the HGD.

Age dates provide chronologic context for the felsic suite in the study area. Ages from vein adularia correlate with the emplacement of the aphanitic rhyolite domes (Tfr) (fig. 86). The porphyritic rhyolite dome dated by Keats, correlates to the Cross-Roads Rhyolite (Tcr), lies within the center of the district and represents a later (~2 m.a.) pulse of felsic volcanism. The Yellow Mountain latite (Tym) is the most expansive felsic unit in the study area, the single age date, of questionable location, is insufficient to date this entire flow (fig. 87).

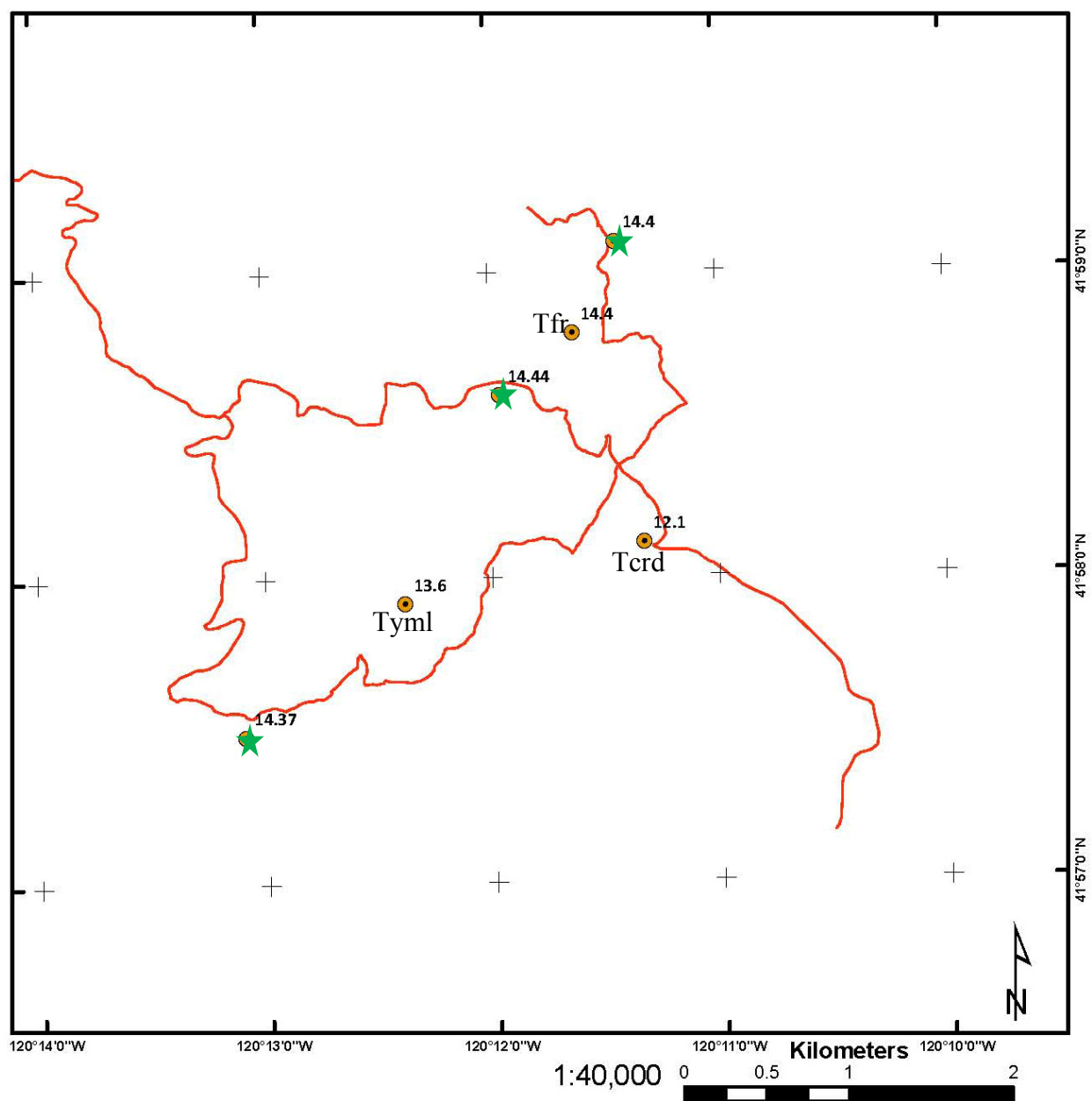


Figure 87. Age dates acquired in the HGD. The three samples of vein adularia analyzed in this study are indicated by green stars. Ages indicated by orange circles are acquired from whole rock analysis.

10. $\delta^{18}\text{O}$ ISOTOPE VALUES

This study obtained eleven $\delta^{18}\text{O}$ isotope values over the HGD. Numerous occurrences of hydrothermal quartz were sampled during the field mapping portion of this study (chapter 7.1). Purified quartz separates were prepared at UTEP from samples contained abundant pure quartz. Samples were given a coarse crush, then handpicked for finer crushing. Finely crushed samples were sorted to remove both a coarse and dust component. The quartz concentrate was hand-picked for pure, clean grains under a 30X reflected light microscope by the author. Samples were submitted to the Queen's University Isotope Lab (www.geol.queensu.ca/isotope_lab) in Kingston, Ontario, Canada for analysis. The yield value is provided as a measure of sample purity, pure quartz returns a value of 16.7. $\delta^{18}\text{O}$ values are presented in comparison to the Vienna Standard Mean Ocean Water (VSMOW). Average values from the contiguous camp/vein systems are presented to the right.

Table 10. Oxygen isotope data returned for vein quartz from the study area. Yield of pure quartz is 16.7, the minor variation is attributable to minor impurities.

Sample	Mineral	Yield	$\delta^{18}\text{O}$ (VSMOW)	area avg.
MMS	Quartz	15.2	3.8	4.074
SS	Quartz	15.7	4.3	
RRT-2	Quartz	16.2	2.7	2.6972
SEKT-7	Quartz	15.4	2.9	
KLON	Quartz	15.2	2.4	
LP-NW	Quartz	15.9	2.9	
BB	Quartz	16.4	2.6	
CSB-12	Quartz	16.0	7.0	7
CT-1	Quartz	15.6	1.7	
CON	Quartz	15.5	1.4	
				1.8293333
NSRD	Quartz	15.8	2.4	

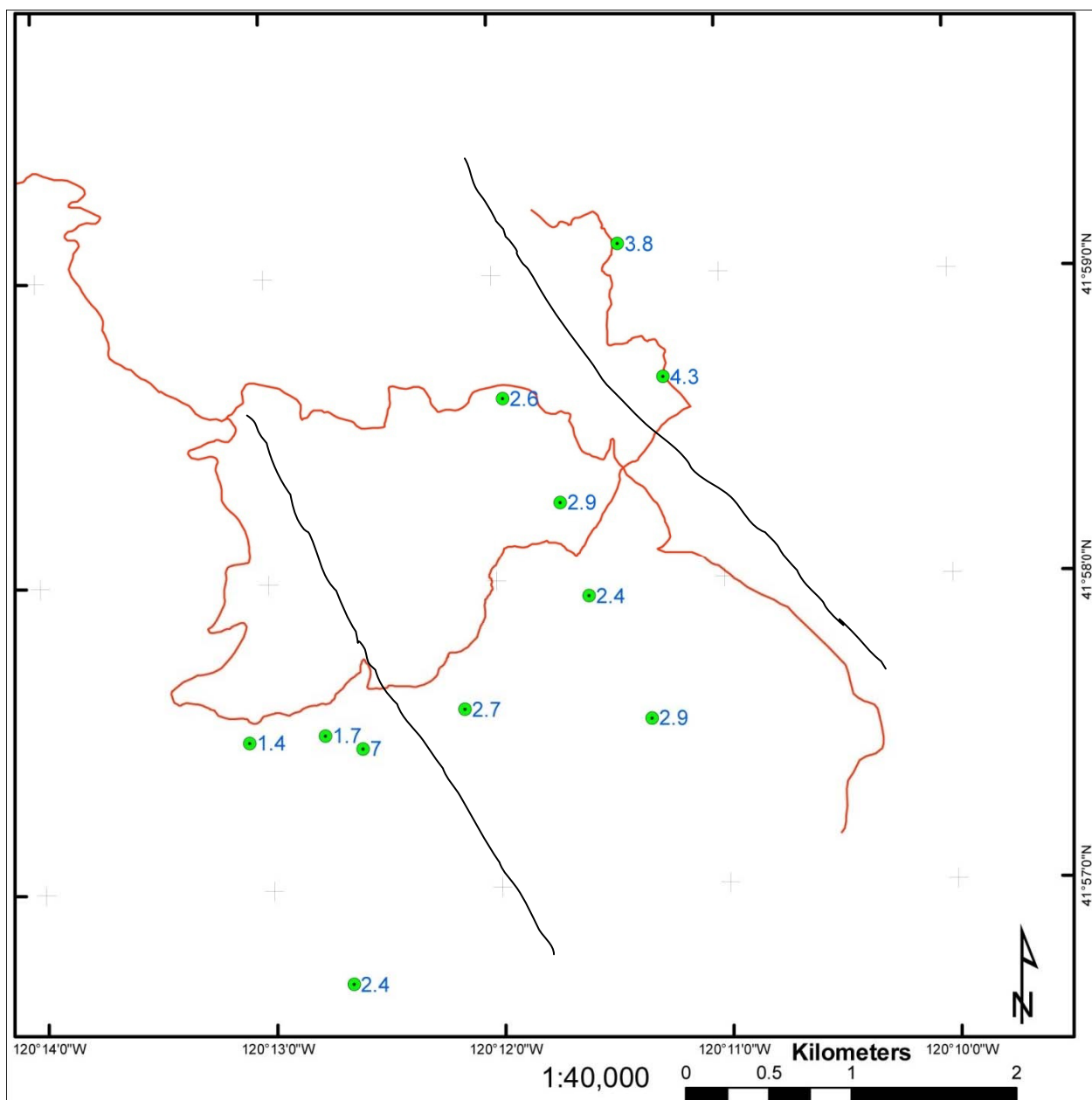


Figure 88. Oxygen isotope values acquired from hydrothermal quartz over the HGD. Black lines are drawn to separate the groups mentioned in table 10.

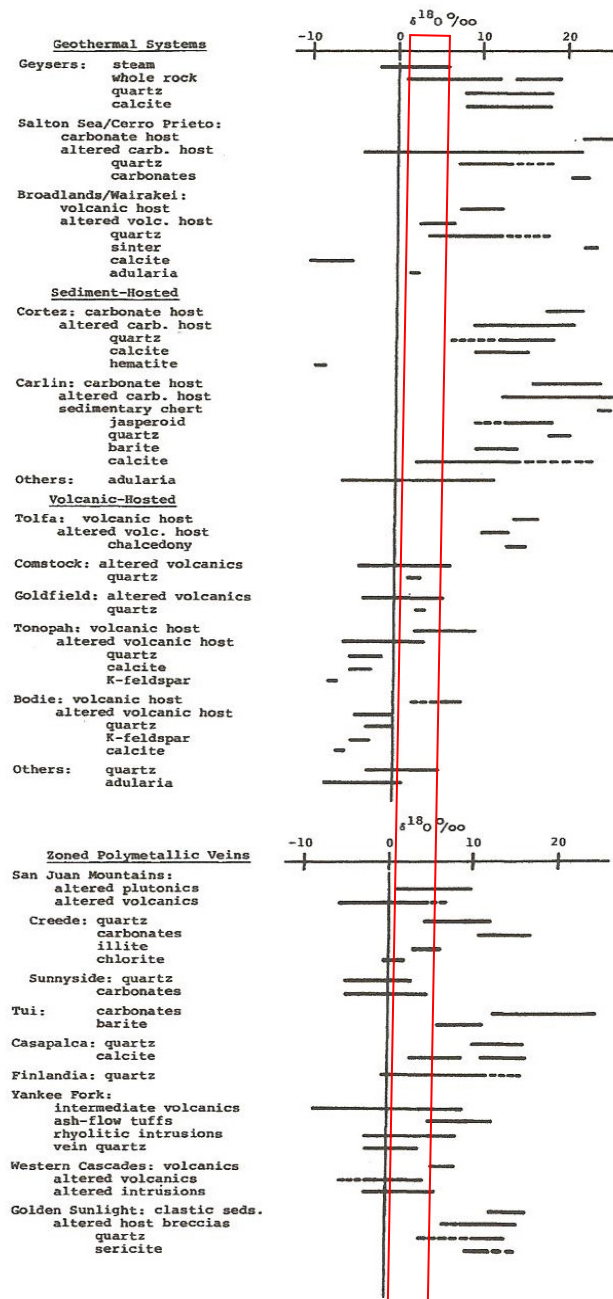


Figure 89. Contours of some average $\delta^{18}\text{O}$ values from gold deposits. The deposits are separated by host environment; values are reported for different gangue minerals and varied rock types. Values returned in this study fall within the red box. (Taylor, H.P., 1997)

10.1 Interpretation - Fluid Transport and Mixing

The variance observed between camps is held consistent along NW trending vein systems (table 10). Values within the NE portion of the district provided values averaging 4.07 and having a standard deviation of 0.37. The central portion of the district, including the area of surface deposit definition, displayed values averaging 2.70, with the smallest standard deviation encountered, of 0.23. The southwest portion of the district returned average values of 1.83, and a standard deviation of 0.51 (excluding outlier value, discussed below). The general trend observed in the study area is approximately one unit $\delta^{18}\text{O}$ per vein system, decreasing from the NE to the SW (table 10, fig. 88).

In the SW portion of the district, several samples from the Consolidated Silica Body (CSB) were analyzed and a dynamic transition area was illuminated (fig. 88). Sample RRT-2 was collected from an outcropping vein on the southwestern slopes of Ruby Ridge, CSB-12 was collected 2,000' away to the SW, and across a major NW-trending structure. This high value within the Consolidated Silica Body (CSB) is met with a sharp decrease as the transition from rhyolite dome to underlying andesite is encountered. The NSRD (North Star Rhyolite Dike; located 2 km south of Consolidated) is included with Consolidated Mine samples for an average 1.83, CSB-12 is a sample from the silica body on the eastern portion of Discovery Mountain. The value returned from CSB-12 is 7.0, this large variation (7 to 1.8) indicates a significant mixing zone between the eastern, rhyolite-hosted silica body and the western, andesite-hosted veining and stockwork.

The further study of hydrothermal quartz for $\delta^{18}\text{O}$ values is necessary to truly evaluate the fluid dynamics during mineralization in the HGD. Several samples from unaltered country rock would be very helpful in providing context to any further $\delta^{18}\text{O}$ investigations. Sub-

millimeter scale $\delta^{18}\text{O}$ investigations have been proven useful guides (Hayashi et al., 2001; Ewers, 1994; Matsuhisa and Aoki, 1994; Ronde and Blattner, 1988) to fluid transport studies and may be applied here to generate future targets.

11. DISCUSSION

Table 11. This table summarizes the total number of samples processed in each method.

# of samples	Field Mapping	Visual Mineralogy	Optical Microscopy	Electron Microprobe	Geochemistry	Temperature & Salinity	Age Date	$\delta^{18}\text{O}$ value
142	X							
264		X						
90			X					
36				X				
129					X			
45						X		
3							X	
11								X

This study has collected datasets from multiple scientific and geologic perspectives. Different processes and characteristics are identified in each geologic method used. 378 samples were collected in the field, samples were prioritized and selected for analysis by suitability (coarse crystalline quartz is preferable for optical microscopy and temperature studies; whereas colloform banded vein material is preferred for electron microprobe). Age dating from this study and the work of others (Egger and Colgan, 2009; Duffield and McKee, 1986; Keats, 1985) has been compiled and integrated with the stratigraphic column of the HGD (fig. 90).

Age	Phase	Map Symbol	Explanation	Host Silicification	Mapper
		Qt	Talus cover		
		Qs	Soil Cover		
	F	Tbv	Bidwell vent/tuff		MF
~10 Ma	F	Tbvo	Bidwell Obsidian		MF
	M	Tb	Steen's Basalt		MF
	F	Tcv	Vitrophyre		MF
	F	Trvb	Pumiceous vent breccia		DK
	F	Tdc	Deep Creek Rhyolite flow		MF
	F	Tai	Andesine Ignimbrite		MF
	F	Tct	O'Connor Blue Tuff		DK
	F	Toi	O'Connor Ignimbrite		MF
12.1	F	Tcd	Crossroads Rhyolite Dome		DK
	F	Tclt	Cave Lake Tuff		MF
	F	Tclv	Cave Lake coarse volcanics		MF
	F	Tkc	Kelly Creek Tuff		MF
	F	Trd	Rhyolite porphyry flow dome	X	DK
	F	Trt	Rhyolite porphyry vitric flow	X	DK
	F	Trp	Vitric rhyolite porphyry		DK
13.6	F	Tym	Yellow Mtn. porphyritic rhyolite	X	DK
	F	Tkq	Klondyke flow/dome; qtz latite porphyry	X	DK
	F	Tbs	Bow Spring Rhyolite	X	MF
	F	Tsp	Sugar Peak Rhyolite porphyry		MF
	F	Tpl	Poison Lake Tuff		MF
	F	Tmvp	Mt. Vida peak Rhyolite porphyry	X	MF
	F	Tmlb	Hydrothermal Breccia	X	MF
adl @ 14.44	F	Tlq	Lodgepole aphyric quartz latite flow/dome	X	MF
	F	Ttss	Sunshine poorly welded silicified lithic tuff	X	MF
adl @ 14.40	F	Tml	Modoc latite flow	X	MF
	F	Tmpr	Moonlight pumiceous rhyolite	X	MF
14.4	F	Tfr	Flow banded aphyric flow domes	X	MF
	F	Ttb	Poorly welded pumiceous brown tuff		MF
adl @ 14.37	F	Tdmr	Discovery Mtn. rhyolite flow/dome	X	DK
	F	Tccr	Consolidated Mtn. rhyolite dome	X	DK
	F	Tcrf	Consolidated Mtn. rhyolite flow	X	DK
25 - 35 Ma	I	Tam	Andesitic Mudflow		DK
	I	Ta	Andesite		DK

Figure 90. Stratigraphic units of the study area. Igneous phase is indicated (M=mafic, I=intermediate, F=felsic) along with geologic mapper (DK=D. Keats, MF=M. Feinstein) and whether a prospective unit displays silicic alteration. Ages for andesite and later obsidian are taken from regional studies (Egger and Colgan, 2009; Duffield

and McKee, 1986), vein adularia ages are placed with host unit, felsic unit age constraints are limited to the work of Keats, 1985.

Temperature data from this study has shown that mineralizing fluids in the HGD are significantly hotter than generally reported from epithermal systems. Salinity measurement is an equivalent value to total dissolved solids and represents the fluid capacity to carry dissolved particles (Hayashi et al., 2001; Ewers, 1994; Matsuhisa and Aoki, 1994; Ronde and Blattner, 1988). The salinity values from HGD are sufficient to carry economic mineralization (compared to Heald et al, 1987) although they only reach a maximum which is half that of salinity recorded at the Golden Cross deposit in New Zealand (fig. 82).

11.1 Integration of Methods

The methods of this study have been integrated to produce the figures and related discussion in this section. This section hypothesizes the true nature of statistical observations made during factor mapping (chapter 6.4), based upon observed geology (chapter 3 and 4) and microscopic mineralogical observations (chapter 7). The geochemical associations established by factors 1 through 6 have been correlated with paragenetic phases in each camp. There are two possible options for some of the factors (fig. 91, 92):

(A) the associated minerals are the effect of hydrothermal deposition, or

(B) these minerals are resistate from the original host rock.

It is important to keep in mind that the entire dataset has been severely leached of all major rock-forming elements (Al, Ca, Na, K, Mg, and Ti are depleted with respect to granitic average; all combined average <5% of whole rock chemistry).

Five of the eight factors discussed in chapter 6.3 are deemed sufficient to integrate with paragenetic observations. Factor 4 does not spatially correlate with any mining camps (appendix 1, fig. 1-31) it is present in the E-W silica body trend from Ruby Ridge to Consolidate Mountain; factor 4 may be result of zircon resistate (Hf only fits into zircon structure). Factor 7 and 8 are poorly understood and repetitious of other factors. For the indicated reasons these factors have been deemed less important and have been withdrawn from paragenetic-factor interpretation.

Part of factor 1 may be hydrothermal (fig. 91), but other parts may be resistate (fig. 92). Monazite and remnant feldspar are concentrated into factor 1 from the total silicification of original rhyolite dome; factor 1 is a resistate factor of the original host rock, therefore strong factor 1 represents total replacement of original rock. Factor 3 represents the eruptive multi-

lithic breccia both chemically and spatially. For these reasons, factors 1 and 3 have been added as paragenetic phases in hypothesis A (fig. 92).

Factors 2.2 and 5.2 are very important for precious metal deposition in the HGD. The strong overlap of these two factors at Sunshine and BlueBell indicate that these targets should be tested further. Factors 2.2 and 5.2 occur coincidentally the West Consolidated camp, the presence of these precious metal factors within the strongest vein trend of the district deserves future drilling.

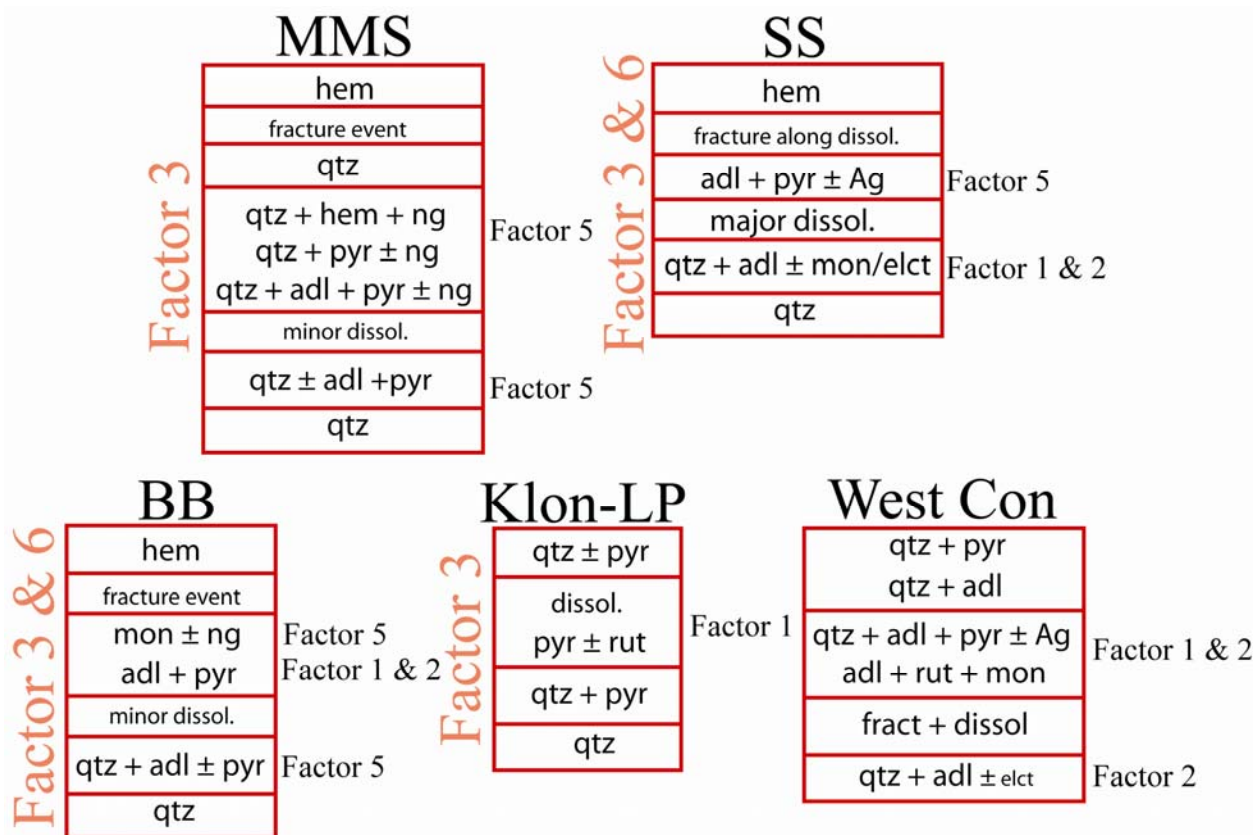


Figure 91. Hypothesis A for the relation of geochemical factors and paragenetic phases. This interpretation takes the perspective that all observed mineralogy is hydrothermal in origin. Factors 3 and 6 are seen to have strong overprints on the paragenetic development of mineralization at Sunshine (SS) and Bluebell (BB).

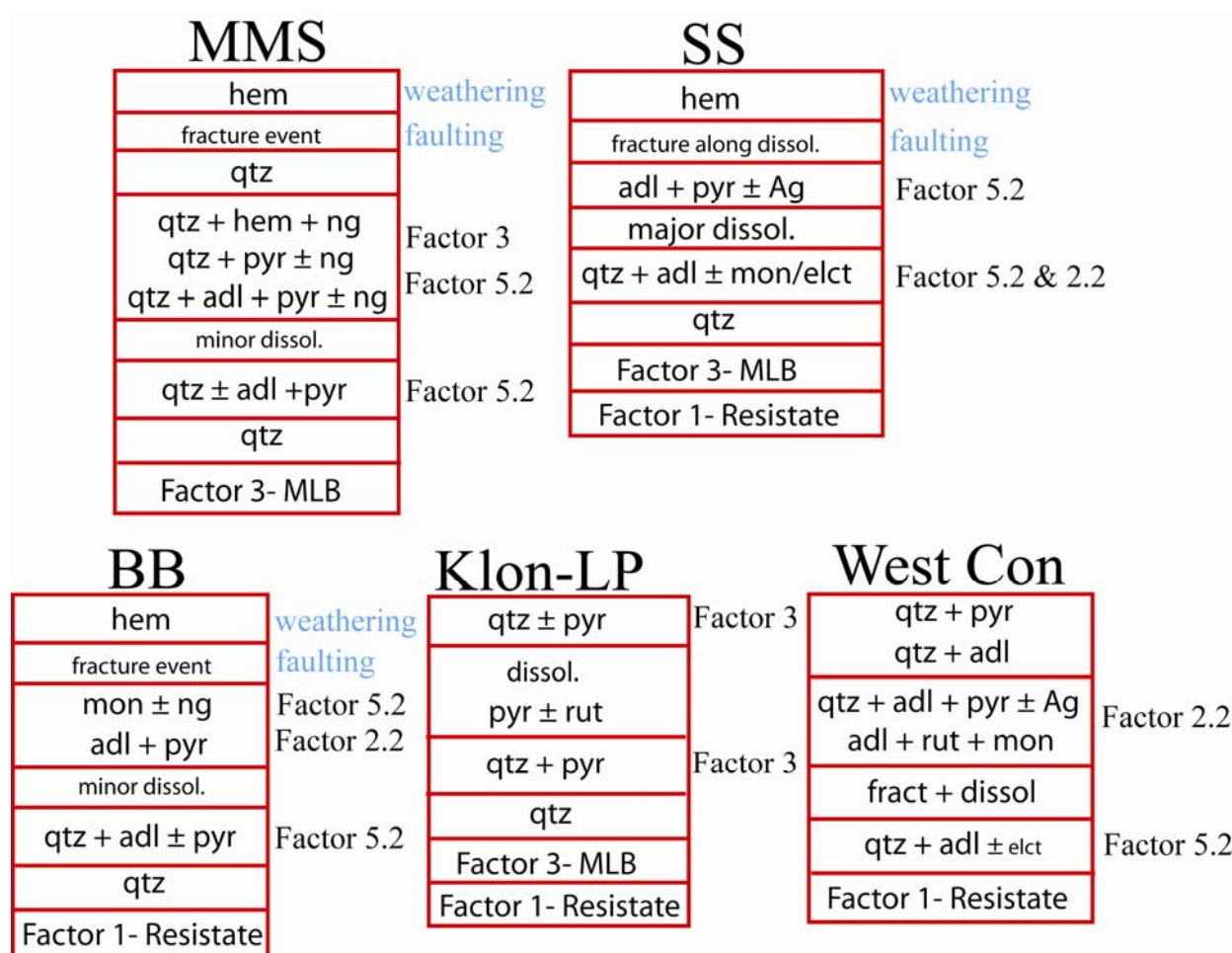


Figure 92. Hypothesis B for the relation of geochemical factors and paragenetic phases. Paragenetic phases of resistate from host rock and multi-lithic breccia are added to the paragenetic columns; epithermal mineralizing factors (factors 2.2, 3, and 5.2) are indicated where present.

The sample set used in this study was selected to characterize the epithermal system. This study helps to confirm the practice of making precise geologic observations based upon statistical processing of geochemical data. The work of others is mentioned here to illustrate the power of using statistical processing of geochemical data to extrapolate geologic influence. Processing low resolution data, such as state-wide stream sediment sampling, yields the presence of geologic formations and human impact (Taisser). Processing systematic surface samples from a porphyry copper system illuminates zoning and multiple alteration types (Lori). Processing

vein samples from an epithermal district yields the different phases of epithermal activity and some relative depth levels in mineralizing system (Feinstein).

11.2 Epithermal Models by Mining Camp

This study attempts to characterize the mineralization in the HGD with laboratory evidence and geologic observations. The accepted method for description of an epithermal precious metal system is through the construction of a district specific model. Models are based upon geologic controls and conceptual ideas that are accepted by the scientific community. Here a model has been constructed from laboratory data for each of the three NW-trending vein systems in the district. Four cross-sections for each NW vein trend are submitted here; these sections provide context for epithermal mineralization with stratigraphy, alteration, temperature/isotope data, and geochemical signature. Observations from this study (indicated in red boxes; fig. 94, 98, 102) are used in the creation of models presented in this chapter, concepts presented in general epithermal models (Romberger, 1993; Berger and Eimon, 1983; Buchanan, 1981) are used to extrapolate the complete vein models presented in this section. The vertical levels of mineralization from the general epithermal model are used to name the levels presented below, the scale and details of each profile are specific to the HGD. The mineralization (chapter 7) and geochemistry (chapter 6) of this study are the basis for epithermal level characteristics used in the following diagrams. The legend below (fig. 93) will be used for all models presented in this chapter. A vertical exaggeration of 2 times has been used on all profiles (fig. 94-105); cross-section lines are shown on District Geology Map (appendix 2, plate 2).

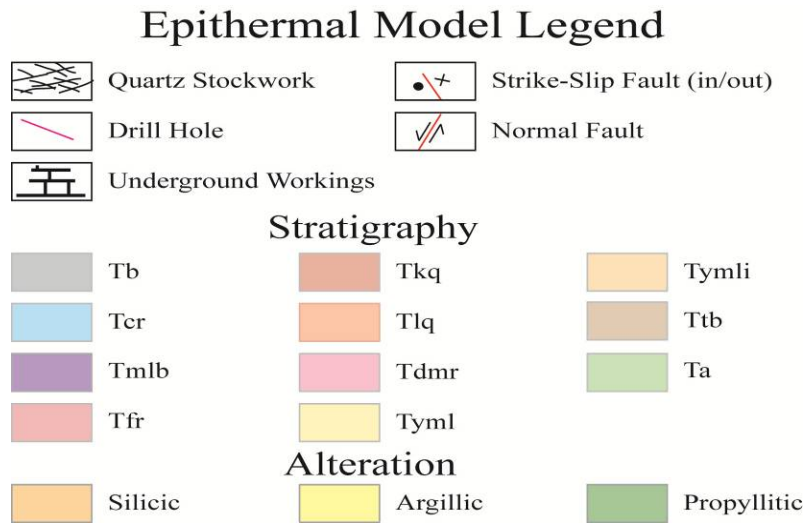


Figure 93. Legend for all epithermal models in chapter 11. Tymli is unmapped, but indicates the intrusive component of the Tyml (Yellow Mtn. Latite).

Discovery Mountain is modeled in figures 94 through 97; stratigraphy, alteration, temperature, and geochemistry are presented, respectively. The variable vertical horizons are named and described by gangue, geochemistry, and prominent mineralogy.

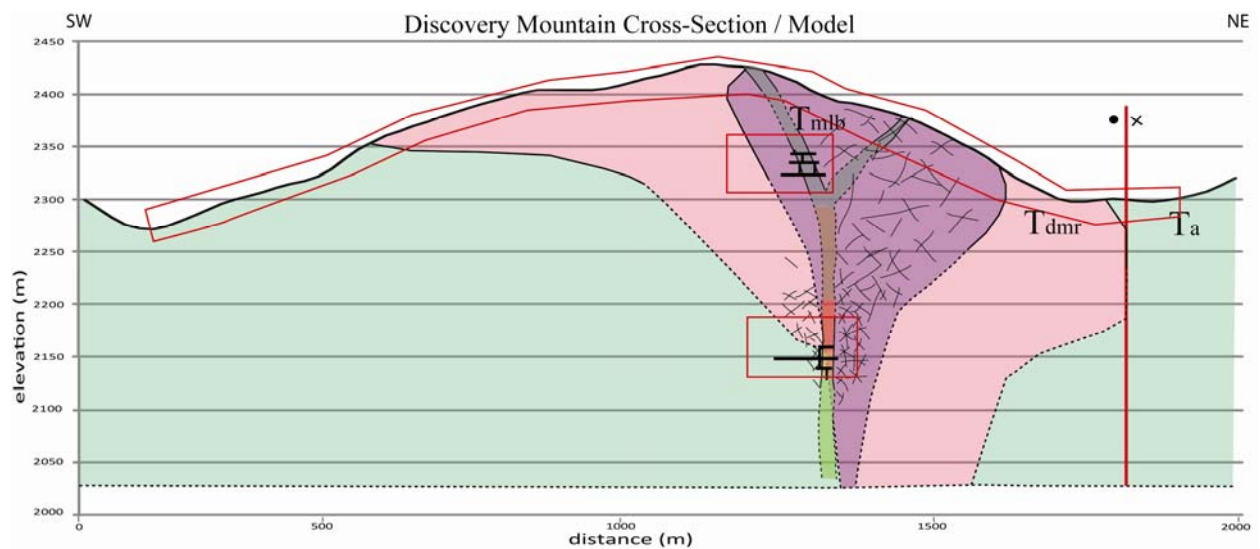


Figure 94. Discovery Mountain epithermal model showing veining and stratigraphy. Red boxes indicate ground control.

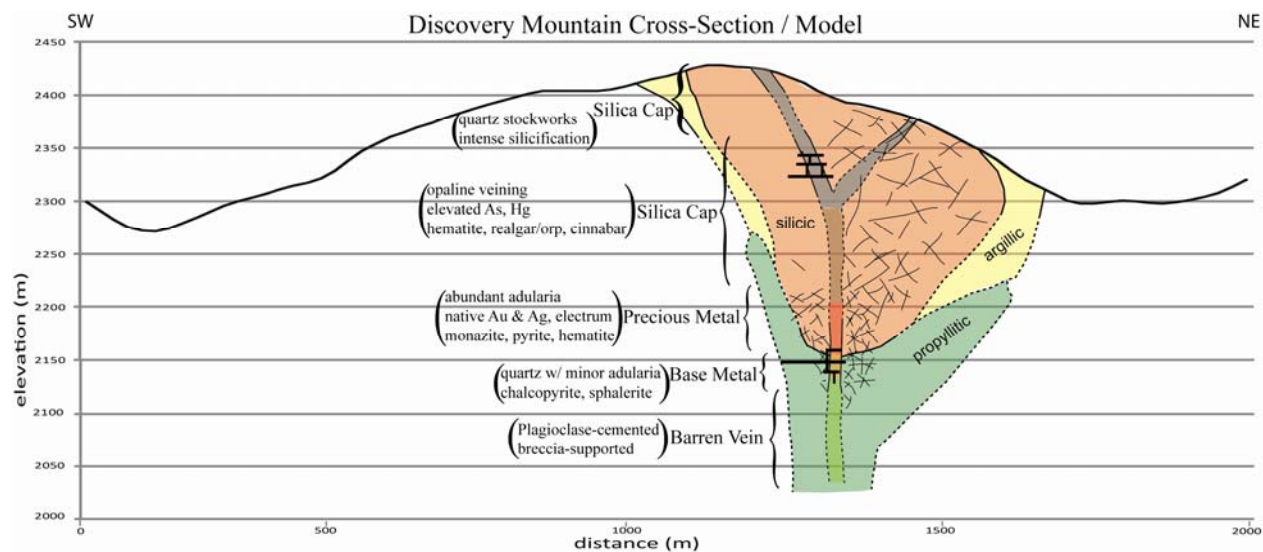


Figure 95. Discovery Mountain epithermal model showing veining and alteration.

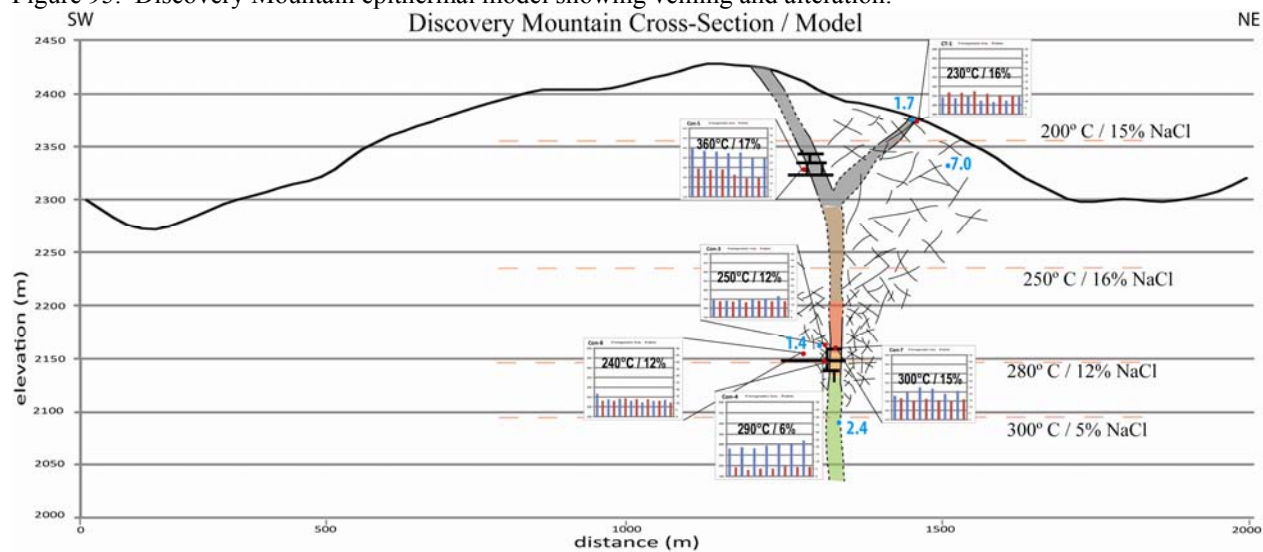


Figure 96. Discovery Mountain epithermal model showing temperature and $\delta^{18}\text{O}$ values.

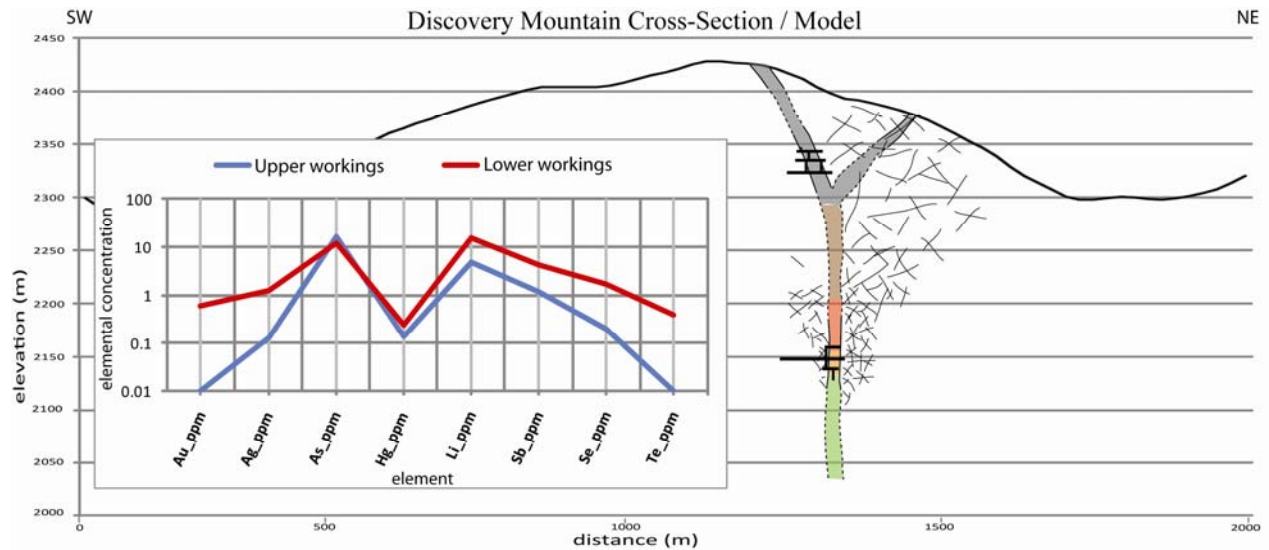


Figure 97. Discovery Mountain epithermal model with the epithermal geochemistry observed in the upper (blue) and lower (red) workings of this NW-trending vein.

In the Alturas hill area, high grade ore shoots occur as lenses concentrated along E-W stress planes; high grade (3+ opt) zones were confirmed in drilling of the 2009 season. Later barren quartz, related to faulting, cuts the breccias and commonly creates a pathway for oxidation. The Alturas Hill area is located in between the Klondyke and Lodgepole camps and within the historic resource (fig. 7) and is modeled in figures 98 through 101; stratigraphy, alteration, temperature, and geochemistry are presented, respectively. The variable vertical horizons are named and described by gangue, geochemistry, and prominent mineralogy.

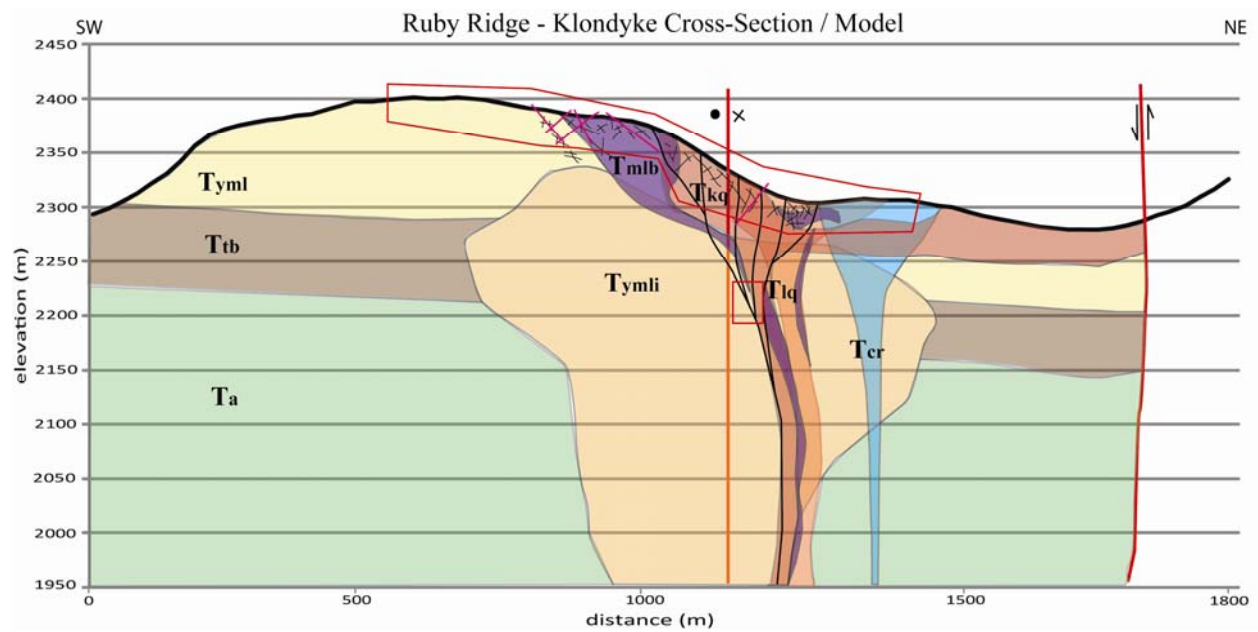


Figure 98. Ruby Ridge - Klondike epithermal model showing veining and stratigraphy. Red boxes indicate ground control.

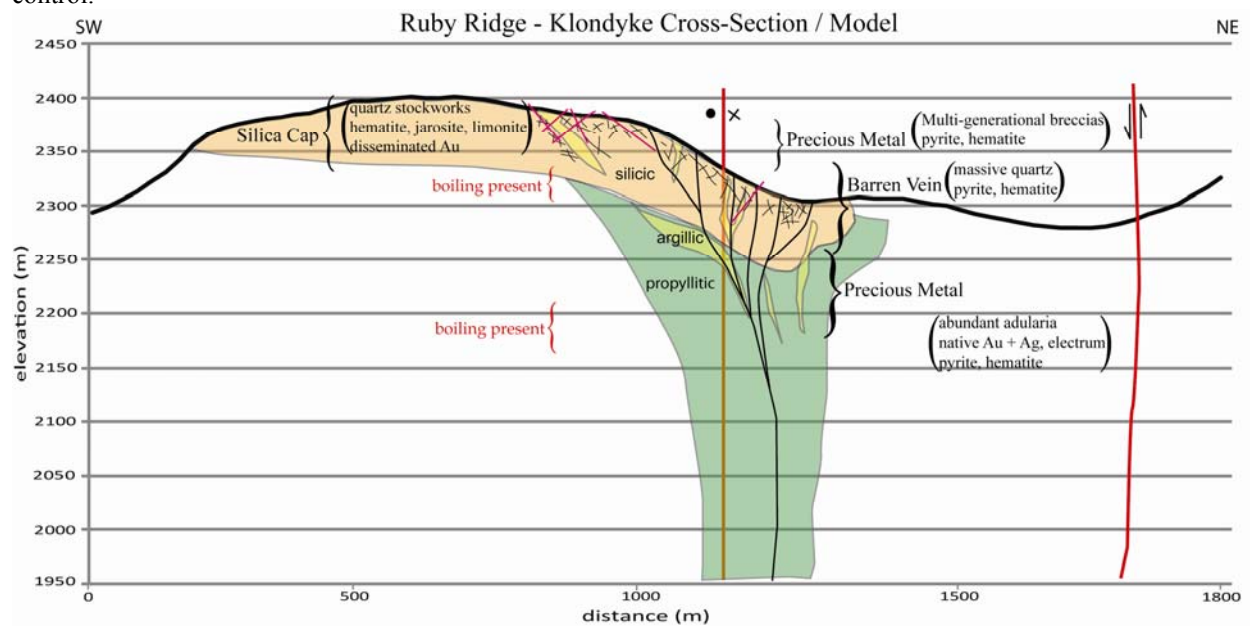


Figure 99. Ruby Ridge - Klondike epithermal model showing veining and alteration

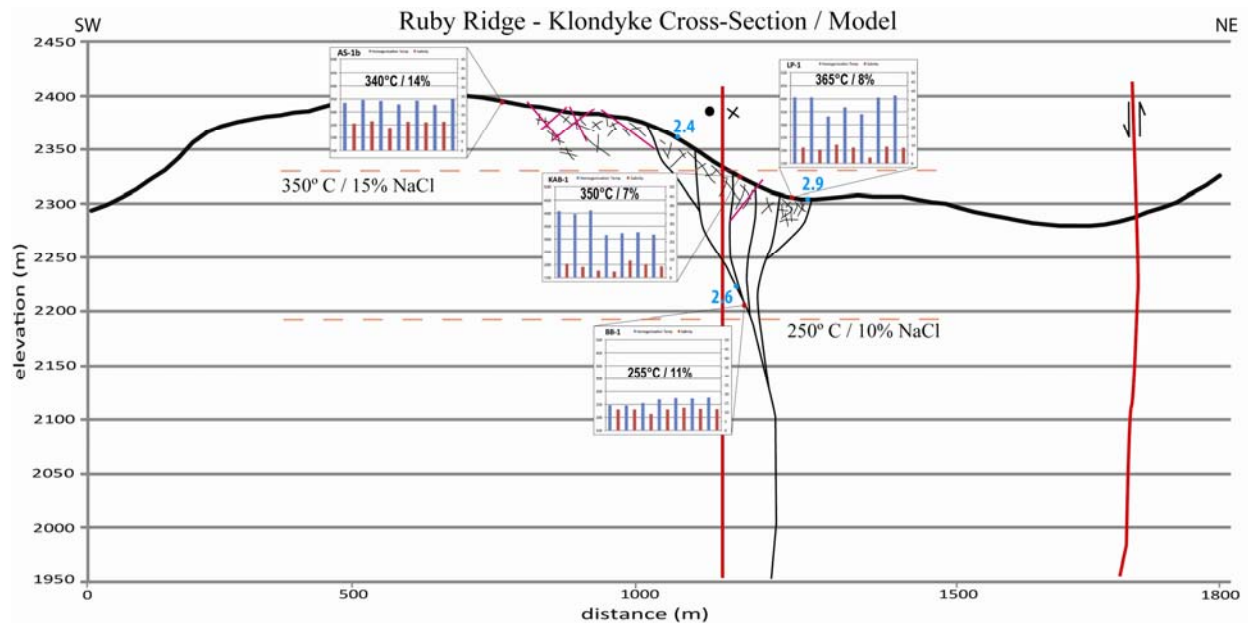


Figure 100. Ruby Ridge - Klondyke epithermal model showing temperature and $\delta^{18}\text{O}$ values.

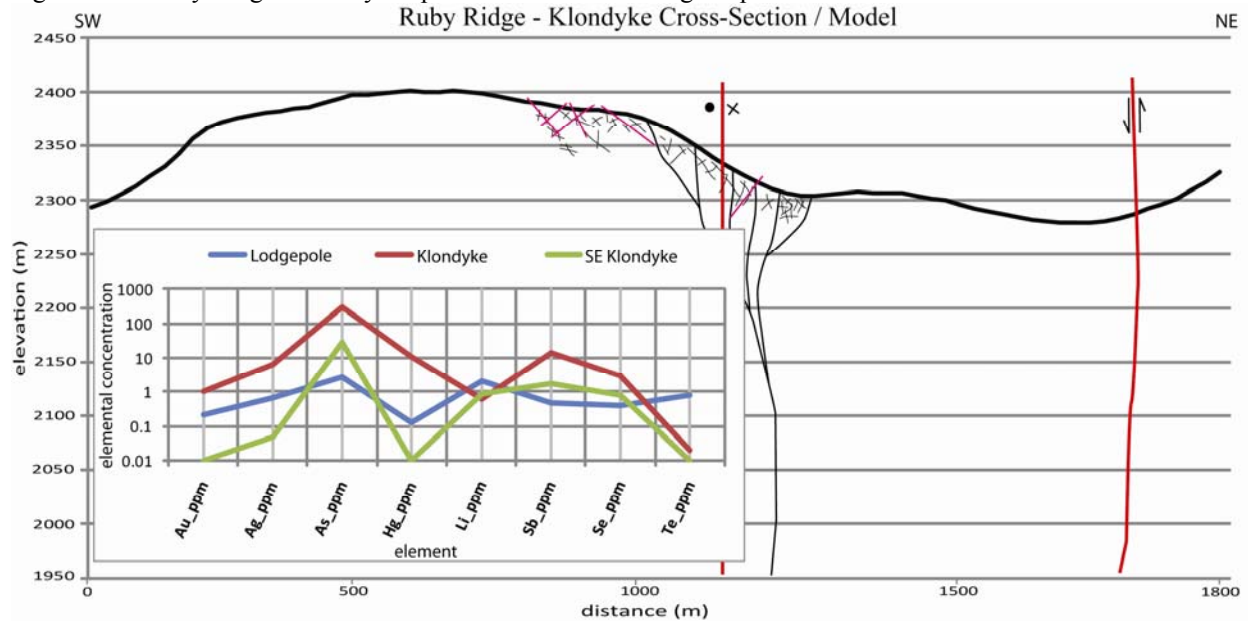


Figure 101. Ruby Ridge - Klondyke epithermal model with the epithermal geochemistry observed in surface samples taken along strike of this vein trend. Lodgepole to Klondyke to SE Klondyke makes a NW-SE traverse along the surface of this vein trend.

The northeastern vein trend in the HGD hosts multiple thin veins and stockworked zones within silicified multi-lithic breccia; it is modeled in figures 102 and 105, stratigraphy, alteration, temperature, and geochemistry are presented, respectively. The Sunshine camp occurs on the

left of model figures, Modoc Mines is located at right. The variable vertical horizons are named and described by gangue, geochemistry, and prominent mineralogy.

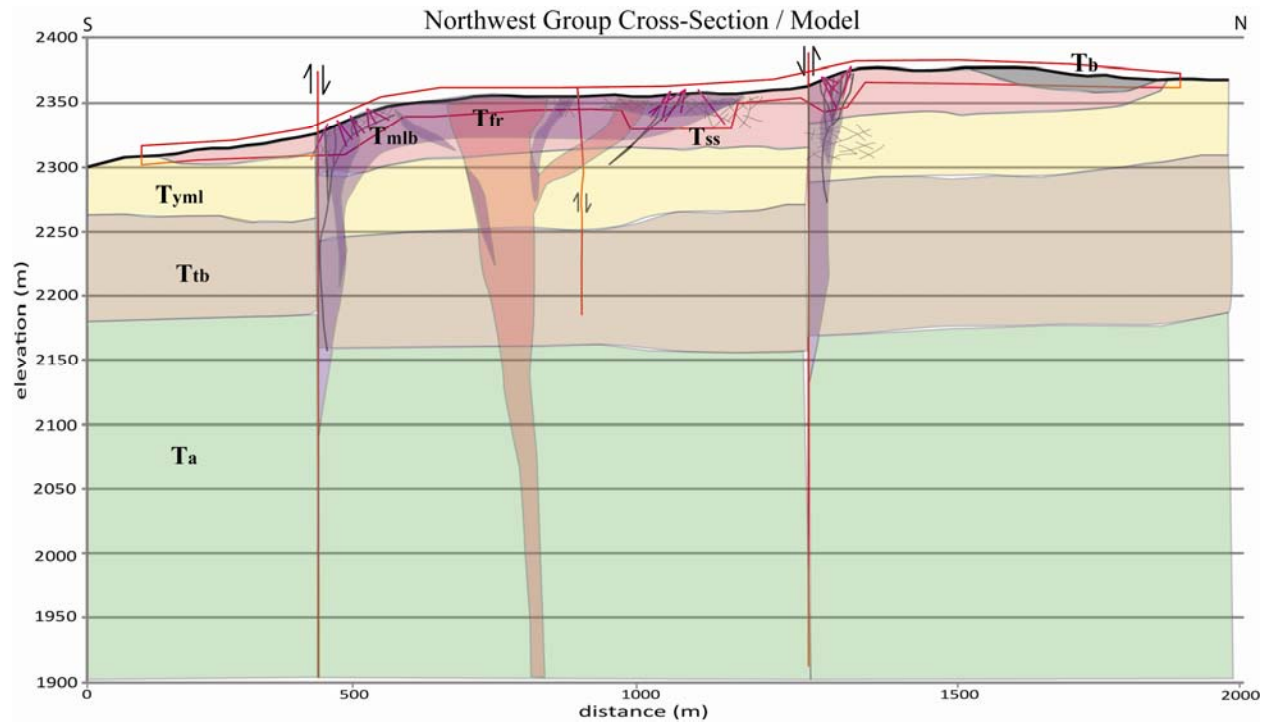


Figure 102. Sunshine - Modoc epithermal model showing veining and stratigraphy. Red box indicates ground control.

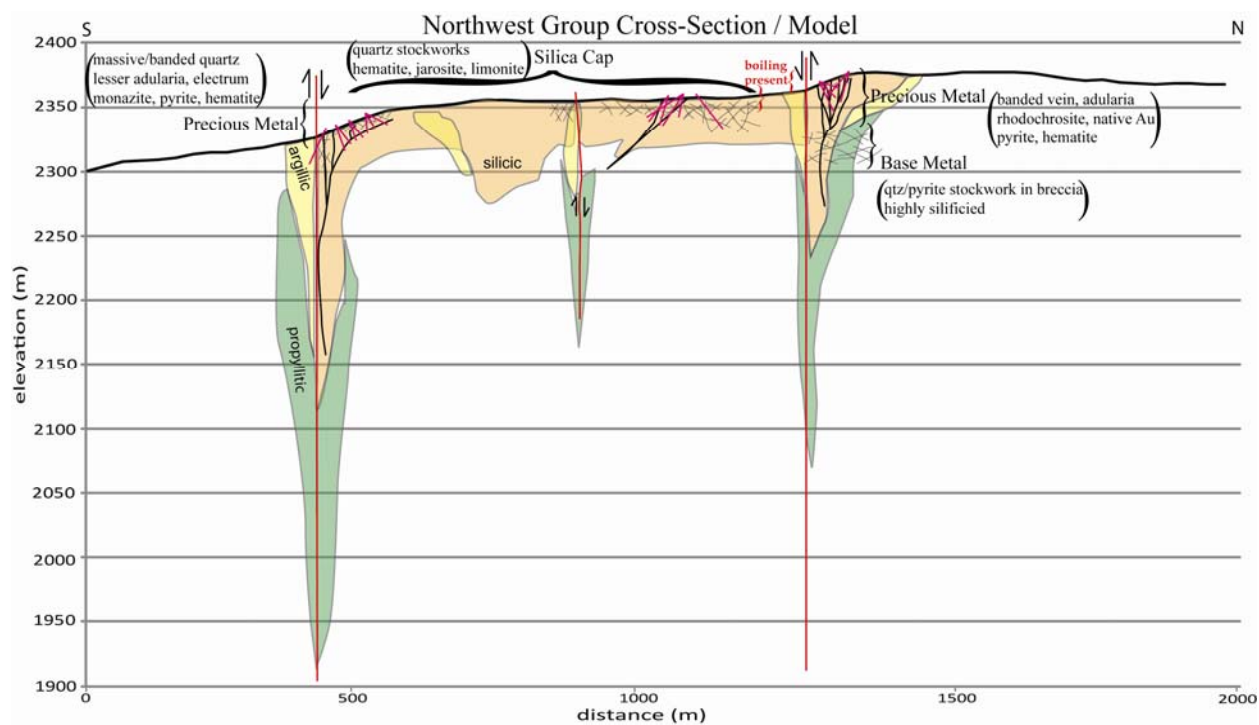


Figure 103. Sunshine - Modoc epithermal model showing veining and alteration.

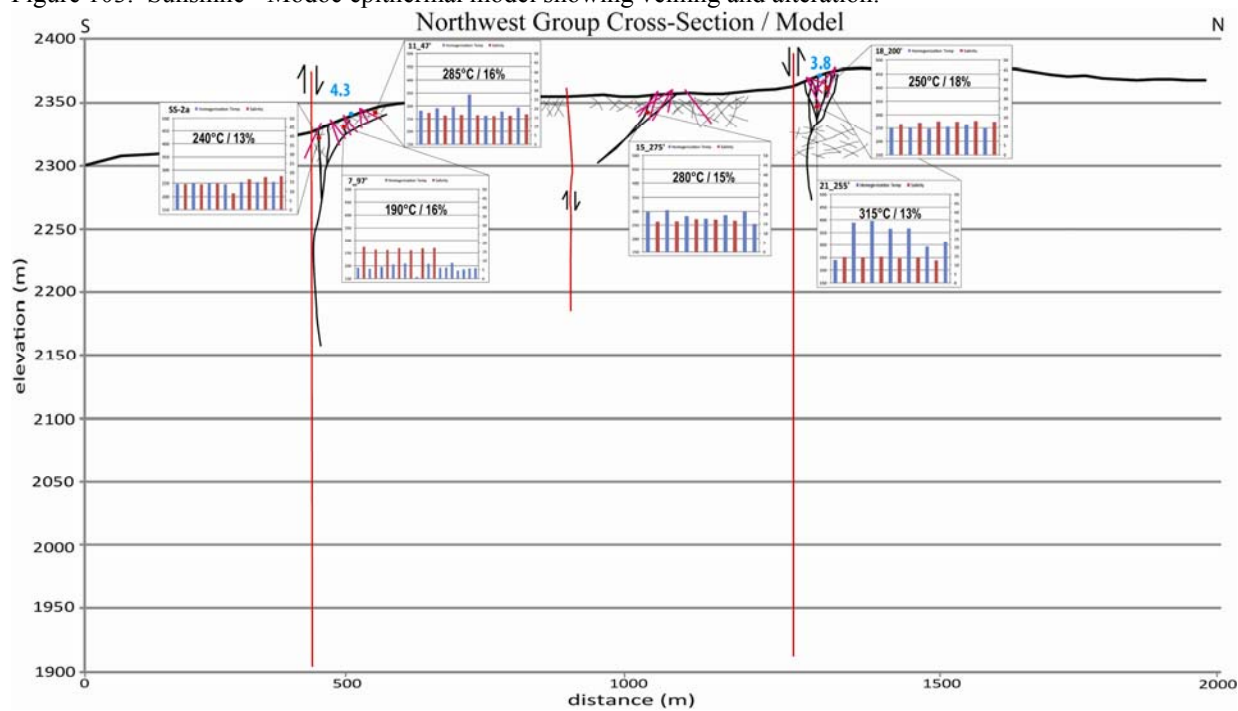


Figure 104. Sunshine - Modoc epithermal model showing temperature and $\delta^{18}\text{O}$ values.

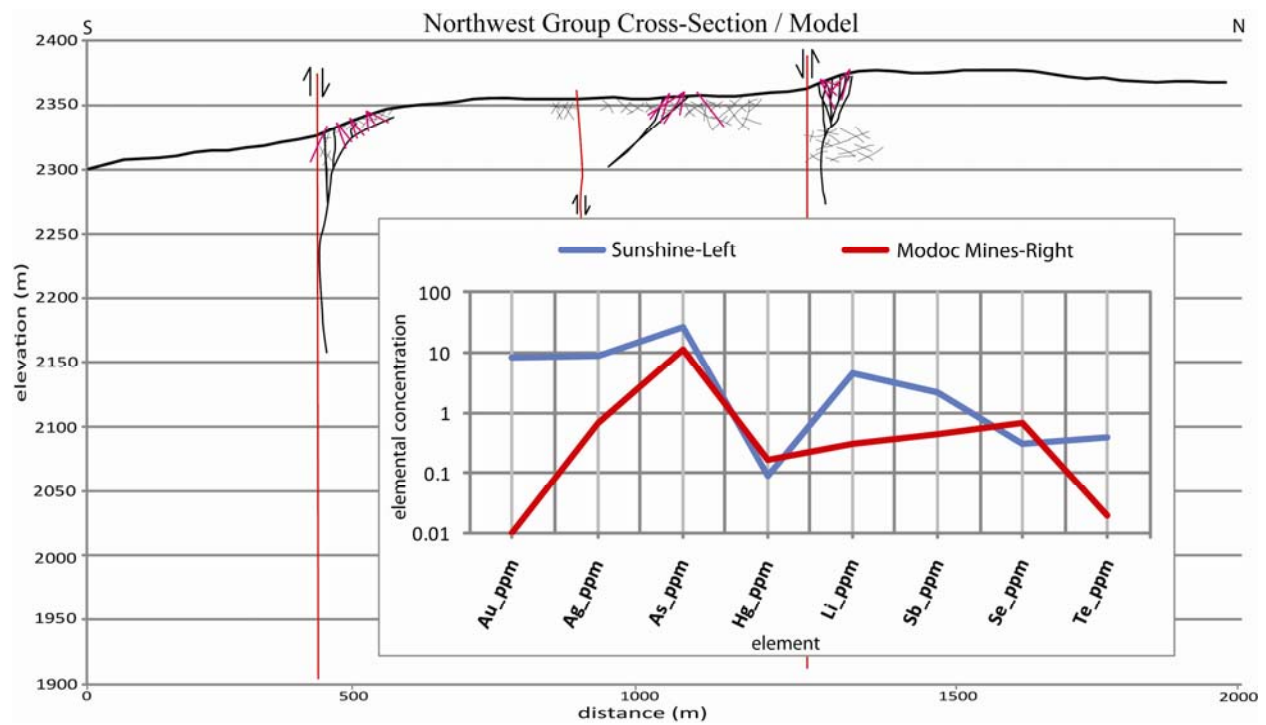


Figure 105. Sunshine-Modoc epithermal model with the epithermal geochemistry observed in this portion of the study area.

11.3 HGD Integrated Conceptual Epithermal Model

The three dominant NW-trending vein systems in the HGD each provide important information to establish district characteristics, but it is necessary to combine the three models to create a complete vertical section (fig. 106). By combining observations from the vein models, an idealized conceptual model for epithermal mineralization over the study area is constructed (fig. 107). A controlling structural feature (fault-zone) creates a pathway for extruding rhyolite to follow, this same pathway is used by eruptive breccias and the mineralizing system. The model is presented on an imaginary surface and a vertical exaggeration of 2x is used.

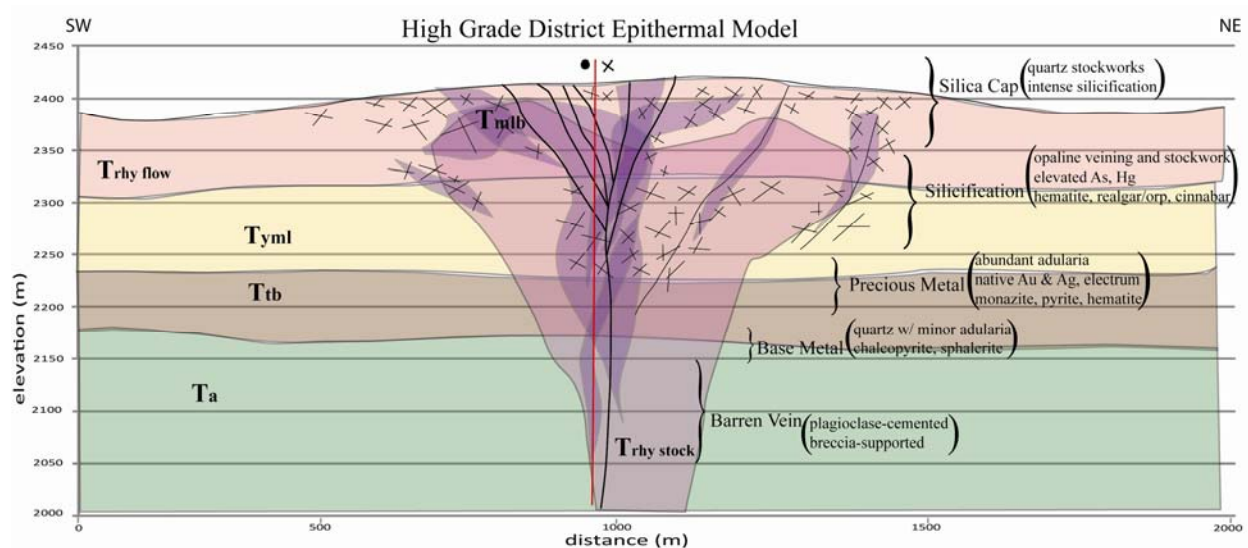


Figure 106. Conceptual epithermal model for HGD epithermal mineralization, imposed on general stratigraphy.

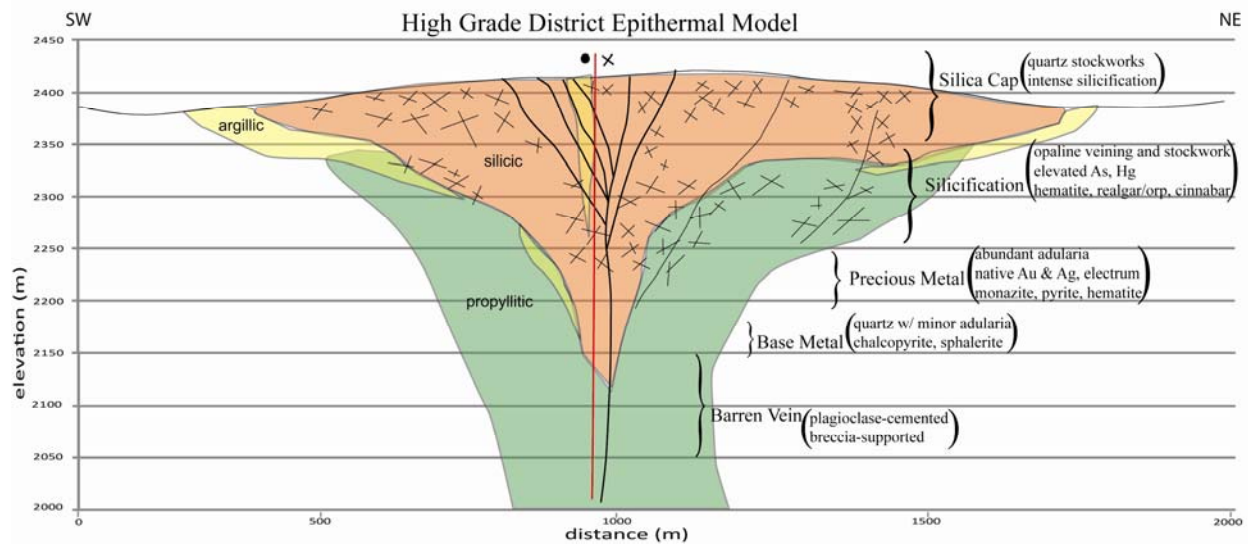


Figure 107. Conceptual epithermal model for HGD epithermal mineralization, imposed on the general alteration pattern observed.

How does this model compare to that of literature? The epithermal mineralization at HGD (fig. 107) is not telescoped (stretched), it is half that of the typical epithermal system (fig. 15). This short system emplaced directly upon the rhyolite domes, not in proximity (along cone fractures). Perhaps the plumbing system of this short hydrothermal cell cannot accommodate venting and the eruptive multi-lithic breccias are the result; this explosive decompression would not have been conducive to significant mineral precipitation (specifically ore minerals).

11.4 District Synthesis

This section takes observations from this study (methodology expressed in chapters 6, 7, 8, and 9) and integrates them with regional tectonics (chapter 1.5) to create a story for the geology and mineralization encountered in the study area.

A large complex of intermediate to mafic volcanic rocks is generated in the back-arc environment of the North American Margin, during Farallon-plate subduction by related arc-magmatism (fig. 9). The emplacement of rhyolite domes in this terrane, occurs during the local shift to a transitional environment (fig. 9 [Basin and Range effects occur much later in the northwestern extent of the province (fig. 13, 14)]). Dome emplacement is closely followed by hydrothermal activity which occurs as veining at depth and massive silica bodies consisting of hydrothermal and/or volcanic breccias, expansive quartz stockworks, and colloform veins displaying boiling textures. The model for epithermal mineralization in the study area is highly compressed, approximately 0.5 km in vertical expanse (fig. 107). This “short” system experienced very chaotic (i.e. boiling/eruption/fracture simultaneously) fracture/depressurization events as the fluids ascended into young rhyolites, this limited the concentration of a specific precious metal horizon based on temperature and pressure conditions.

Did multiple epithermal periods of activity occur progressively over the district, or did one period of activity cause HGD mineralization? This question poses the conclusion that a singular period of epithermal activity will have a consistent generative depth, excluding influence from paleo-topography. Age dating studies performed on vein adularia (chapter 9) have indicated that a single event causes HGD mineralization (fig. 86). This being the case, the depth to barren vein (plagioclase-cemented, metal barren) from Consolidated can be extrapolated to provide a depth of system to the other vein trends in the HGD.

The conclusion is suggested that basement heating is a likely source for the rhyolite dome field expressed in the study area (fig. 108). Within the upper crust a significant section of felsic material existed, which was then made semi-molten by impinging basaltic sills that generate heat for country rock melting. With continued heating from basaltic impingement, the felsic magma differentiates and eruptive pulses are expelled upward. These eruptive pulses are recorded by the numerous rhyolite domes in the study area, mineralization is syn-magmatic and utilizes the structural control of dome emplacement (fig. 107). The passage of the Columbia River-Yellowstone hotspot at 15 Ma (fig. 12; Camp and Ross, 2004; Smith, 1994) is spatially and temporally correlative with magmatism of the HGD.

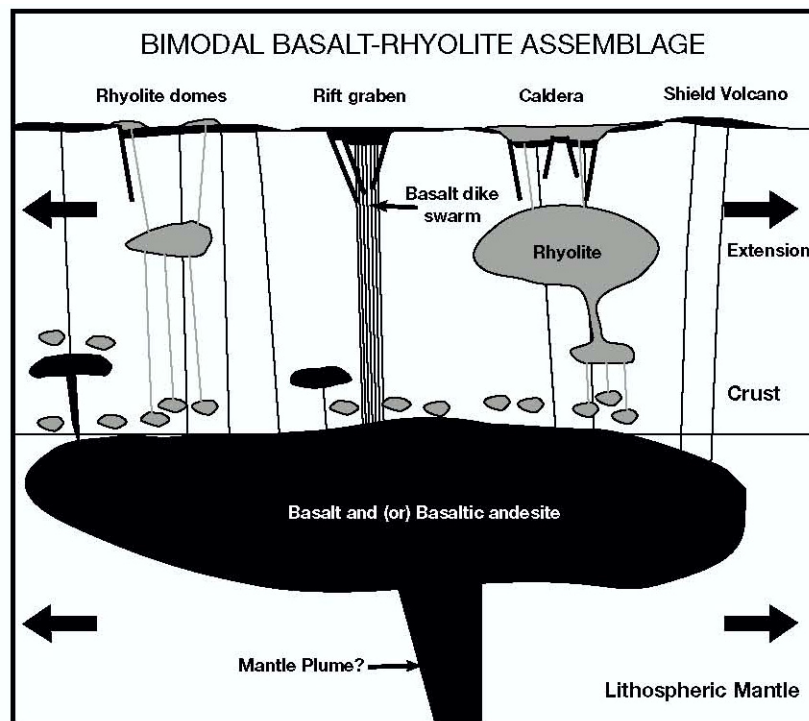


Figure 108. Conceptual model showing the magmatic-tectonic setting of the bimodal basalt-rhyolite assemblage in the northern Great Basin. This upwelling mafic body acts as a significant heat source to generate and drive felsic magmatism (John, 2001).

11.5 Mineral Resource Potential of the District

Science proceeds in using multiple working hypotheses to not overlook possibilities. This study has developed and attempts to explain multiple possible conclusions. Option 1: the anticipated “high-grade” roots of the epithermal system in the HGD exist; drilling needs to intercept these zones at greater depth. Option 2: the hot springs system at HGD was silica-flooded, extremely hot and short-lived; these conditions were not amenable to creating evolved roots.

Option 1:

The surface resource could be doubled or tripled, by drilling the additional silica bodies in the district. There is no mineralization away from silica bodies, the high grade vein targets are located underneath and as feeder structures to silica bodies. To sufficiently test the high-grade roots of the epithermal system, an intercept 800 to 1,000 ft (240 to 300 m) below the surface is necessary. All veins in the district are approximately vertical, the strongest zones need to be tested at sufficient depth for the epithermal system here.

Six targets are presented on the topographic map of the district (fig. 109); black lines indicate veins, the blue polygon indicates the significant mixing zone observed within the consolidated silica body. Results of this study give priority to testing the never-drilled mineralization of Discovery Mountain in the more eroded southwest portion of the HGD. Another priority for further exploration is the intriguing bowspring rhyolite dome (Tbs), located northwest of the HGD in Oregon; this large multi-lithic breccia is a good target and currently unheld.

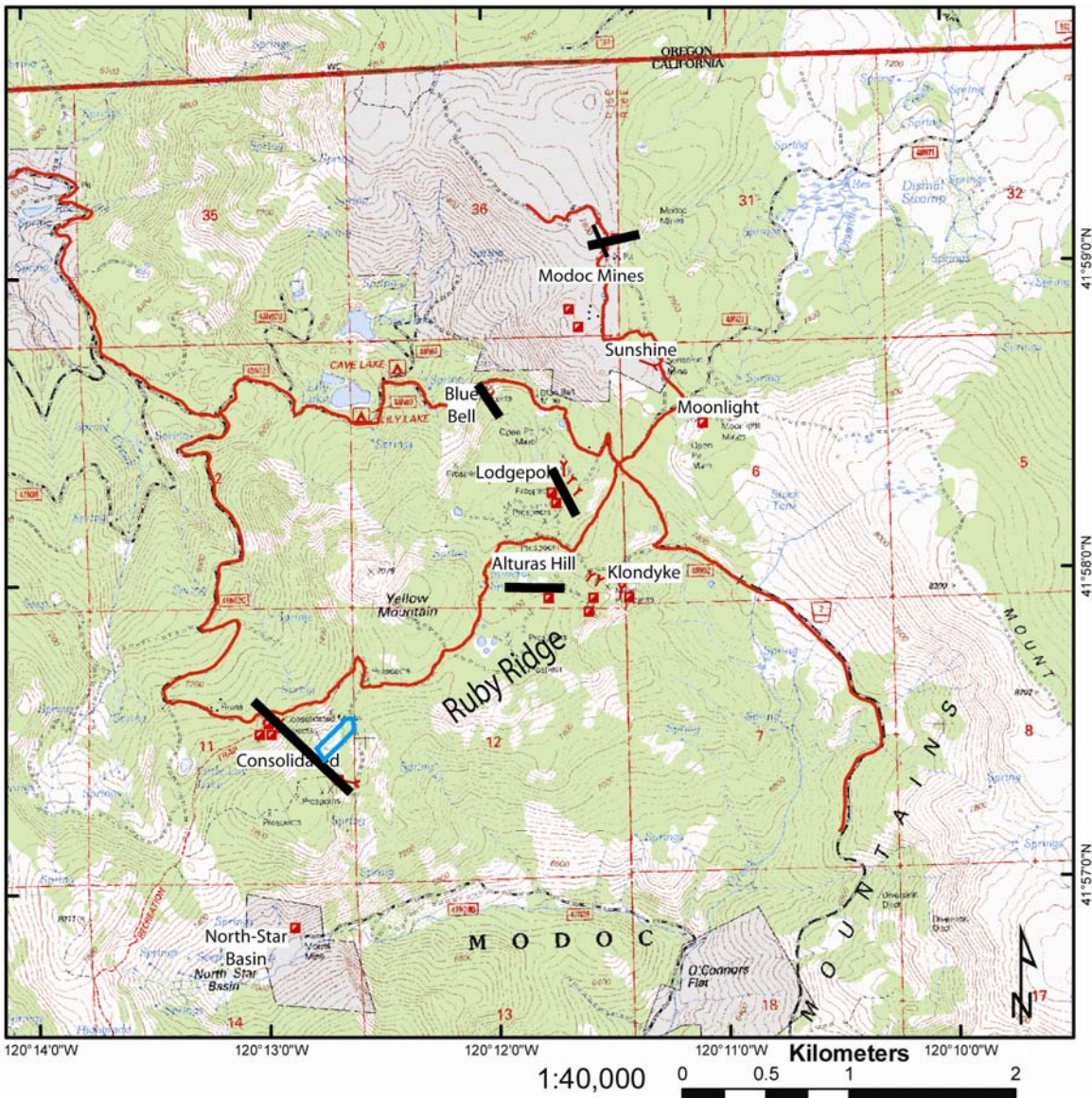


Figure 109. Priority targets for exploration drilling in the HGD. Black lines indicate vein, the blue polygon represents the strong mixing zone of Discovery Mountain.

Option 2:

Is precious metal mineralization in the HGD significant enough to warrant subsequent exploration? There are several factors that may be significant in discrediting the study area from further exploration:

A) Temperatures are high for the generic low-sulfidation system

- B) System was short-lived, only one period of epithermal activity, no overprinting
- C) A poorly developed plumbing system
- D) Vein trends are parallel to regional stress fields (prohibitive to opening)

11.6 Future Work

One hundred thousand ounces of gold reserves were established by Golden Phoenix Minerals (fig. 6), this resource could be enlarged with drilling of anomalous silica bodies at Sunshine and Consolidated. Further investigation of the multi-generational hydrothermal breccias is necessary to determine which sequence of hydrothermal/eruptive events is responsible for bonanza-grade mineralization. With the further exploration and development of precious metal mineralization in the study area it will be possible to attain more located samples and build more control into the district models.

The prominent mineralization on Discovery Mountain and encountered in the Consolidated camps deserves further investigation. Oxygen isotope analysis of Discovery Mtn. yields a major mixing anomaly in hydrothermal quartz mineralization between the Discovery Mtn Rhyolite (Tdmr) and the Consolidated Mtn Rhyolite Flows (Tcrf) (fig. 88). Vein trends in this portion of the district should be tested near this contact, as heavy metals may be concentrated in the mixing zone.

The Yellow Mountain Latite (Tym) is poorly understood and although largely un-mineralized this unit appears to host the felsic units of the auriferous phase of magmatism. This unit is dated in previous studies (Keats, 1985), but the sample is poorly located and dated by K/Ar methods (which are less accurate; Solid[K] to Gas[Ar] ratios are difficult to measure precisely). This unit should be dated again using $\text{Ar}^{40}/\text{Ar}^{39}$ methods on a GIS-located sample of unaltered Tym. This unit age should be open to interpretation until other data is available. Future studies should incorporate a detailed petrographic study of this unit, based upon systematically collected samples.

Silica Bodies should be systematically sampled for geochemical studies and mapped in detail to identify adularia showings. An adularia trend is a likely indicator for precious metal deposition and may indicate veining at depth.

A Gravimetric Survey of the Northern Warner Mountains will identify any rhyolite domes under basaltic (Tb) cover. Bouger corrected gravity (appendix 1, fig. 1-1, 1-2) shows anomalous highs within the rhyolite dome field, the lack of ground control points in this area could be a focus for additional studies.

The work of others (Hayashi et al., 2001; Ewers, 1994; Matsuhisa and Aoki, 1994; Ronde and Blattner, 1988) studying oxygen isotope interaction in epithermal precious metal systems can be a guide for future fluid transport studies of the HGD. The further analysis of quartz obtained from unaltered rhyolite domes in the area is necessary to definitively put constraints on the amount of mixing involved. As well, further investigation of sub-millimeter scale quartz banding analysis would be beneficial to better understand the hydrothermal system.

11.7 Qualification of Observations

In constructing models for the three main vein trends over the district there are some important issues regarding quality of data to address. The weakness of the data is the lack of available located samples; only the camps, themselves, are known. Samples are collected from the surface where limited bedrock is exposed; float in vegetated areas, silicified boulder fields and mine dumps were the source of sampling. Sample locations (within the vertical epithermal model) have been guided by mineralogical and textural observations described elsewhere in epithermal literature (Brathwaithe and Faure, 2002; Simmons and Browne, 2000; Hollister and Silberman, 1995; Cunningham et al., 1991; Berger and Henley, 1988; Hayba et al., 1985; Buchanan, 1981).

This study is limited in its effectiveness to create diagrams depicting mineralization in the HGD by the lack of available data to be used for ground control. Historic activities were shallow in nature and poor records are retained. If mining activities in the district had been more prolific, sampling could have been collected systematically from a vertical column of mineralization. If more expansive and systematic sampling were to be carried out, then spatial observations would have significantly more strength. This is the nature of geology.

11.8 Related Areas

Volcanic-Dome Hosted Epithermal Systems in Bolivia

Epithermal precious metal systems, hosted in rhyolite dome fields, have been studied and described in Bolivia by multiple geologists (Pinto-Vasquez, 1993; Cunningham et al, 1991). HGD mineralization is also hosted in a rhyolite dome field, therefore the models of emplacement and related mineralization are considered here. The main differences between these locations are host stratigraphy, tectonic environment, and dome size. Bolivian rhyolite domes are emplaced during cordilleran volcanism (Pinto-Vasquez, 1993), whereas rhyolites in the study area are part of a bimodal magmatic system related to lower crustal heating in a transitional tectonic setting. Rhyolite domes of the study area are significantly smaller in size and experience more complete silicification.

The Bolivian dome field is emplaced into a thick sequence of sandstones and conglomerates of a terrestrial basin. These rhyolite domes are emplaced in the model described below (fig. 110- A, B, C). Notable deposits (fig. 110, examples are given on left of main model figure) occur along the boundaries of and structures nearby to dome volcanism. Major ore deposits occur as disseminated deposits near the surface of these domes and as high grade veins located semi-conically to the dome.

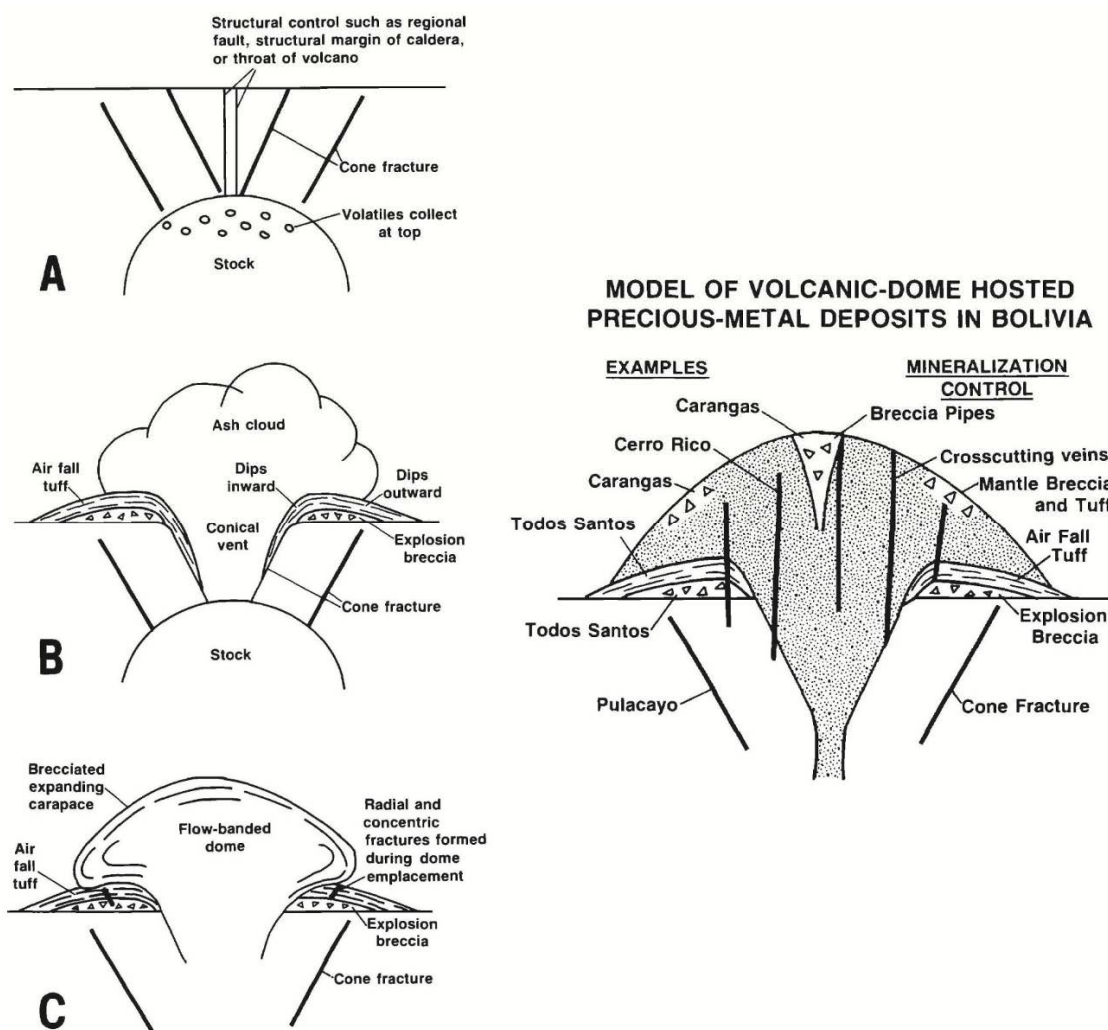


Figure 110. A, B, and C illustrate the sequence of events that takes place during emplacement of volcanic domes. The diagram, at right, provides the example deposit names and, symmetrically, the forms (i.e. vein, stockwork, breccias, etc.) that the mineralization has taken in the respective deposit. This diagram is taken from Cunningham et al., 1991.

Mineralization at Bodie, CA and Oatman, AZ

Geologic investigations on mined epithermal deposits have been carried out in numerous locations within the Great Basin of the western US. This section will discuss the models constructed from geologic observations of others at Bodie, California (fig. 111; Hollister and Silberman, 1995; Herrera, 1993; Berger, 1988; Berger and Silberman, 1985) and Oatman, Arizona (Drier, 1984; During and Buchanan, 1985, Buchanan, 1981). Numerous scientific

documents have been created regarding these locations and the main conclusions will be revisited in this section. The following statements summarize the main ideas which are presented in the indicated literature.

The geochemical signature observed at Bodie is dominated by As, Sb, B, Tl, and Hg. Fluid-inclusion and isotopic data from the low-sulfide, silver-gold veins at Bodie suggest a vein formation temperature of approximately 240°C from a low salinity, dominantly-meteoric derived fluid. Some inclusions in quartz within polymetallic veins display up to four daughter minerals and enrichment in $\delta^{18}\text{O}$ (Hollister and Silberman, 1995; Herrera, 1993; Berger, 1988; Berger and Silberman, 1985). HGD mineralization has a similar geochemical signature (elevated As, Hg, Mo, Sb, Se), but temperatures are significantly higher and $\delta^{18}\text{O}$ values indicate a significant magmatic component to mineralizing fluids.

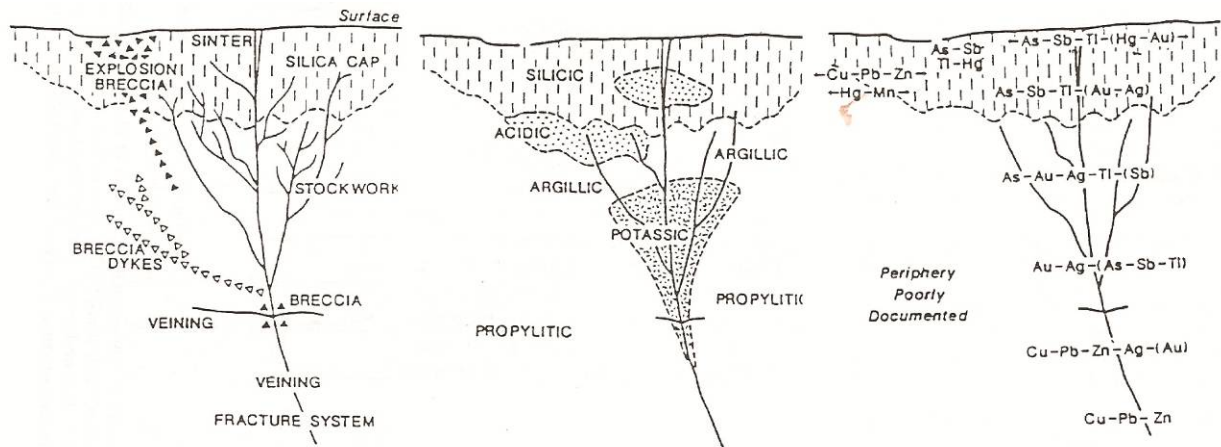


Figure 111. Working genetic models from the Bodie District, California. From left, structural features, alteration styles, and geo-chemical zoning. From Herrera et al. (1993) and modified from Berger and Eimon (1983).

Detailed descriptive classification, based on mineralogy, is made of the propylitic, illitic, and silicic alteration observed at Oatman, Arizona (Daring and Buchanan, 1984). Silicification is the dominant alteration style seen at Oatman. It is noted that permeable ash, tuff, and brecciated layers were much more susceptible to propylitic and illitic alteration than were dense,

hard latite flows. The ore bodies at Oatman contain quartz, calcite, adularia, chlorite, and electrum in fissure fillings. Gold tenor increases with adularia content in the vein (Drier, 1984; During and Buchanan, 1985, Buchanan, 1981). HGD mineralization is similar to that at Oatman; mineral assemblages, alteration zoning, and dominant silicification are characteristics the two districts share.

Observations from Ohaaki-Broadlands, NZ

The Ohaaki-Broadlands District, New Zealand, is an active hydrothermal precious metal system that has been examined thoroughly (Brathwaite and Faure, 2002; Simpson et al., 2001; Simmons and Browne, 2000; Ronde and Blattner, 1988). Many of the physical processes at work in epithermal systems are studied and quantified in this active hydrothermal field. The following observations are reported from New Zealand and are mentioned here to give insight into the conditions at play within the plumbing system of a hydrothermal system.

It is of interest to study the precipitation of gold in response to the fundamental process of boiling (phase separation) which occurs in dynamic hydrothermal systems. In the upper 3 to 5km of hydrothermal systems, pressures are approximated by a hot hydrostatic head; that is, a column of water (solution) at boiling point throughout its length. This implies a permeability connection to the surface. In reality, hydrothermal fluids in deep reservoirs are over-pressured by up to 15% due to an increase in pressure caused by buoyancy-induced upflow as well as restricted near-surface permeability. Thus, a hydrothermal fluid ascending buoyantly to the surface reaches a depth at which the confining hydrostatic pressure is equal to the equilibrium-saturated vapor pressure. At this point, boiling occurs and the two-phase conditions predominate as the fluid rises farther. The depth at which boiling commences varies greatly with the gas

content of the ascending fluid. The Ohaaki-Broadlands fluids are very gassy, and deep drilling indicates that boiling takes place at depths >2.5km (Brathwaite and Faure, 2002; Simpson et al., 2001; Simmons and Browne, 2000; Ronde and Blattner, 1988). Within the study area the hydrothermal system is six times shorter than that of Ohaaki-Broadlands. The short epithermal system in the HGD may have been too dynamic to develop well constrained levels where precious metal precipitation could concentrate.

Compilation Studies on Epithermal Systems

Numerous distinguished economic geologists have created summary documents to characterize epithermal metal deposits (John, 2001; Simmons and Browne, 2000; Romberger, 1993; Heald et al., 1987; Hayba et al., 1985; Silberman and Berger, 1985; Wilkins, 1984; Berger and Eimon, 1983; Buchanan, 1981). The evolution of ideas about the genesis of epithermal deposits is directly related to advances in scientific analytical capabilities available to geologic researchers. Significant advances in the understanding of these deposits began in the 1980's and have steadily continued. The purpose of this section is not to re-iterate the work of others, but to give weight to the value of proper literature review. The geologists cited here should be referenced by anyone hoping to understand epithermal mineralization. A table from Heald outlines the general characteristics of low-sulfidation (adularia-sericite) deposits, it has been modified below (table 12) to compare with mineralization of the HGD.

Table 12. This table compares characteristics from general low-sulfidation epithermal deposits (at left; Heald et al., 1985) with characteristics of the HGD (at right).

	<u>Adularia-Sericite</u>	<u>High Grade District</u>
Structural Setting	Structurally complex volcanic environments, commonly in calderas	Structurally complex, bimodal volcanic center in an extensional terrane
District Dimension (length: width)	Variable; some very large, usually 3:1 or greater	8km : 2km = 4:1
Host Rocks	Silicic to intermediate volcanic	Intermediate basement; felsic host suite, later mafics
Timing of ore and host	Ages of host and ore distinct (>1 m.y.)	Host and Mineralization dated at 14.4 ± 1 m.y.
Mineralogy	Argentite, tetrahedrite, tennantite, native silver and gold, base-metal sulfides Chlorite common Selenides present Mn gangue present No bismuthinite	Electrum, native gold, pyrite, Ag-sulfides, monazite, trace base-metal sulfides Mafic accessory Chlorite uncommon Selenides absent Mn gangue prominent No bismuthinite
Alteration	Sericitic to Argillic Supergene alunite Occasional kaolinite Abundant adularia	Propylitic to Argillic Intense silicification Abundant adularia
Temperature	200° to 300° C	170° to 350° C
Salinity	0 to 13 wt% NaCl eq.	2 to 21% NaCl eq.
Source of fluids	Dominantly meteoric	Magmatic and Meteoric

12. CONCLUSIONS

There are approximately 12 different rhyolite flows/domes related to the precious metal mineralization within the district, these domes impinge on one another and flow morphology is poorly constrained. Regional mapping was carried out in the hope of gaining insight into the felsic suite which hosts mineralization. Regional mapping defined 10 additional rhyolite flows/domes occurring along the trend of the district to the NW and SW, these units are easily mapped (comparatively) and a distinction is made between rhyolite texture and flow extent/morphology. Field observations, cataloguing the wide variety of quartz textures observed over the district are presented here.

Age dating, carried out in this study, supports the theory that a single epithermal system (~100,000 yrs) is responsible for the auriferous mineralization. Later faulting, due to extension, is accompanied by a barren phase of silicification (fig. 91, 92). Temperature data from this study indicates a higher formation temperature than is generally observed in epithermal systems (fig. 82). The hydrothermal activity in the study area is hypothesized to have emplaced shallowly and occurred as a short-lived, hot, chaotic system.

Nine general conclusions can be made about the epithermal system of the study area:

1. One mineralizing event (single period of epithermal activity)
2. Elevated concentrations of epithermal indicator elements
3. Hosted within rhyolite dome field
4. Syn-magmatic mineralization
5. Widespread, dominating silicification
6. District emplacement along NW-faults (magmatism and mineralization)

7. Compressed hydrostatic column
8. Elevated temperatures from general epithermal environments
9. Low-sulfidation system (no hybridization; no alunite)

13. REFERENCES

- Asrow, E., 1991, Mt. Vida Planning Area: Record of Decision, Modoc National Forest, USDA Forest Service, 25 p.
- Berger, B.R., Eimon, P.I., 1983, Conceptual models of epithermal precious-metal deposits, *in* Shanks, W.C.I., ed., Cameron volume on unconventional mineral deposits, New York Society of Mining Engineers, p. 191-205.
- Berger, B.R., Silberman, M.L., 1985, Relationship of trace-element patterns to geology in hot-spring type precious-metal deposits, *in* Berger, B.R., Bethke, P.M., ed., *Geology and Geochemistry of Epithermal Systems*, Volume 2: Reviews in Economic Geology.
- Berger, B.R., Henley, R.W., 1988, Advances in the Understanding of Epithermal Gold-Silver Deposits, with Special Reference to the Western United States, *in* Keays, R.R., Ramsay, W.R.H., Groves, D.L., ed., *The Geology of Gold Deposits: The Perspective in 1988*, Volume Economic Geology Monograph 6, p. 405-424.
- Blaske, A.R., Bornhorst, T.J., Brady, J.M., Marsh, T.M., McKittrick, S.A., 1991, The Shumake Volcanic Dome-Hosted Epithermal, Precious Metal Deposit, Western Mojave Desert, California: *Economic Geology*, v. 86, p. 1646-1656.
- Brathwaite, R.L., Faure, K., 2002, The Waihi Epithermal Gold-Silver-Base Metal Sulfide-Quartz Vein System, New Zealand: Temperature and Salinity Controls on Electrum and Sulfide Deposition: *Economic Geology*, v. 97, p. 269-290.
- Buchanan, L.J., 1981, Precious Metal Deposits Associated with Volcanic Environments in the Southwest, *in* Dickinson, W.R., Payne, W.D., ed., *Relations of Tectonics to Ore Deposits in the Southern Cordillera*, Volume 14, *Arizona Geological Society Digest*, p. 237-262.
- Camp, V.E., Ross, M.E., 2004, Mantle dynamics and genesis of mafic magmatism in the intermontane Pacific Northwest: *Journal of Geophysical Research*, v. 109, p. 14.
- Carmichael, I.S.E., Lange, R.A., Hall, C.M., Renne, P.R., 2006, Faulted and Tilted Pliocene olivine-tholeiite lavas near Alturas, NE California, and their bearing on the uplift of the Warner Range: *Geological Society of America Bulletin*, v. 118, p. 1196-1211.
- Colgan, J.P., 2005, Timing and Magnitude of Basin and Range Extension in Northwestern Nevada [Ph.D. Dissertation thesis], Stanford University.
- Colgan, J.P., Dumitru, T.A., McWilliams, M., Miller, E.L., 2006, Timing of Cenozoic volcanism and Basin and Range extension in northwestern Nevada: New constraints from the northern Pine Forest Range: *Geological Society of America Bulletin*, v. 118, p. 126-139.
- Conrad, J.E., McKee, E.H., Rytuba, J.J., Nash, J.T., Utterback, W.C., 1993, Geochronology of the Sleeper Deposit, Humboldt County, Nevada: Epithermal Gold-Silver Mineralization Following Emplacement of a Silicic Flow-Dome Complex: *Economic Geology*, v. 88, p. 317-327.
- Cox, J.W., 1985, Progress Report: High Grade Project, FMC Minerals Exploration Department, Pacific District, p. 24 p.

- Cox, J.W., 1985, High Grade Project Final Summary Report, FMC Minerals Exploration Department, Pacific District, p. 12 p.
- Cummings, M.L., Evans, J.G., Ferns, M.L., Lees, K.R., 2000, Stratigraphic and structural evolution of the middle Micoene synvolcanic Oregon-Idaho graben: Geological Society of America Bulletin, v. 112, p. 668-682.
- Cunningham, C.G., McNamee, J., Vasquez, J.P., and Ericksen, G.E., 1991, A Model of Volcanic Dome-Hosted Precious Metal Deposits in Bolivia: Economic Geology, v. 82, p. 415-421.
- Drier, J., 1984, Regional Tectonic Control of Epithermal Veins in the Western United States and Mexico, *in* Wilkins, J.J., ed., Gold and Silver Deposits of the Basin and Range Province Western USA, Volume 15, Arizona Geological Society Digest, p. 29-50.
- Duffield, W.A., McKee, E.H., 1986, Geochronolgy, structure, and basin-range tectonism of the Warner Range, northeastern California: Geological Society of America Bulletin, v. 97, p. 142-146.
- Durning, W.P., Buchanan, L.J., 1984, The Geology and Ore Deposits of Oatman, Arizona, *in* Wilkins, J.J., ed., Gold and Silver Deposits of the Basin and Range Province Western USA, Volume 15, Arizona Geological Society Digest, p. 141-158.
- Egger, A.E., Colgan, J.P., 2009, Evolution of the northwestern margin of the Basin and Range: Insights from new geologic mapping in northeastern California: Geological Society of America Annual Meeting 2009.
- Ewers, G.R., Mackenzie, D.E., Wyborn, D., Oversby, J.M., Andrew, A.S., 1994, Regional ^{18}O depletions in Igneous Rocks from the northern Drummond Basin, Queensland, Australia, and their Implications for Epithermal Gold Mineralization: Economic Geology, v. 89, p. 662-673.
- Faulds, J.E., Henry, C.D., Coolbaugh, M.F., Garside, L.J., Castor, S.B., 2005, Late Cenozoic strain field and tectonic setting of the northwestern Great Basin, western USA: Implications for geothermal activity and mineralization: Reno, Nevada, 1091-1104 p.
- Feinstein, M.N., Goodell, P.C., Hembree, D.R., 2008, An Epithermal Quartz Texture Case-Study: High-Grade District, California: Northwest Mining Association Conference.
- Fuis, G.S., Zucca, J.J., Mooney, W.D., Milkereit, B., 1987, A geologic interpretation of seismic-refraction results in northeastern California: Geological Society of America Bulletin, v. 98, p. 53-65.
- Goldfarb, R.J., Leach, D.L., Rose, S.C., Landis, G.P., 1988, Fluid Inclusion Geochemistry of Gold-Bearing Quartz Veins of the Juneau Gold Belt, Southeastern Alaska: Implications for Ore Genesis, *in* Keays, R.R., Ramsay, W.R.H., Groves, D.L., ed., The Geology of Gold Deposits: The Perspective in 1988, Volume Economic Geology Monograph 6, p. 363-376.
- Hayashi, K.I., Maruyama, T., Satoh, H., 2001, Precipitation of Gold in a Low-Sulfidation Epithermal Gold Deposit: Insights from a Submillimeter-scale Oxygen Isotope Analysis of Vein Quartz: Economic Geology, v. 96, p. 211-216.

- Hayba, D.O., Bethke, P.M., Heald, P., Foley, N.K., 1985, Geologic, Mineralogic, and Geochemical Characteristics of Volcanic-Hosted Epithermal Precious Metal Deposits, *in* Berger, B.R., Bethke, P.M., ed., *Geology and Geochemistry of Epithermal Systems*, Volume 2: Reviews in Economic Geology, p. 129-167.
- Heald, P., Foley, N.K., Hayba, D.O., 1987, Comparative Anatomy of Volcanic-Hosted Epithermal Deposits: Acid-Sulfate and Adularia-Sericite Types: *Economic Geology*, v. 82, p. 1-26.
- Herrera, P.A., Closs, L.G., Silberman, M.L., 1993, Alteration and geochemical zoning in Bodie Bluff, Bodie mining district, eastern California: *Journal of Geochemical Exploration*, v. 48, p. 259-275.
- Hill, J.M., 1915, High Grade District, Modoc County, California: *USGS Bulletin*, v. 594, p. 38-48.
- Hollister, V.F., Silberman, M.L., 1995, Silver-Gold and Polymetallic Quartz Veins in the Bodie Mining District, East-Central California - Are they related to a Porphyry Cu-Mo System at Depth?: *Arizona Geological Society Digest*, v. 20, p. 297-305.
- John, D.A., 2001, Micoene and Early Pliocene Epithermal Gold-Silver Deposits in the Northern Great Basin, Western United States: Characteristics, Distribution, and Relationship to Magmatism: *Economic Geology*, v. 96, p. 1827-1853.
- Keats, D.G., 1982, Preliminary: Geology and Mineralization in the High Grade District, Modoc County, California, Atlas Minerals Division, p. 14 p. + maps.
- Keats, D.G., 1985, Geology and Mineralization of the High Grade District, Modoc County, California, University of Oregon.
- Lerch, D.W., Klemperer, S.L., Egger, A.E., Colgan, J.P., Miller, E.L., 2009, The northwestern margin of the Basin-and-Range Province, part 1: Reflection profiling of the moderate-angle (~30°) Surprise Valley Fault: *Tectonophysics*, v. 488, p. 143-149.
- Martz, P.W., 1970, The geology of a portion of the northern Warner mountains, Modoc County, California [M.S. thesis], University of California-Davis.
- Matsuhisa, Y., Aoki, M., 1994, Temperature and Oxygen Isotope Variations During Formation of the Hishikari Epithermal Gold-Silver Veins, southern Kyushu, Japan: *Economic Geology*, v. 89, p. 1608-1613.
- Matthewson, D., 2003, Summary Geological and Exploration Report: High Grade District, Modoc County, California, Great American Minerals Exploration, p. 15 p. + appendices.
- Palmer, K.A., 1993, Caveat Emptor: The High Grade Mining District, 1866-1936 (Modoc County, Northeastern California), University of California at Santa Barbara.
- Pease, R.W., 1969, Normal Faulting and Lateral Shear in Northeastern California: *Geological Society of America Bulletin*, v. 80, p. 715-720.
- Peters, L., 2009, ⁴⁰Ar/³⁹Ar Geochronology Results for the High Grade District, NE Modoc County, California, New Mexico Geochronology Research Laboratory, p. 20 p.
- Pinto-Vasequez, J., 1993, Volcanic Dome-Associated Precious and Base Metal Epithermal

- Mineralization at Pulacayo, Bolivia: *Economic Geology*, v. 88, p. 697-700.
- Ponce, D.A., Glen, J.M.G., Egger, A.E., Bouligand, C., Watt, J.T., Morin, R.L., 2009, Geophysical Studies in the Vicinity of the Warner Mountains and Surprise Valley, Northeast California, Northwest Nevada, and Southern Oregon, US Geological Survey, p. 25.
- Reighard, K.F., 1988, Status Report and Proposed Exploration Drilling Program: High Grade Project, NEVORO regional program, p. 8 p.
- Roedder, E., 1984, Fluid Inclusions, Mineralogical Society of America, 644 p. p.
- Romberger, S.R., 1993, A Model for Bonanza Gold Deposits, *in* Sheahan, P.A., Cherry, M.E., ed., Ore Deposit Models: Volume 2, Geological Association of Canada, p. 77-86.
- Ronde, C.E.J., Blattner, P., 1988, Hydrothermal Alteration, Stable Isotopes, and Fluid Inclusions of the Golden Cross Epithermal Gold-Silver Deposit, Waihi, New Zealand: *Economic Geology*, v. 83, p. 895-918.
- Sampson, I., Anderson, A., Marshall, D., 2003, Fluid Inclusions: Analysis and Interpretation: Vancouver, Mineralogical Association of Canada, 374 p.
- Sander, M.V., Black, J.E., 1988, Crystallization and Recrystallization of Growth-zoned Vein Quartz Crystals from Epithermal Systems-Implications for Fluid Inclusion Studies: *Economic Geology*, v. 83, p. 1052-1060.
- Schuler, M., 1986, Summary Report: High Grade Project, Nord Resources Corporation, p. 8 p. + appendices.
- Schultz, D., 1991, Mt. Vida Planning Area: Final Environmental Impact Statement, Modoc National Forest, USDA Forest Service, p. 375 p.
- Seward, T.M., 1988, The Hydrothermal Chemistry of Gold and its Implications for Ore Formation: Boiling and Conductive Cooling as Examples, *in* Keays, R.R., Ramsay, W.R.H., Groves, D.L., ed., The Geology of Gold Deposits: The Perspective in 1988, Volume Economic Geology Monograph 6, p. 398-405.
- Silberman, M.L., Berger, B.R., 1985, Relationship of trace-element patterns to alteration and morphology in epithermal precious-metal deposits, *in* Berger, B.R., Bethke, P.M., ed., Geology and Geochemistry of Epithermal Systems, Volume 2: Reviews in Economic Geology.
- Simmons, S.F., Browne, P.R.L., 2000, Hydrothermal Minerals and Precious Metals in the Broadlands-Ohaaki Geothermal System: Implications for Understanding Low-Sulfidation Epithermal Environments: *Economic Geology*, v. 95, p. 971-999.
- Simpson, M.P., Mauk, J.L., Simmons, S.F., 2001, Hydrothermal Alteration and Hydrologic Evolution of the Golden Cross Epithermal Au-Ag Deposit, New Zealand: *Economic Geology*, v. 96, p. 773-796.
- Smith, R.B., Braile, L.W., 1994, The Yellowstone Hotspot: *Journal of Volcanology and Geothermal Research*, v. 61, p. 121-187.
- Stines, N.C., 1910, Hoag District, California: Mineral and Science Press, p. 382-386.

- Storms, W.H., 1912, The High Grade mining district: Mineral and Science Press, p. 273-275.
- Taubeneck, W.H., 1971, Idaho Batholith and Its Southern Extension: Geological Society of America Bulletin, v. 82, p. 1899-1928.
- Taylor, D.T., Hendrickson, R., 1998, High Grade Project Manual Resource Evaluation, Golden Phoenix Minerals, p. 12 p.
- Tucker, W.B., 1919, Modoc County, High Grade mining district, v. 15, p. 241-250.
- Van Buer, N.J., Miller, E.L., Dumitru, T.A., 2009, Early Tertiary paleogeologic map of the northern Sierra Nevada batholith and the northwestern Basin and Range.: Geology, v. 37, p. 371-374.
- Vance, R.B., Shwertfeger, T.R., 2001, 2000 Annual Exploration Report: High Grade Project, Newmont Mining Corp., p. 11 p.
- Wilkins, J.J., 1984, The Distribution of Gold- and Silver-bearing Deposits in the Basin and Range Province, Western United States, *in* Wilkins, J.J., ed., Gold and Silver Deposits of the Basin and Range Province Western USA, Volume 15, Arizona Geological Society Digest, p. 1-27.

14. APPENDICES

These appendices contain the complete datasets acquired in this study for all methods used in this dissertation. This appendix should be actively consulting in the reading of this document

The numbering system of figures in appendix 1 was chosen to accommodate the word processing software used in the creation of this document. There cannot be two “figure 1” in a document, therefore the prefix “1-“ is given to all figures in appendix 1.

Appendix 2 contains the regional and district geologic maps created in this study.

Appendix 3 contains all geochemical data and the manipulated datasets, along with additional statistical and PC components; all data here is discussed in chapter 6.

14.1 Appendix 1

	page
Figure 1-1. Magnetic and gravity data.....	200
Figure 1-2. Gravity data.....	201
Figure 1-3. Sample drill log from Freeport McMoran in 1984.....	202
Figure 1-4. Sample drill log from Nord Resources in 1982.	203
Figure 1-5. Sample drill log from Golden Predator drilling in 2009.	204
Figure 1-6. Sample drill-hole profile constructed from RC-drilling in 2009.	205
Figure 1-7. Histograms for (Bi, Ca, Cd, Ce, Co, Cr) multi-element analysis.....	206
Figure 1-8. Histograms for (Cs, Cu, Fe, Ga, Ge, Hf) multi-element analysis	207
Figure 1-9. Histograms for (Hg, In, K, La, Li, Mg) multi-element analysis	208
Figure 1-10. Histograms for (Mn, Mo, Nb, Na, Ni, P) multi-element analysis.....	209
Figure 1-11. Histograms for (Pb, Rb, Sb, Sc, Se, Sn) multi-element analysis	210
Figure 1-12. Histograms for (Sr, Te, Th, Ti, Tl, U) multi-element analysis	211
Figure 1-13. Histograms for (V, W, Y, Zn, Zr) multi-element analysis.....	212
Figure 1-14. Outlier histograms for (Ag, Al, As, Au, Ba, Be) multi-element analysis	213
Figure 1-15. Outlier histograms for (Bi, Ca, Cd, Ce, Co, Cr) multi-element analysis	214
Figure 1-16. Outlier histograms for (Cs, Cu, Fe, Ga, Ge, Hf) multi-element analysis.....	215
Figure 1-17. Outlier histograms for (Hg, K, La, Li, Mg) multi-element analysis	216
Figure 1-18. Outlier histograms for (Mn, Mo, Nb, Na, Ni, P) multi-element analysis	217
Figure 1-19. Outlier histograms for (Pb, Rb, Sb, Sc, Se, Sn) multi-element analysis.....	218
Figure 1-20. Outlier histograms for (Sr, Te, Th, Ti, Tl, U) multi-element analysis	219

Figure 1-21. Outlier histograms for (V, W, Y, Zn, Zr) multi-element analysis	220
Figure 1-22. Principal component (PC) for surface samples dataset, Factor 1.....	221
Figure 1-23. PC for surface samples dataset, Factor 2.	221
Figure1- 24. PC for surface samples dataset, Factor 4.	222
Figure 1-25. PC for surface samples dataset, Factor 5.	222
Figure 1-26. PC for surface samples dataset, Factor 6.	223
Figure 1-27. PC for surface samples dataset, Factor 7.	223
Figure 1-28. PC for surface samples dataset, Factor 8.	224
Figure 1-29. Natural Neighbor modeling of factor 1.....	225
Figure 1-30. Natural Neighbor modeling of factor 2.....	226
Figure 1-31. Natural Neighbor modeling of factor 4.....	227
Figure 1-32. Natural Neighbor modeling of factor 5.....	228
Figure 1-33. Natural Neighbor modeling of factor 6.....	229
Figure 1-34. Natural Neighbor modeling of factor 7.....	230
Figure 1-35. Natural Neighbor modeling of factor 8.....	231
Figure 1-36. Map of Ag outlier values.....	232
Figure 1-37. Map of Al% outlier values.	233
Figure 1-38. Map of As outlier values	234
Figure 1-39. Map of Ba outliers values.	235
Figure 1-40. Map of Bi outlier values.....	236
Figure 1-41. Map of Co outlier values.....	237
Figure 1-42. Map of Fe% outliers values.....	238
Figure 1-43. Map of Li outliers values	239

Figure 1-44. Map of Mn outlier values.....	240
Figure 1-45. Map of P outlier values	241
Figure 1-46. Map of Sb outlier values	242
Figure 1-47. Map of Se outliers values.....	243
Figure 1-48. Map of Te outliers values.....	244
Figure 1-49. Map of Tl outlier values.....	245
Figure 1-50. Map of outlier values for Cu, Zn, Pb, Hg, and U.....	246
Figure 1-51. Electron Microprobe (EM) images and paragenetic observations.....	247
Figure 1-52. EM images and paragenetic observations, Section: Con_6, E&F	248
Figure 1-53. EM images and paragenetic observations, Section: Con_6, G&H	249
Figure 1-54. EM images and paragenetic observations, Section: Con_7, A&B.....	250
Figure 1-55. EM images and paragenetic observations, Section: Con_7, C&D.....	251
Figure 1-56. EM images and paragenetic observations, Section: Con_7, E&F	252
Figure 1-57. EM images and paragenetic observations, Section: Con_9, A&B.....	253
Figure 1-58. EM images and paragenetic observations, Section: DS_2a, A&B	254
Figure 1-59. EM images and paragenetic observations, Section: DS_2a, C&D	255
Figure 1-60. EM images and paragenetic observations, Section: DS_2a, E&F	256
Figure 1-61. EM images and paragenetic observations, Section: KAB-1, A&B	257
Figure 1-62. EM images and paragenetic observations, Section: KAB-1, C&D	258
Figure 1-63. EM images and paragenetic observations, Section: KAB-1, E&F	259
Figure 1-64. EM images and paragenetic observations, Section: LM-1, A&B.....	260
Figure 1-65. EM images and paragenetic observations, Section: LM-3a, A&B	261
Figure 1-66. EM images and paragenetic observations, Section: LM-3a, C&D	262

Figure 1-67. EM images and paragenetic observations, Section: MMS-1d, A&B.....	263
Figure 1-68. EM images and paragenetic observations, Section: MMS-1d, C&D.....	264
Figure 1-69. EM images and paragenetic observations, Section: MMS-1f, A&B	265
Figure 1-70. EM images and paragenetic observations, Section: MMS-1h, A&B.....	266
Figure 1-71. EM images and paragenetic observations, Section: SS-2, A&B	267
Figure 1-72. EM images and paragenetic observations, Section: SS-3, A&B	268
Figure 1-73. Quantitative Microprobe (QM) point scans on electrum	269
Figure 1-74. QM point scans on electrum grains from Sunshine Vein, 3	270
Figure 1-75. QM point scans on electrum grains from Sunshine Vein, 4	271
Figure 1-76. QM point scans on electrum grains from Sunshine Vein, 5	272
Figure 1-77. QM line traverses on Fe/Ag nodules from Consolidated, 2.....	273
Figure 1-78. QM line traverses on Fe/Ag nodules from Consolidated, 3.....	274
Figure 1-79. QM line traverses on Fe/Ag nodules from Consolidated, 4.....	275
Figure 1-80. Fluid inclusion data from the indicated samples.....	276
Figure 1-81. Fluid inclusion data from the indicated samples.....	277
Figure 1-82. Fluid inclusion data from the indicated samples.....	278
Figure 1-83. Fluid inclusion data from the indicated samples.....	279
Figure 1-84. Reconnaissance of indicated thick-sections	280
Figure 1-85. Reconnaissance of indicated thick-sections	281
Figure 1-86. Reconnaissance of indicated thick-sections	282
Figure 1-87. Reconnaissance of indicated thick-sections	283
Figure 1-88. Discovery Mountain epithermal model with 21 element geochemistry	284
Figure 1-89. Ruby Ridge - Klondyke epithermal model with 21 element geochemistry	284

Figure 1-90. Sunshine-Modoc epithermal model with 21 element geochemistry	285
---	-----

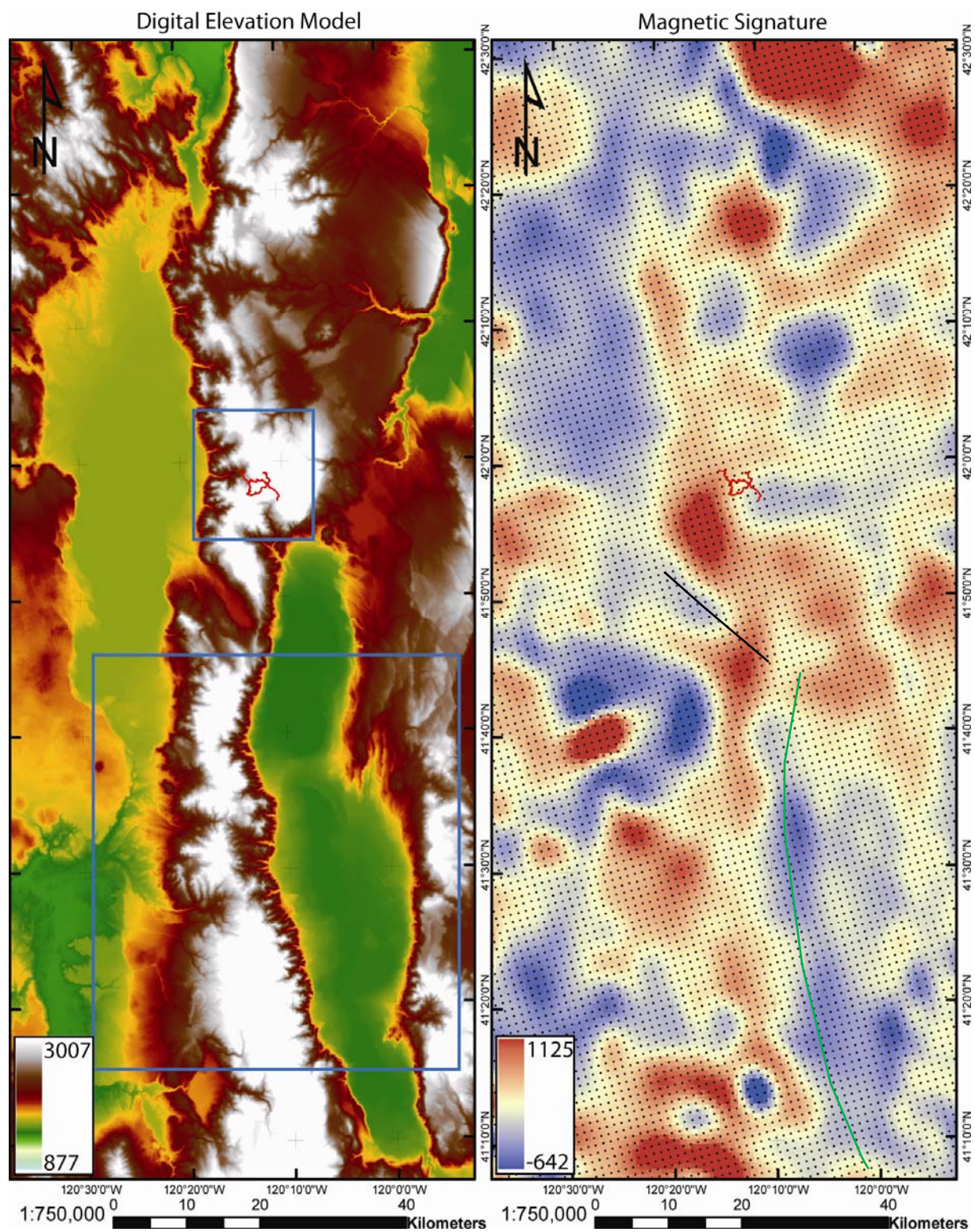


Figure 112-1. The DEM (left) gives geographic context to magnetic and gravity data. Blue boxes indicate the extent of detailed geologic mapping (Feinstein, North; Egger and Colgan, South). Magnetic data is displayed using a spherical kriging model. The eastern boundary fault of the Warner Mtn. Horst Block is distinguishable (green), as is Fandango Pass (black).

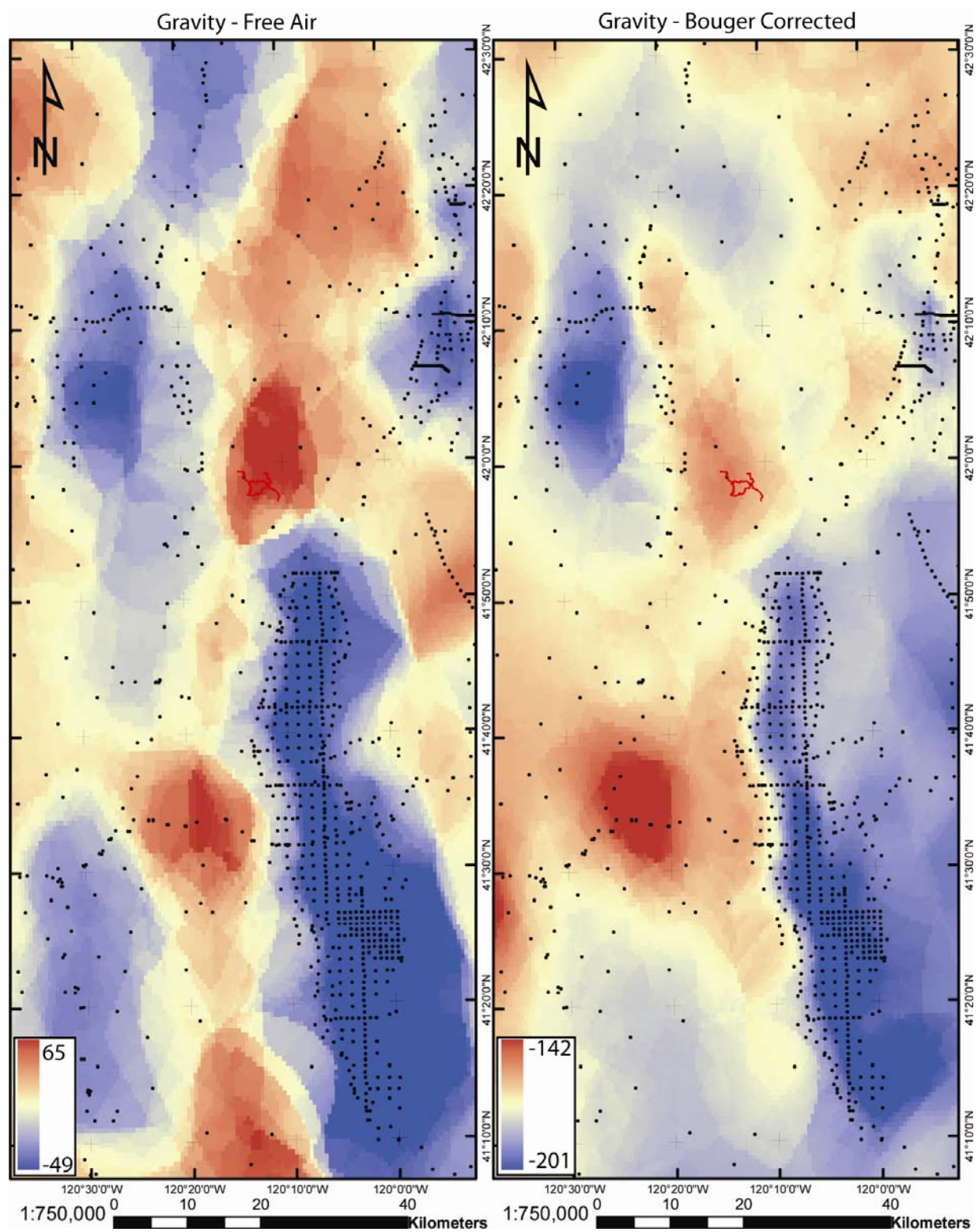


Figure 1-2. Gravity data is modeled from the indicated control points using a spherical kriging method. Free Air gravity data mimics the topography seen in the DEM (fig. 1-1). Bouguer Corrected data displays an anomalous high, correlating with felsic sequence of the HGD. Detailed gravimetric studies may define covered rhyolite domes.

ANOMALY					HOLE NO. 84H-13		PAGE 2 OF 3	
SAMPLE NUMBER	FM	PPM Au	ROAST AA OZ/T	COLO CN OZ/T	DEPTH FEET	GRAPHIC LOG	DESCRIPTION	
					0-78		rhyolite, it's gray and grayish orange (color variations) (see 23) typical granitic - gray has minor, less sig. orange in it (d.s.) narrow glt zones, (unpy) vults common, some mbs, maybe > vults & mbs in higher grade intervals, rock is moderately siliceous (massive area due to alteration)	
33836		.21			10	~		
37		.10			15	~		
38		.11			20	~		
39		.47			25	~		
40		.15			30	~		
41		.14			35	~		
42		.28			40	~		
43		.15			45	~		
44		.16			50	~		
45		.13			55	~		
46		.31			60	~		
47		1.88			65	~		
48		.29			70	~		
49		.16			75	~		
50		.12			80	~	tuff - variable lithology, overall siliceous, some less siliceous rhyolite, some color dominant, also to some extent some lithic fragments	
51		.32			85	~		
52		.48			90	~		
53		.23			95	~		
33854		.21			100	~		

Figure 1-3. Sample drill log from Freeport McMoran in 1984.

DRILL HOLE LOG

Page 1 of 2

Logged by M. Schuler

W. Harrison

Coordinates 11145 1341W

Sec. 12 TNSHP 47N RNG 15E

County Modoc

Type Drill Reverse Circulation

DRILL HOLE NO. HGDH-4

PROJECT High Grade

STATE California

Date Started August 12, 1982

Date Bottomed August 14, 1982

Collar Elev. 7820

Inclination 60°

Bearing S69°W

Length 375 feet

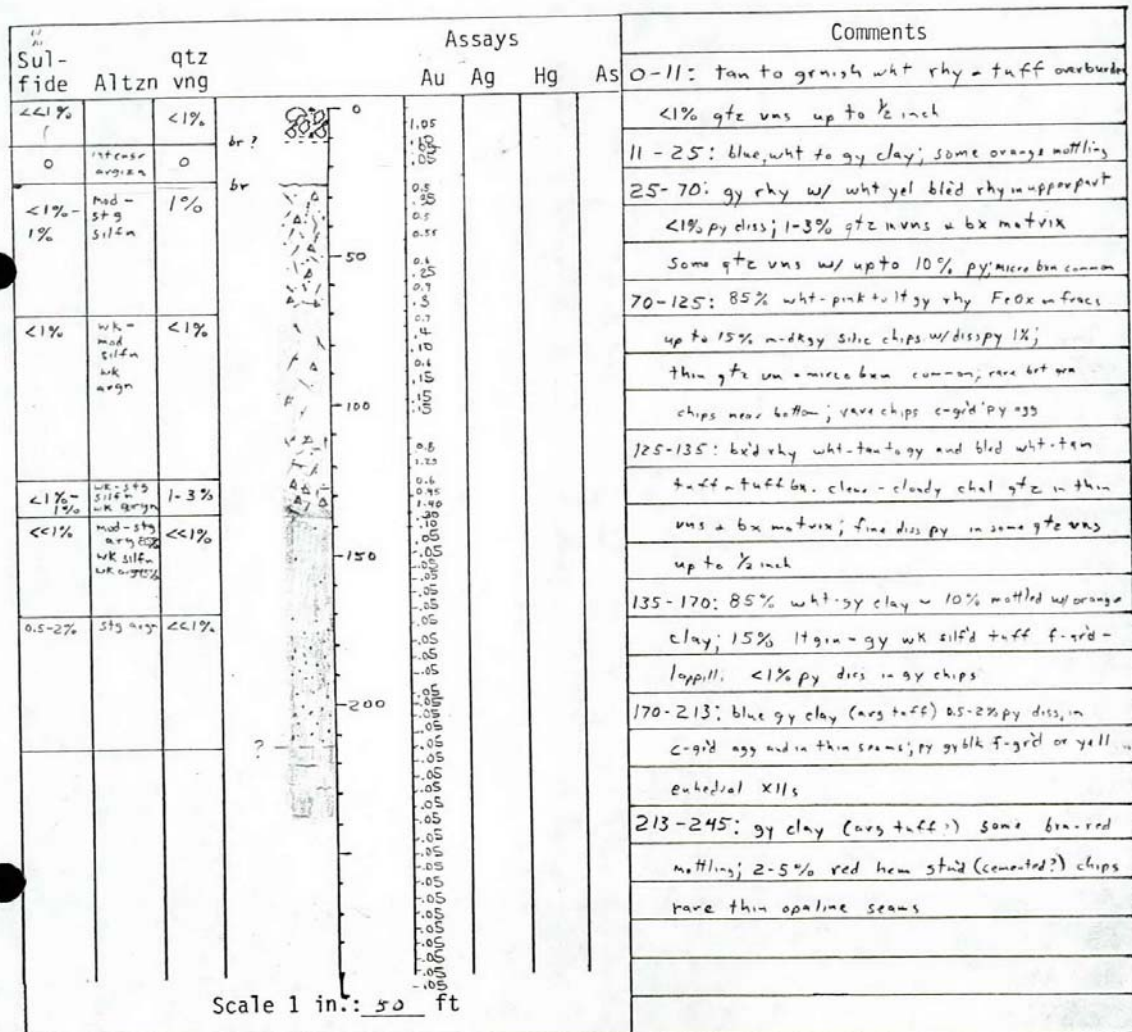



Figure 1-4. Sample drill log from Nord Resources in 1982.



GOLDEN PREDATOR GOLD EXPLORATION
RC DRILLHOLE LOGGING FORM

LOGGED BY: MF HOLE ID: GPER014 DATE: _____

FROM	TO	COLOR	REGCODE	ROCKCODE	MODIFYCODE	GRAIN SIZE	SULF	SULF PERC	VEIN TYPE	VEIN PERC	STRUCTURE	ALTER1	ALTER2	ALT1 INT	ALT2 INT	MIN1	MIN PERC	MIN2	MIN2 PERC	OXYDE CODE	ORIGINAL CODE
255	260	gg		tuf								Si	3							UN	
260	262.5	gg		tuf					QV	2		Si	3							OX	
262.5	270	gg		tuf								Si	3							UN	
270	277.5	gg		tuf			Py	2				PR	3	Si	2	CL	10			PO	
277.5	282.5	gg		tuf			Py	1				Si	3							PO	
282.5	285	mod		tuf	bx				QV	30		Si	3							OX	
285	287.5	gg		tuf	bx		Py	2	QV	5		Si	3	GO	2	mn	2			OX	
287.5	290	gg		tuf			Py	5	QV	10		Si	3	GO	3	mn	5			OX	
290	300	gg		tuf								Si	3			mn	1			OX	
300	302.5	gg		tuf					QV	10		Si	3	Ar	2	mn	3			OX	Bleached host - Stackwork
302.5	305	gg		tuf					QAD	10		Si	3	Ar	2	mn	2			OX	Bleached host - Vein
305	307.5	gg		tuf					QV	3		Si	3	Ar	2					OX	Bleached host - end Vein
307.5	310	gg		tuf								Si	3	GO	2	mn	3			OX	
310	312.5	gg		tuf					QV	5		Si	3	GO	3	mn	5			OX	
312.5	315	gg		tuf								Si	3	GO	3	mn	5			OX	

Figure 1-5. Sample drill log from Golden Predator drilling in 2009.

DRILL HOLE SUMMARY SHEET

Hole# GPR004 Property GOLDEN RIDGE County Modoc State Ca
 T. R. S. Coord: N, E Elev.
 Depth 160 Bearing N 20 E Incl. - 45 Date 6-23-09 Logged by D.R. Hembree
 Type Drilling RVC Drill Co. DRIFT Driller
 Full Return Hammer

CROSS SECTION

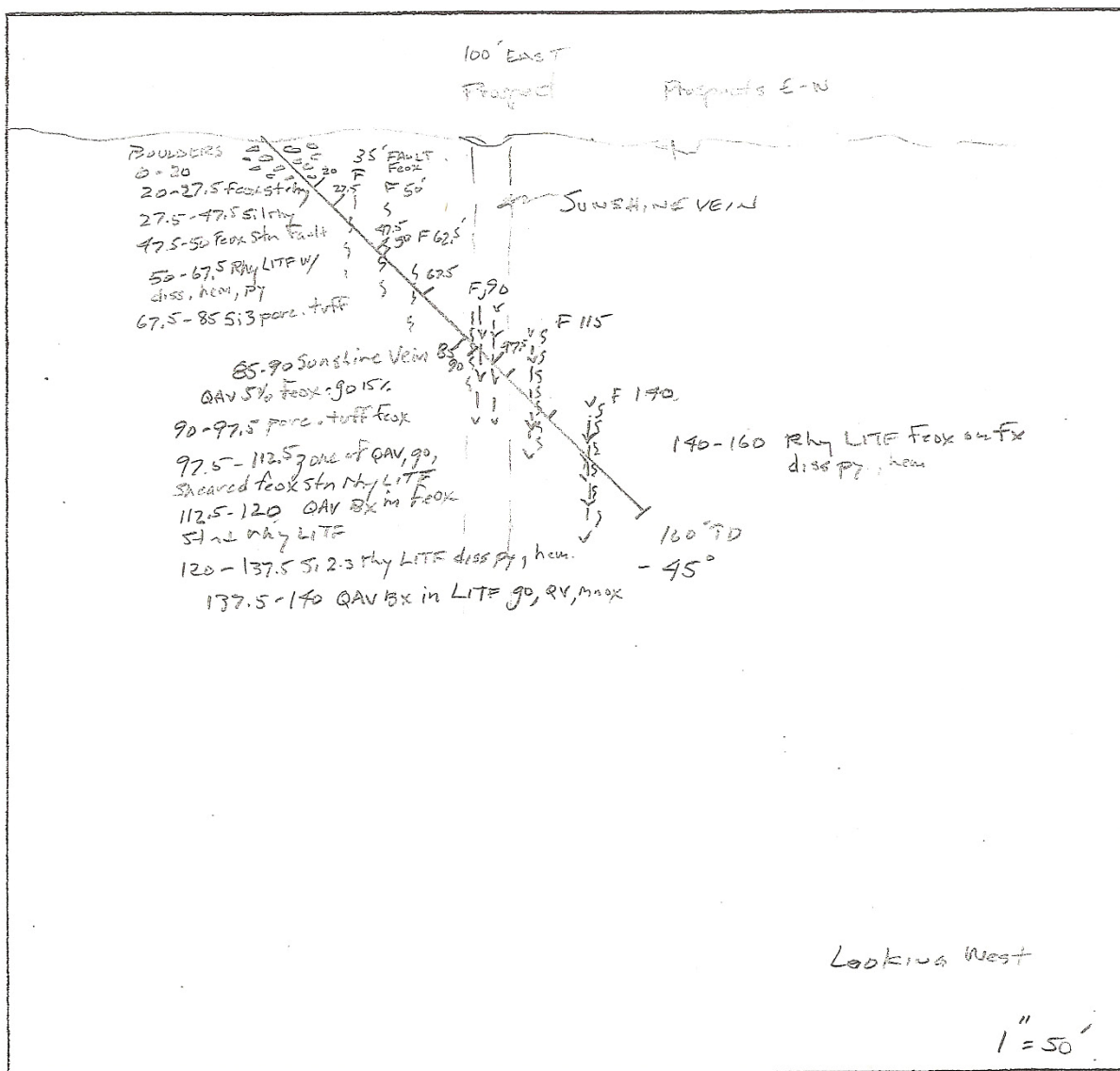


Figure 1-6. Sample drill-hole profile constructed from RC-drilling in 2009.

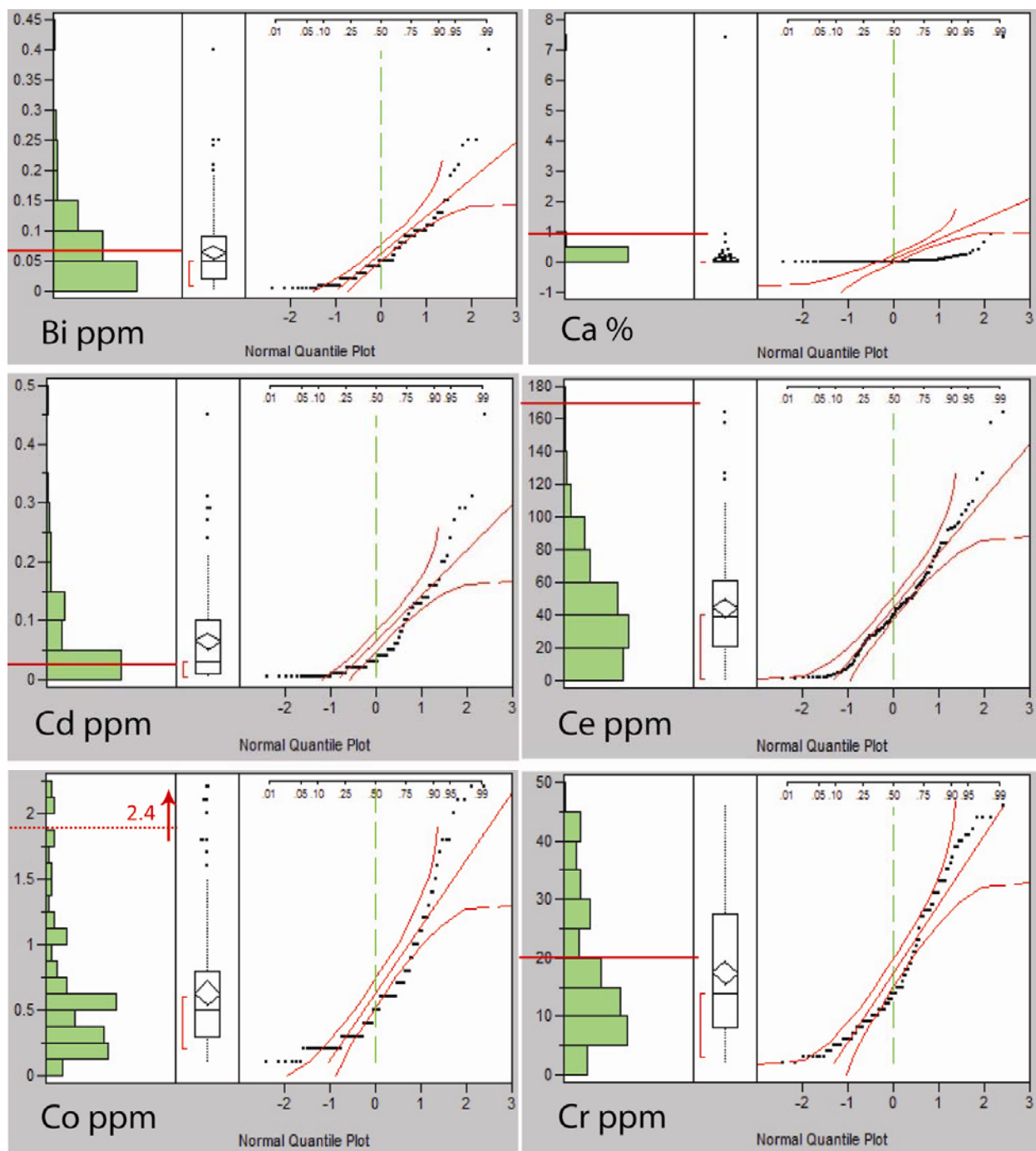


Figure 1-7. Histograms for 6 (Bi, Ca, Cd, Ce, Co, Cr) multi-element analysis of surface samples, outliers removed. Average granitic composition is indicated by the red line.

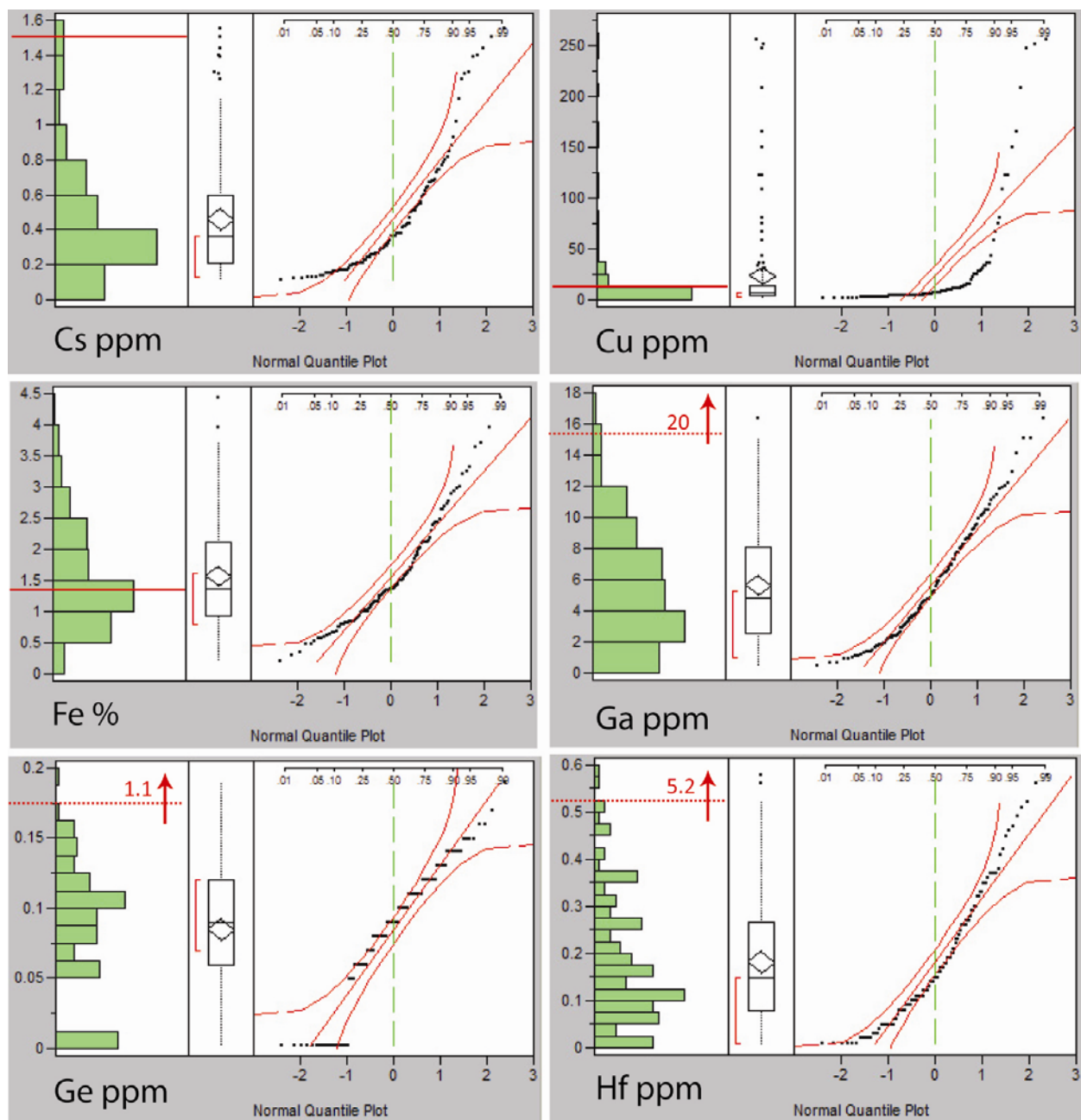


Figure 1-8. Histograms for 6 (Cs, Cu, Fe, Ga, Ge, Hf) multi-element analysis of surface samples, outliers removed. Average granitic composition is indicated by the red line.

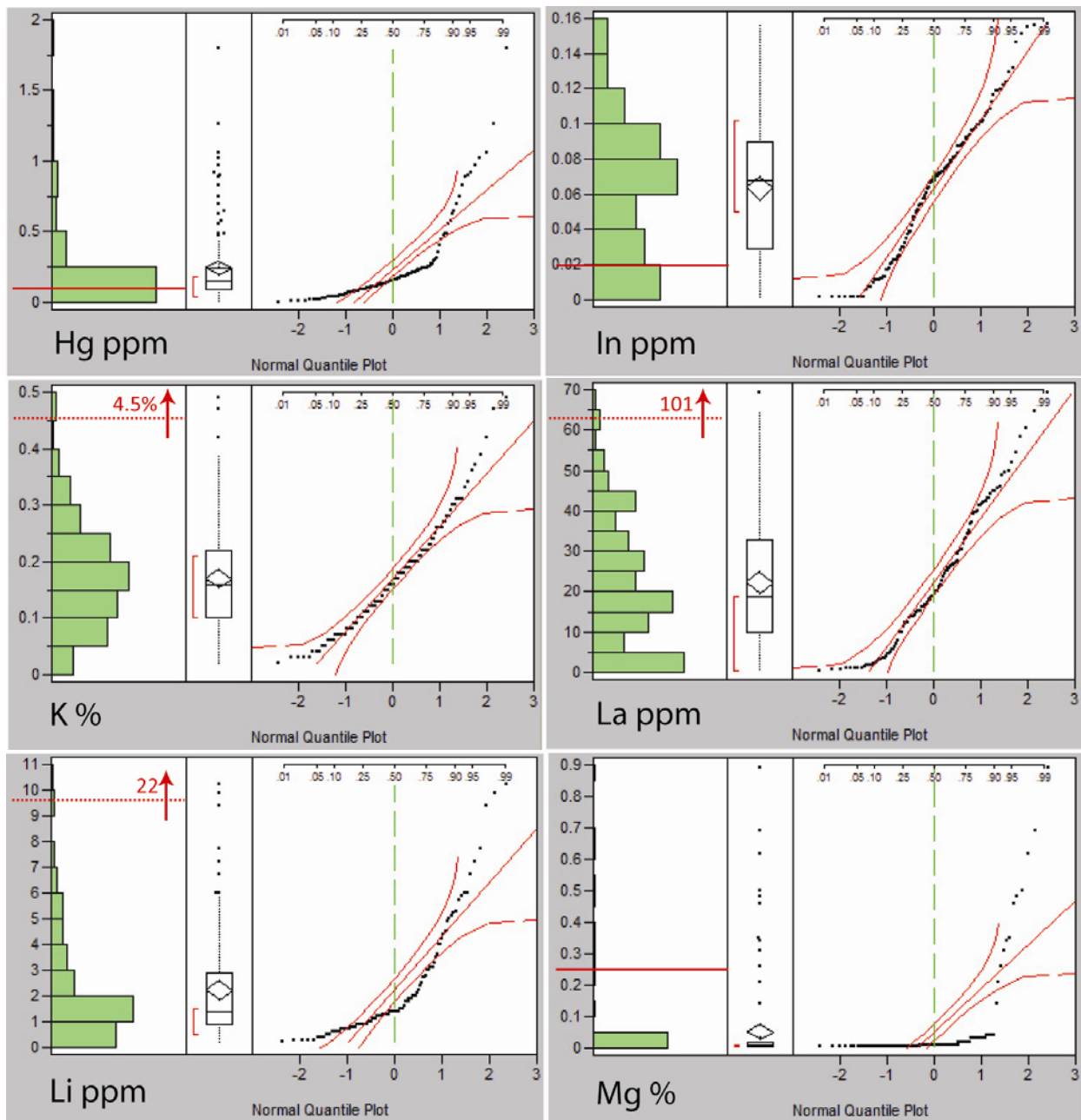


Figure 1-9. Histograms for 6 (Hg, In, K, La, Li, Mg) multi-element analysis of surface samples, outliers removed. Average granitic composition is indicated by the red line.

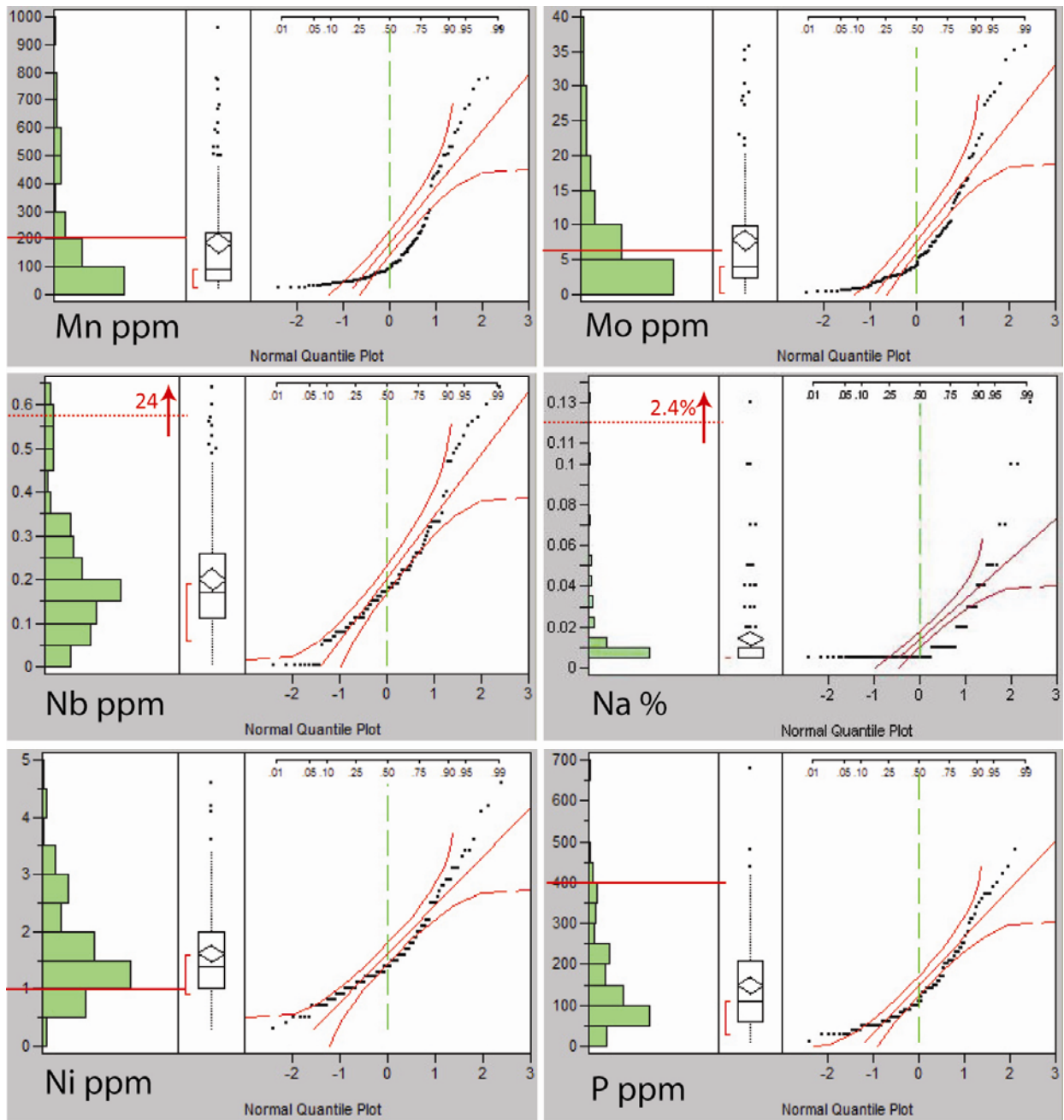


Figure 1-10. Histograms for 6 (Mn, Mo, Nb, Na, Ni, P) multi-element analysis of surface samples, outliers removed. Average granitic composition is indicated by the red line.

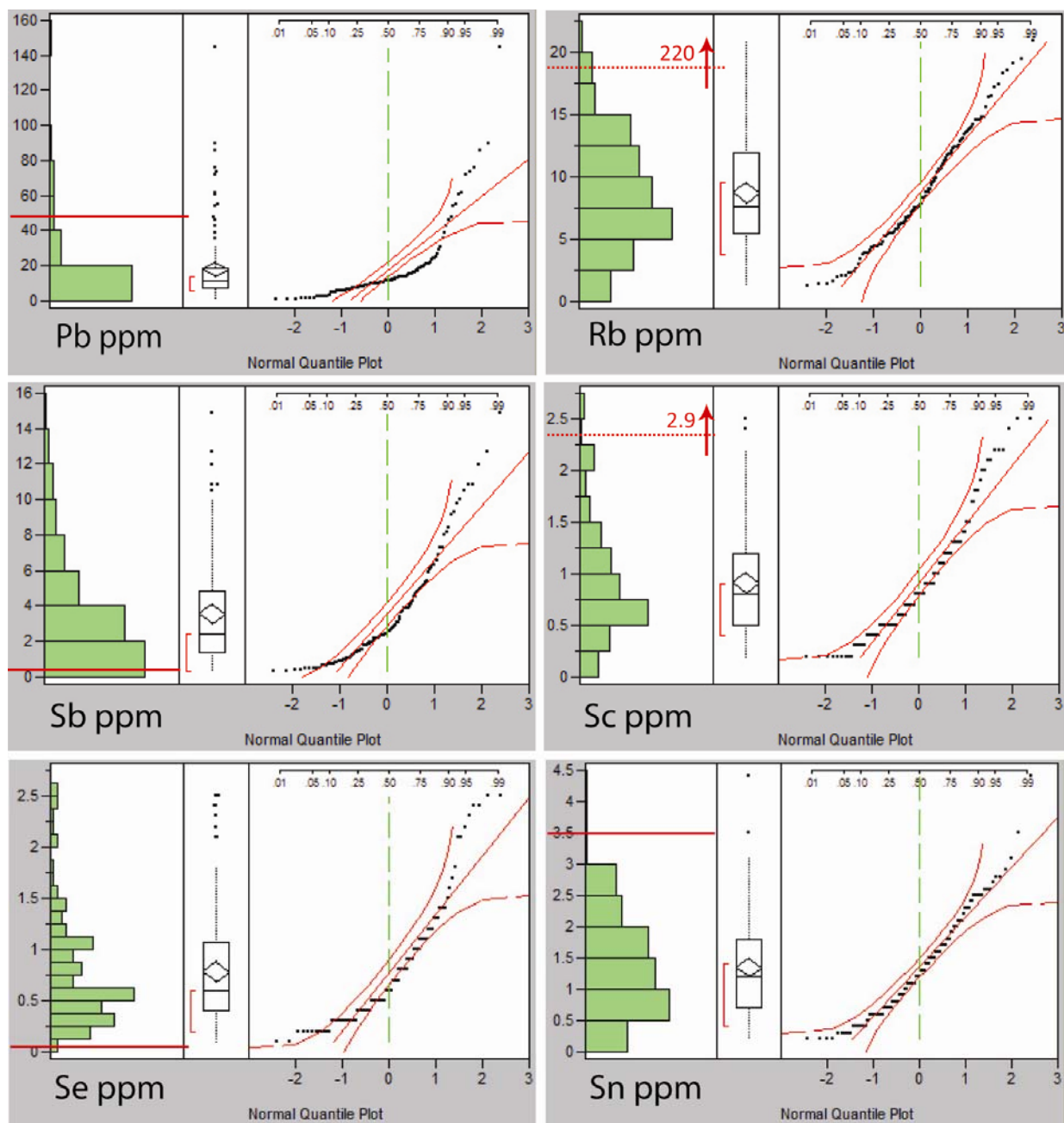


Figure 1-11. Histograms for 6 (Pb, Rb, Sb, Sc, Se, Sn) multi-element analysis of surface samples, outliers removed. Average granitic composition is indicated by the red line.

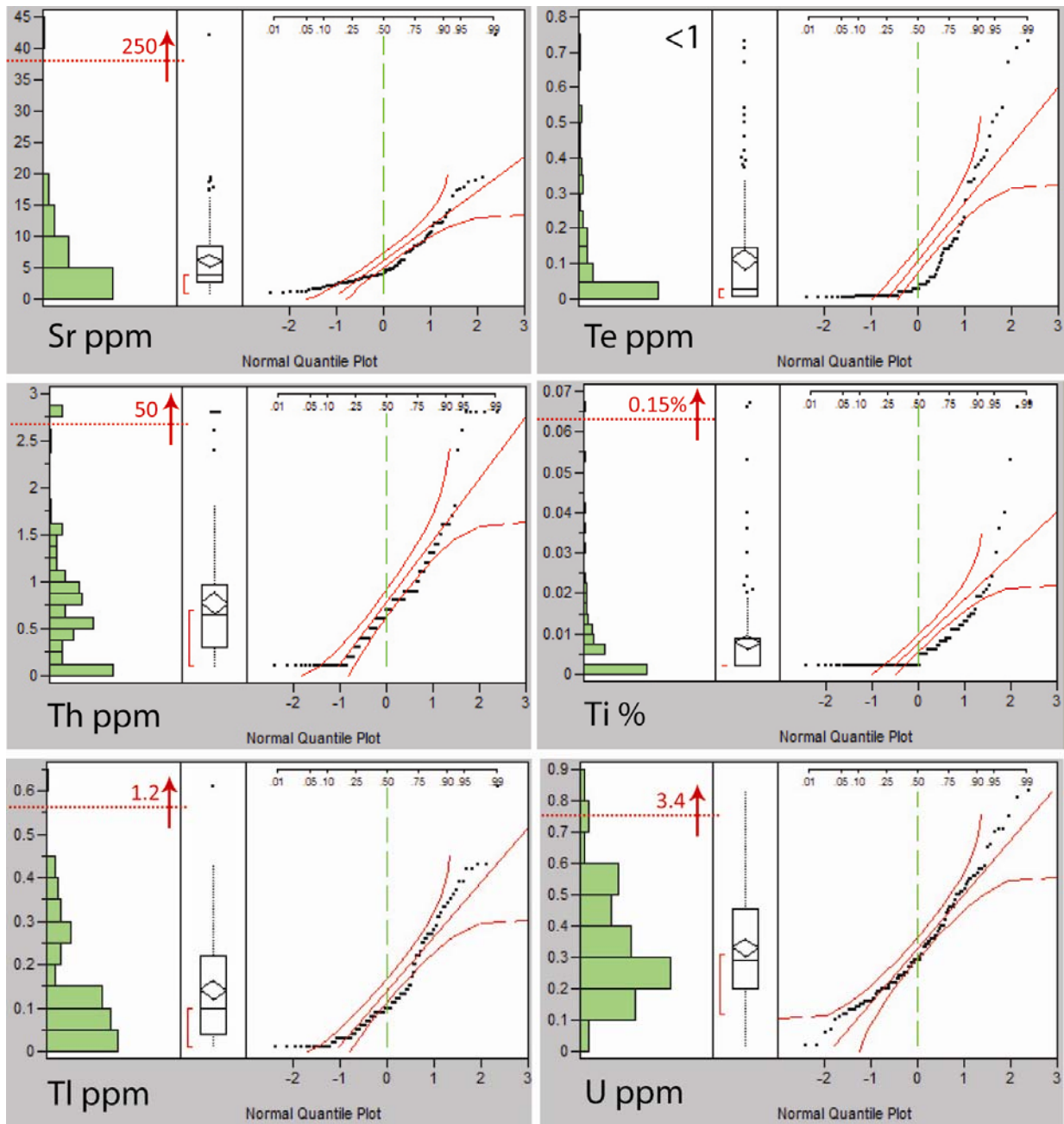


Figure 1-12. Histograms for 6 (Sr, Te, Th, Ti, Tl, U) multi-element analysis of surface samples, outliers removed. Average granitic composition is indicated by the red line.

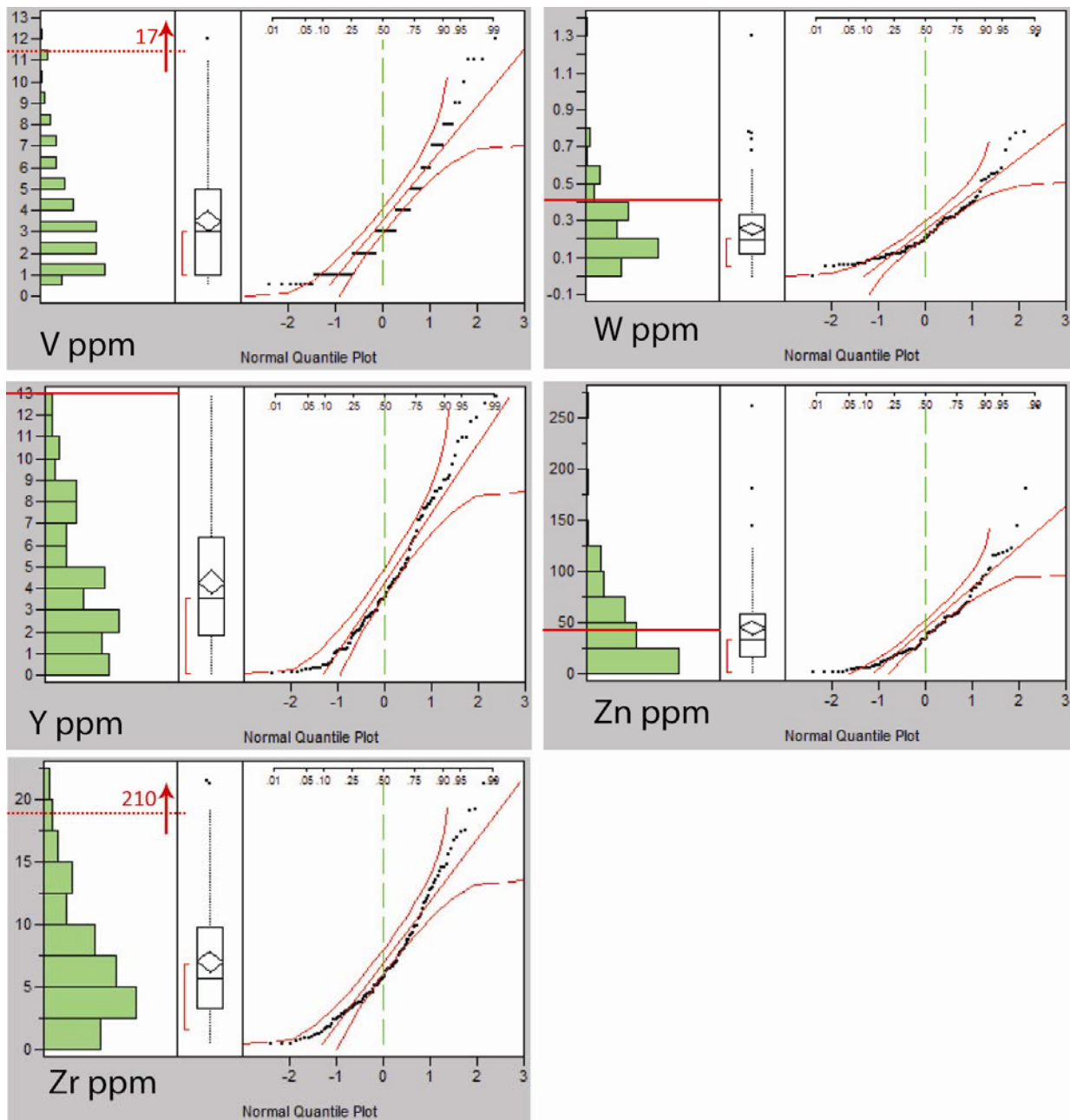


Figure 1-13. Histograms for 5 (V, W, Y, Zn, Zr) multi-element analysis of surface samples, outliers removed. Average granitic composition is indicated by the red line.

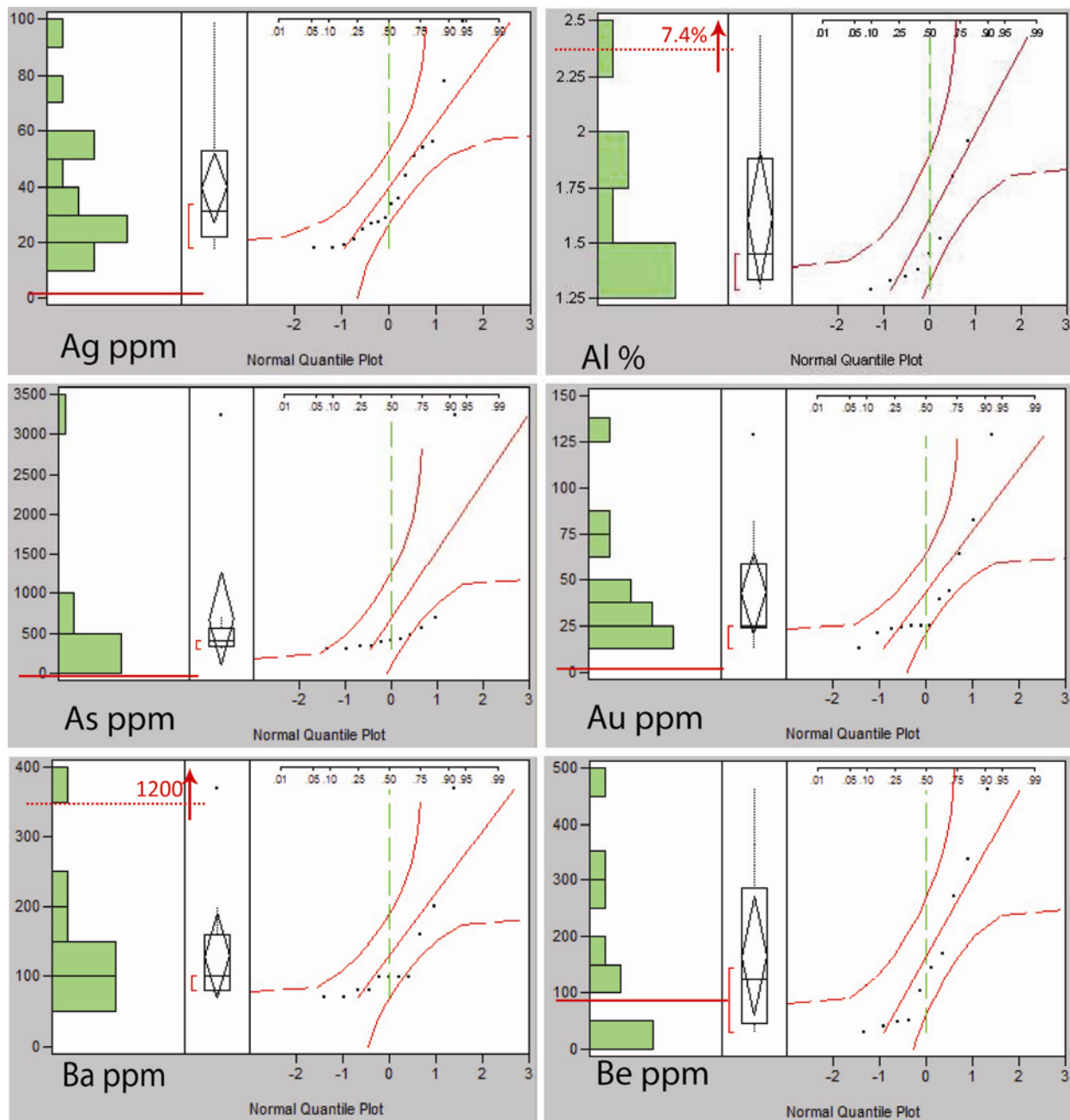


Figure 1-14. Outlier histograms for 6 (Ag, Al, As, Au, Ba, Be) multi-element analysis of surface samples.

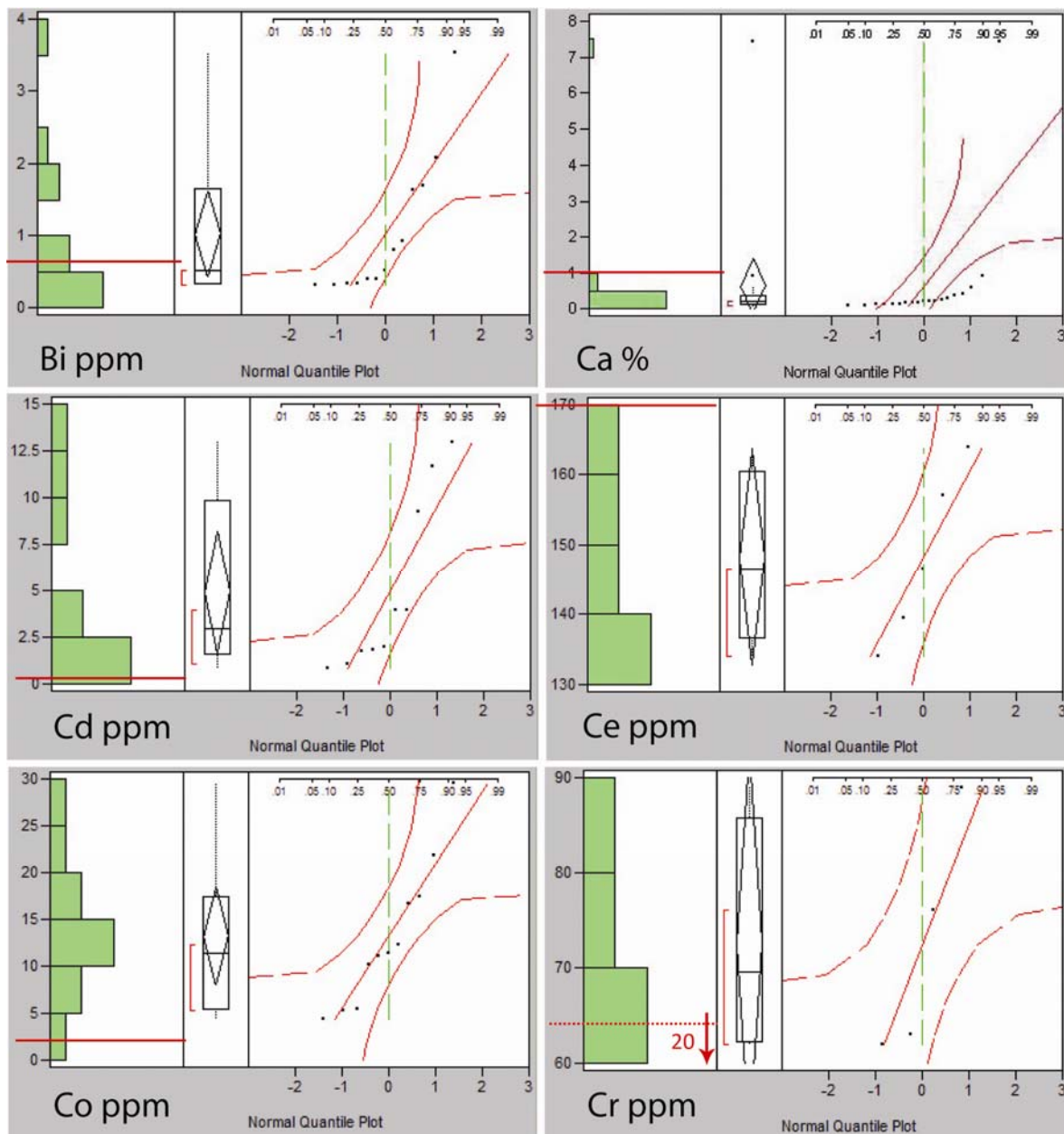


Figure 1-15. Outlier histograms for 6 (Bi, Ca, Cd, Ce, Co, Cr) multi-element analysis of surface samples.

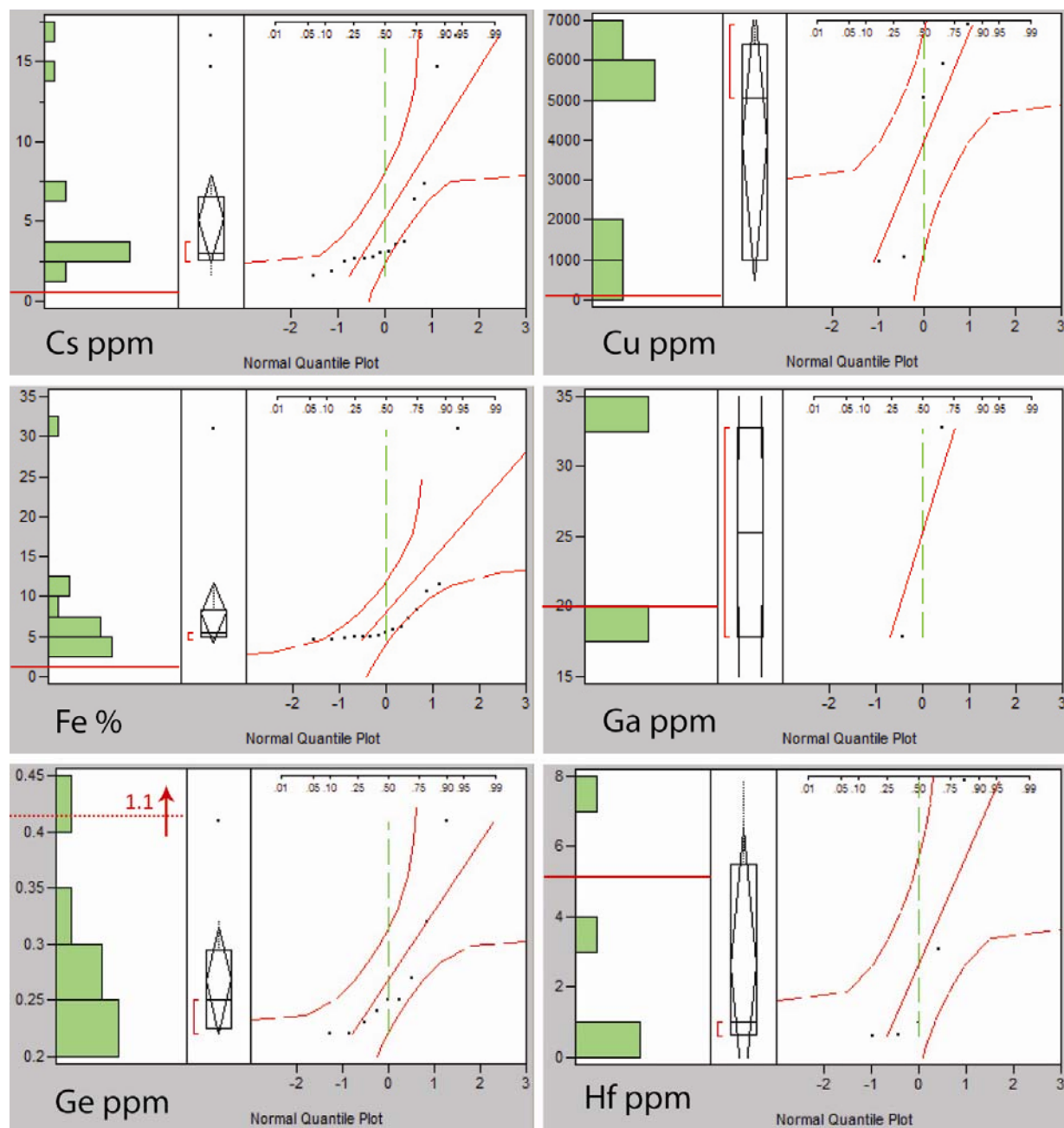
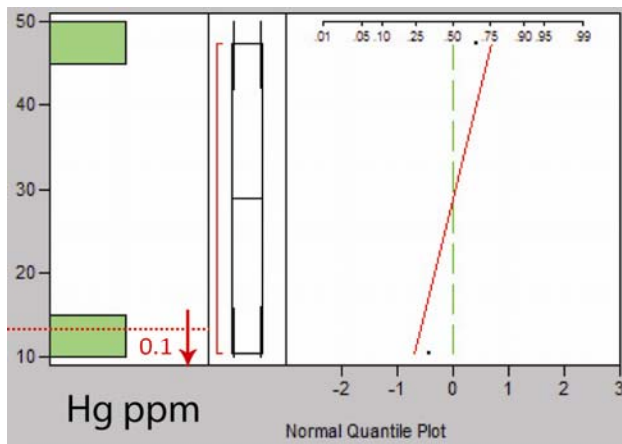


Figure 1-16. Outlier histograms for 6 (Cs, Cu, Fe, Ga, Ge, Hf) multi-element analysis of surface samples.



No Outliers for
Indium (In)

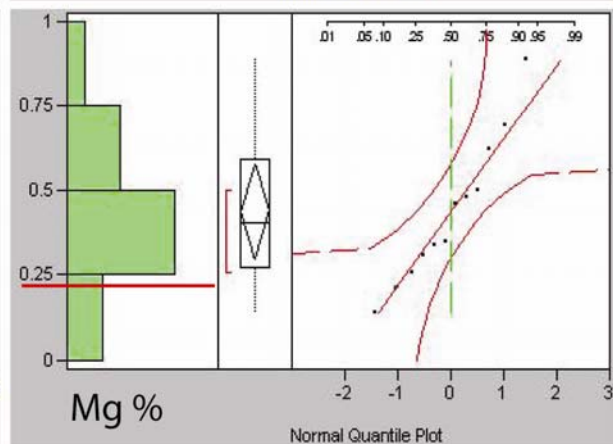
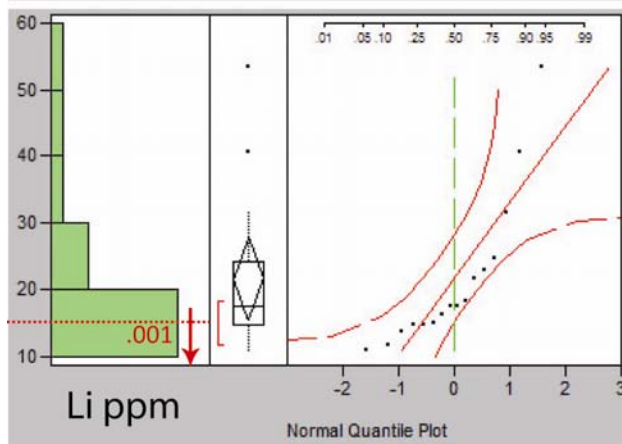
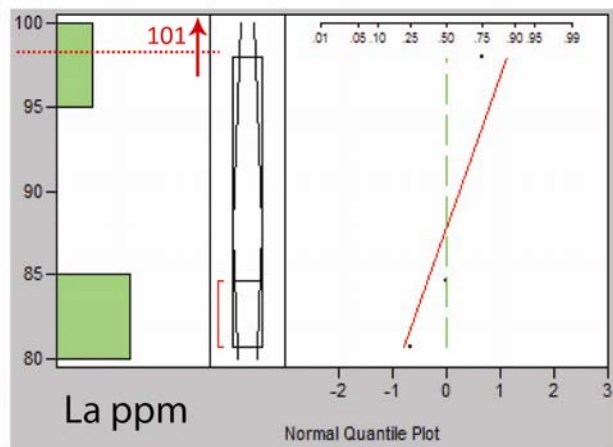
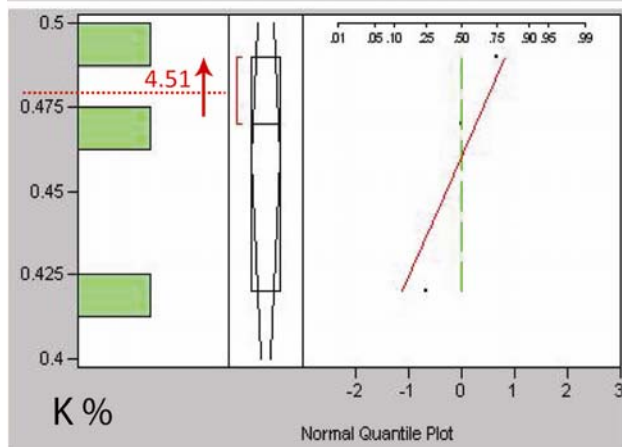


Figure 1-17. Outlier histograms for 5 (Hg, K, La, Li, Mg) multi-element analysis of surface samples.

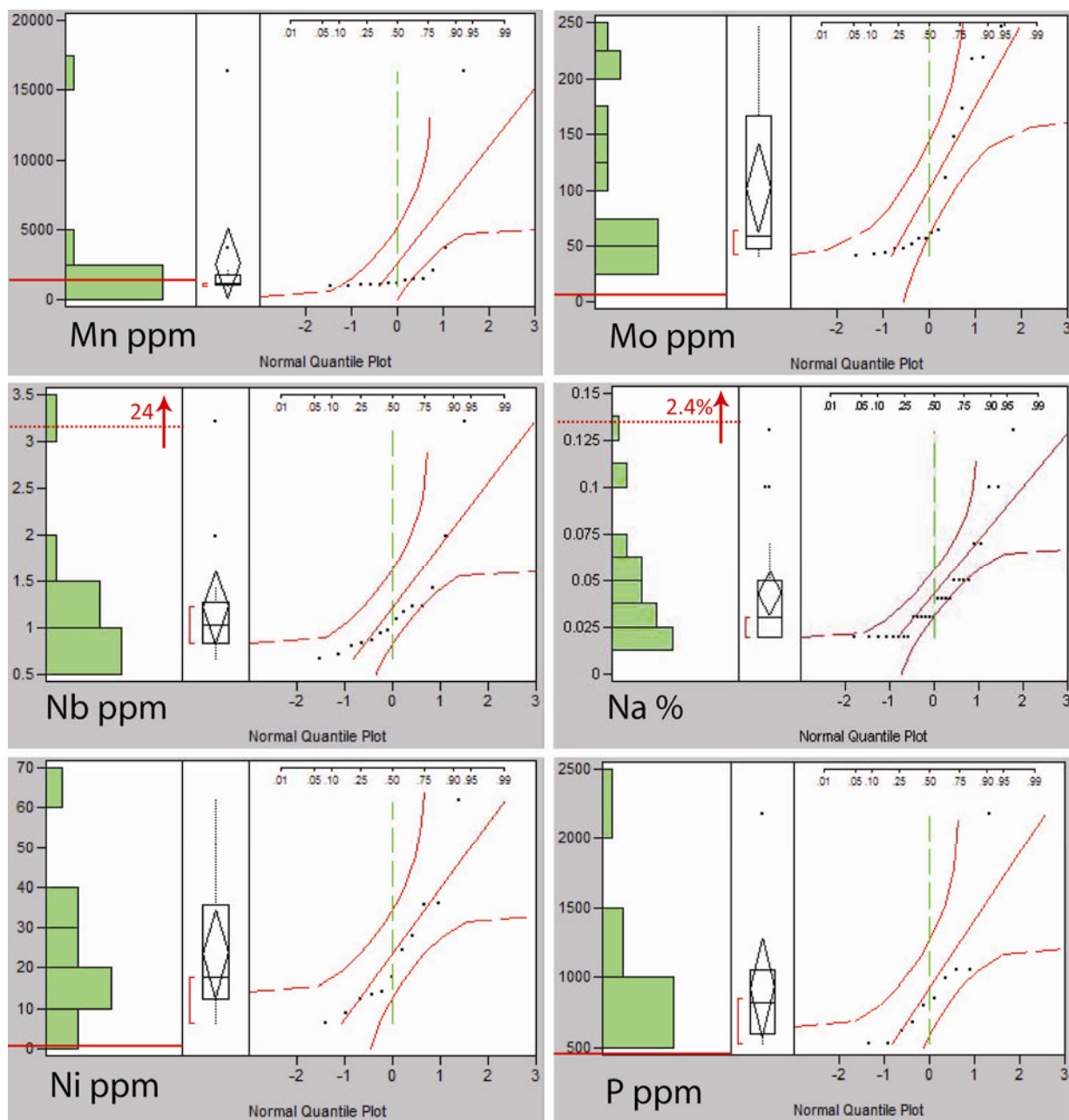


Figure 1-18. Outlier histograms for 6 (Mn, Mo, Nb, Na, Ni, P) multi-element analysis of surface samples.

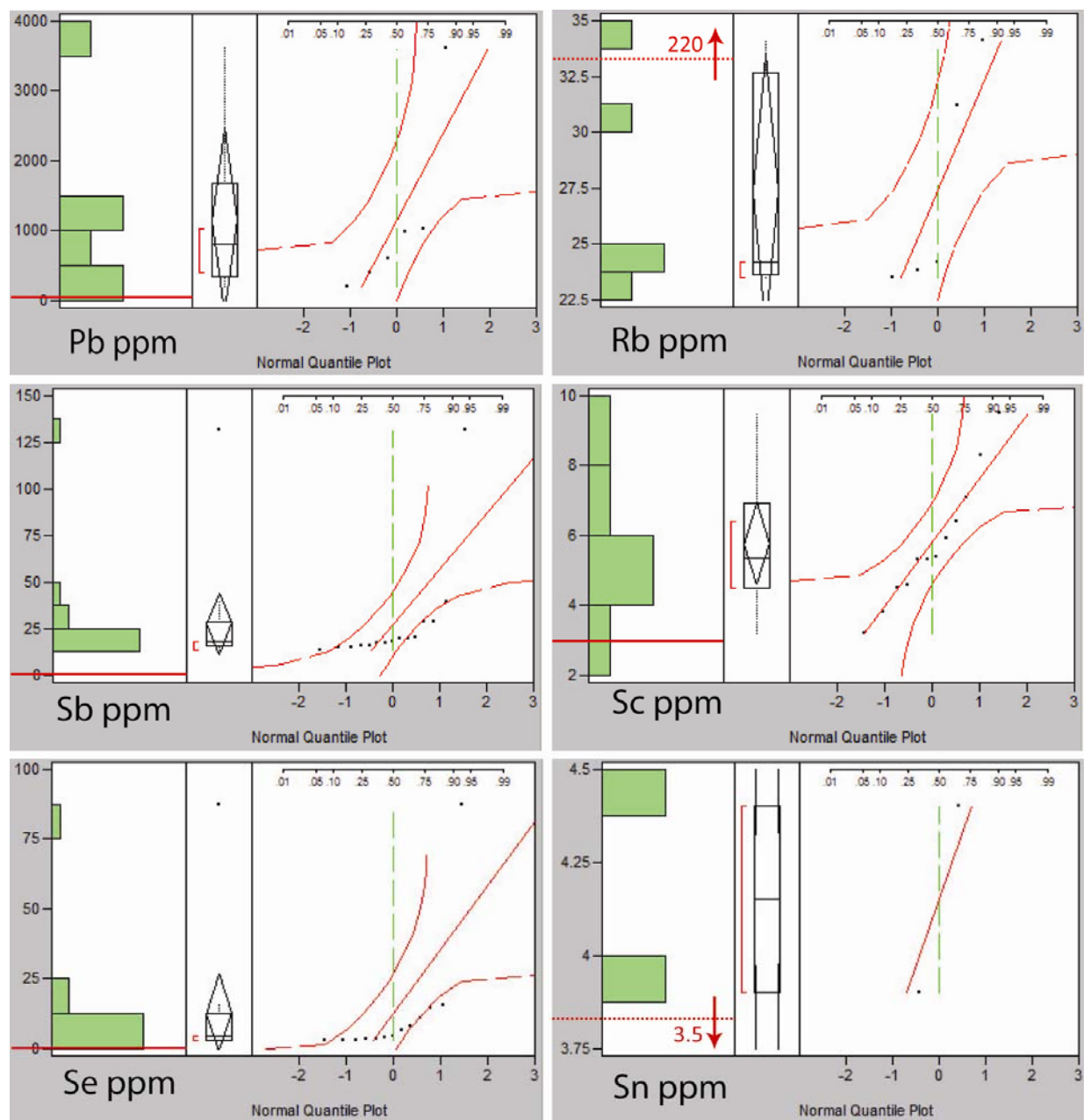


Figure 1-19. Outlier histograms for 6 (Pb, Rb, Sb, Sc, Se, Sn) multi-element analysis of surface samples.

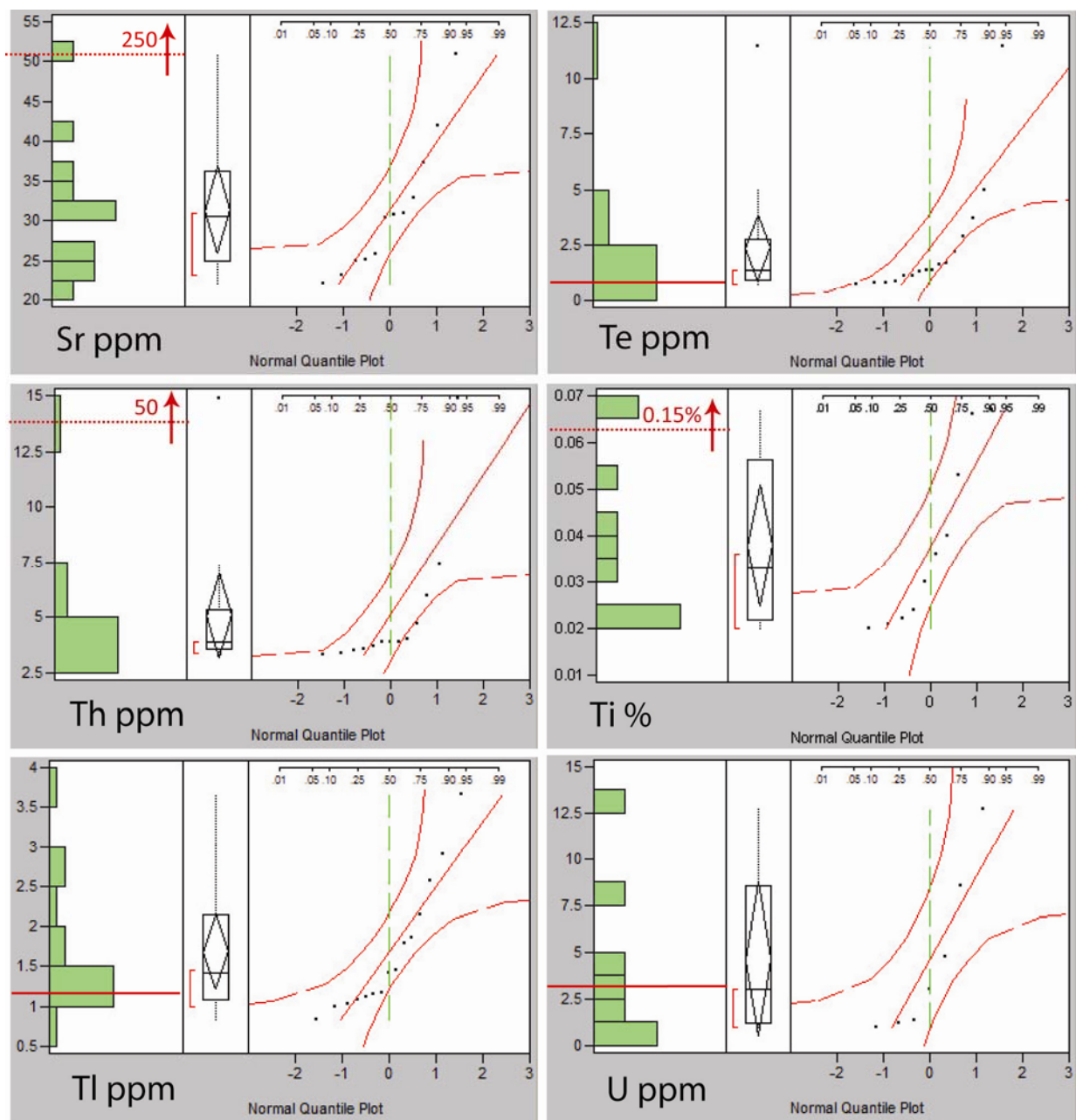


Figure 1-20. Outlier histograms for 6 (Sr, Te, Th, Ti, Tl, U) multi-element analysis of surface samples.

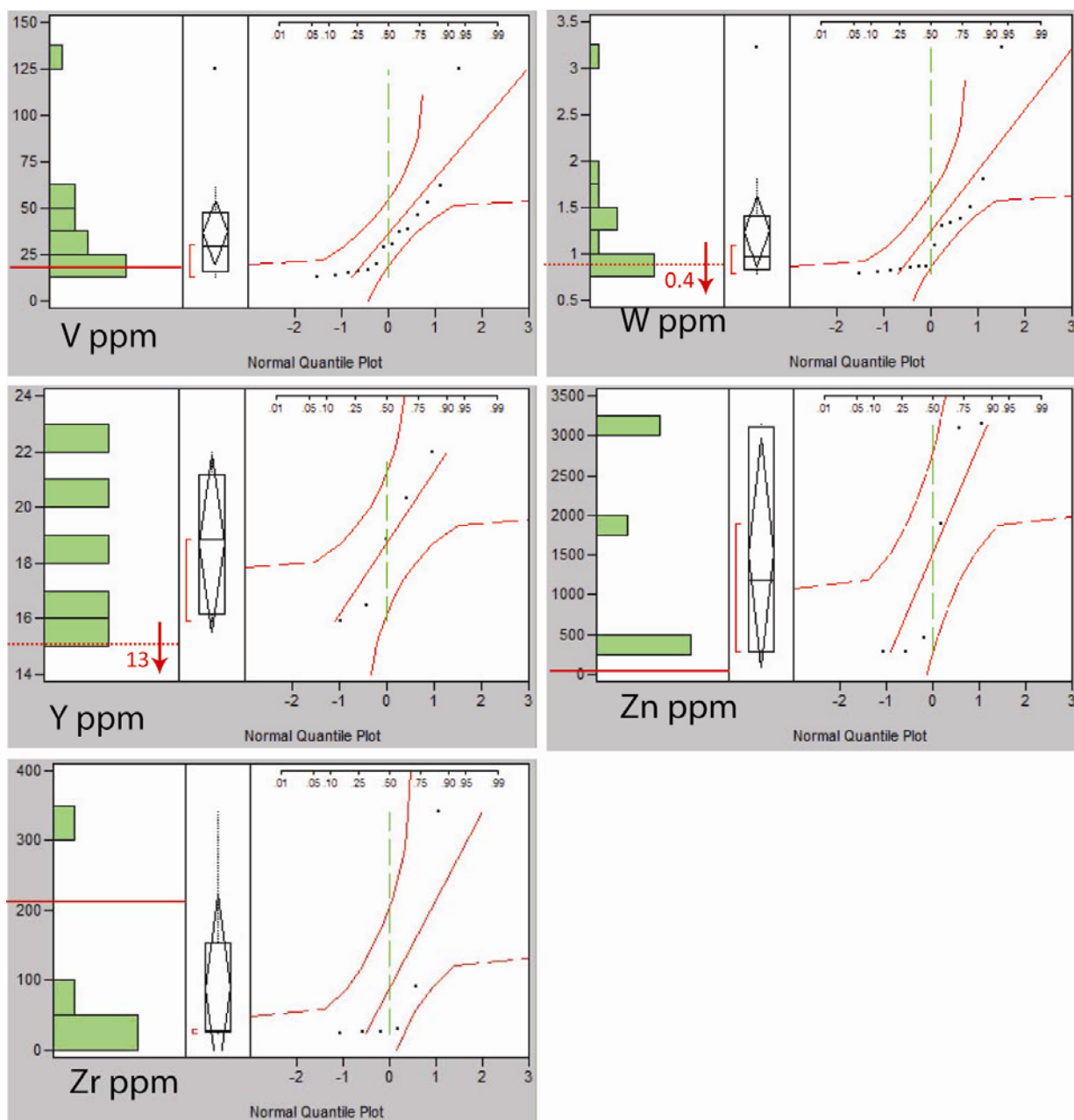


Figure 1-21. Outlier histograms for 5 (V, W, Y, Zn, Zr) multi-element analysis of surface samples.

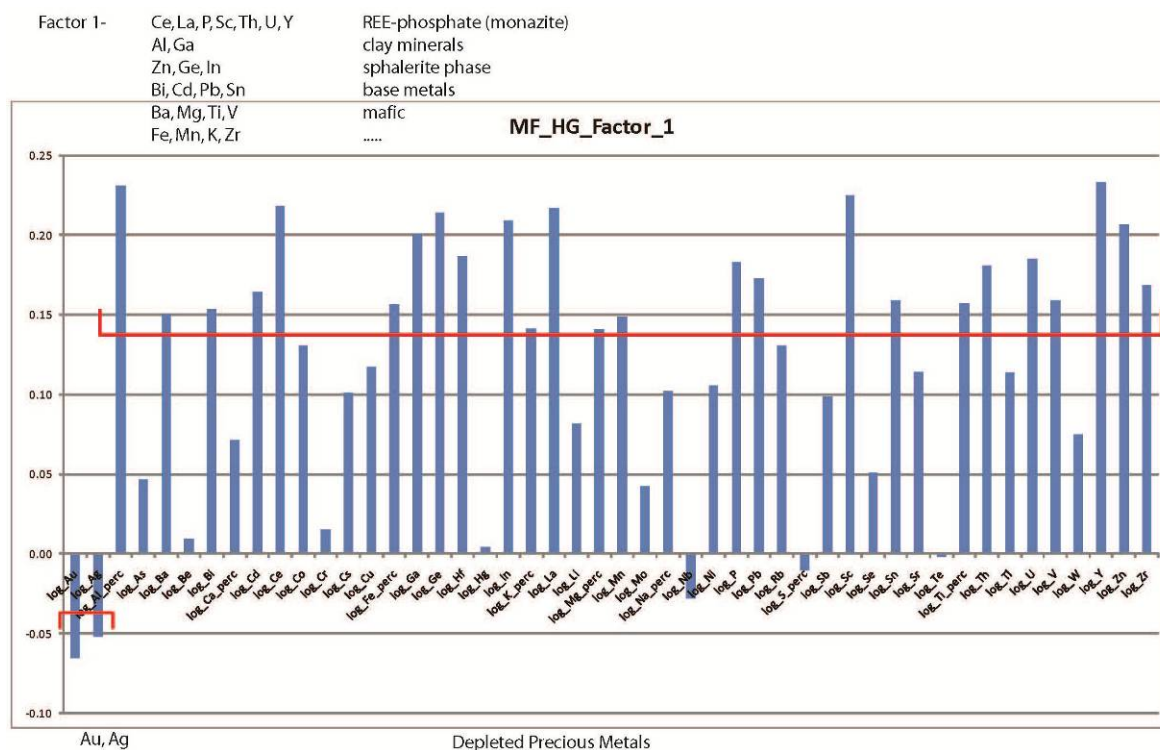


Figure 1-22. Principal component (PC) for surface samples dataset, Factor 1.

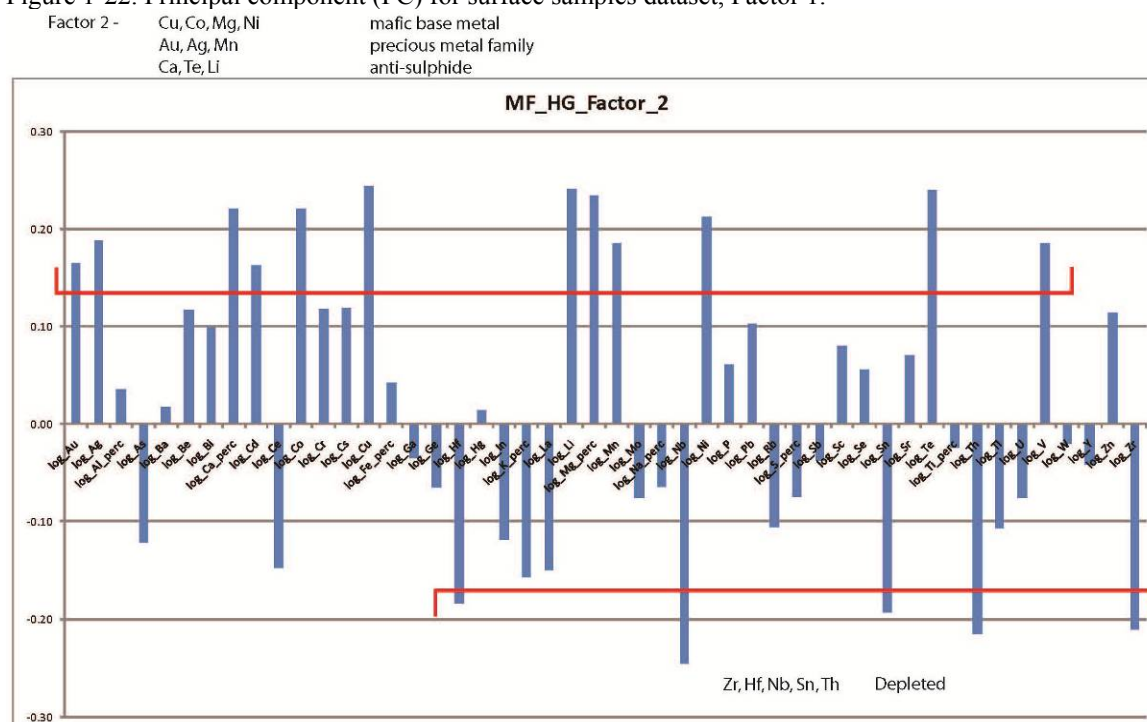


Figure 1-23. PC for surface samples dataset, Factor 2.

Factor 4 - Bi, Pb, Te
epithermal
Na, Be, Zr, Hf, Nb, W
Alkaline hydrothermal

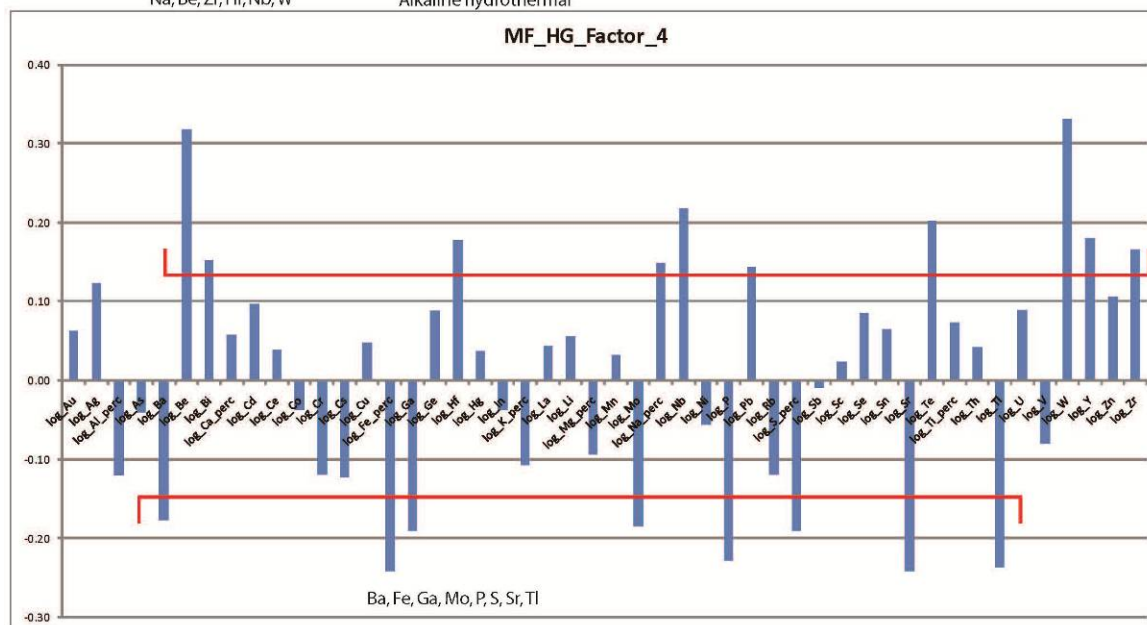


Figure1-24. PC for surface samples dataset, Factor 4.

Factor 5 - Li, Be, Cs, Rb
alkaline hydrothermal
Au, Al, Ga, K, Te
gold in feldspar (adularia)
V
.....

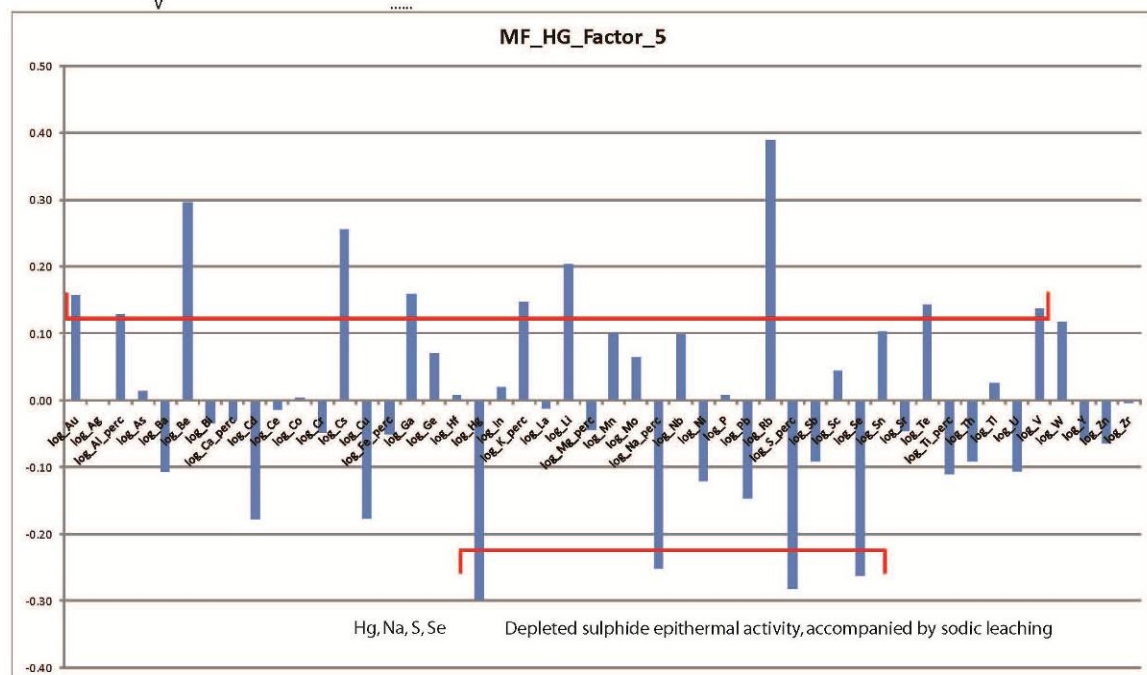


Figure 1-25. PC for surface samples dataset, Factor 5.

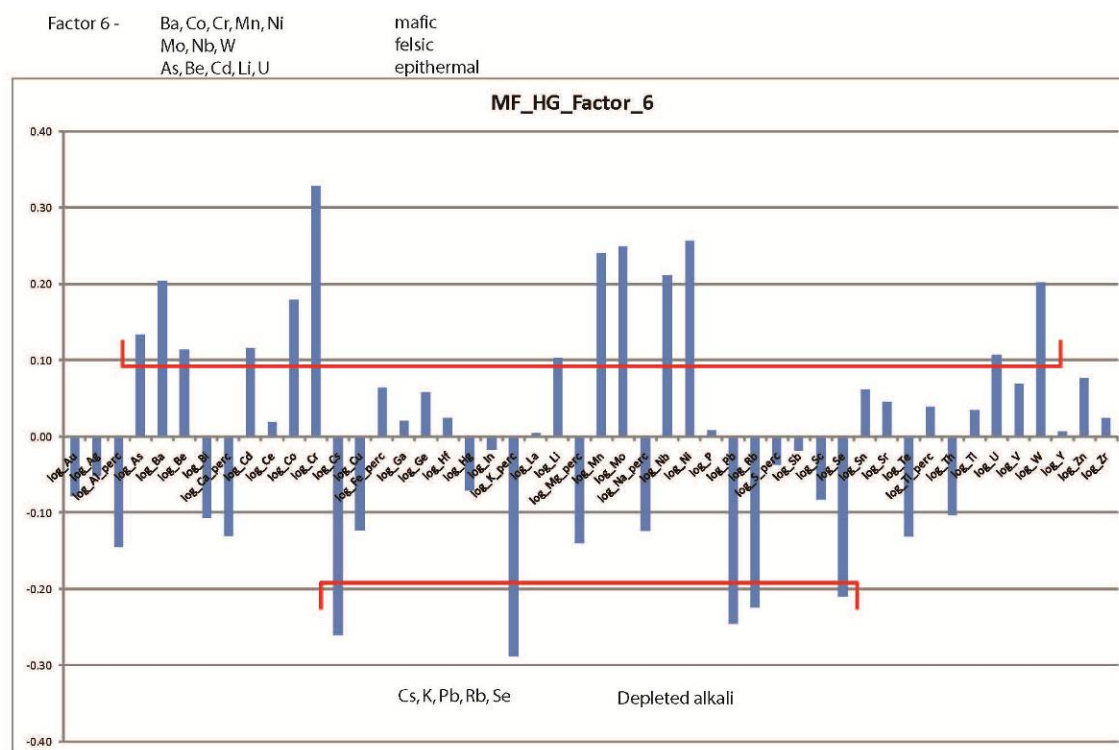


Figure 1-26. PC for surface samples dataset, Factor 6.

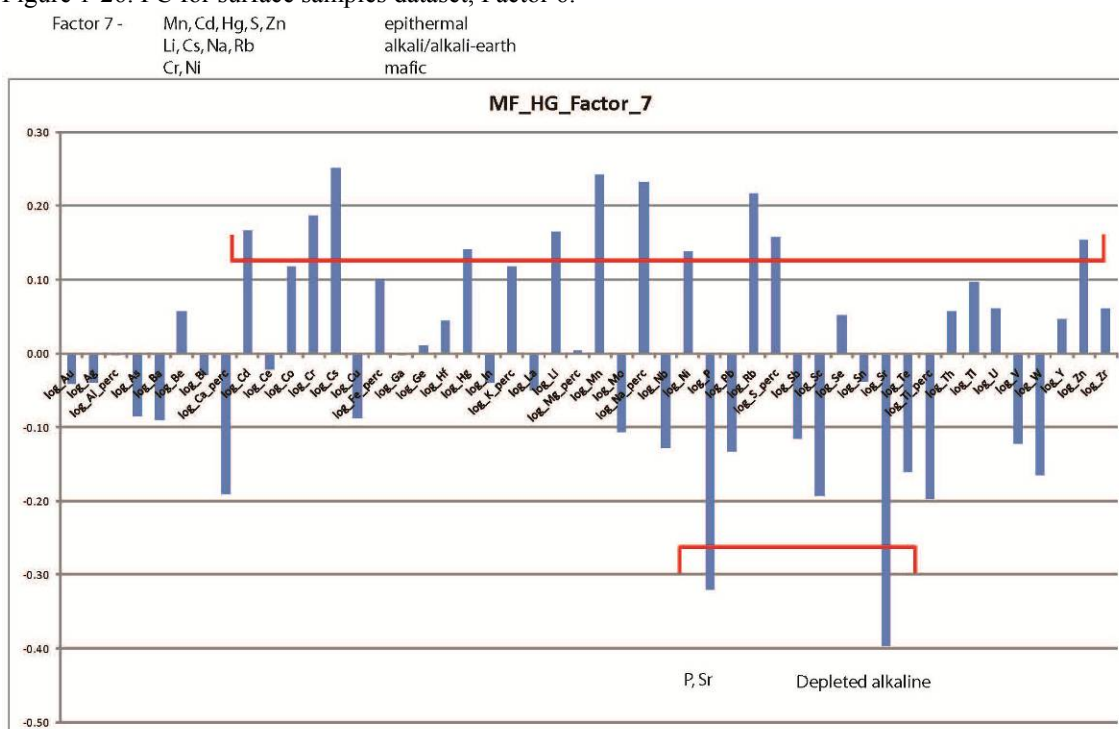


Figure 1-27. PC for surface samples dataset, Factor 7.

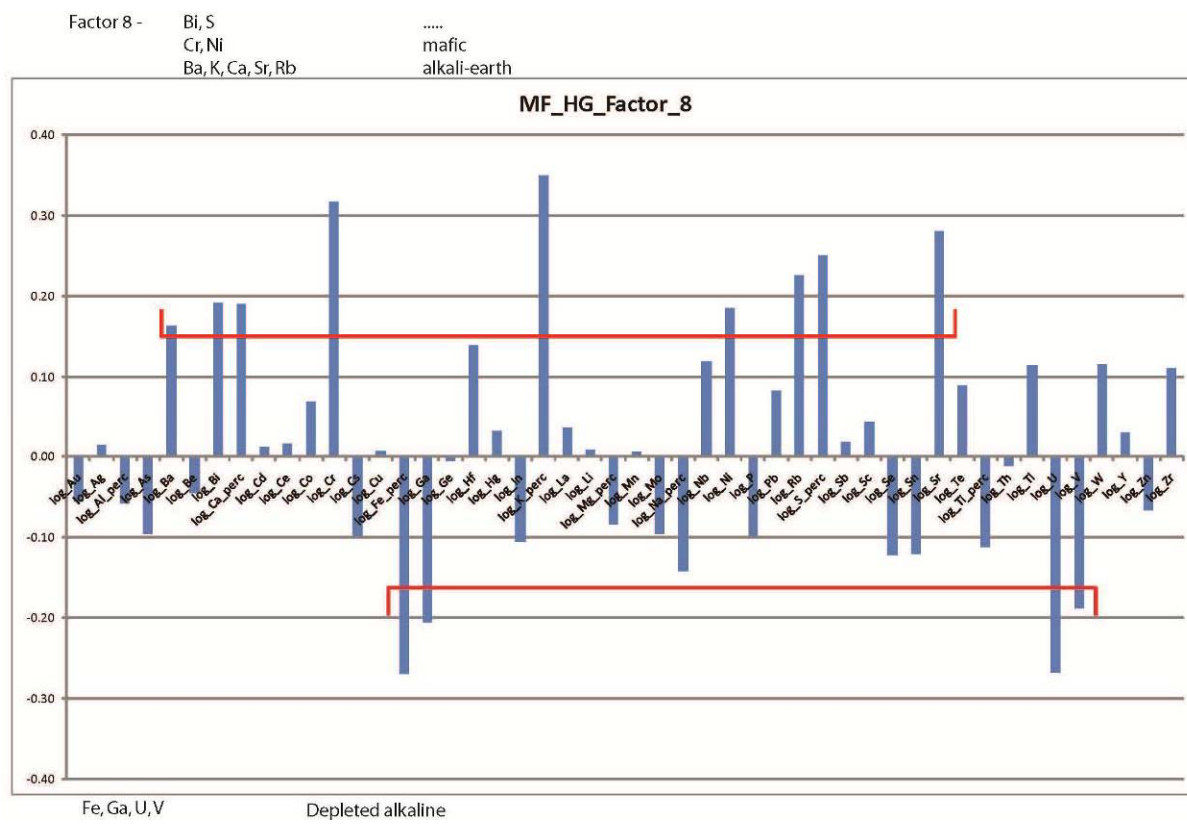


Figure 1-28. PC for surface samples dataset, Factor 8.

Factor 1 - Natural Neighbor

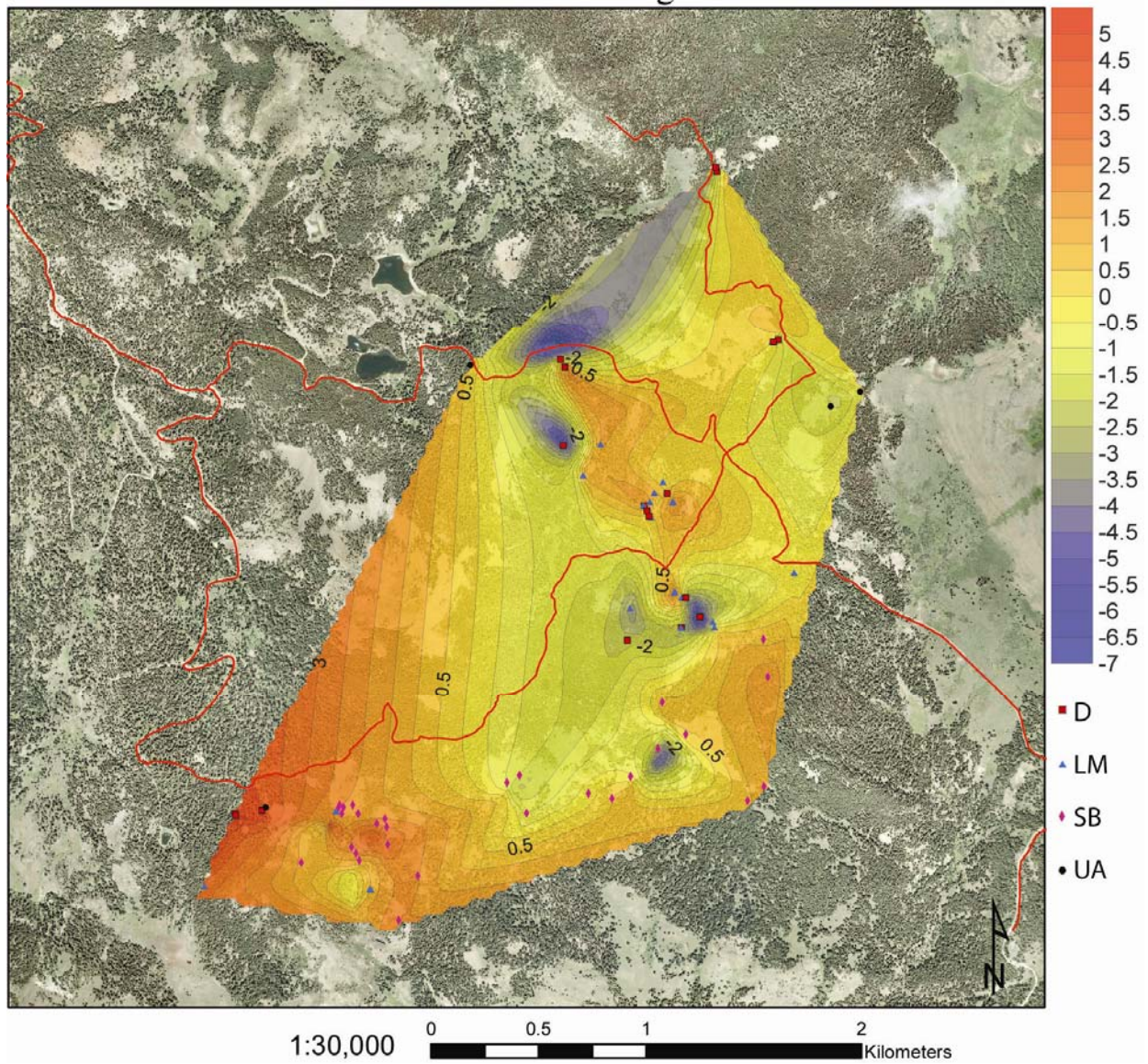


Figure 1-29. Natural Neighbor modeling of the sample scores for factor 1 yield this contoured surface of the HGD.

Factor 2 - Natural Neighbor

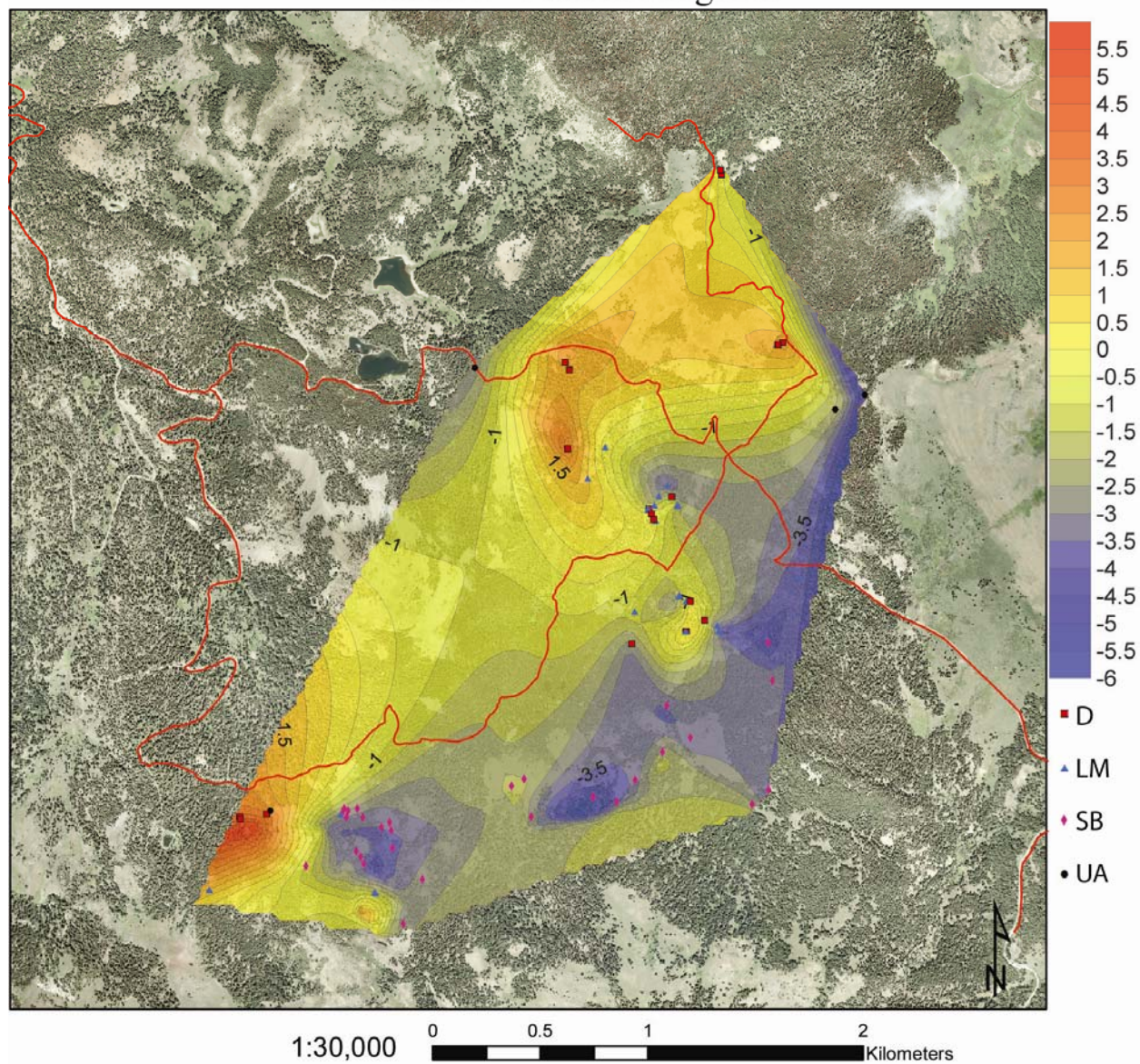


Figure 1-30. Natural Neighbor modeling of the sample scores for factor 2 yield this contoured surface of the HGD.

Factor 4 - Natural Neighbor

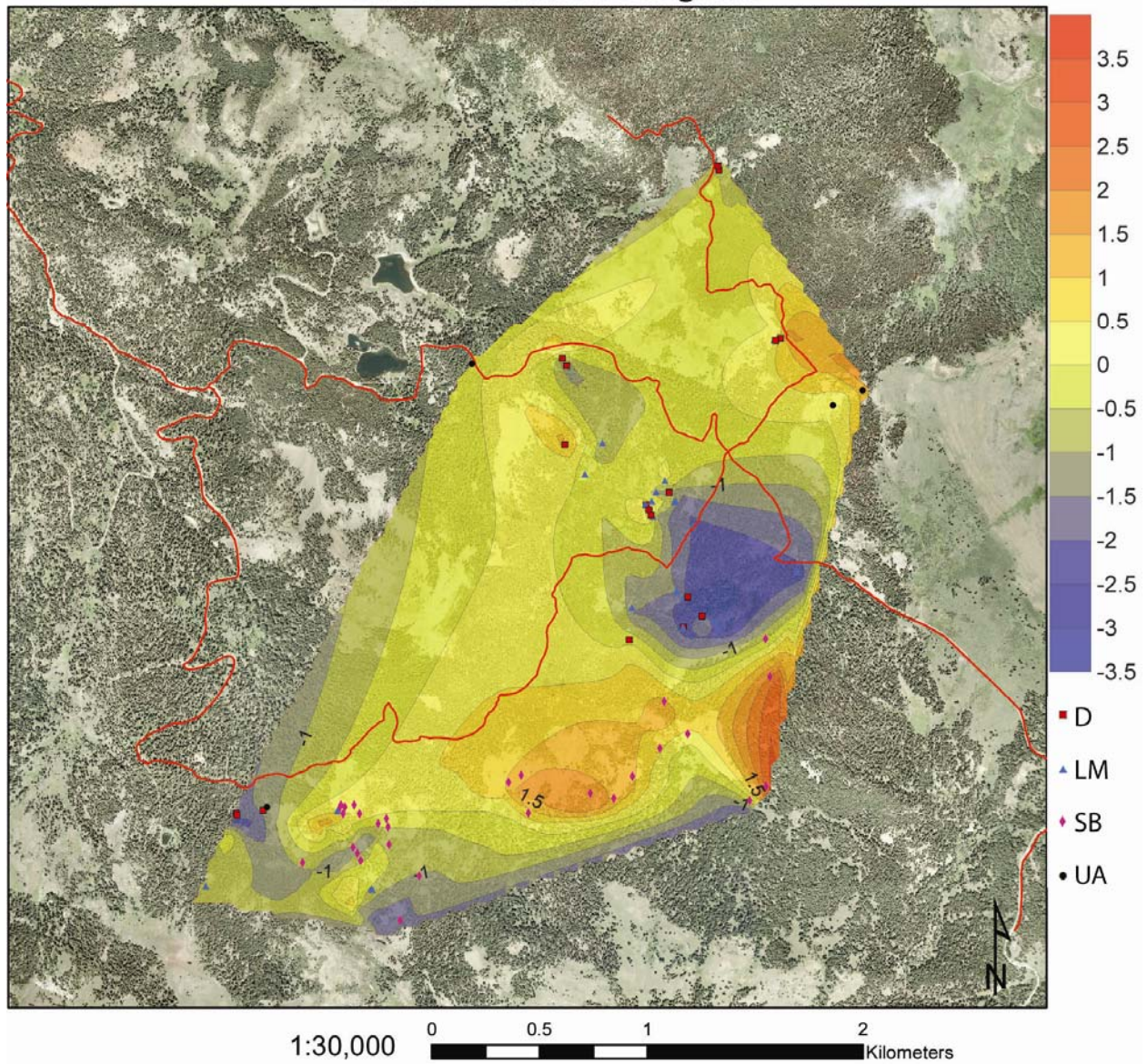


Figure 1-31. Natural Neighbor modeling of the sample scores for factor 4 yield this contoured surface of the HGD.

Factor 5 - Natural Neighbor

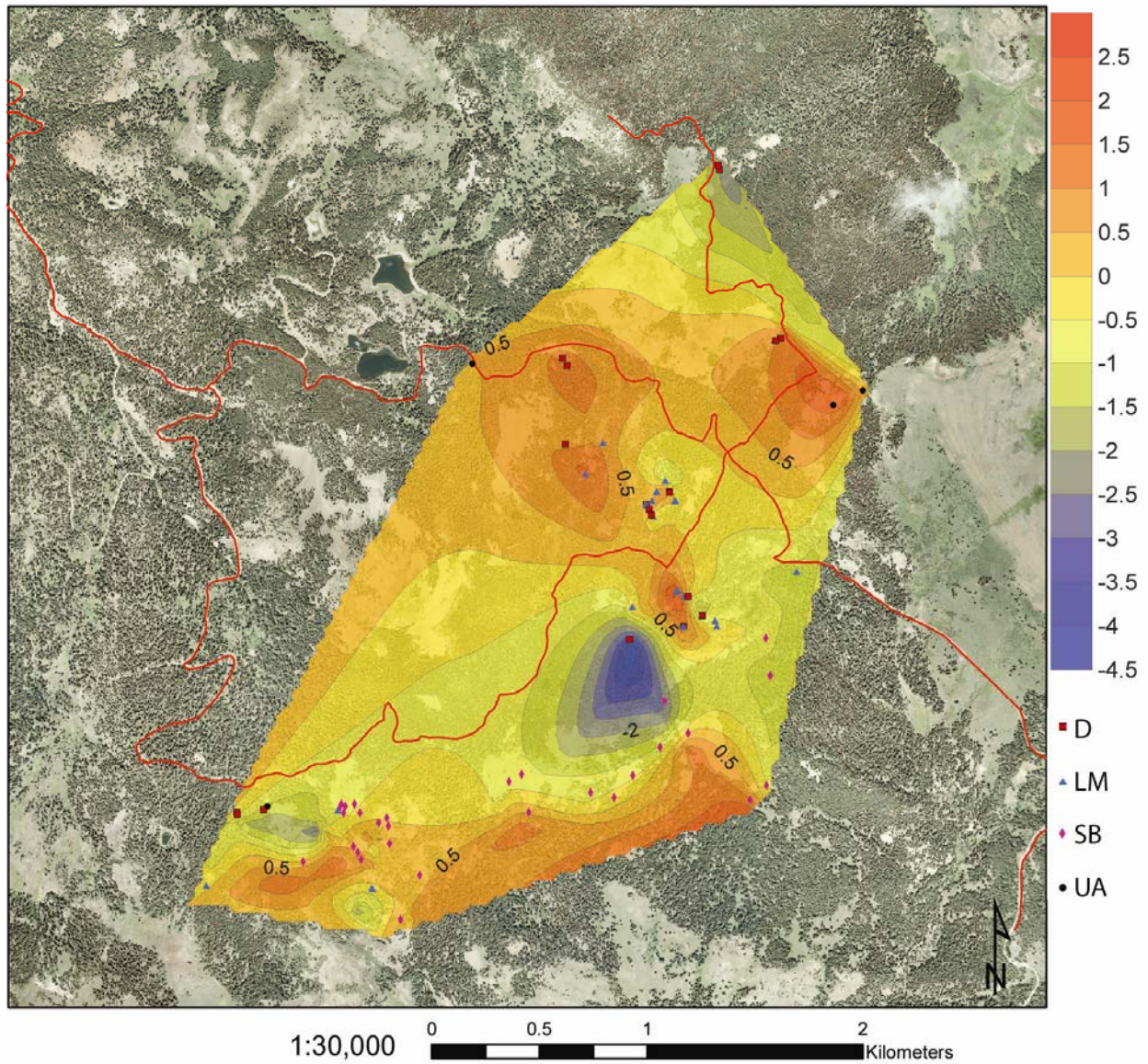


Figure 1-32. Natural Neighbor modeling of the sample scores for factor 5 yield this contoured surface of the HGD.

Factor 6 - Natural Neighbor

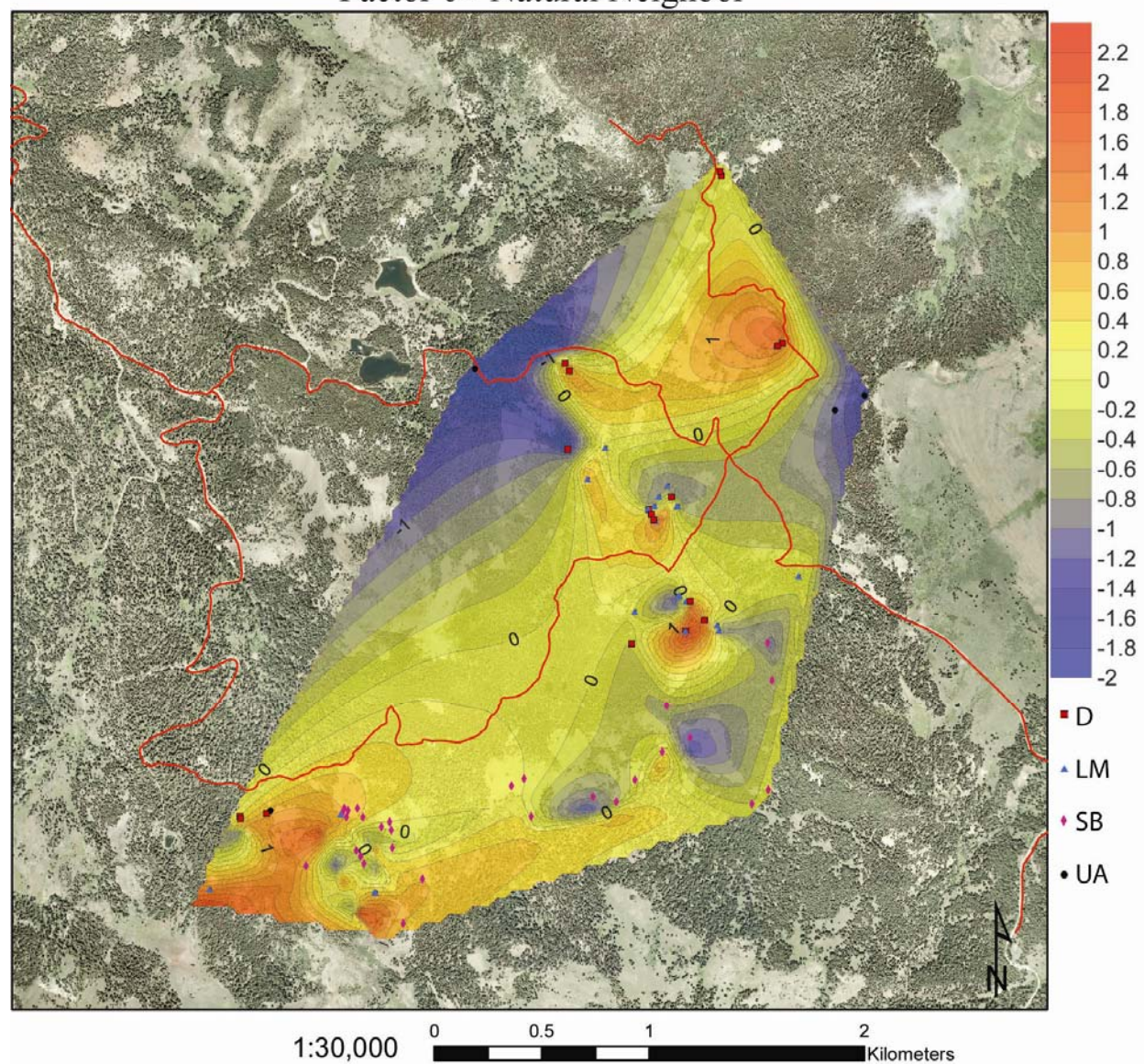


Figure 1-33. Natural Neighbor modeling of the sample scores for factor 6 yield this contoured surface of the HGD.

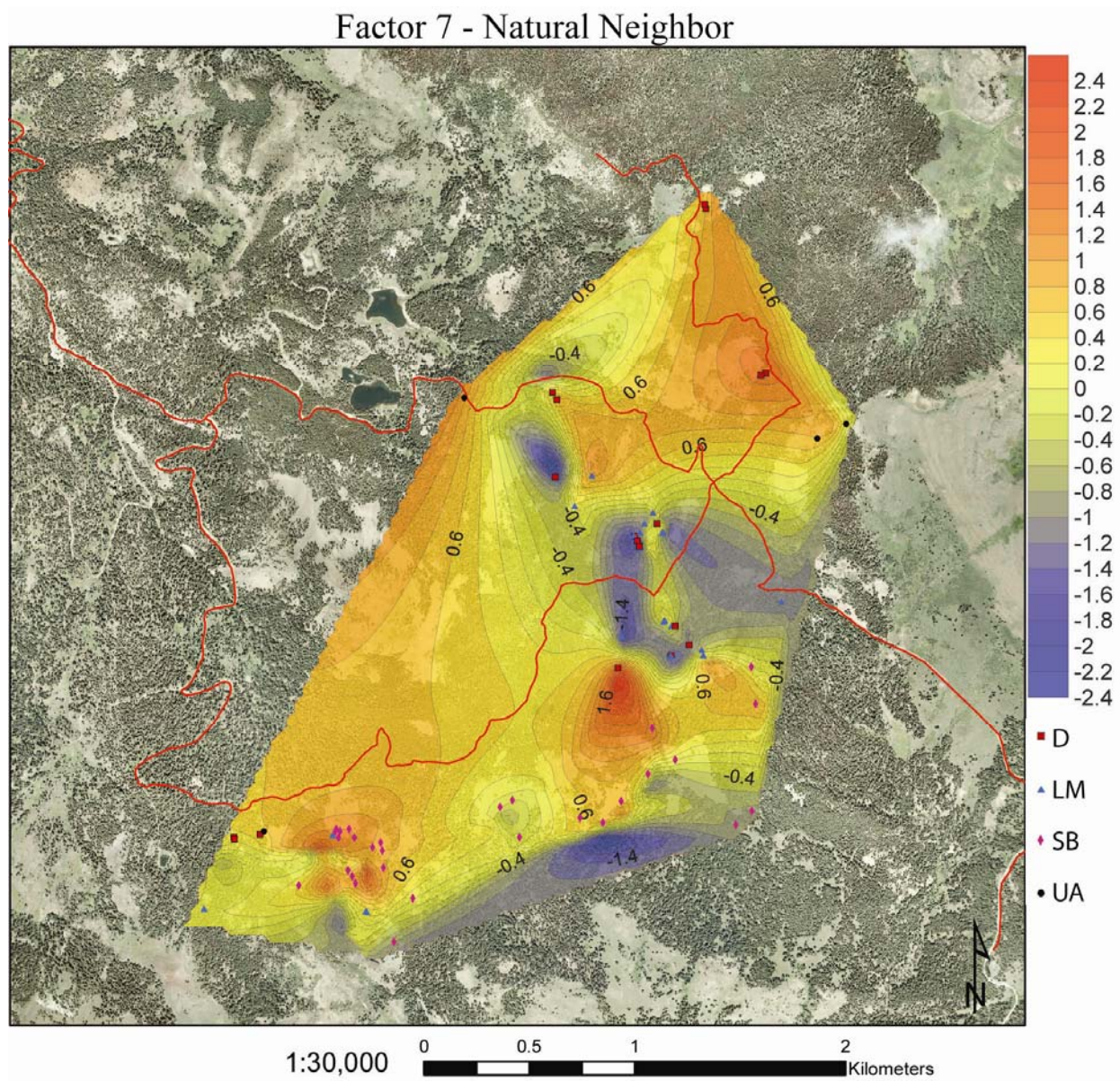


Figure 1-34. Natural Neighbor modeling of the sample scores for factor 7 yield this contoured surface of the HGD.

Factor 8 - Natural Neighbor

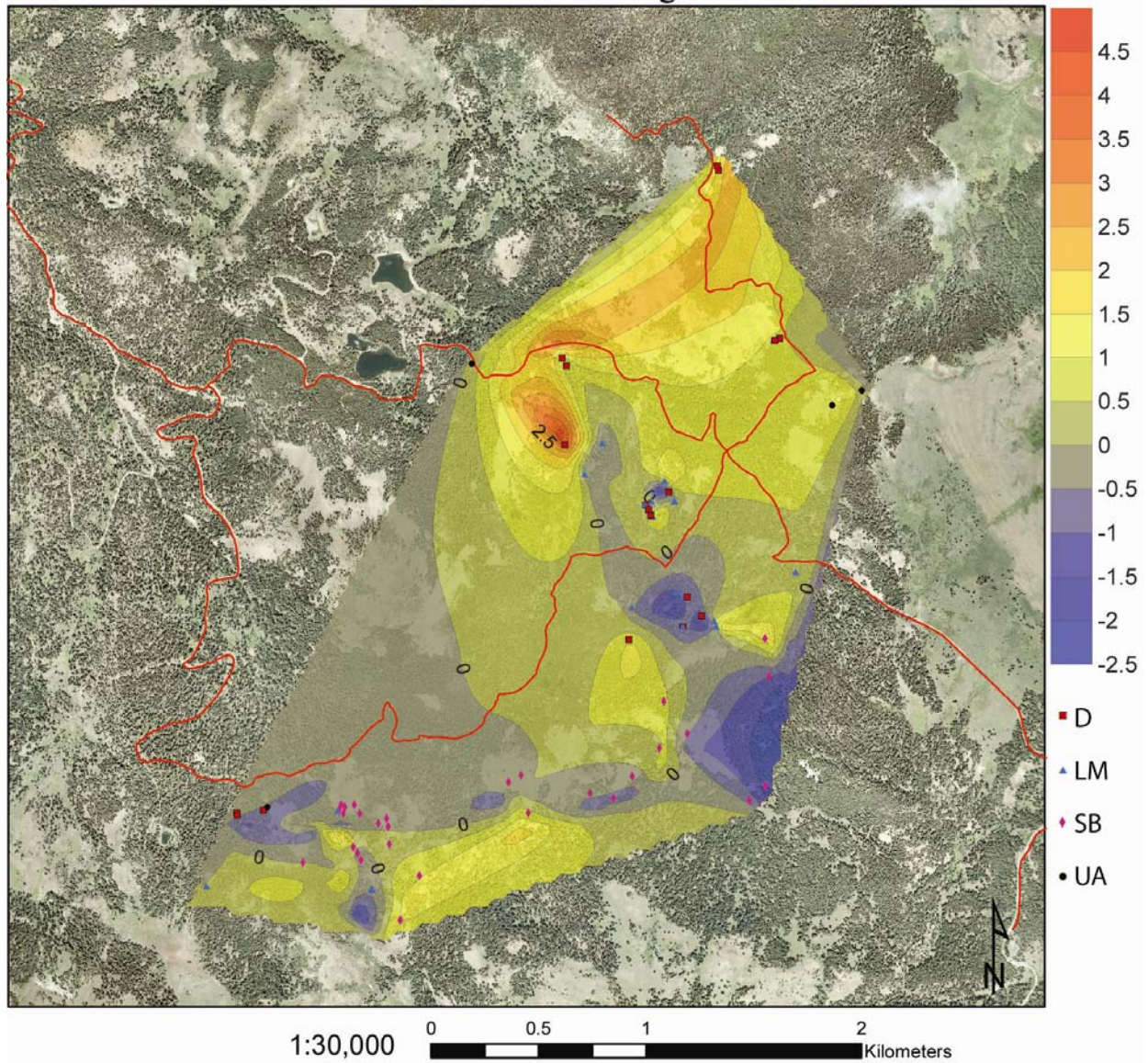


Figure 1-35. Natural Neighbor modeling of the sample scores for factor 8 yield this contoured surface of the HGD.

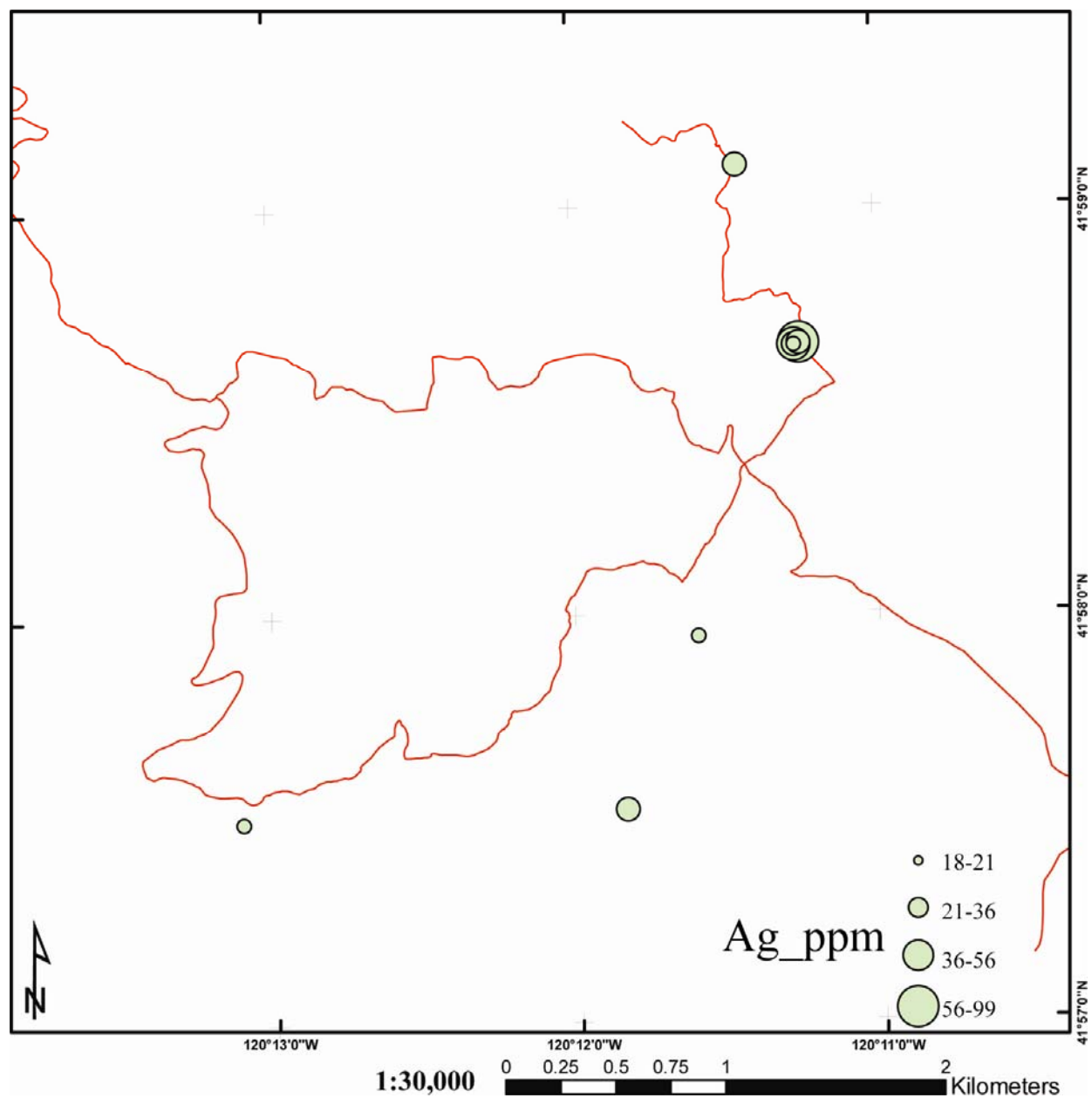


Figure 1-36. Map of Ag outlier values. Numerous highs are concentrated in the sunshine camp, as with Au.

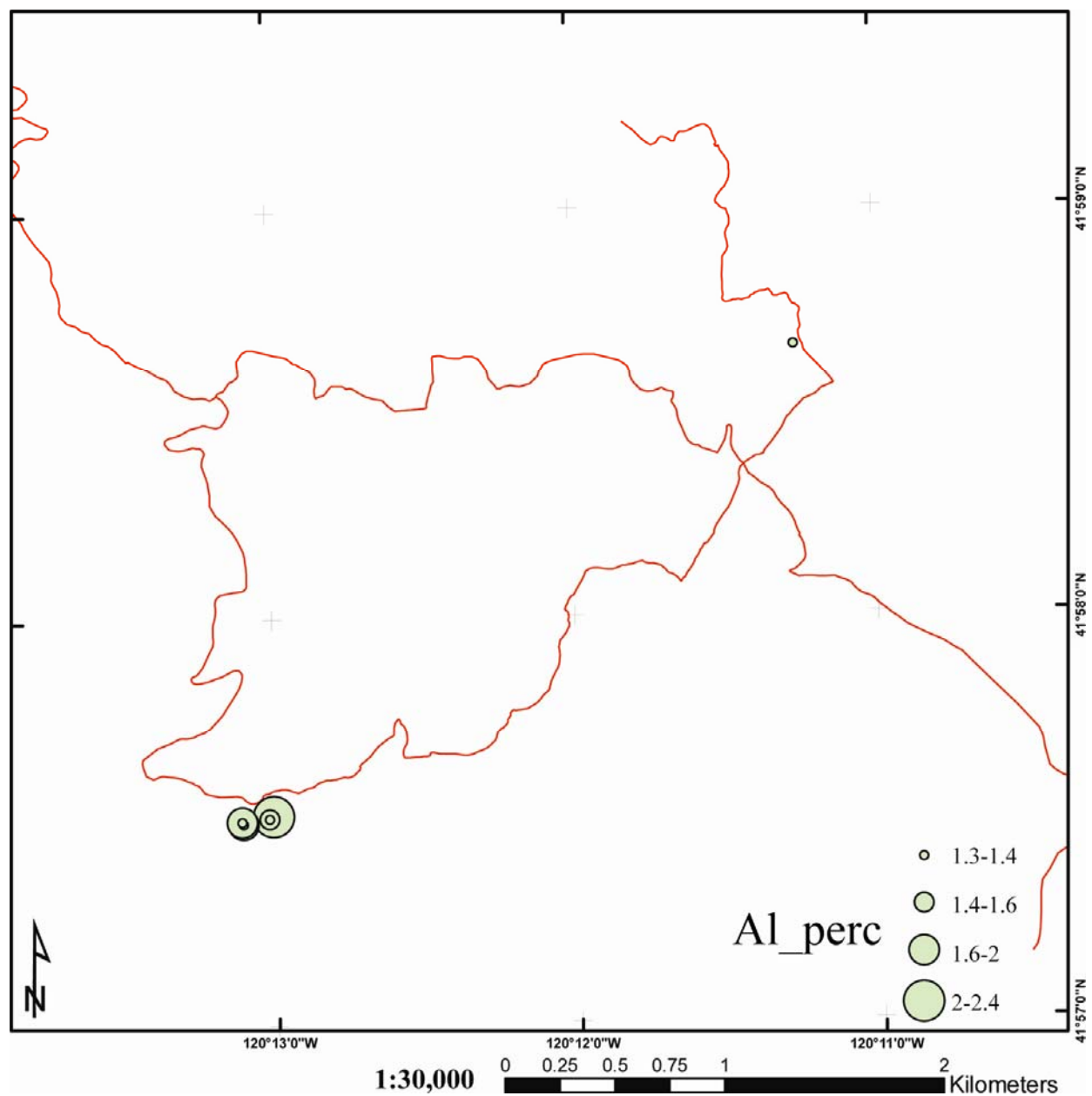


Figure 1-37. Map of Al% outlier values. Numerous highs are concentrated in the West Consolidated Camp.

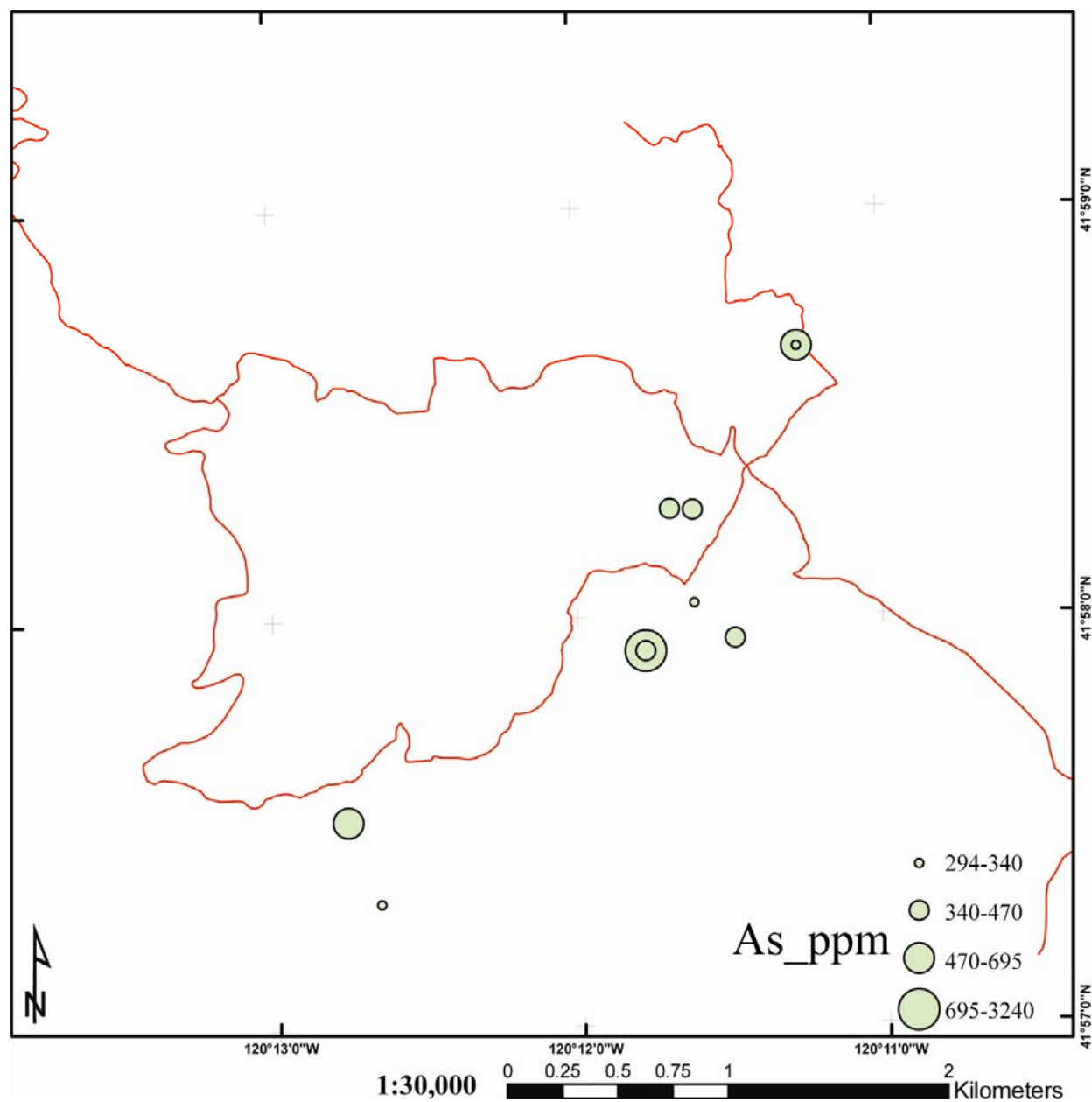


Figure 1-38. Map of As outlier values.

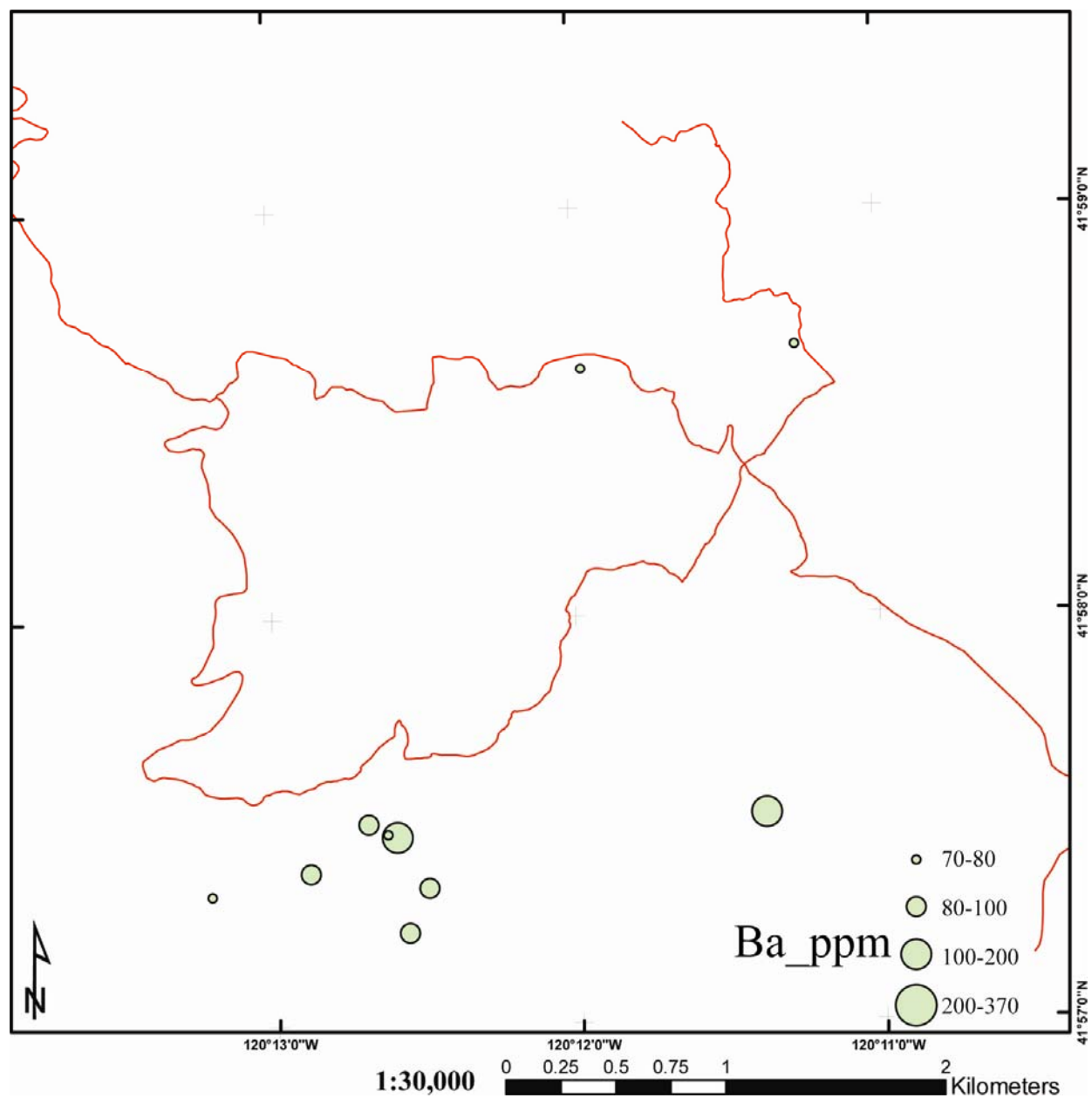


Figure 1-39. Map of Ba outliers values. Ba is an active component to the mafic factor within the district. Concentrations are seen in the Consolidated silica body.

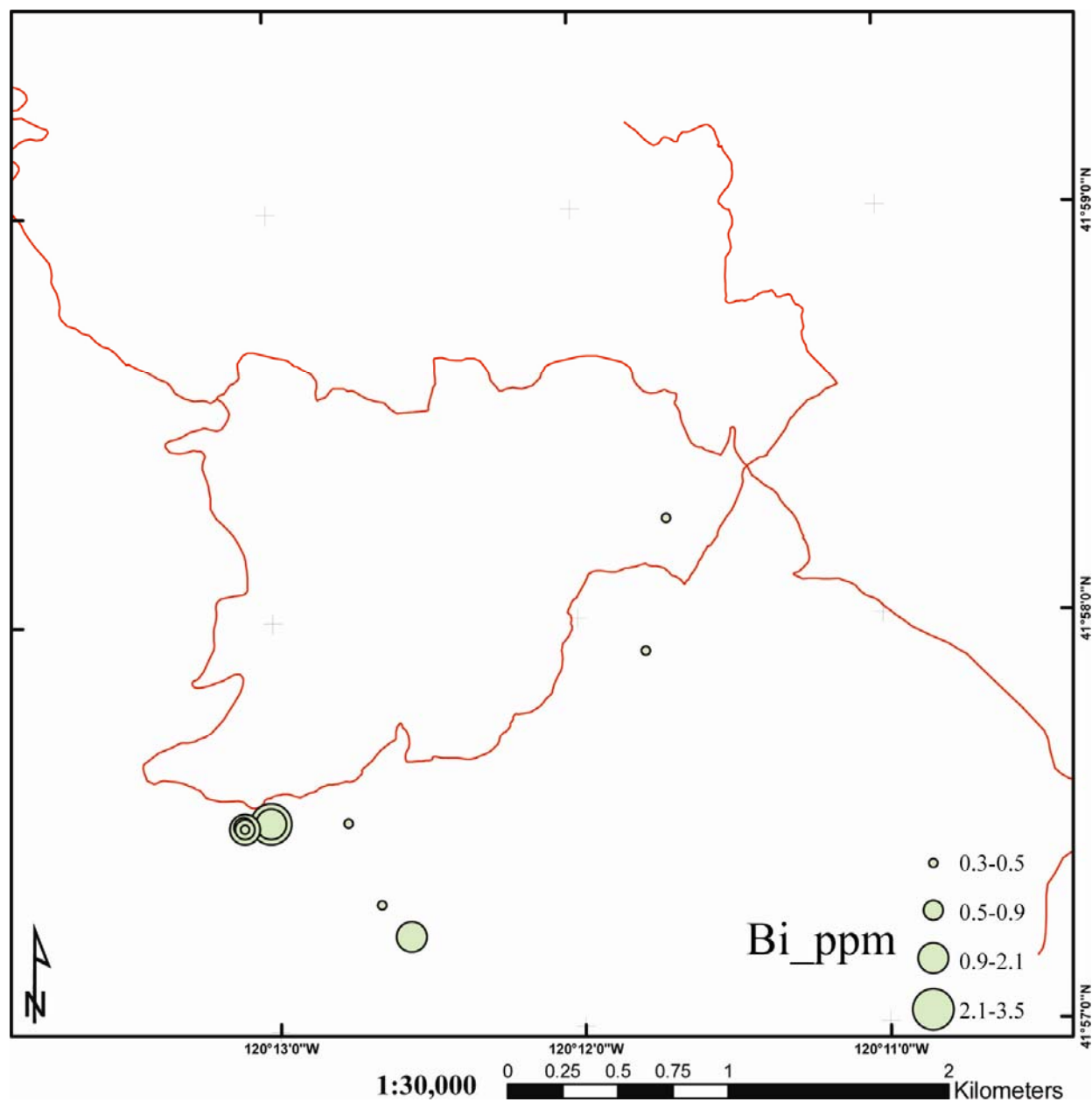


Figure 1-40. Map of Bi outlier values.

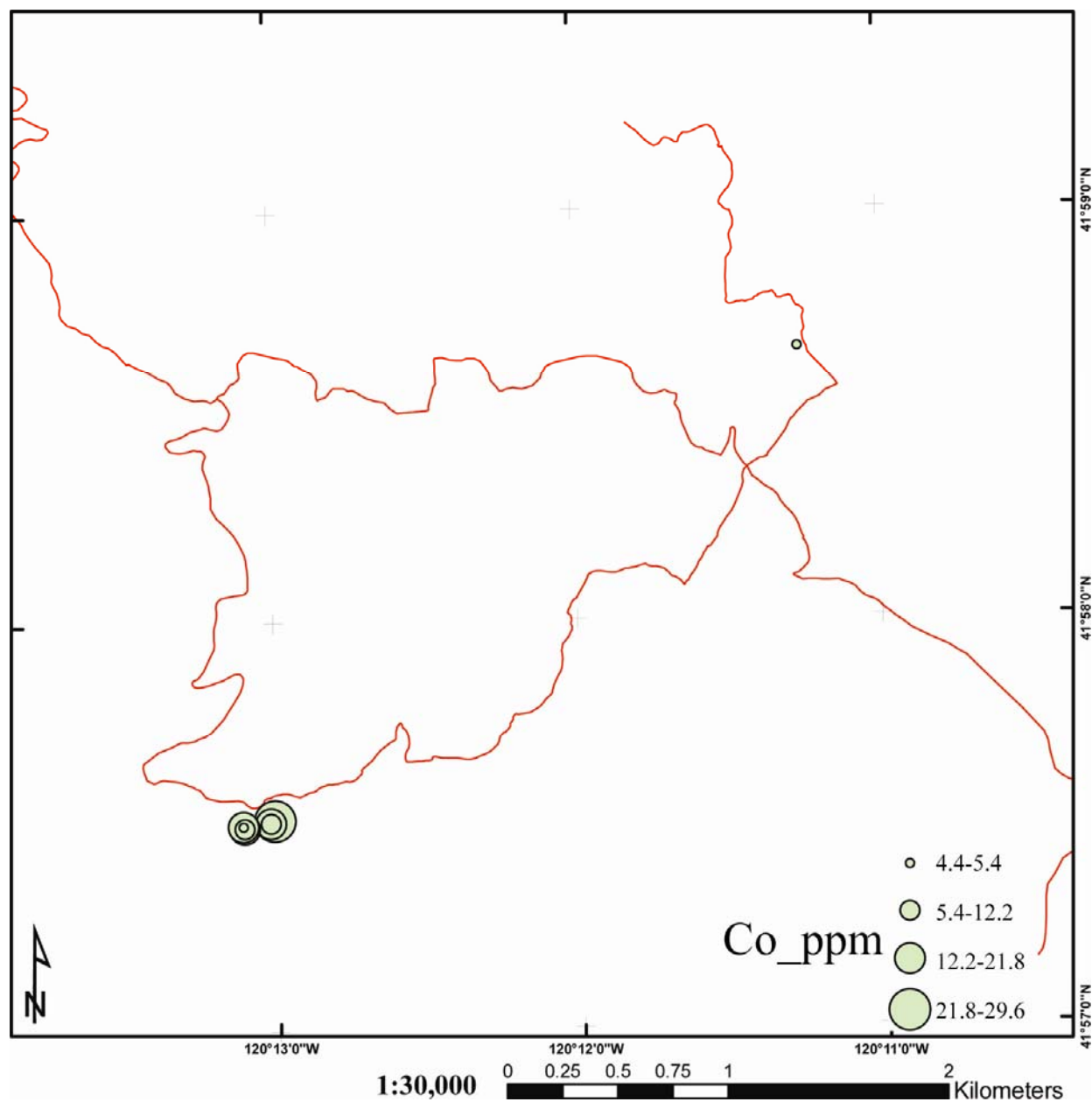


Figure 1-41. Map of Co outlier values. Numerous

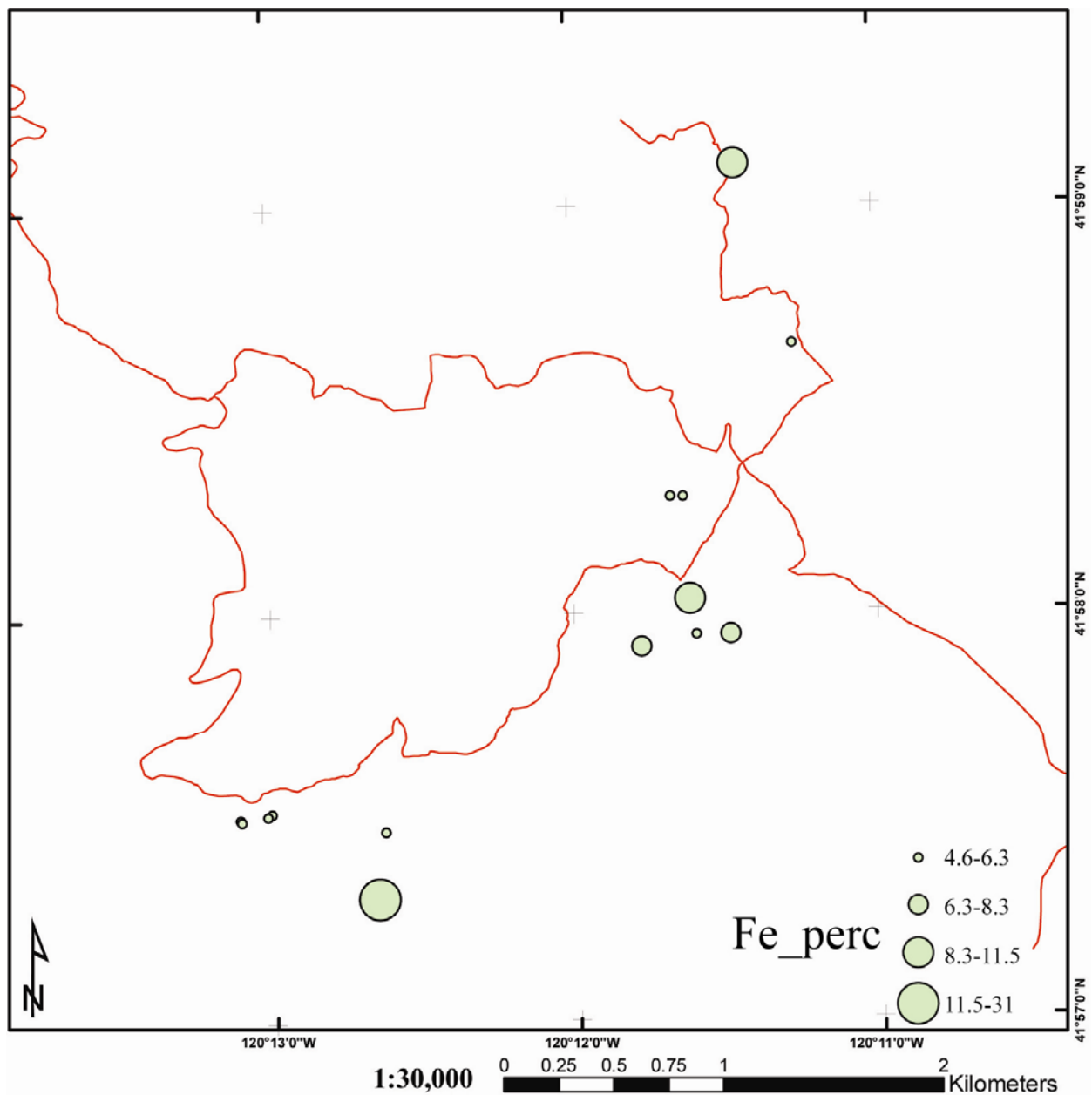


Figure 1-42. Map of Fe% outliers values. Fe maximums are found within the pyritized breccias of Alturas Hill, intensely hematized & silicified gouge of Modoc Mines, and limonite-rich opaline sinter of East Consolidated.

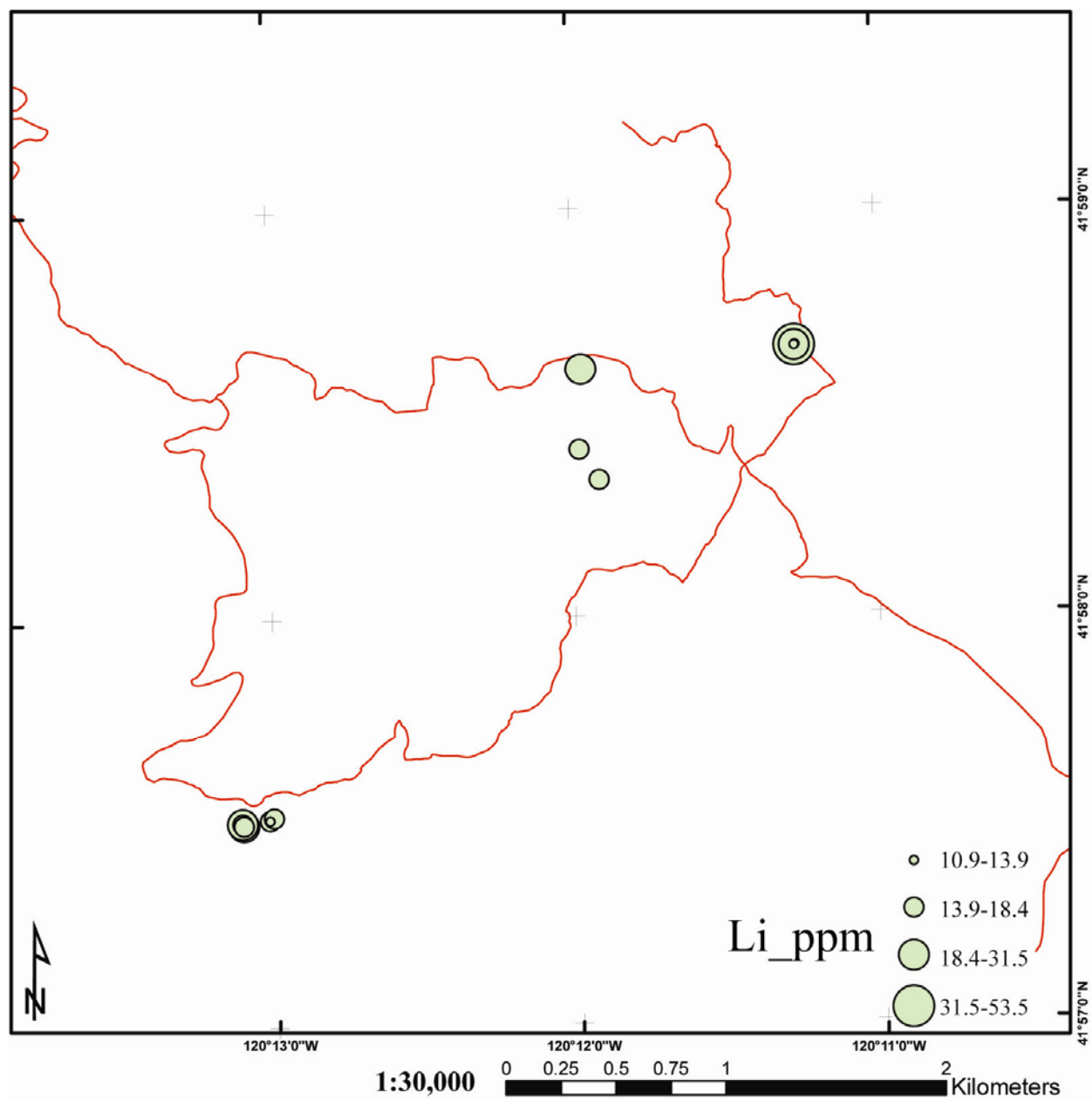


Figure 1-43. Map of Li outliers values. Li is an active component to the epithermal system.

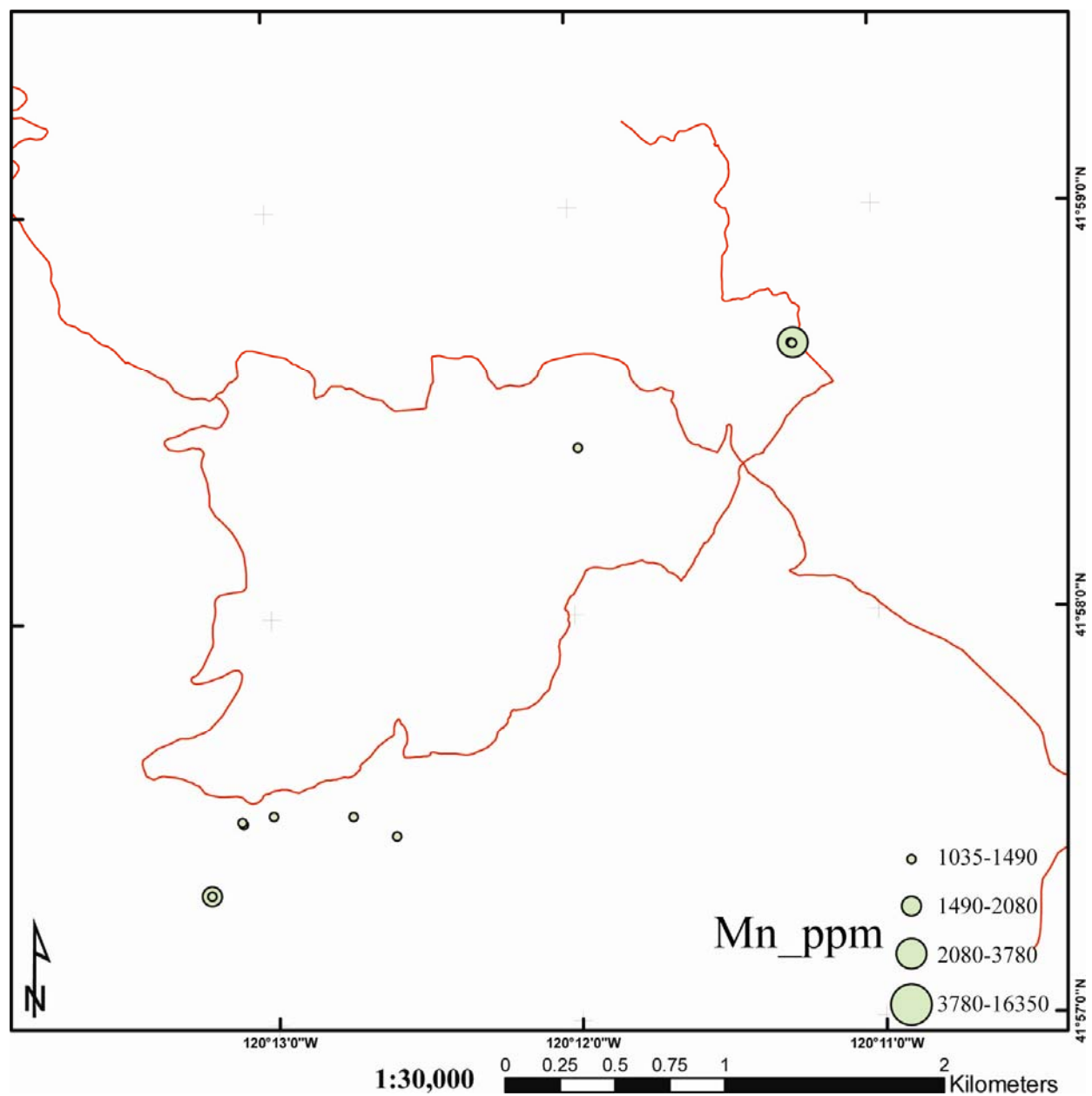


Figure 1-44. Map of Mn outlier values. Notable highs are encountered in the sunshine and consolidated camps.

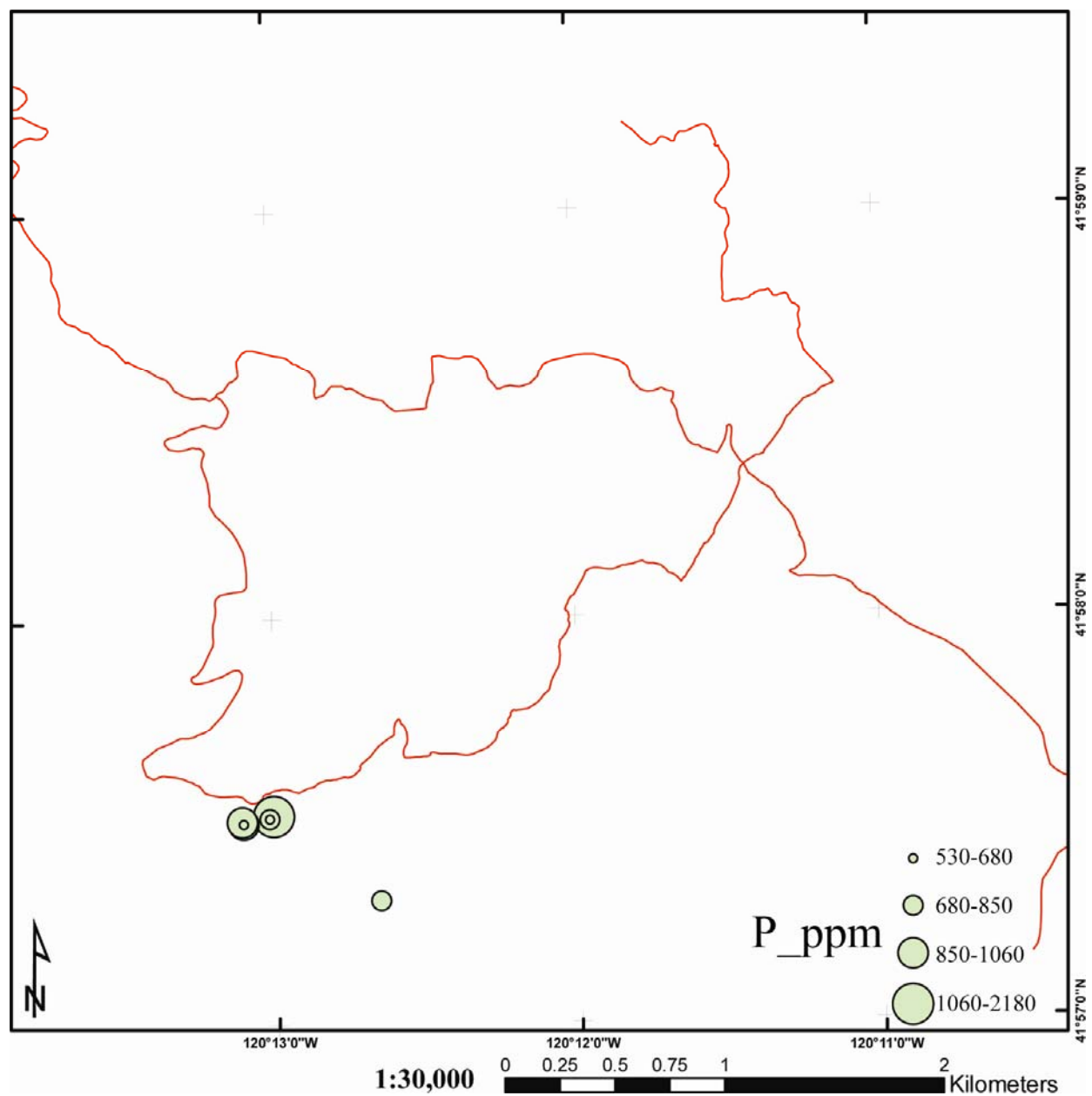


Figure 1-45. Map of P outlier values. All the outliers are concentrated along the NW-trending vein system of the Consolidated camps.

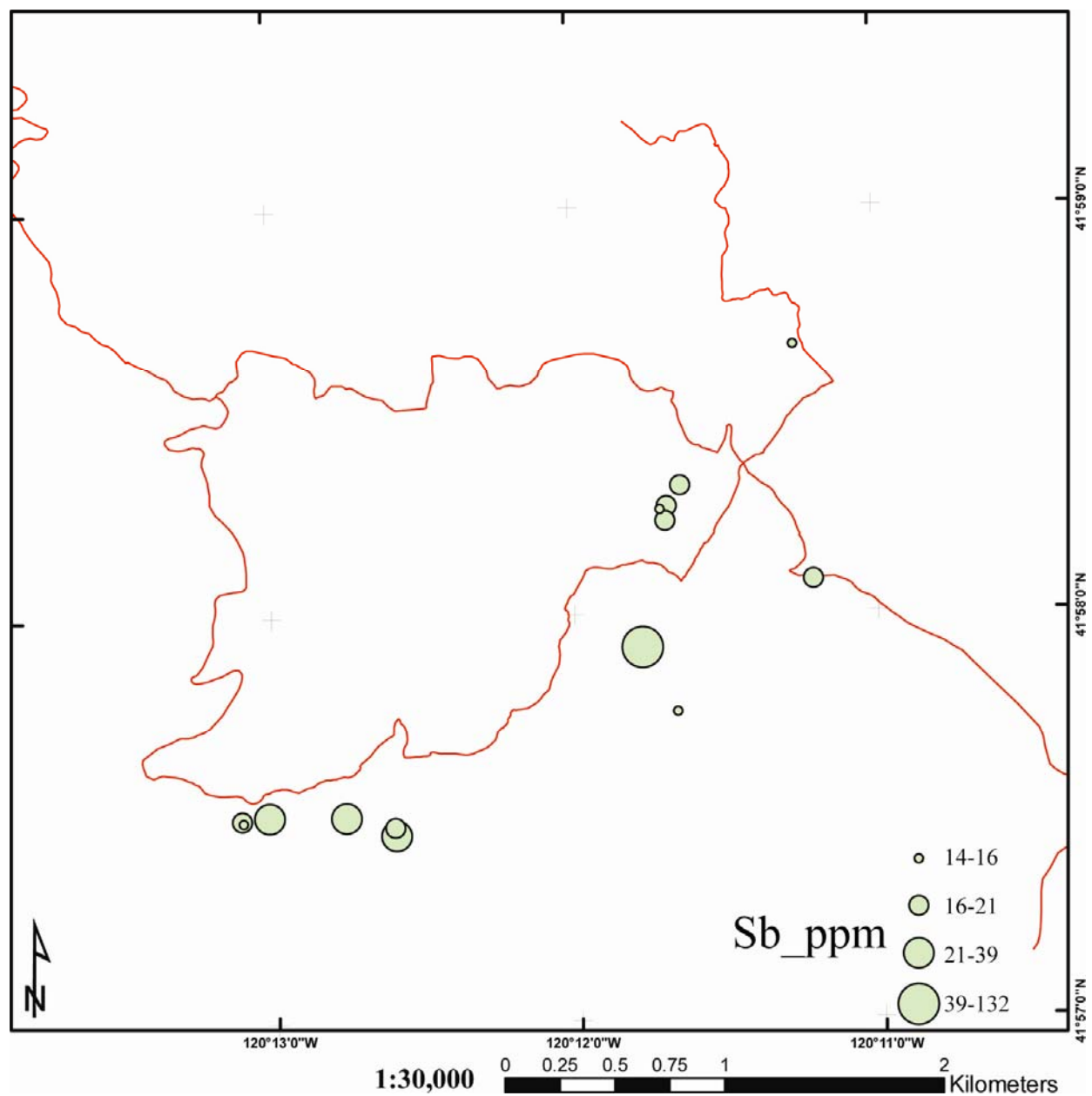


Figure 1-46. Map of Sb outlier values. Sb is a strong epithermal indicator and highs are concentrated in areas of maximum silicic alteration.

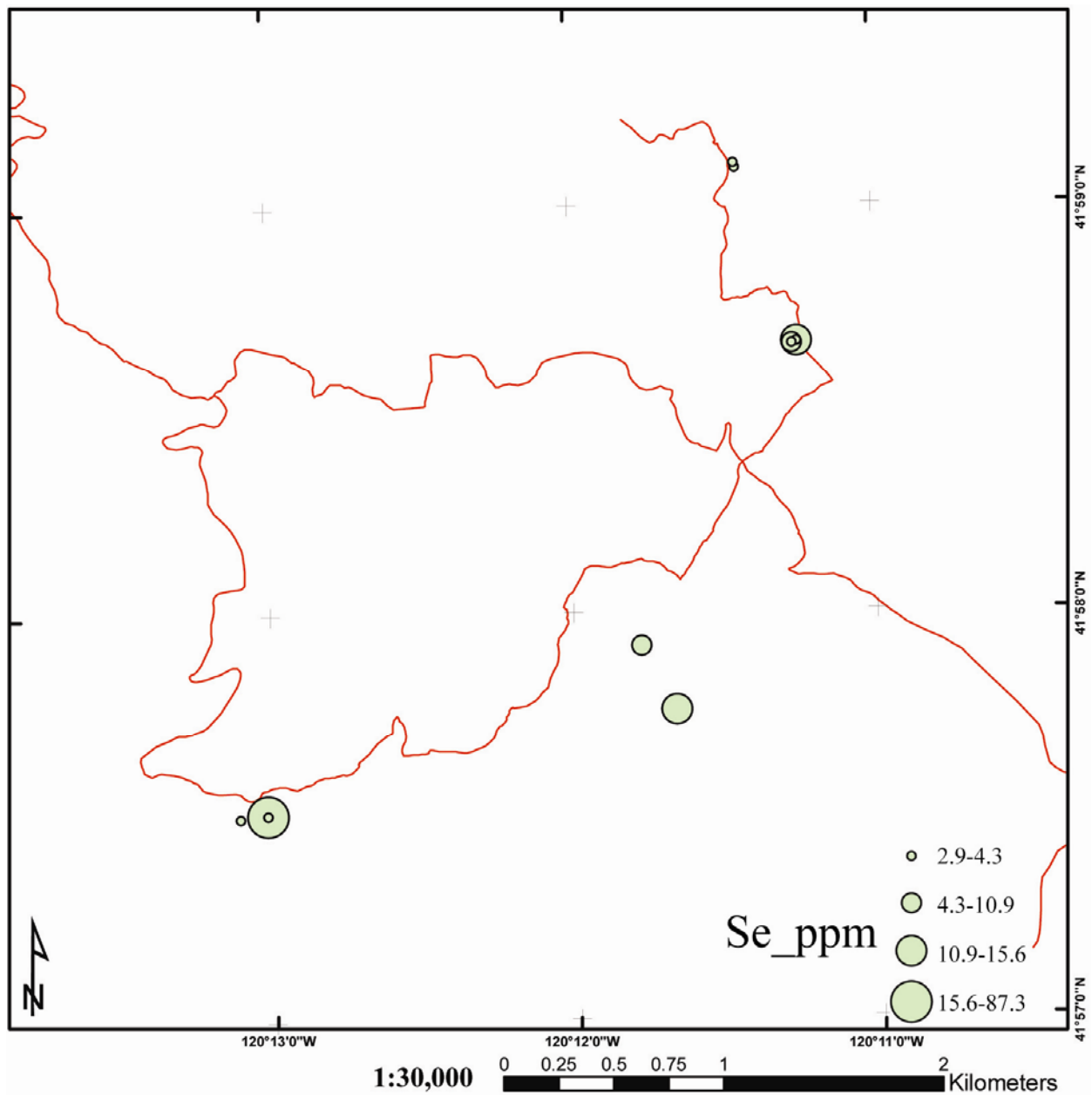


Figure 1-47. Map of Se outliers values. Se is an active component to the epithermal system.

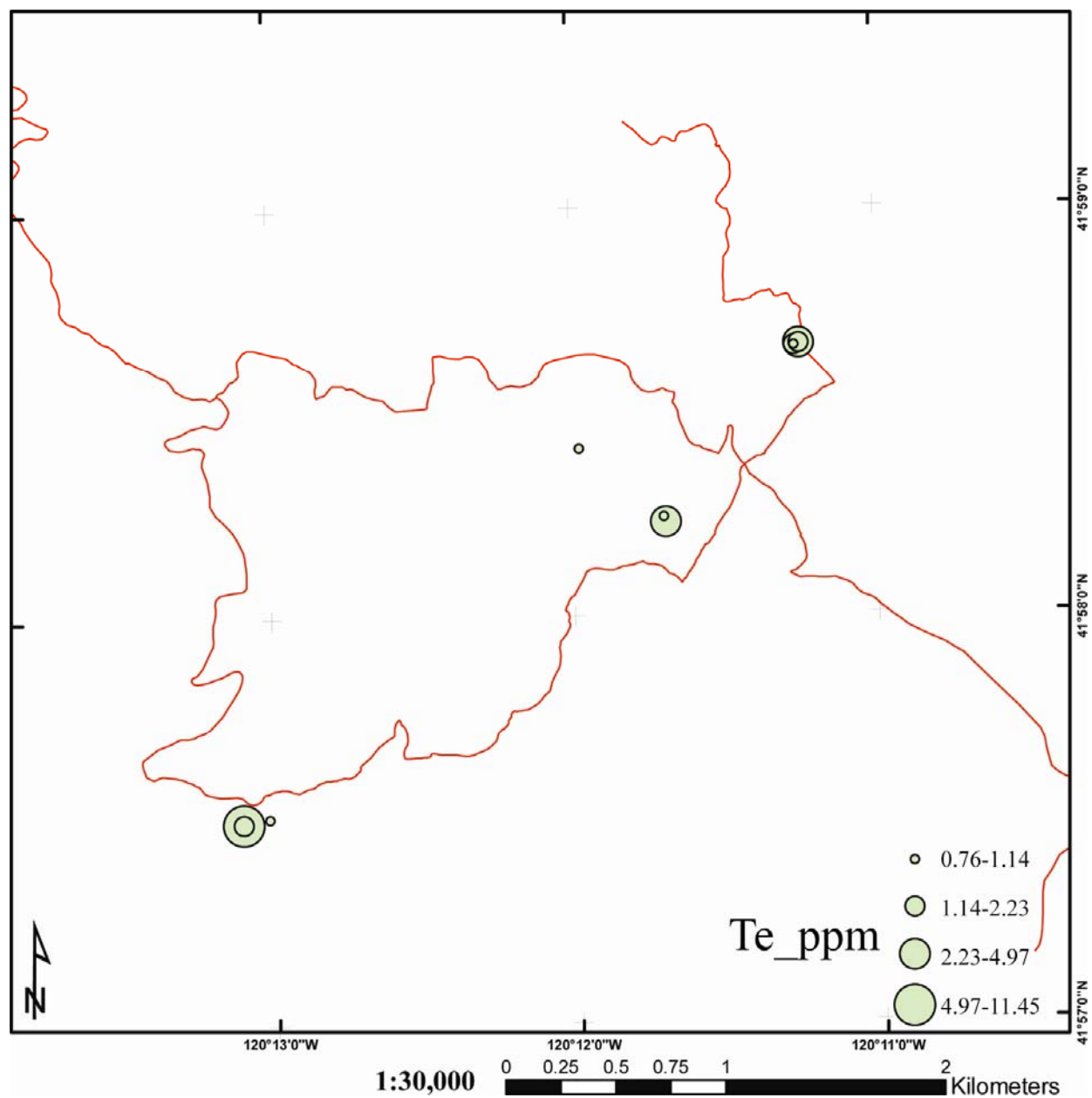


Figure 1-48. Map of Te outliers values. Te is a minor component to the epithermal system.

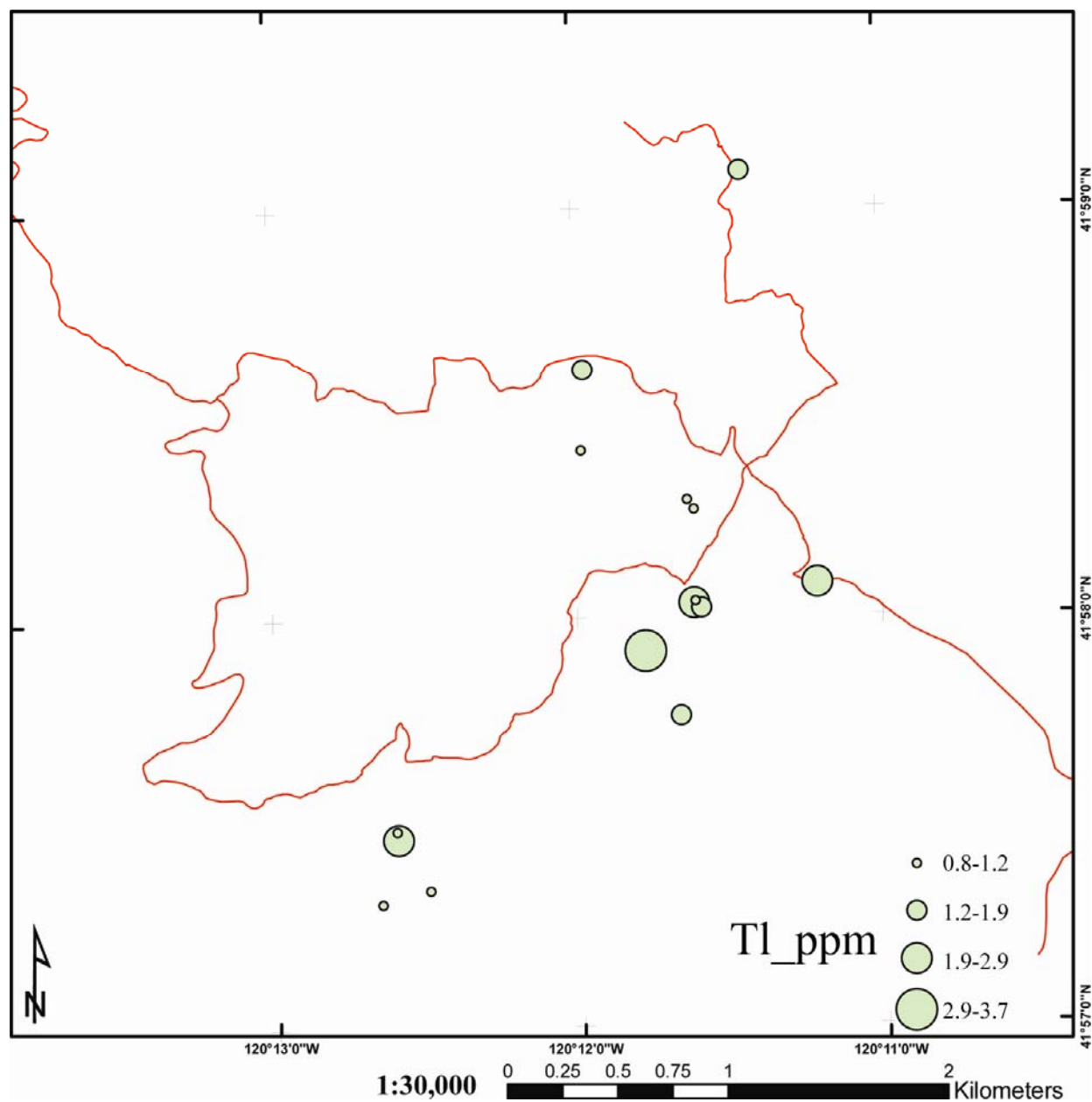


Figure 1-49. Map of Tl outlier values. Numerous highs are concentrated in the West Consolidated Camp.

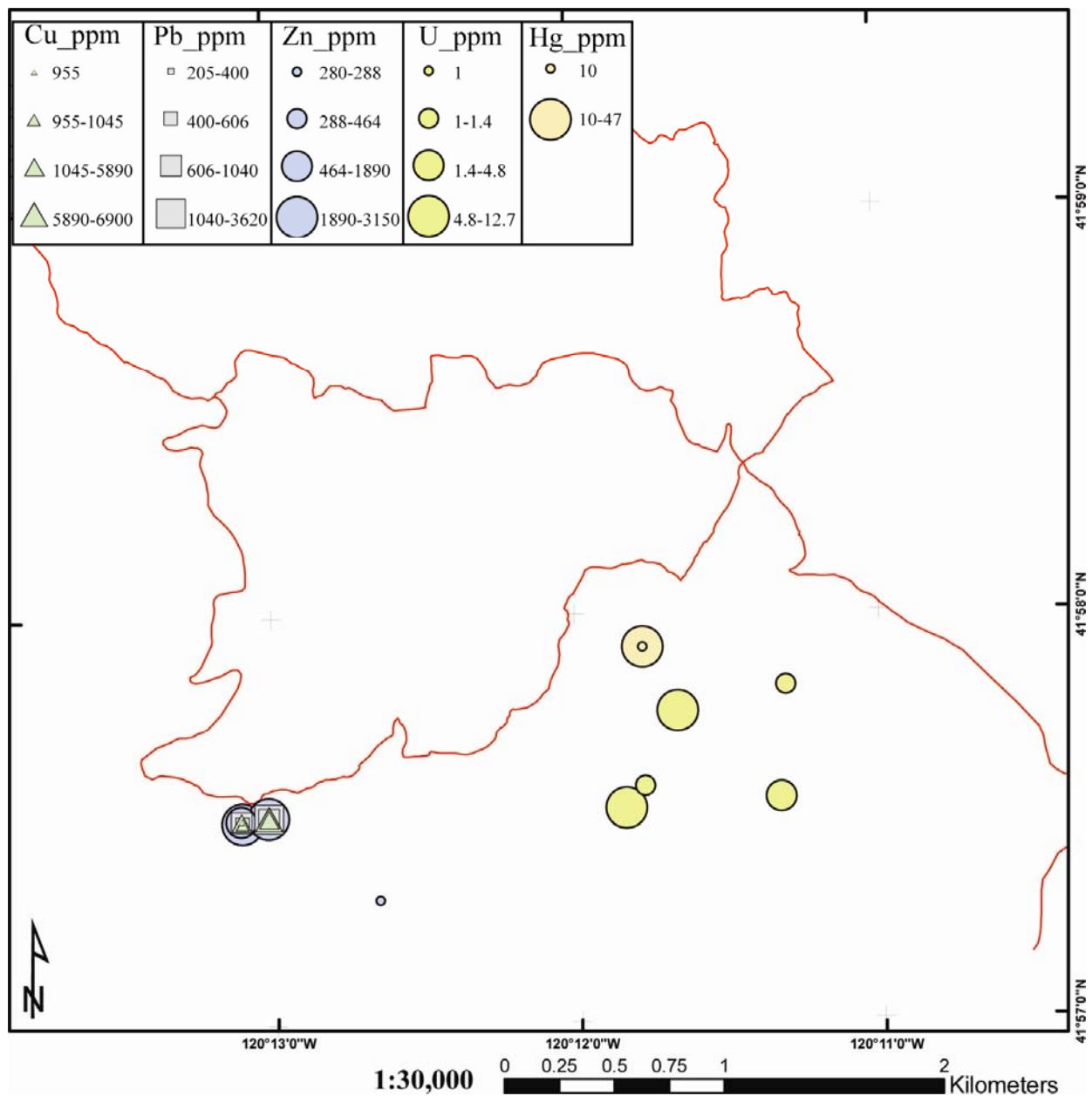


Figure 1-50. Map of outlier values for Cu, Zn, Pb, Hg, and U. These are all epithermal indicator elements, however values did not produce more than 7 seven outliers for each of these elements. Base metal (Cu, Pb, Zn) outliers are limited to the workings of West Consolidated.

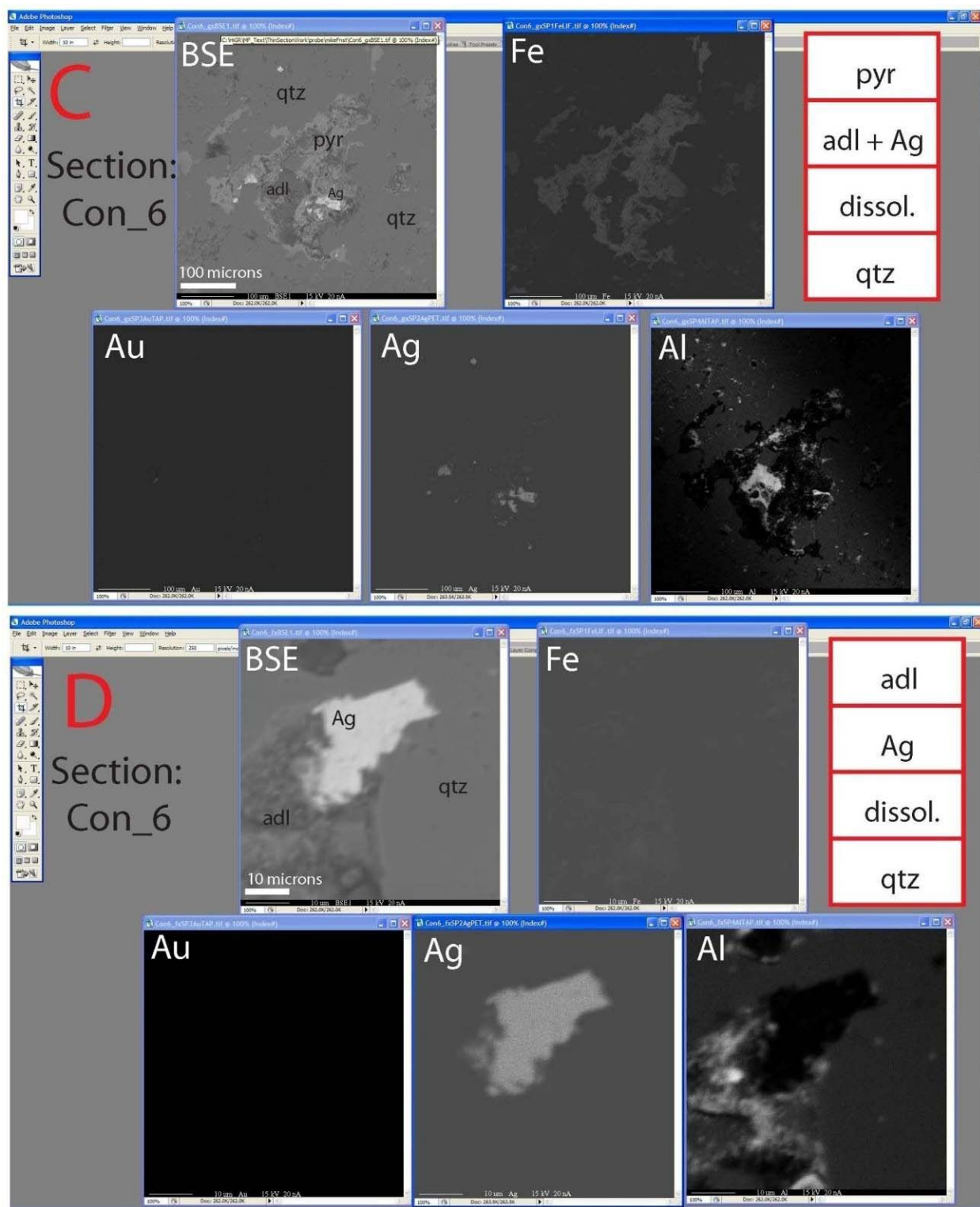


Figure 1-51. Electron Microprobe (EM) images and paragenetic observations, Section: Con_6, C&D

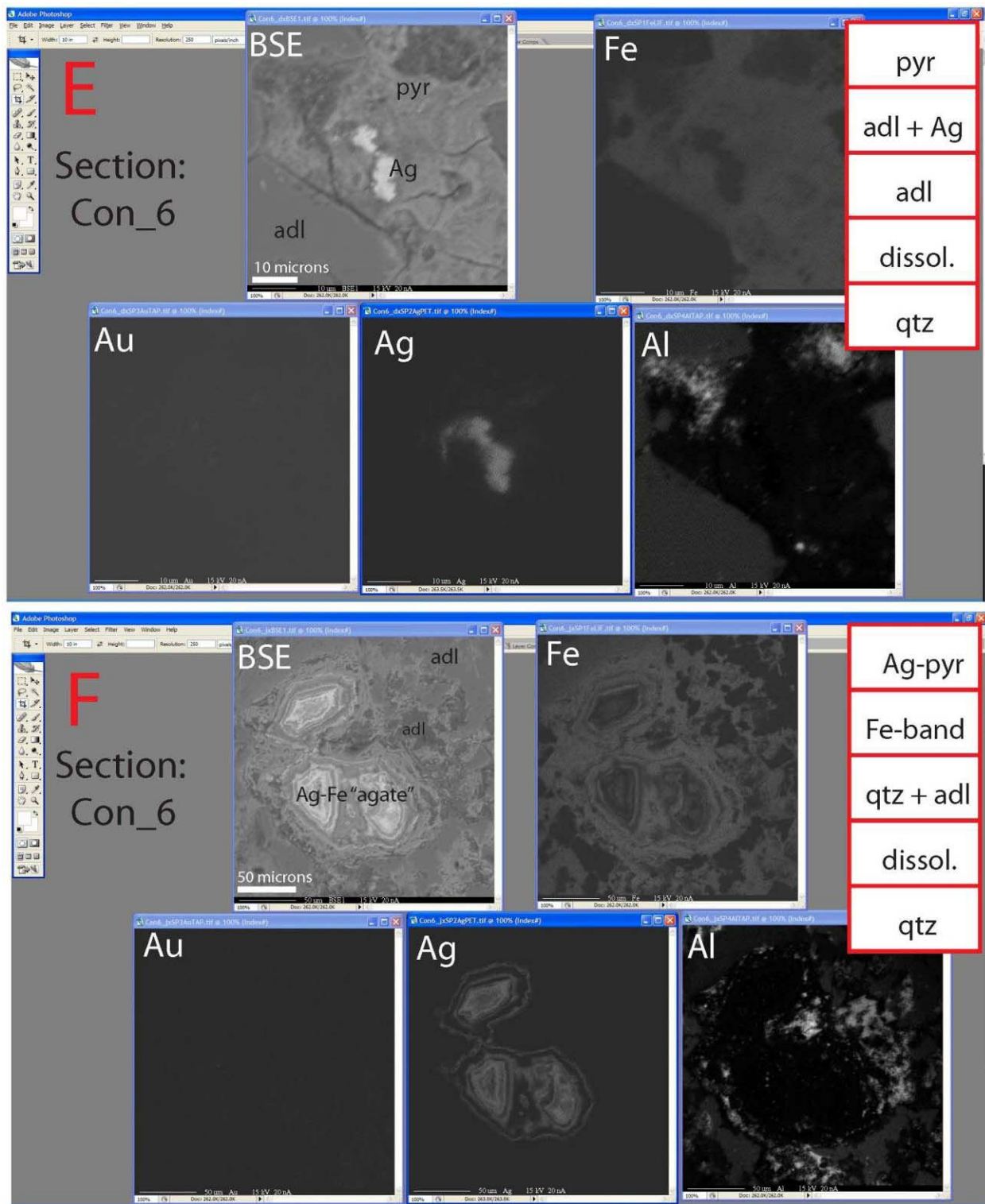


Figure 1-52. EM images and paragenetic observations, Section: Con_6, E&F

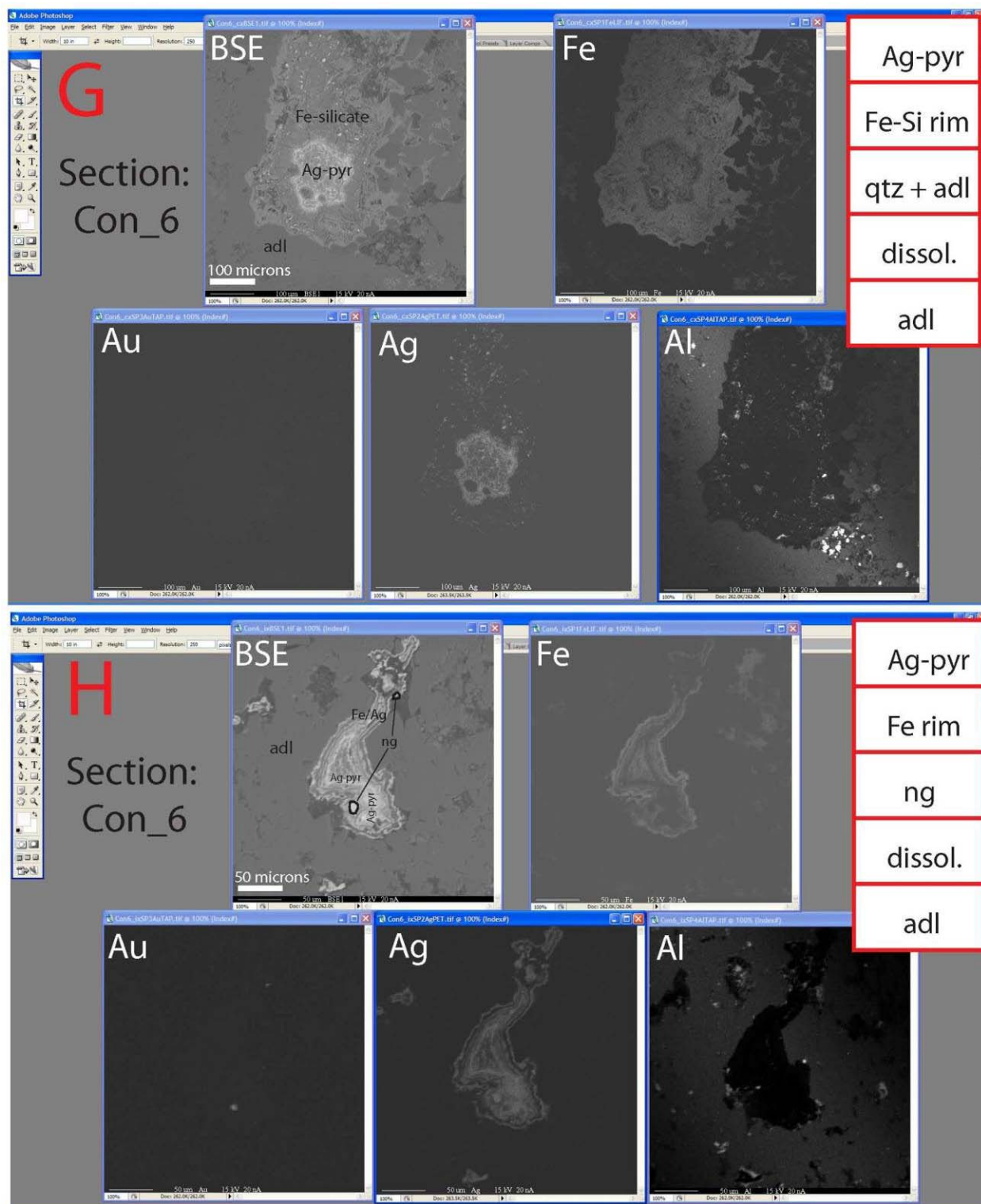


Figure 1-53. EM images and paragenetic observations, Section: Con_6, G&H

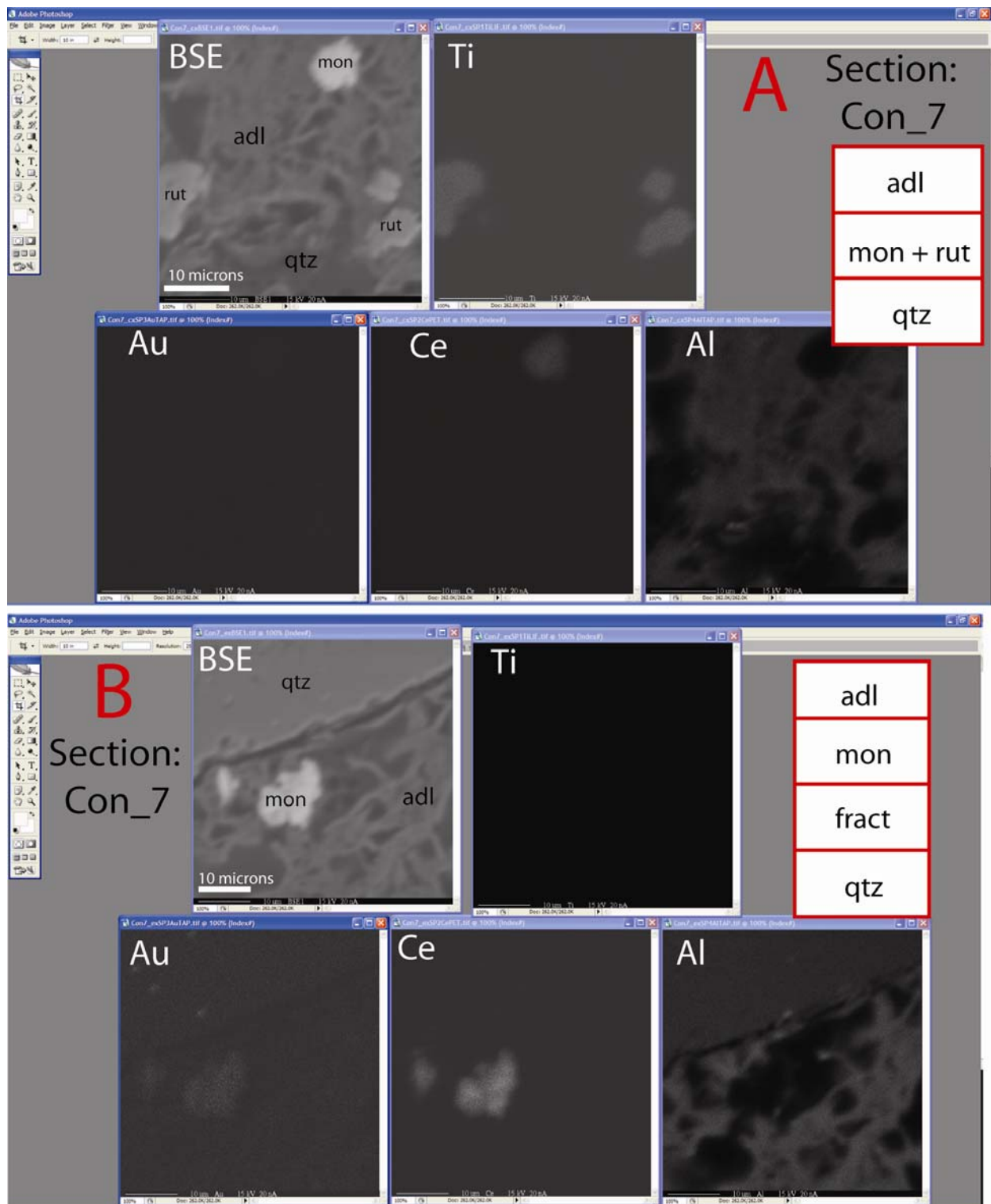


Figure 1-54. EM images and paragenetic observations, Section: Con_7, A&B

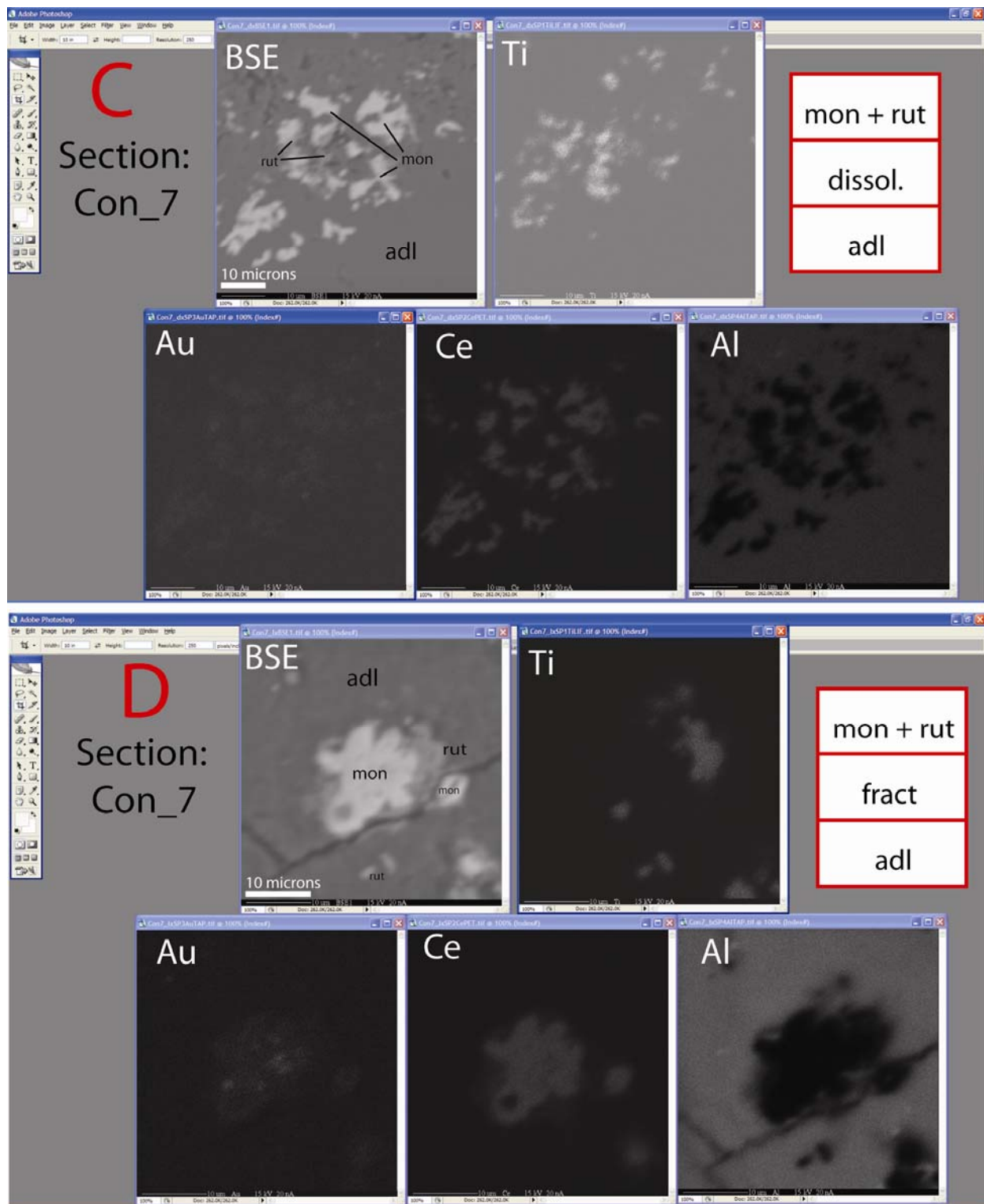


Figure 1-55. EM images and paragenetic observations, Section: Con_7, C&D

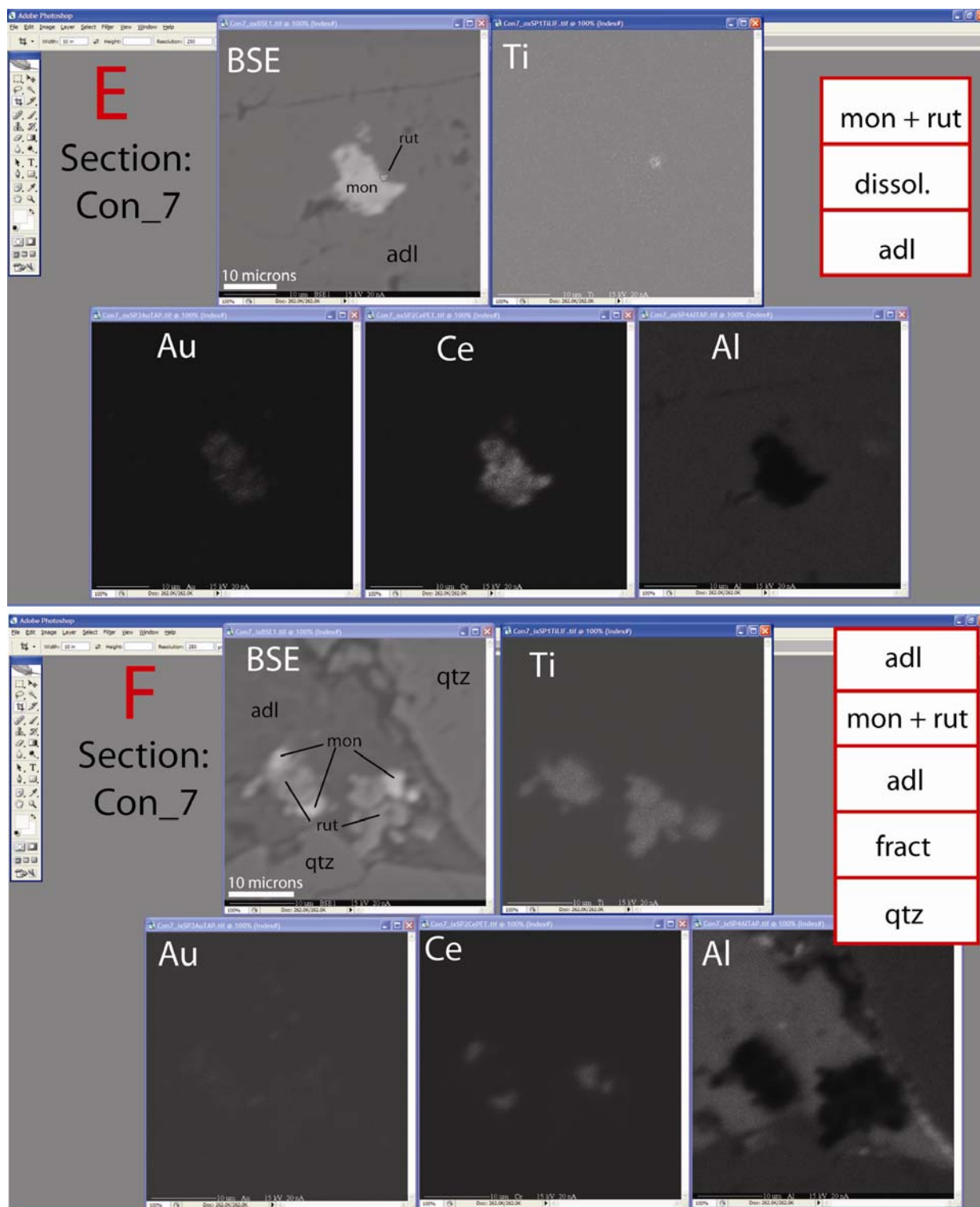


Figure 1-56. EM images and paragenetic observations, Section: Con_7, E&F

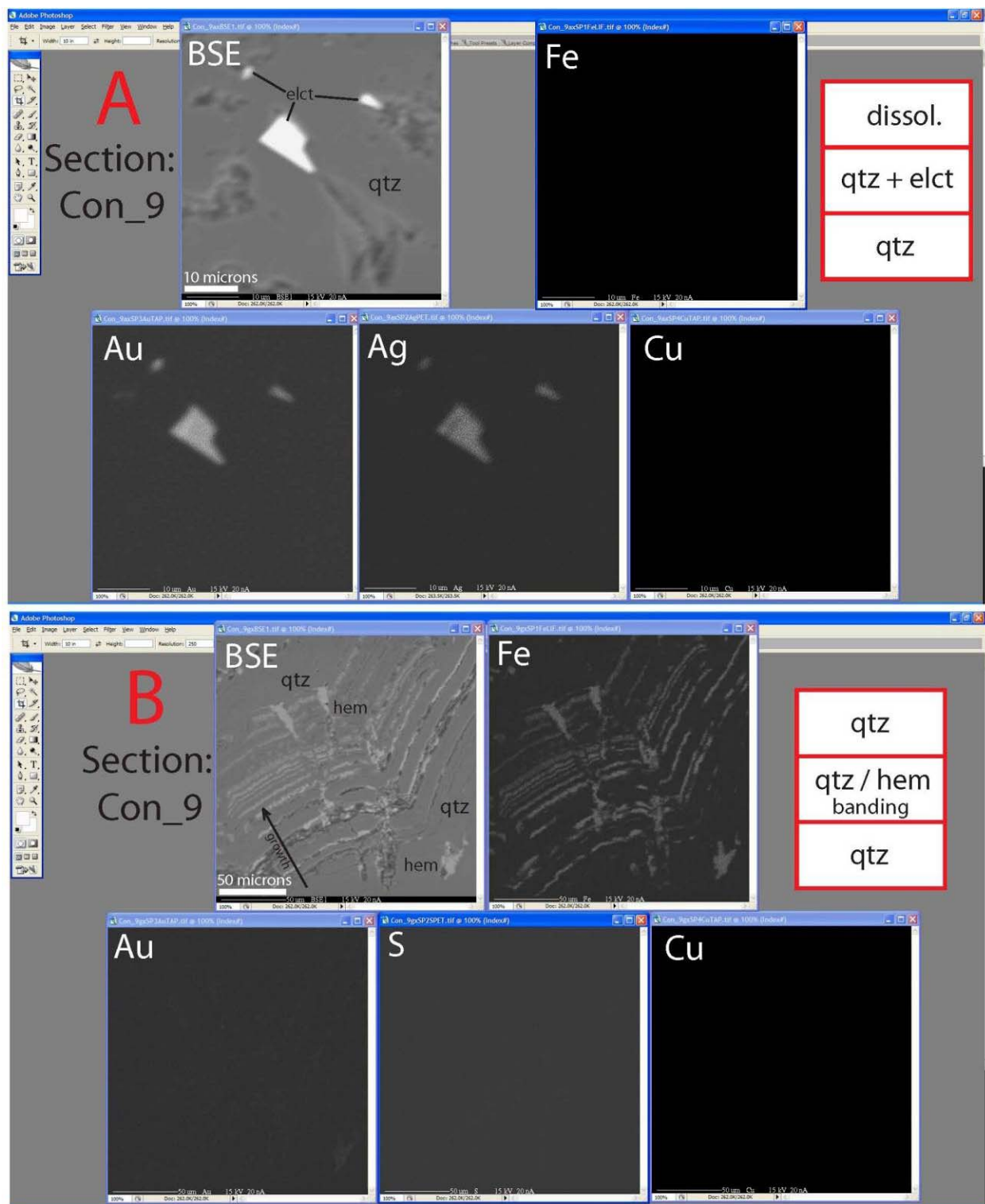


Figure 1-57. EM images and paragenetic observations, Section: Con_9, A&B

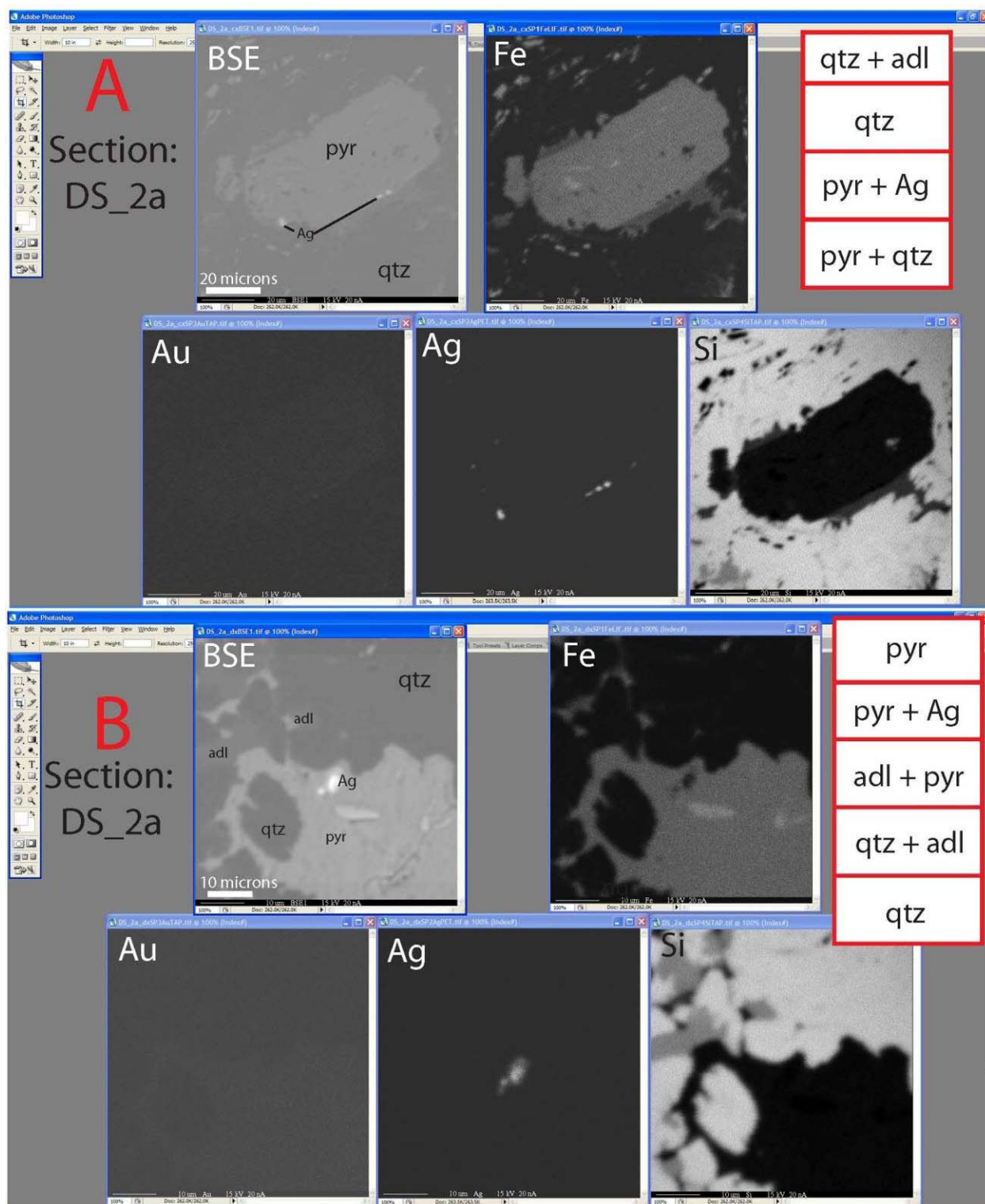


Figure 1-58. EM images and paragenetic observations, Section: DS_2a, A&B

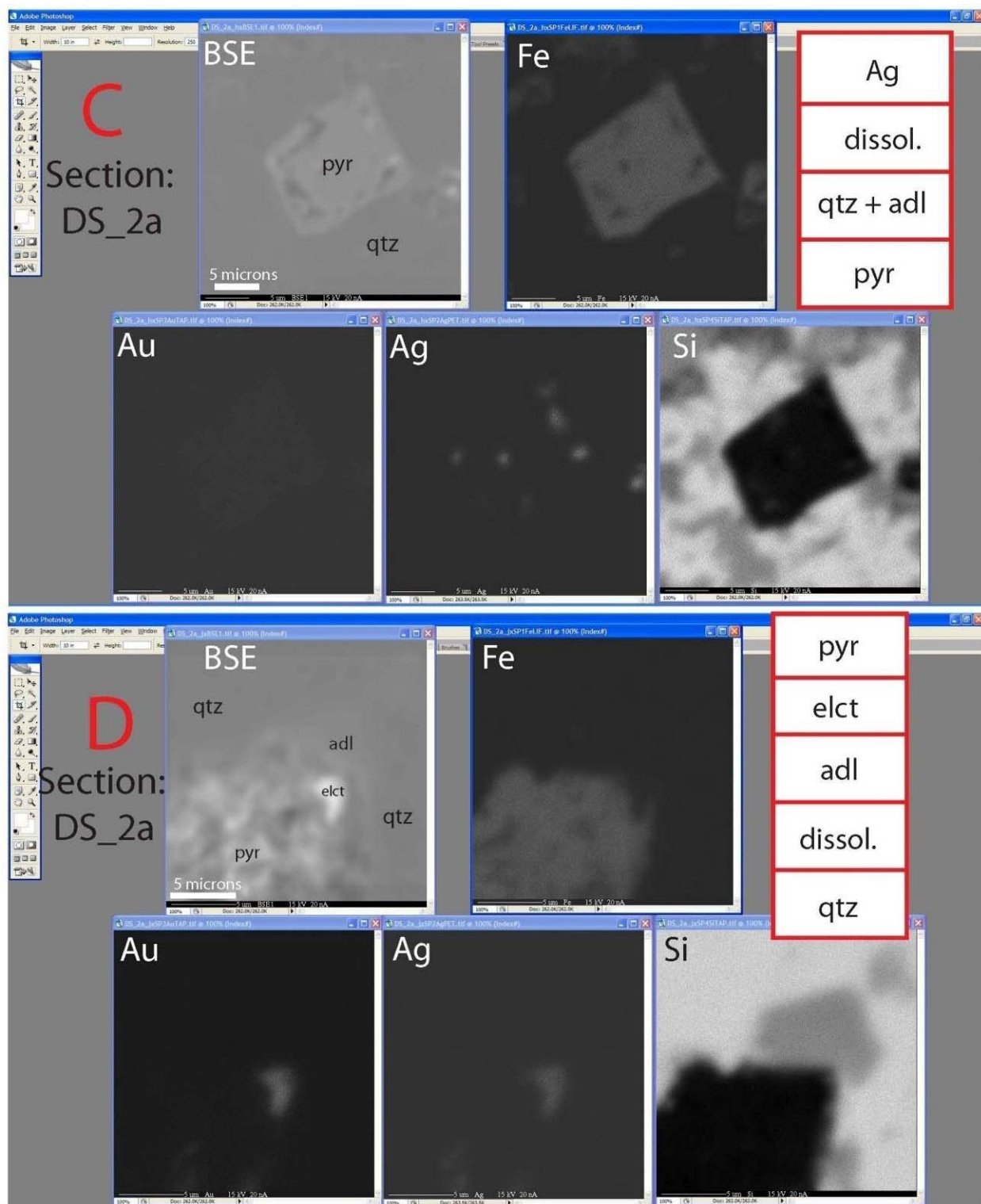


Figure 1-59. EM images and paragenetic observations, Section: DS_2a, C&D

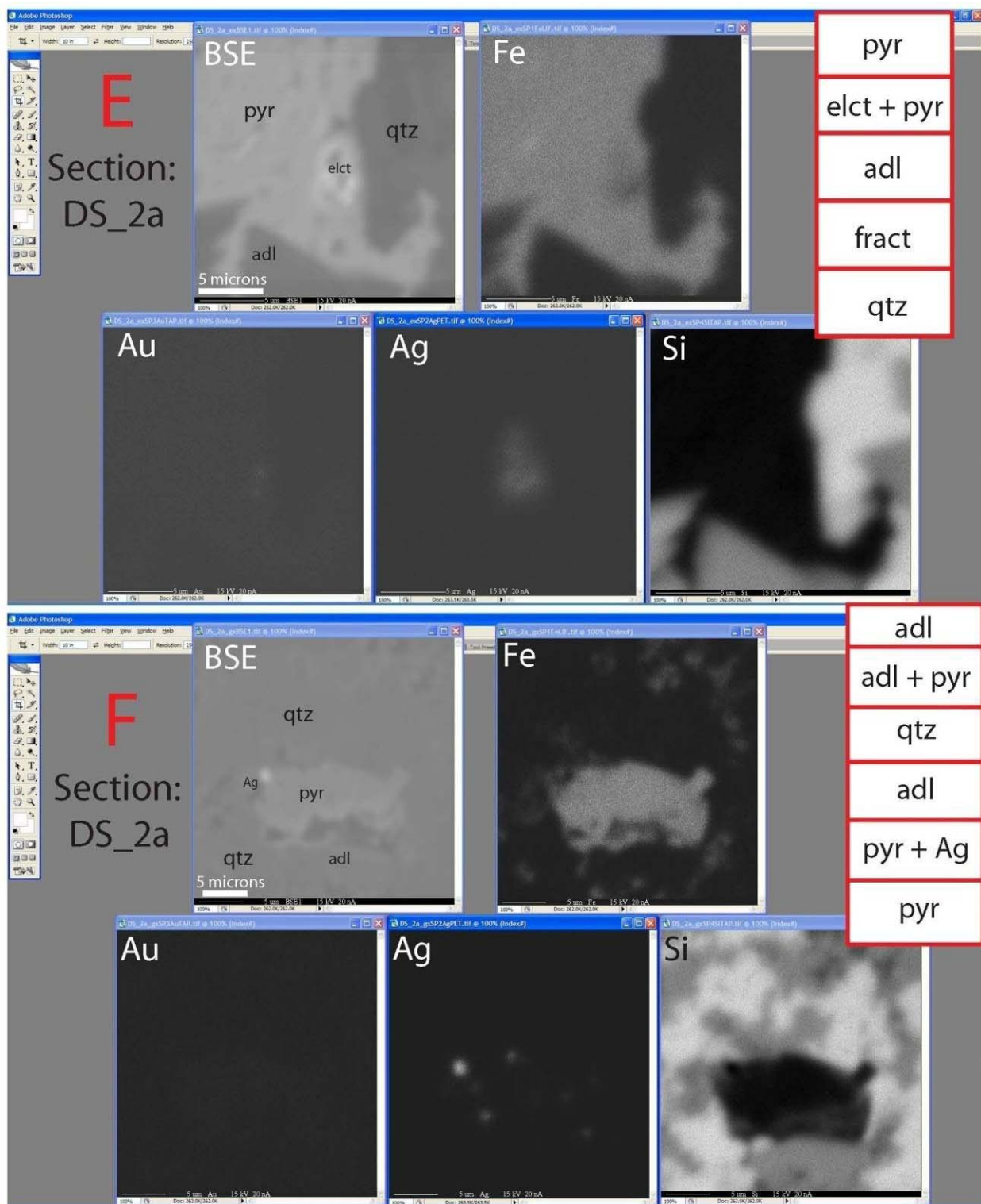


Figure 1-60. EM images and paragenetic observations, Section: DS_2a, E&F

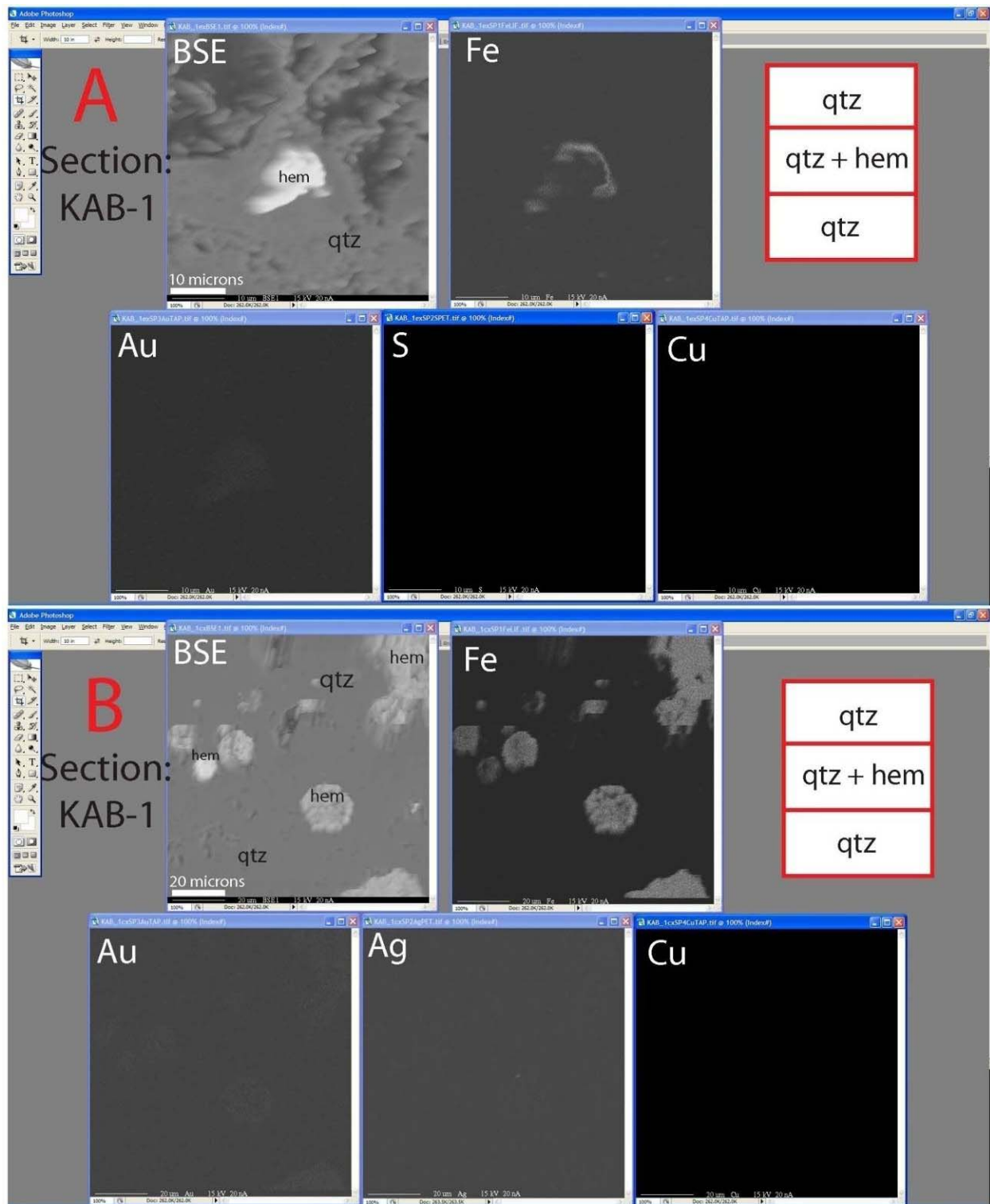


Figure 1-61. EM images and paragenetic observations, Section: KAB-1, A&B

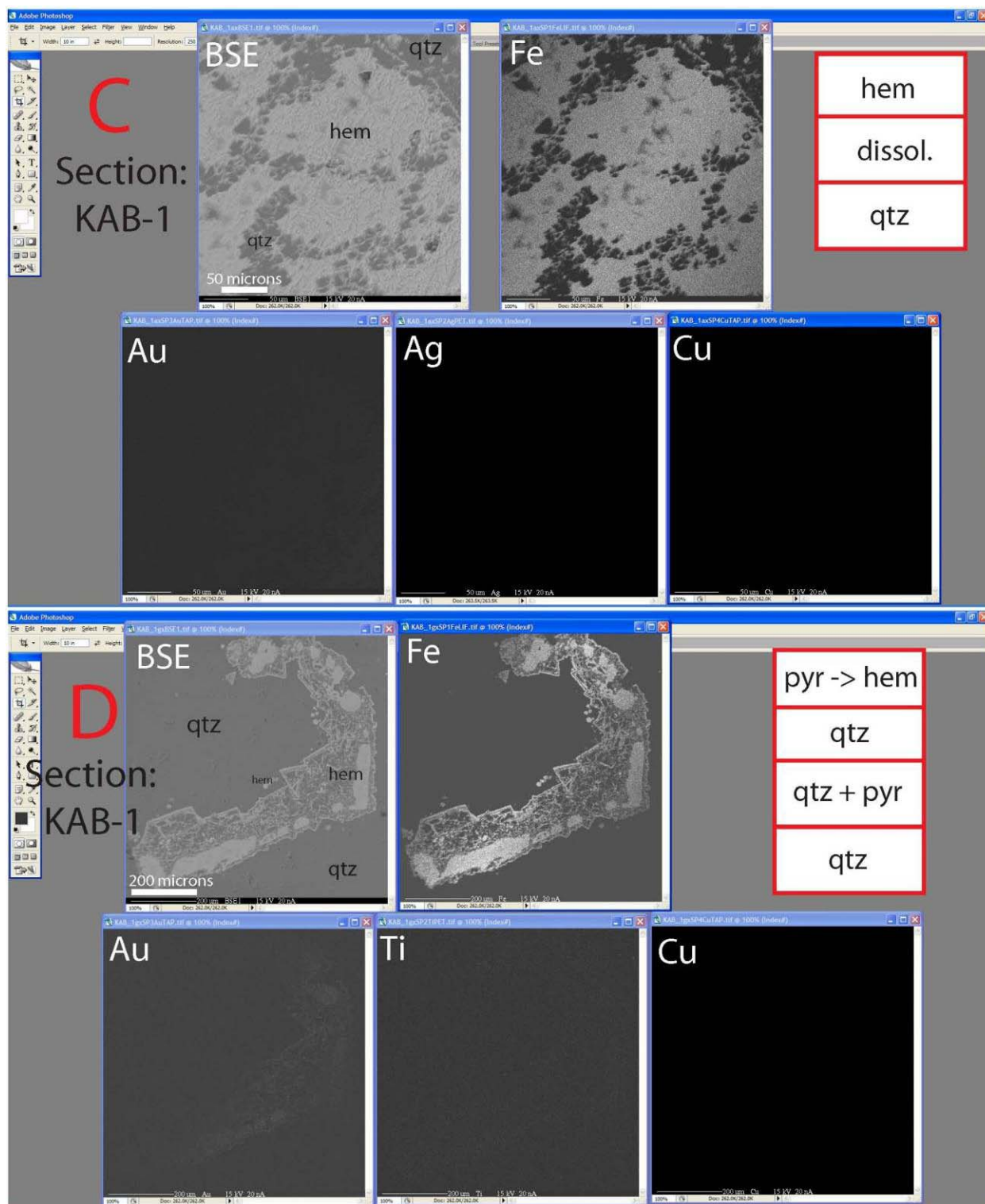


Figure 1-62. EM images and paragenetic observations, Section: KAB-1, C&D

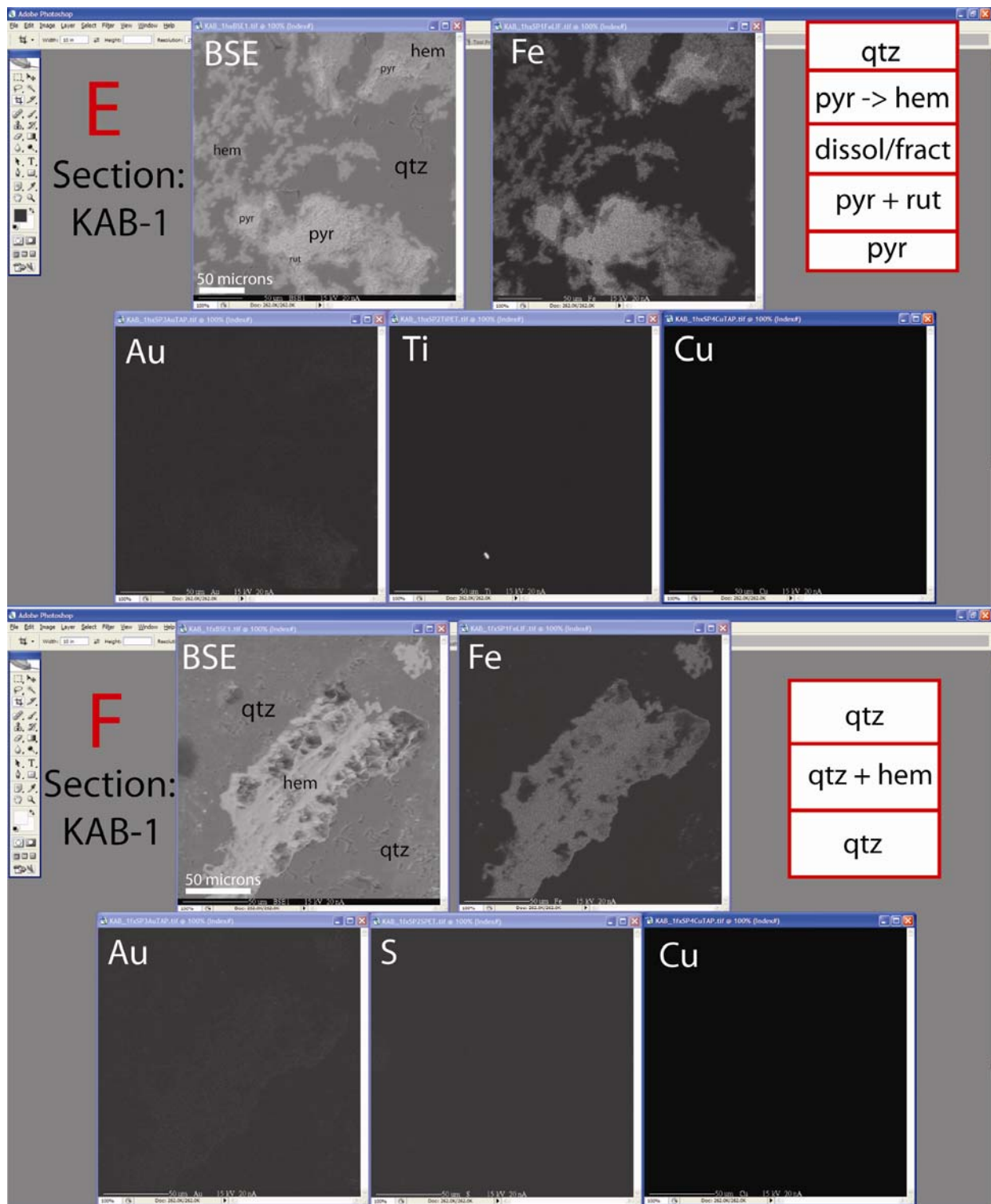


Figure 1-63. EM images and paragenetic observations, Section: KAB-1, E&F

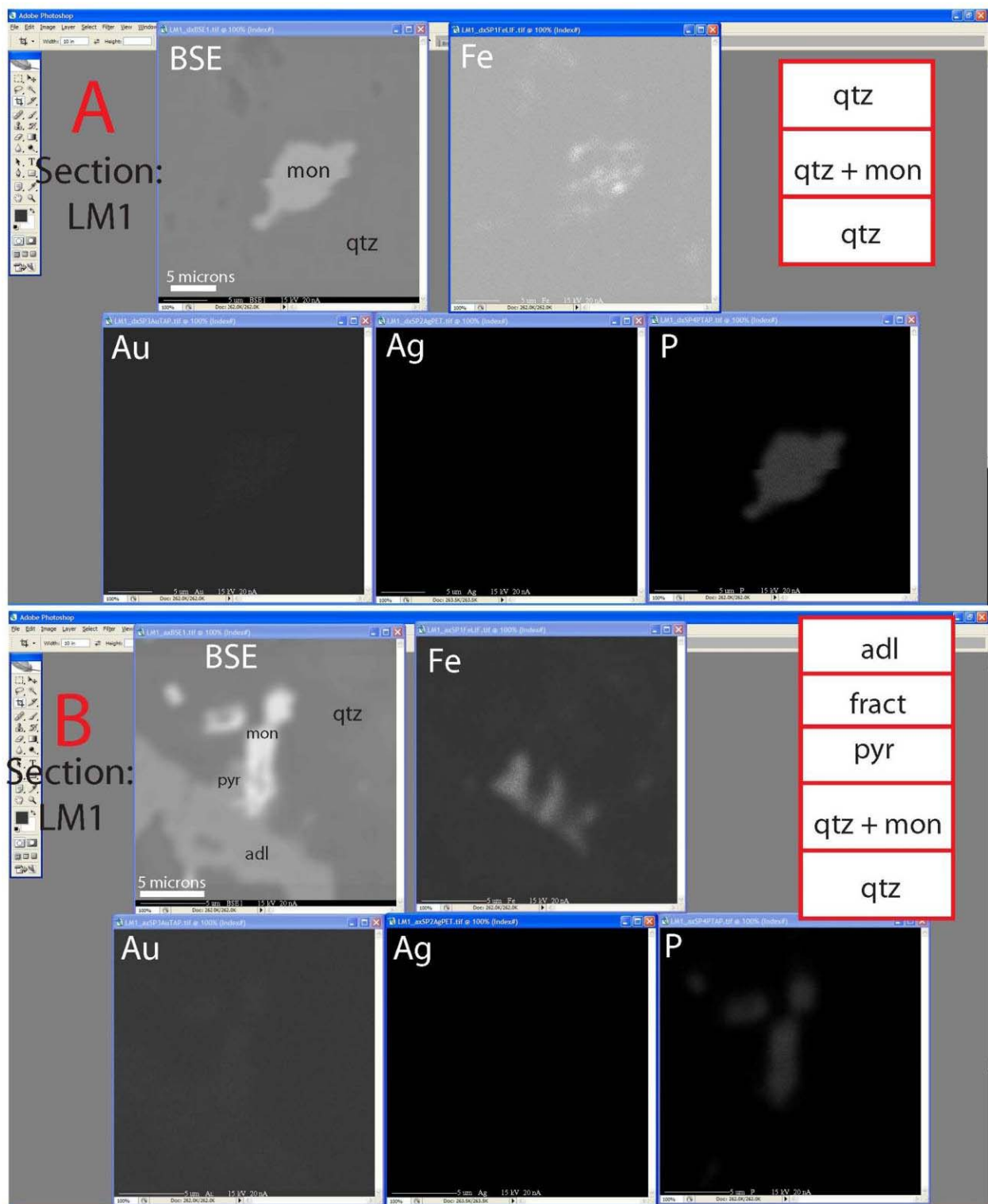


Figure 1-64. EM images and paragenetic observations, Section: LM-1, A&B

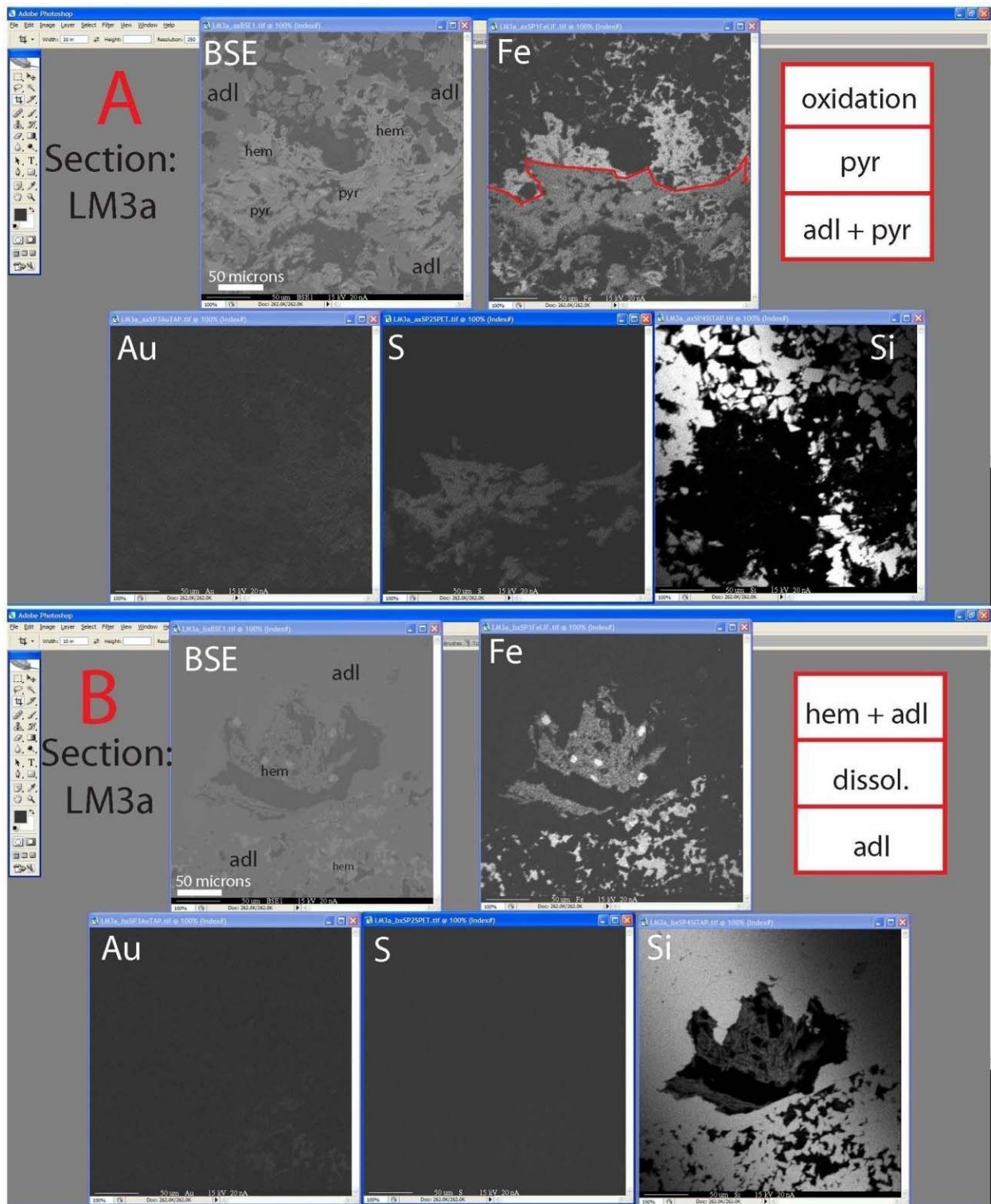


Figure 1-65. EM images and paragenetic observations, Section: LM-3a, A&B

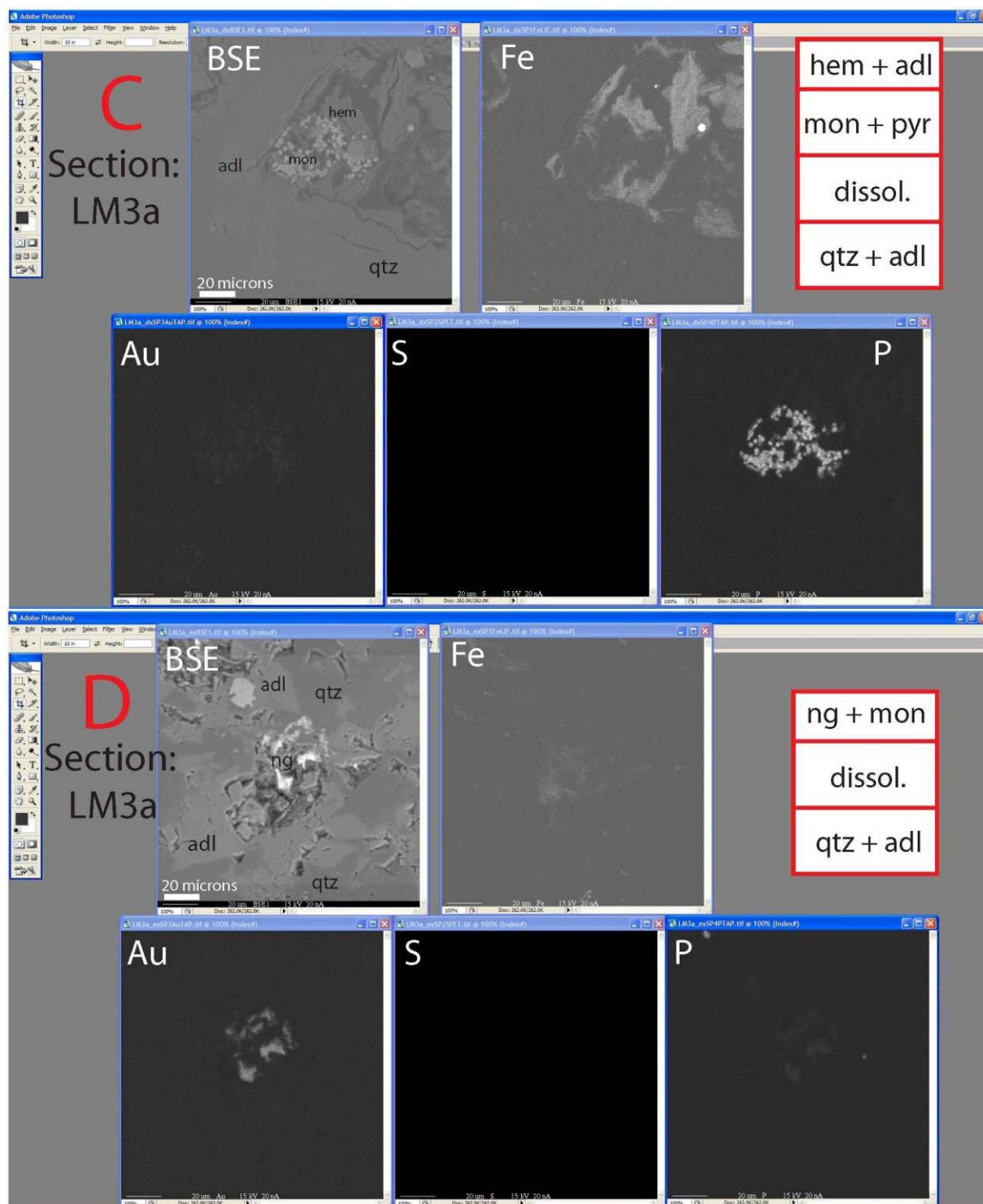


Figure 1-66. EM images and paragenetic observations, Section: LM-3a, C&D

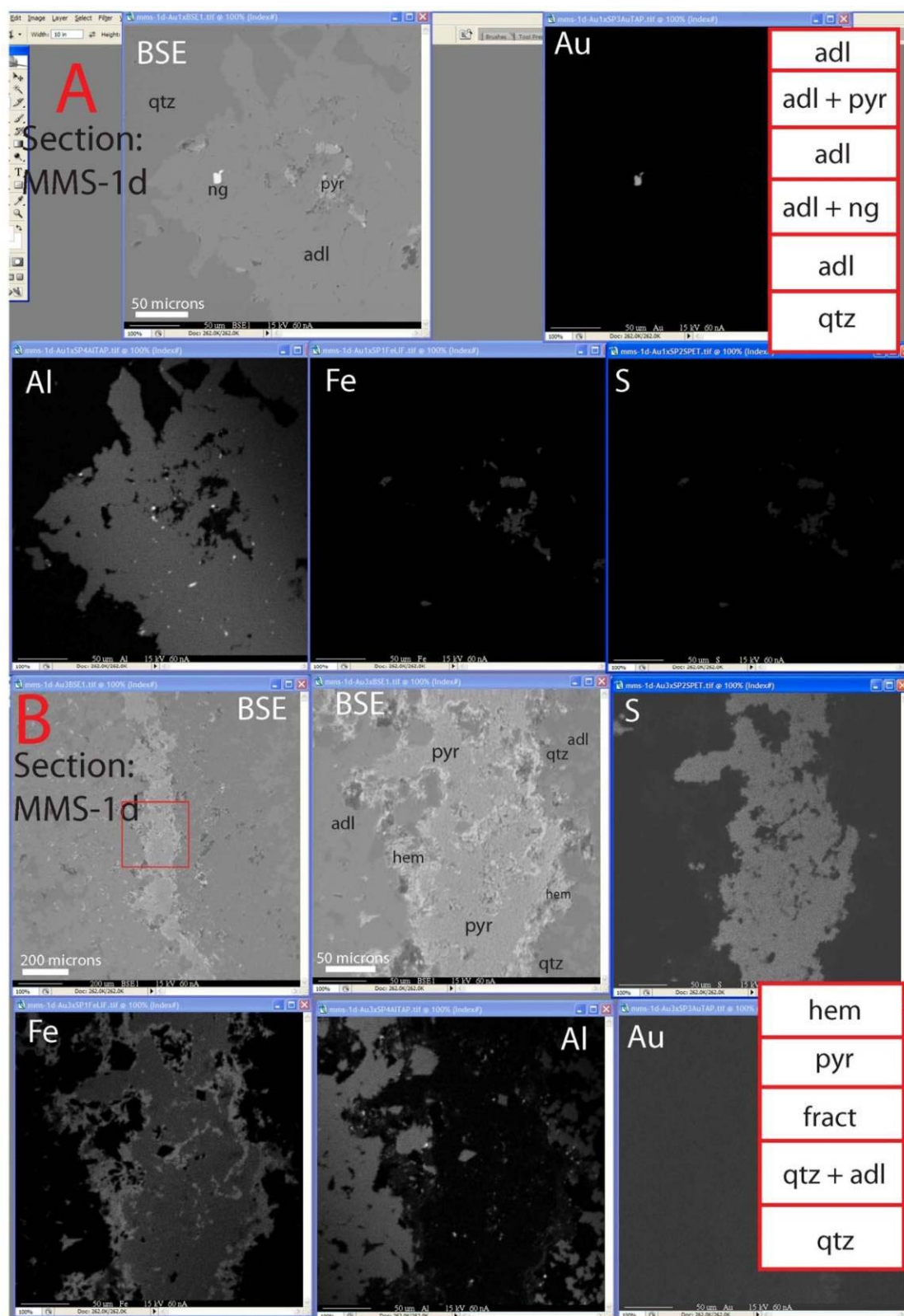


Figure 1-67. EM images and paragenetic observations, Section: MMS-1d, A&B

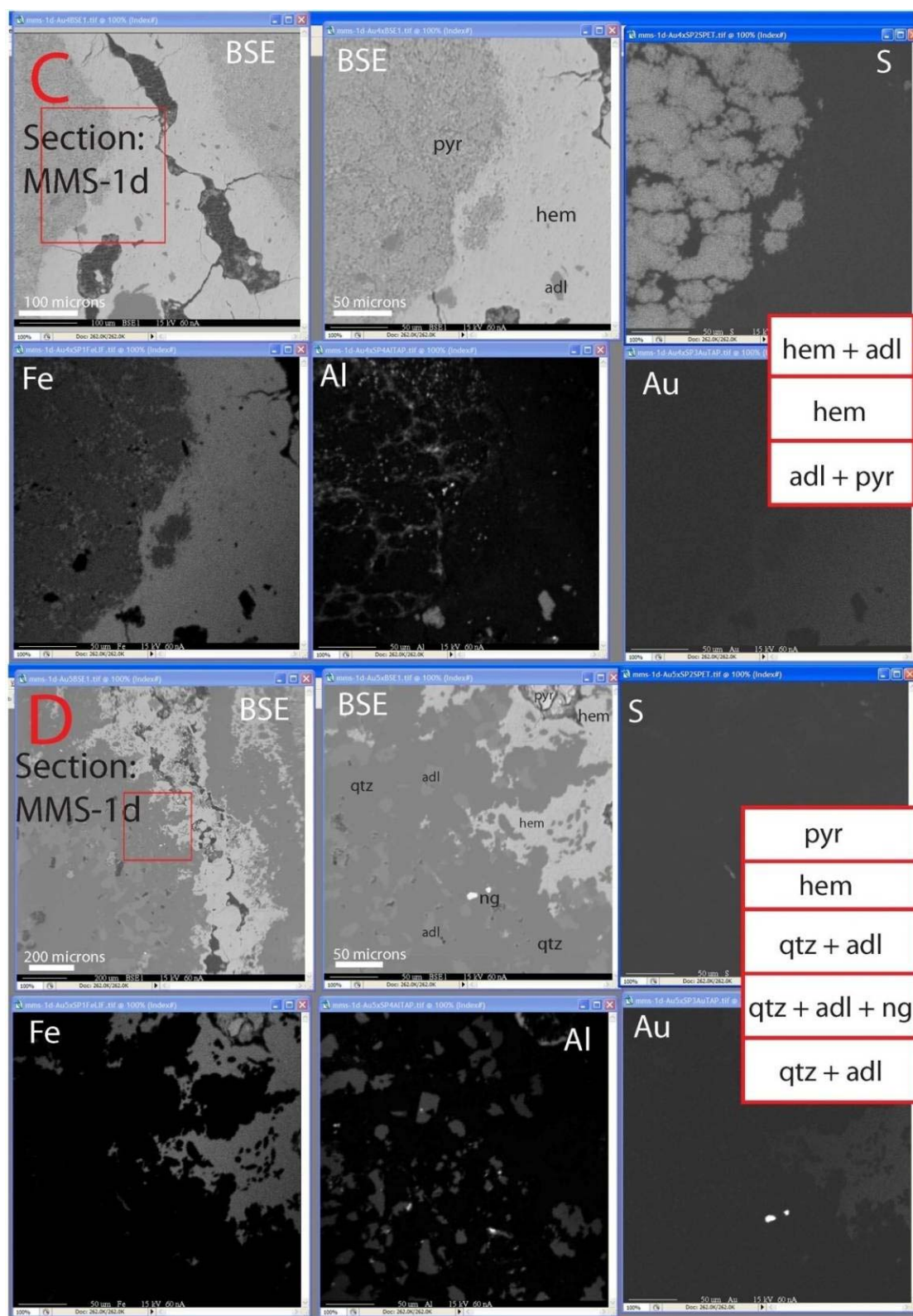


Figure 1-68. EM images and paragenetic observations, Section: MMS-1d, C&D

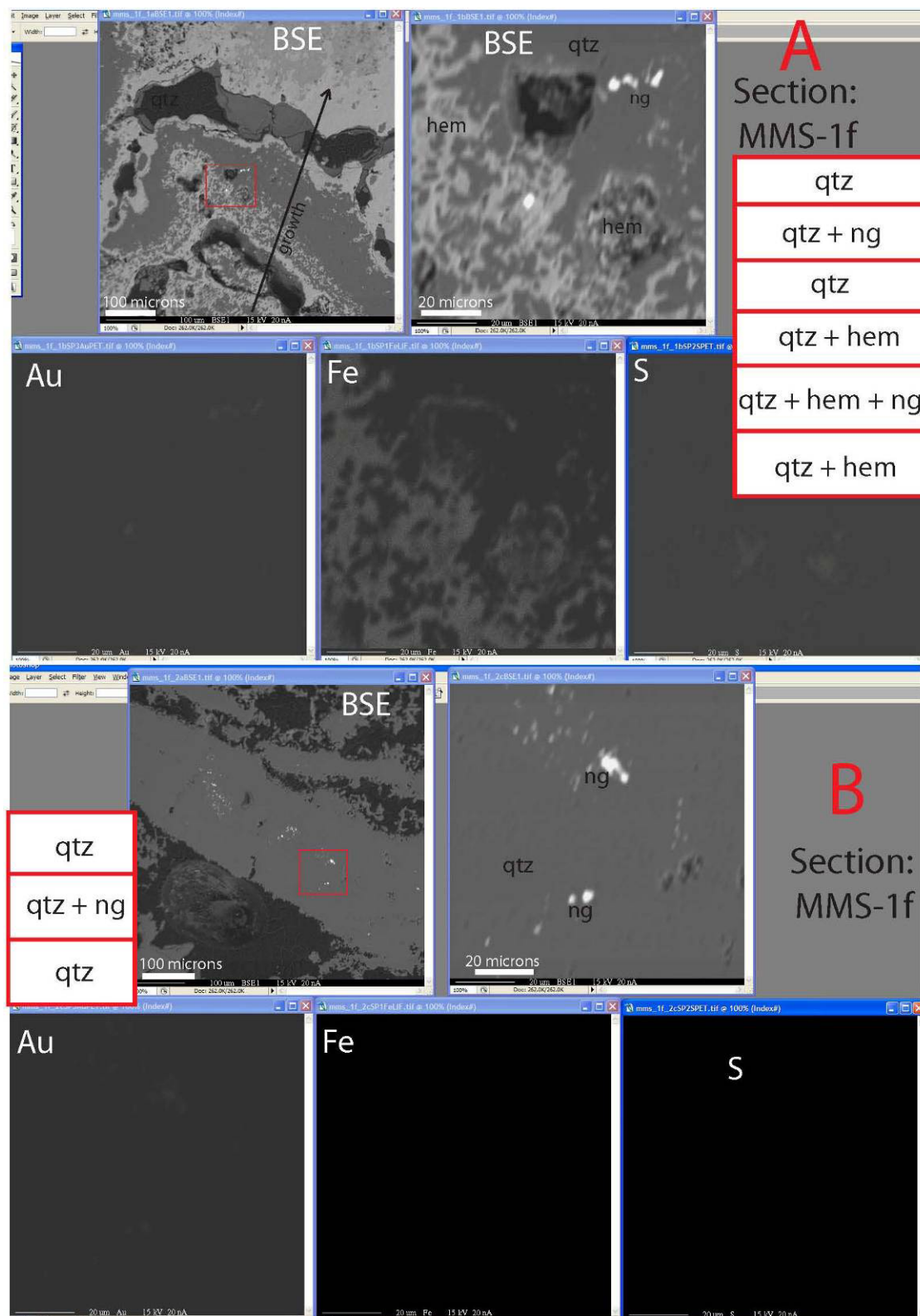


Figure 1-69. EM images and paragenetic observations, Section: MMS-1f, A&B

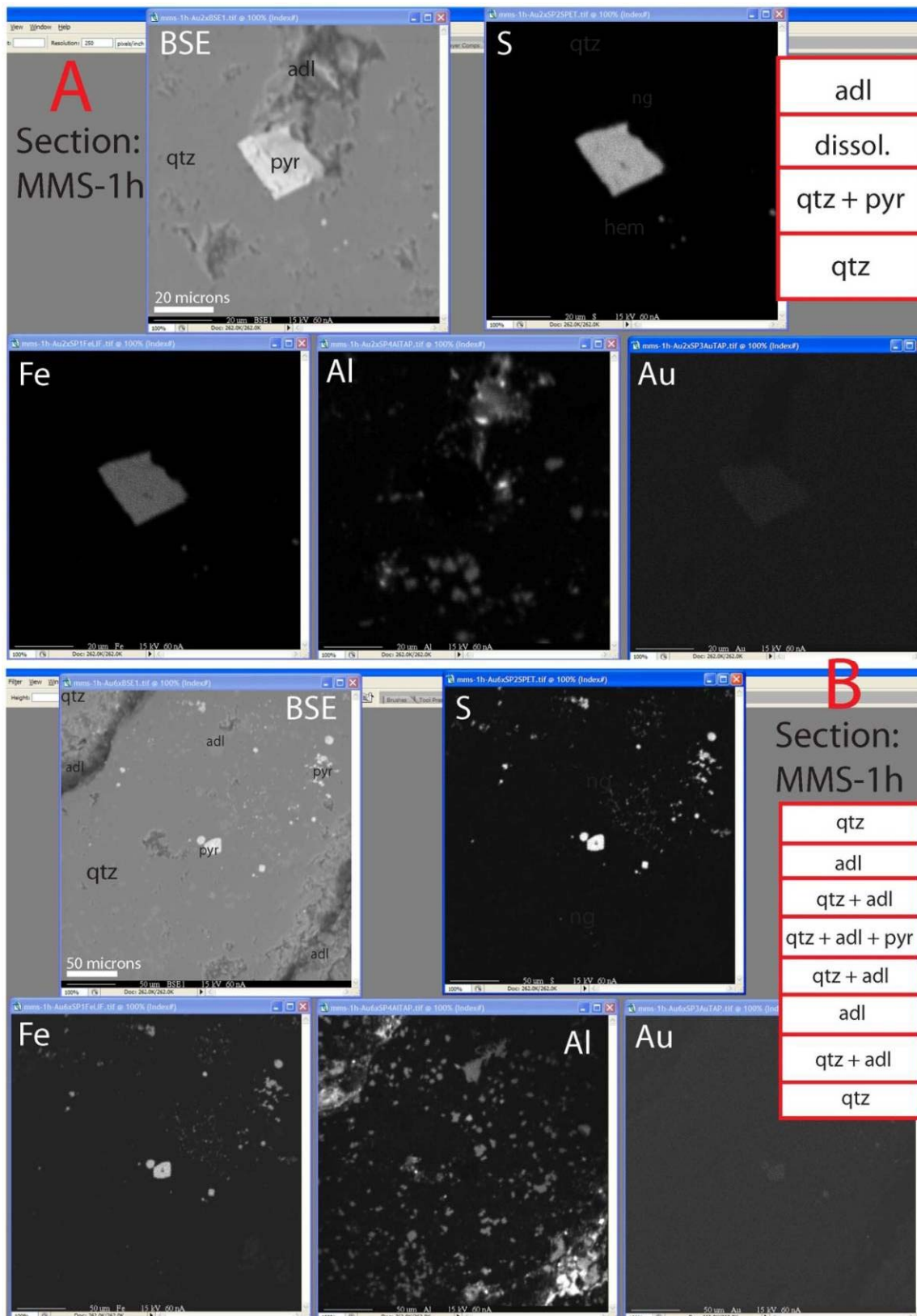


Figure 1-70. EM images and paragenetic observations, Section: MMS-1h, A&B

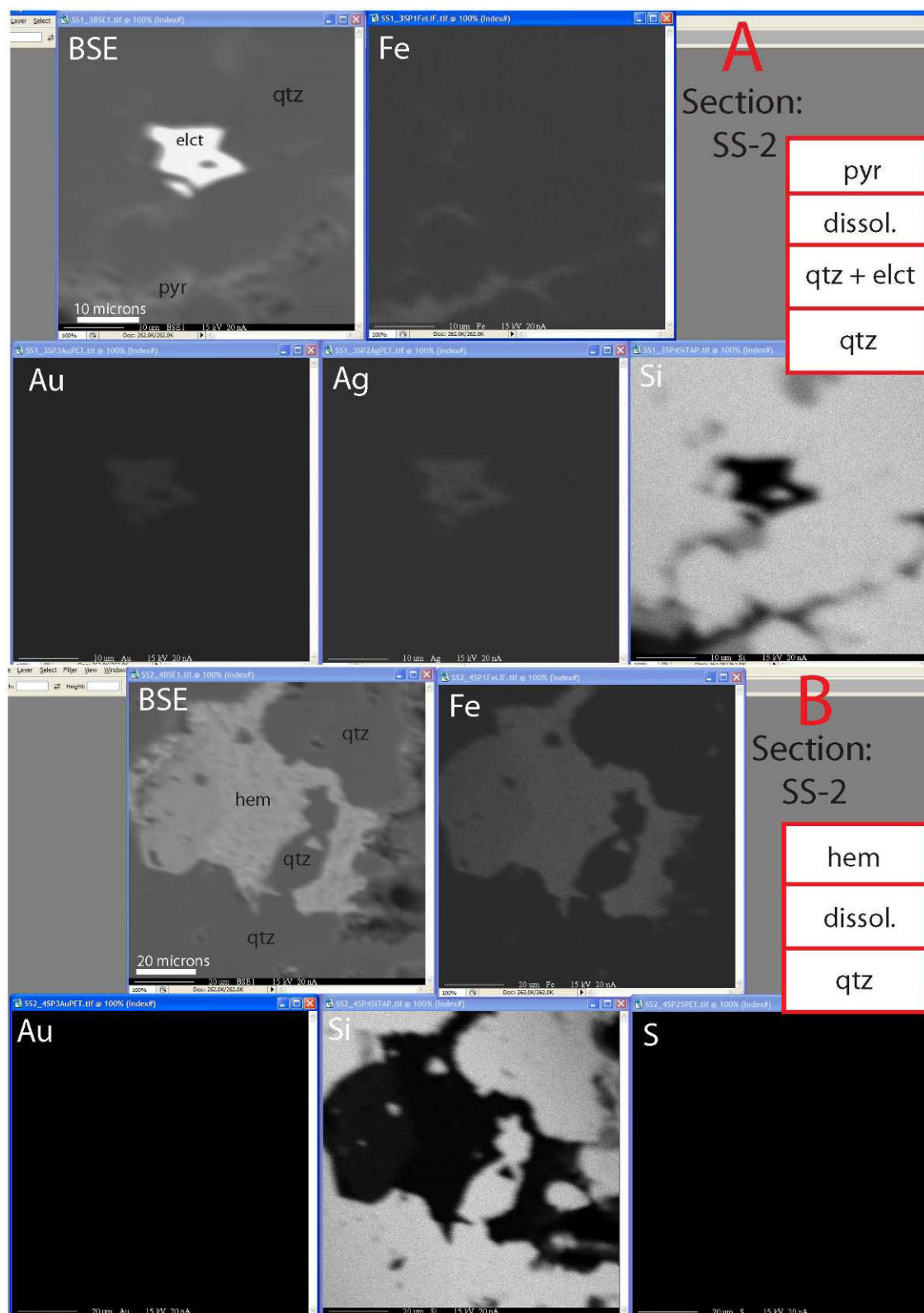


Figure 1-71. EM images and paragenetic observations, Section: SS-2, A&B

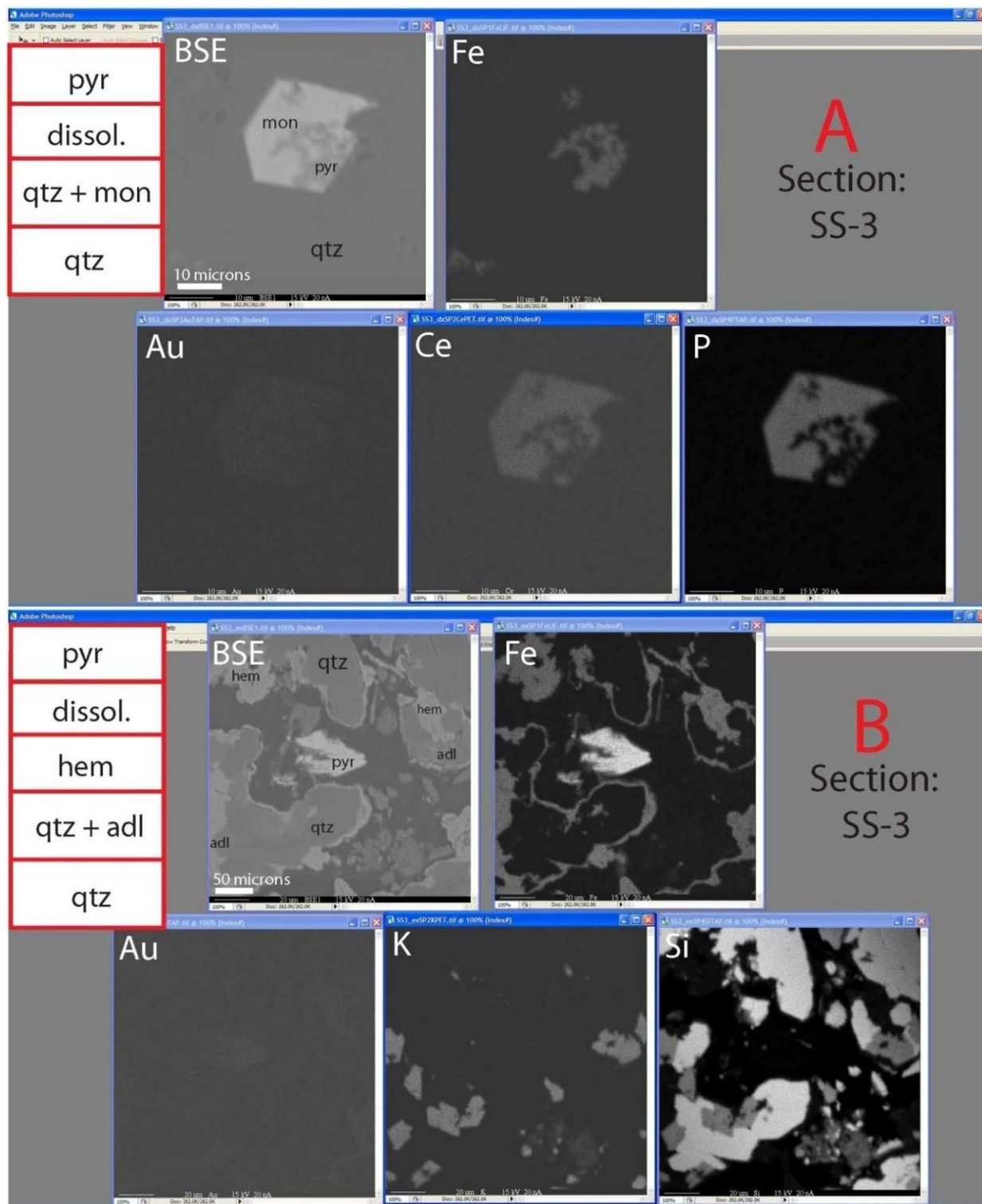
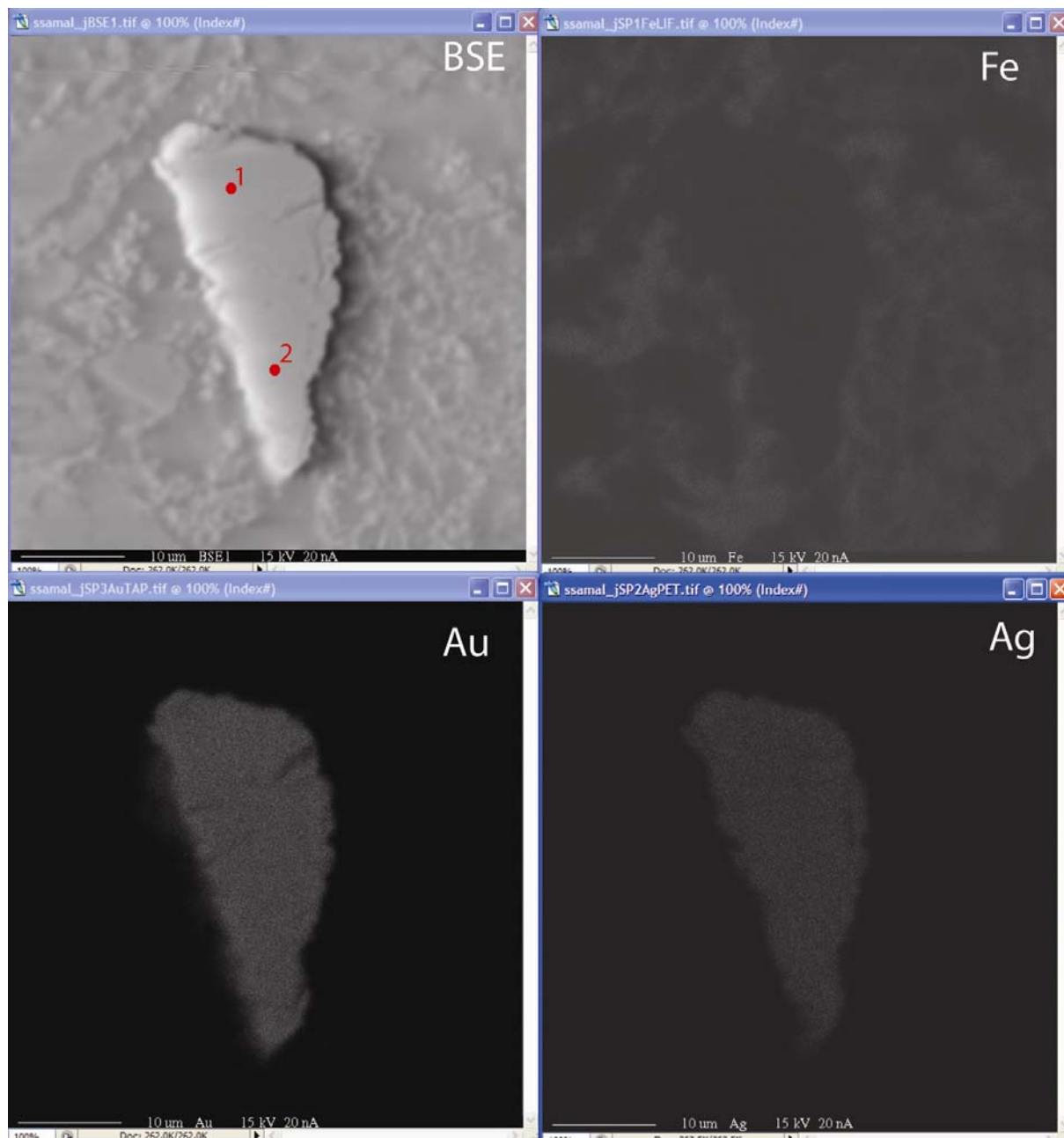


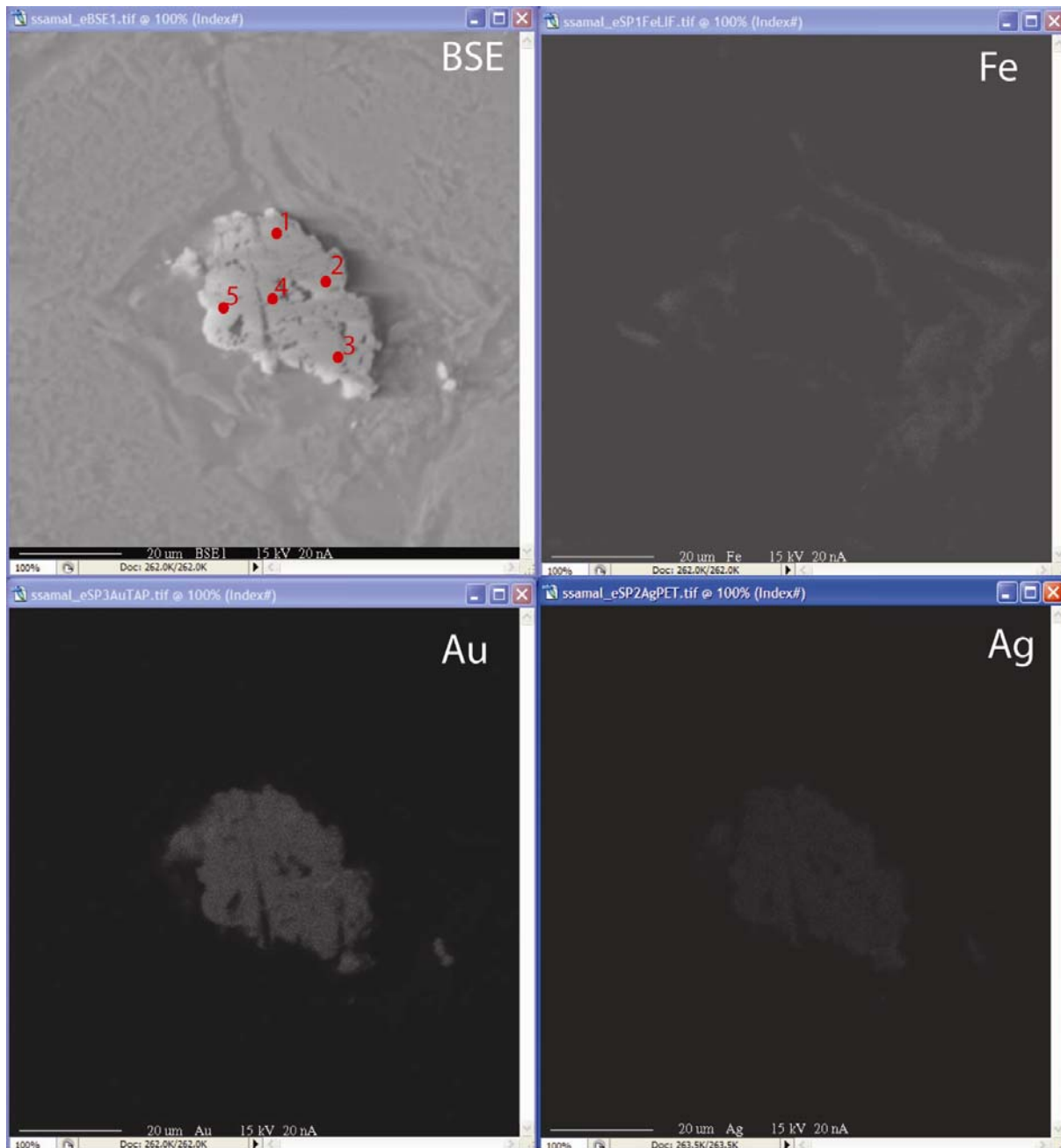
Figure 1-72. EM images and paragenetic observations, Section: SS-3, A&B



point	Au%	Ag%
1	63.8	36.8
2	64.2	38.6

	Au%	Ag%
average	64.00	37.70
std. dev.	0.28	1.27

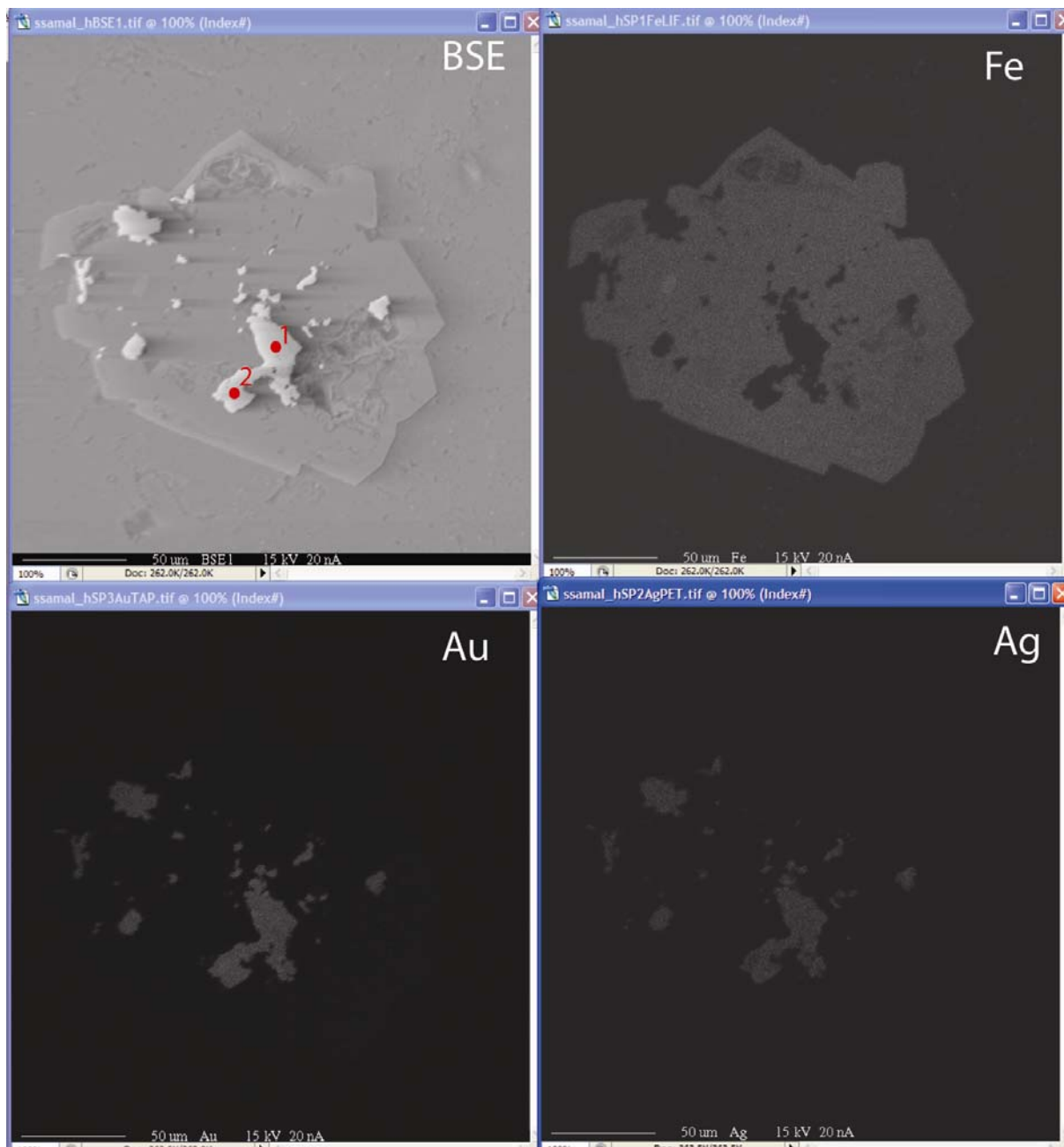
Figure 1-73. Quantitative Microprobe (QM) point scans on electrum grains from Sunshine Vein, 2



point	Au%	Ag%
1	63	33
2	65	34
3	60	31
4	36.7	65.9
5	64	34

	Au%	Ag%
average	57.74	39.58
std. dev.	11.91	14.76

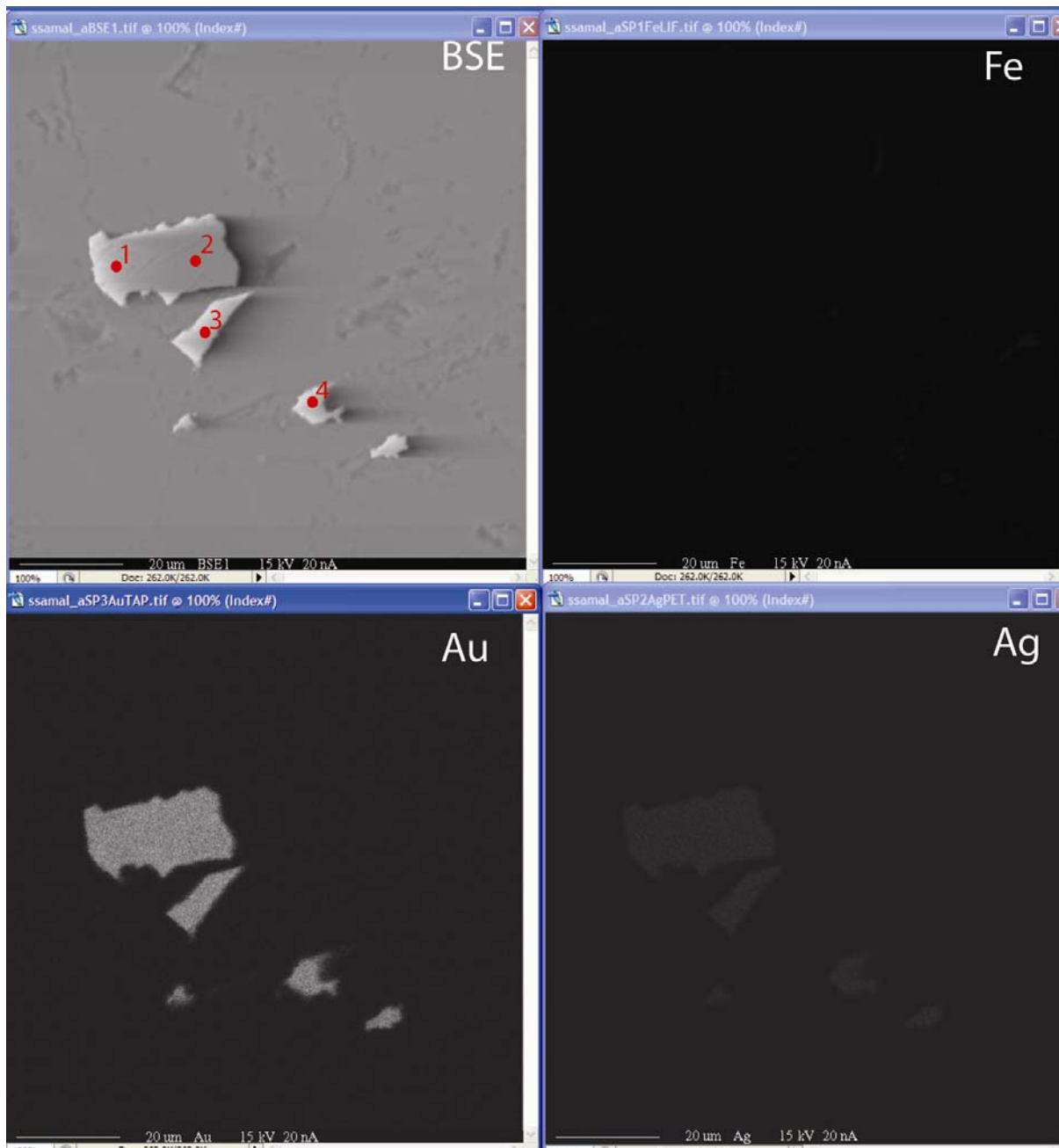
Figure 1-74. QM point scans on electrum grains from Sunshine Vein, 3



point	Au%	Ag%
1	66	39.2
2	62.2	37.5

	Au%	Ag%
average	64.10	38.35
std. dev.	2.69	1.20

Figure 1-75. QM point scans on electrum grains from Sunshine Vein, 4



point	Au%	Ag%
1	61.2	41.7
2	58.5	42.2
3	59.4	38
4	61.2	39

	Au%	Ag%
average	60.08	40.23
std. dev.	1.35	2.04

Figure 1-76. QM point scans on electrum grains from Sunshine Vein, 5

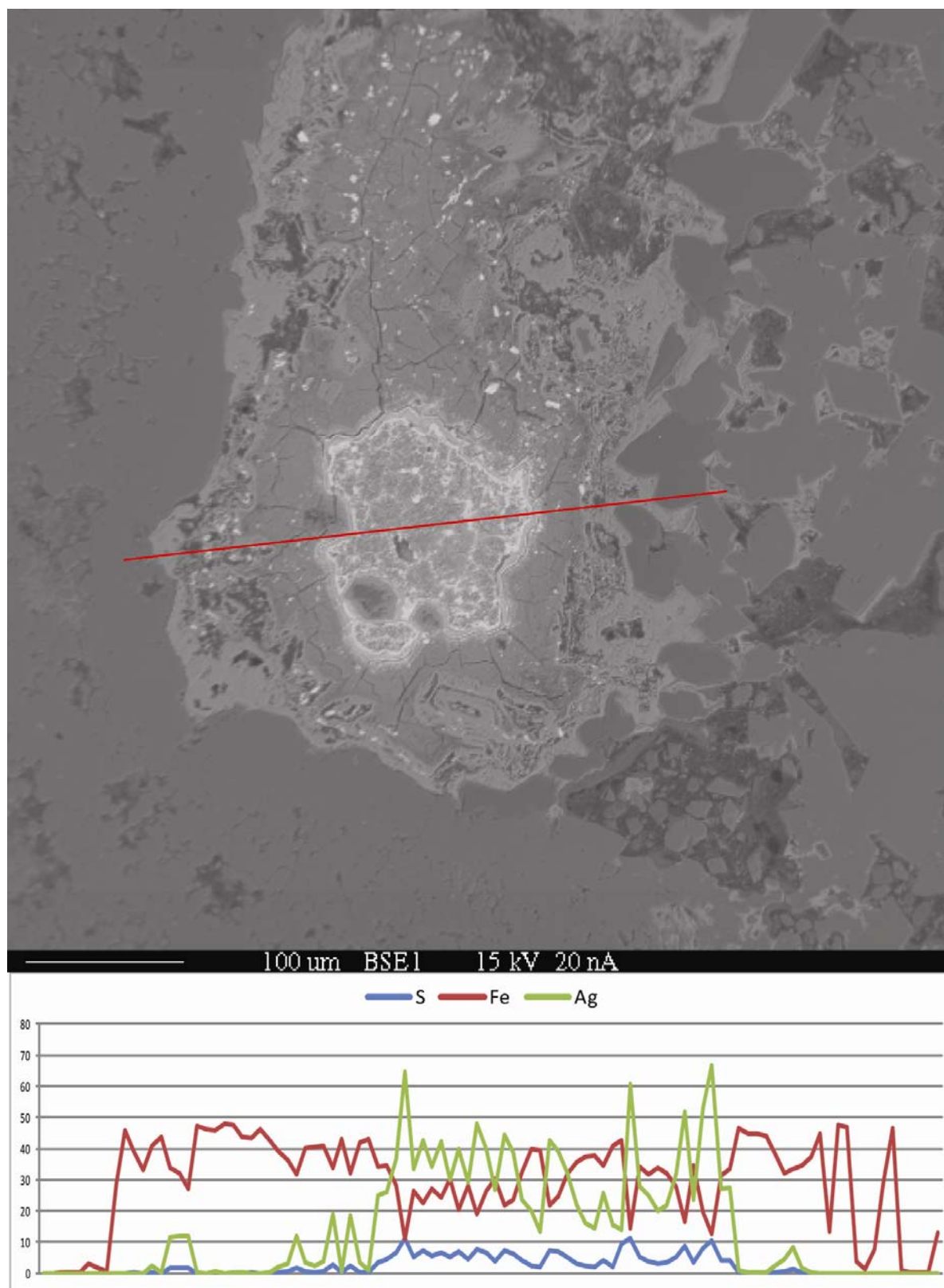


Figure 1-77. QM line traverses on Fe/Ag nodules from Consolidated, 2

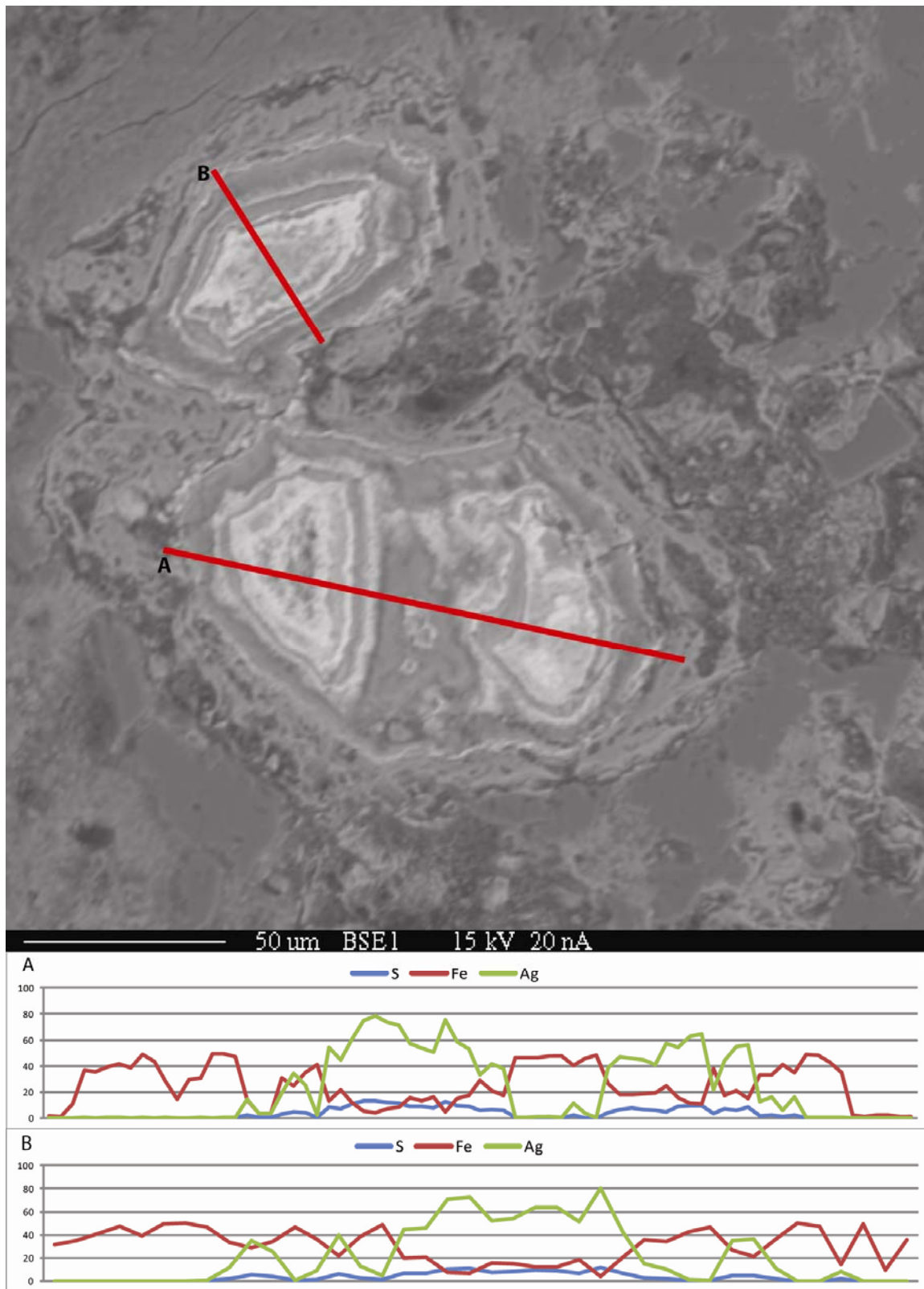


Figure 1-78. QM line traverses on Fe/Ag nodules from Consolidated, 3

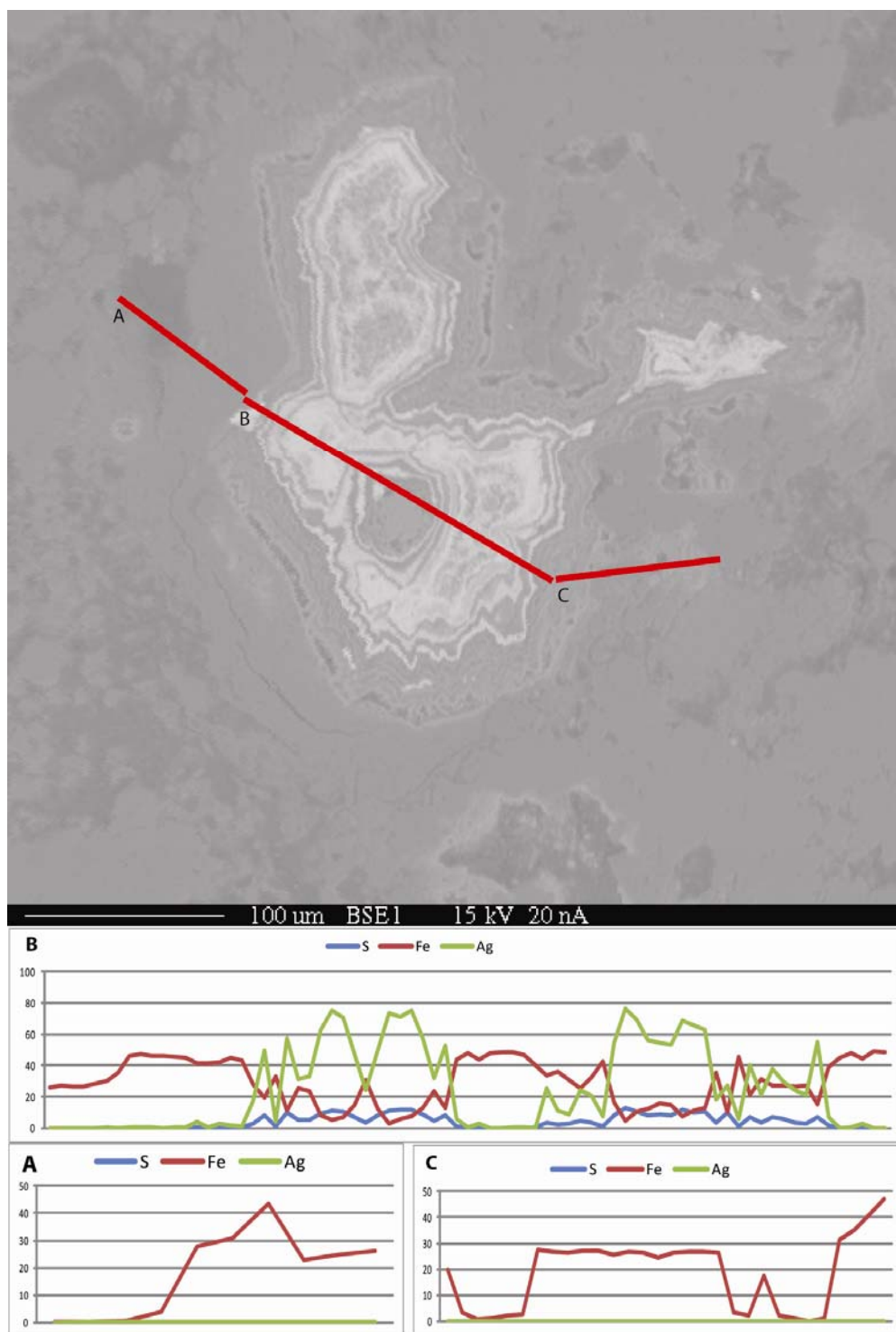


Figure 1-79. QM line traverses on Fe/Ag nodules from Consolidated, 4

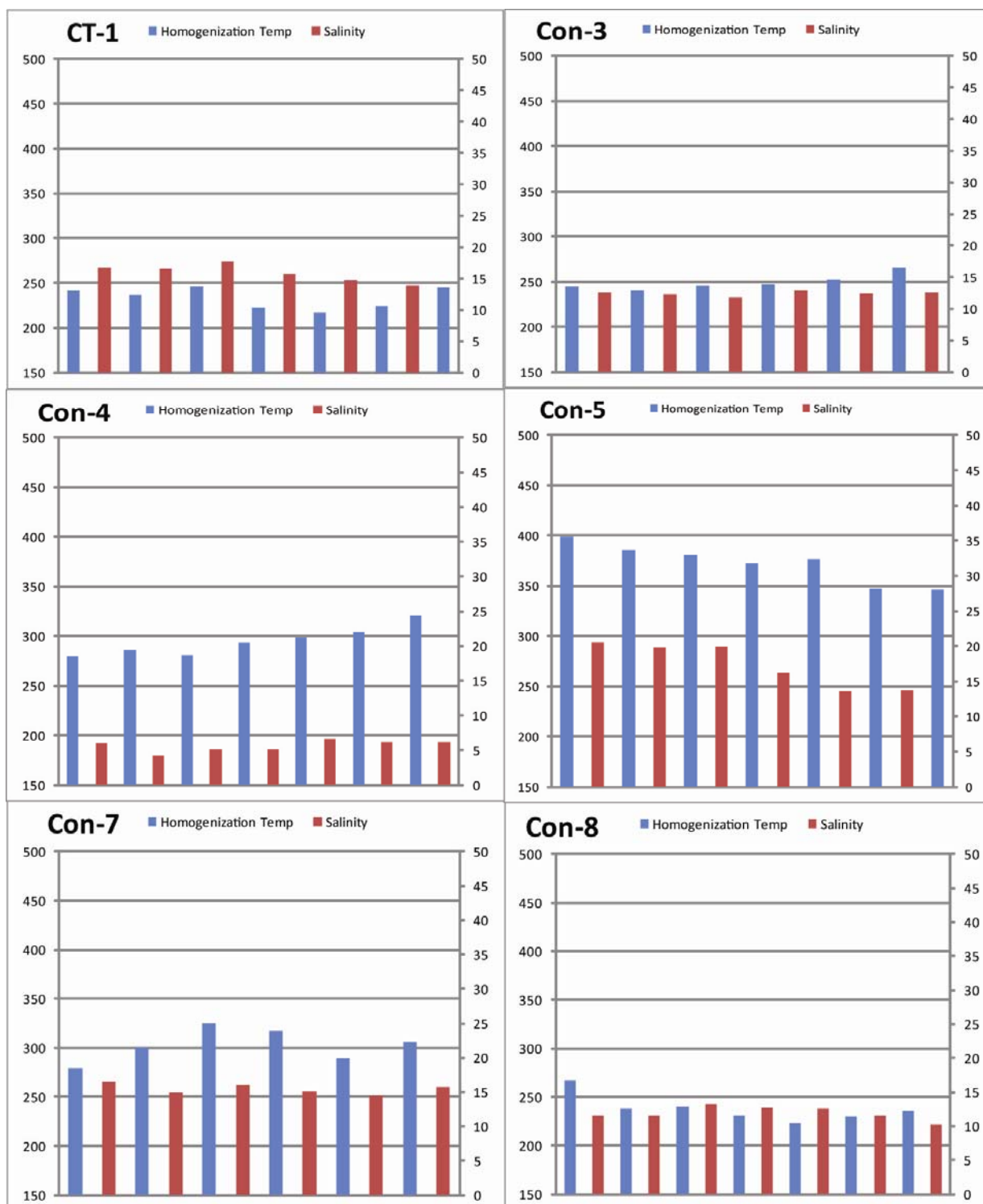


Figure 1-80. Fluid inclusion data from the indicated samples of the Consolidated Camp. Figure 78 explains chart format.

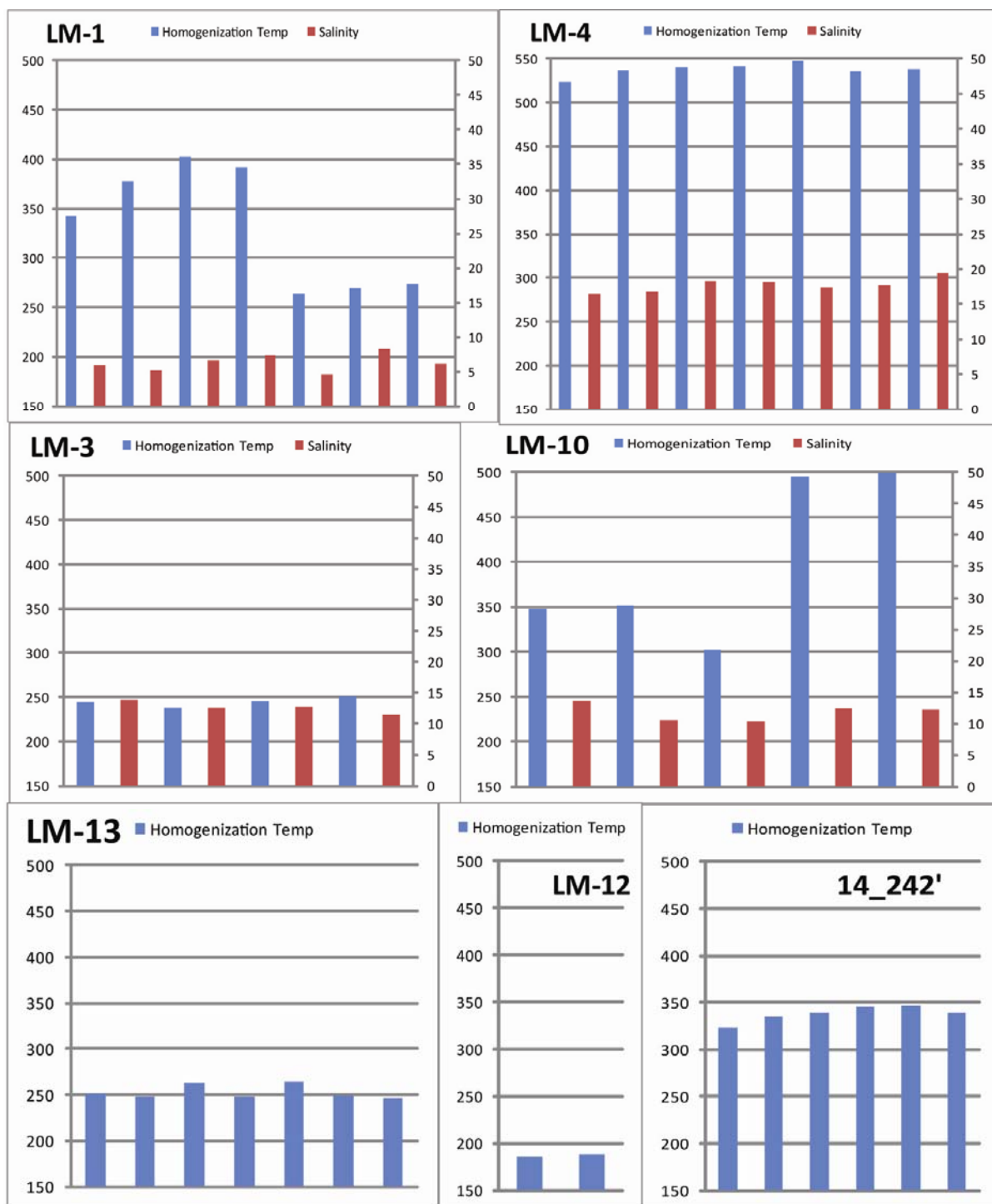


Figure 1-81. Fluid inclusion data from the indicated samples of hydrothermal quartz in bedrock (also one RC sample). Figure 78 explains chart format.

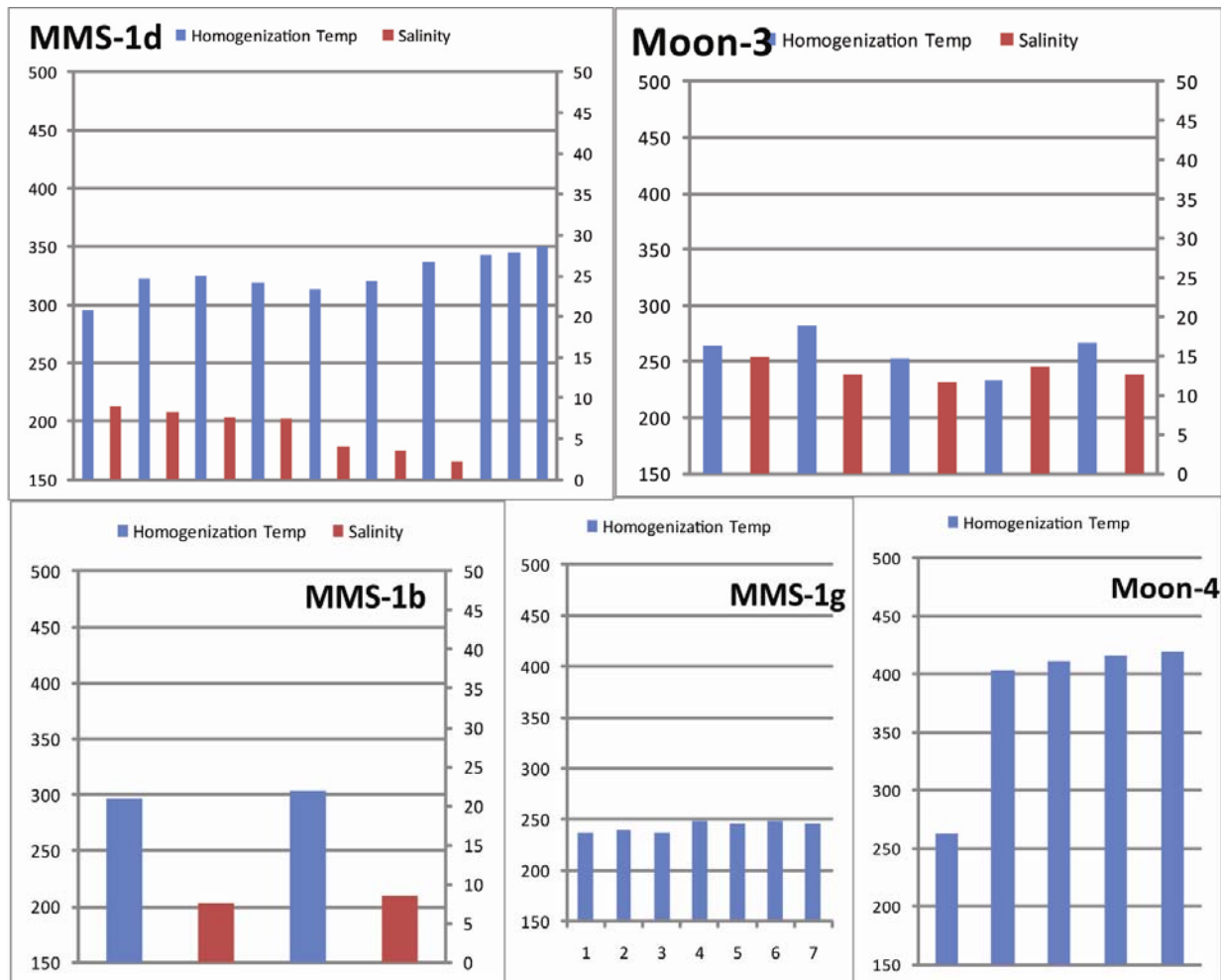


Figure 1-82. Fluid inclusion data from the indicated samples of the Modoc Mines Shaft. Figure 78 explains chart format.

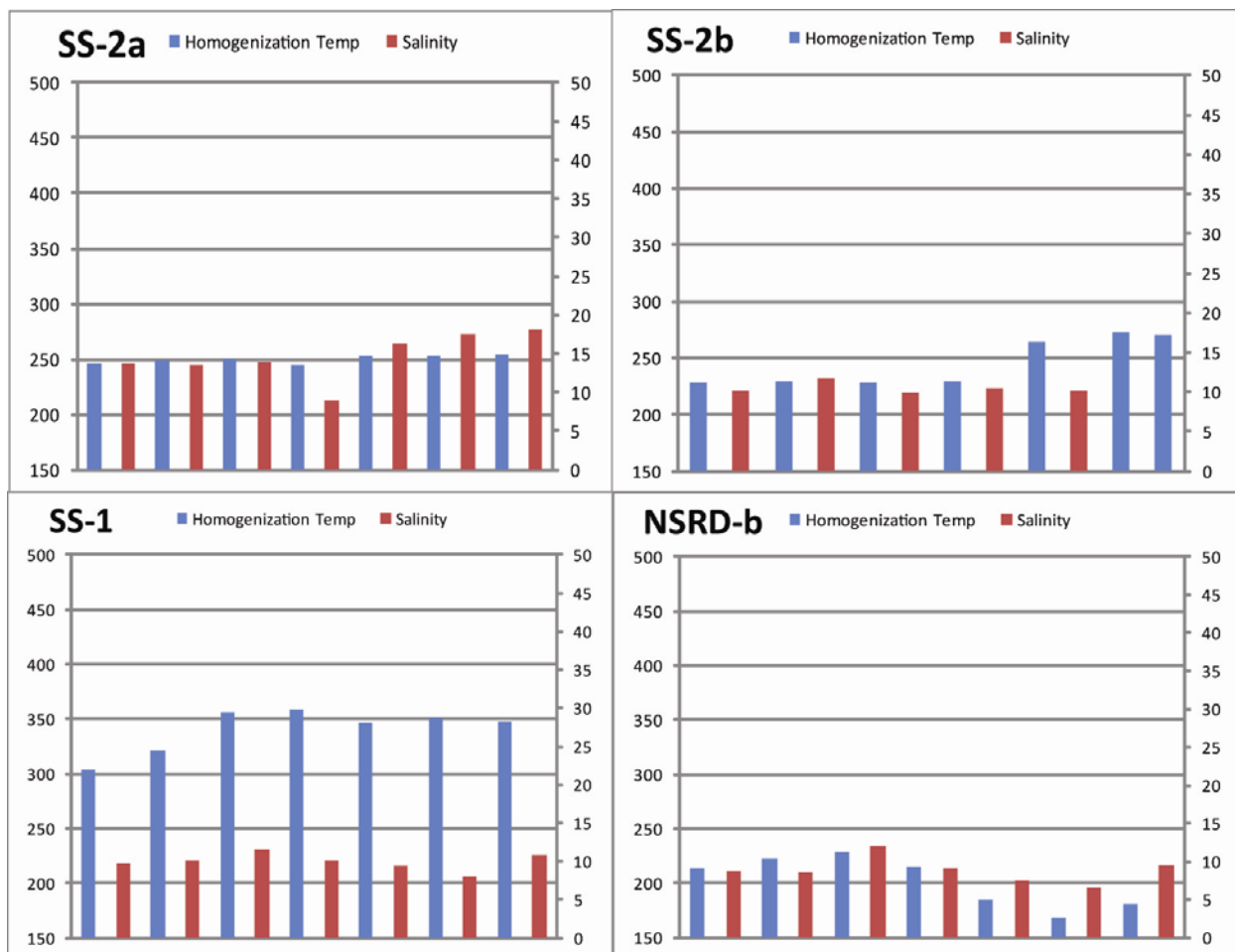


Figure 1-83. Fluid inclusion data from the indicated samples of the Sunshine Vein and Northstar Basin (NSRD). Figure 78 explains chart format.

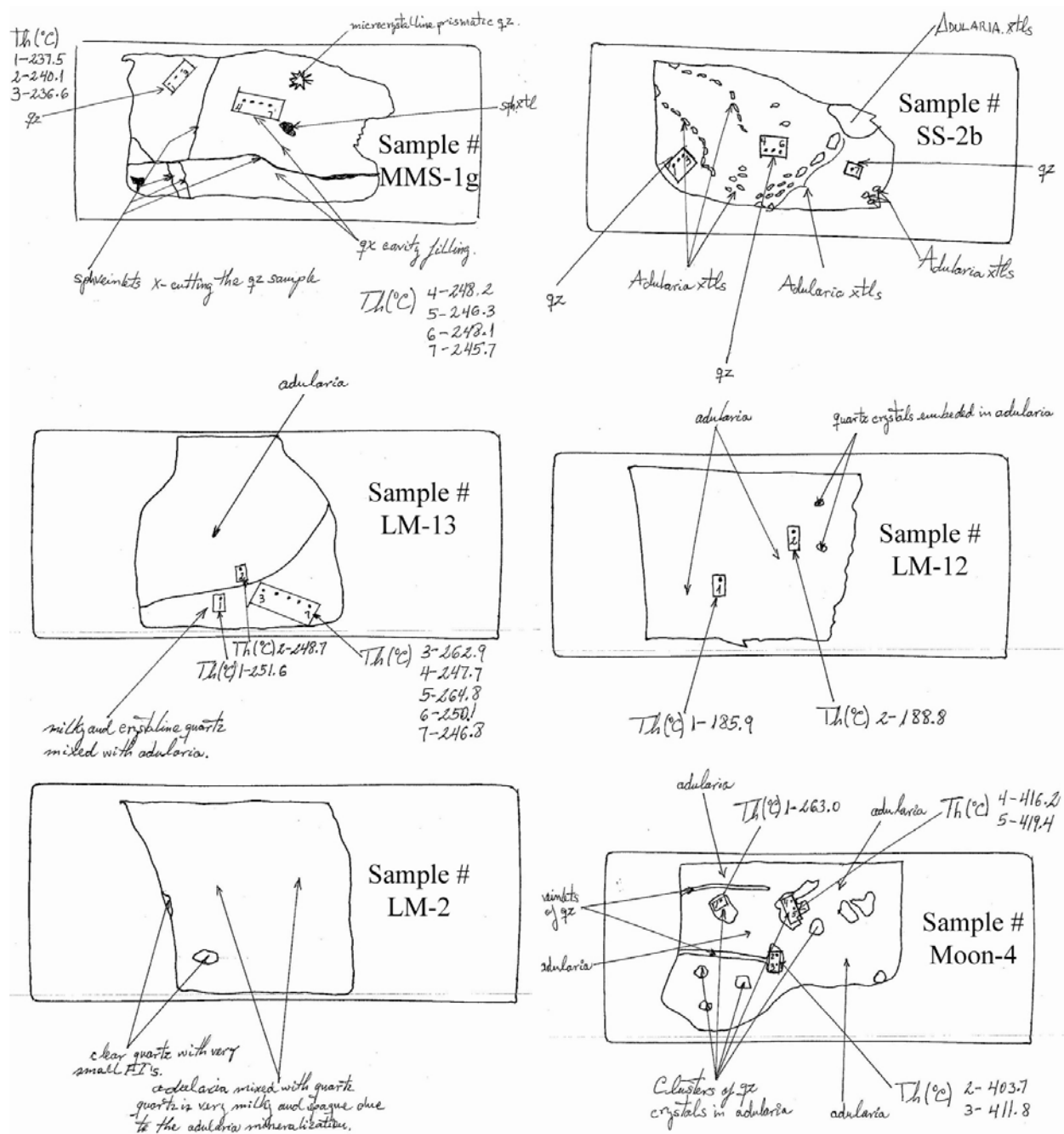


Figure 1-84. Reconnaissance of indicated thick-sections as related to fluid inclusion data interpretation.

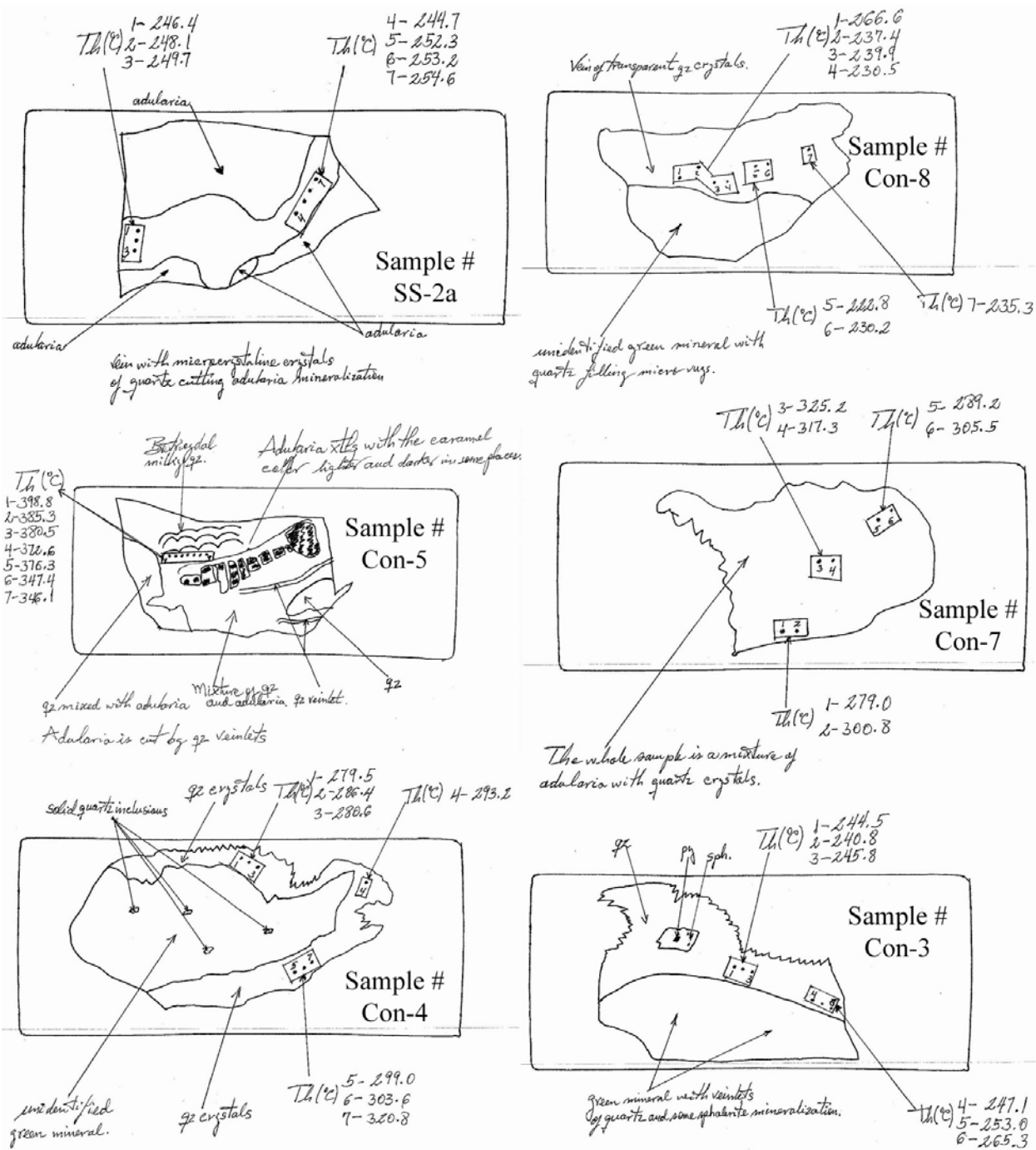


Figure 1-85. Reconnaissance of indicated thick-sections as related to fluid inclusion data interpretation.

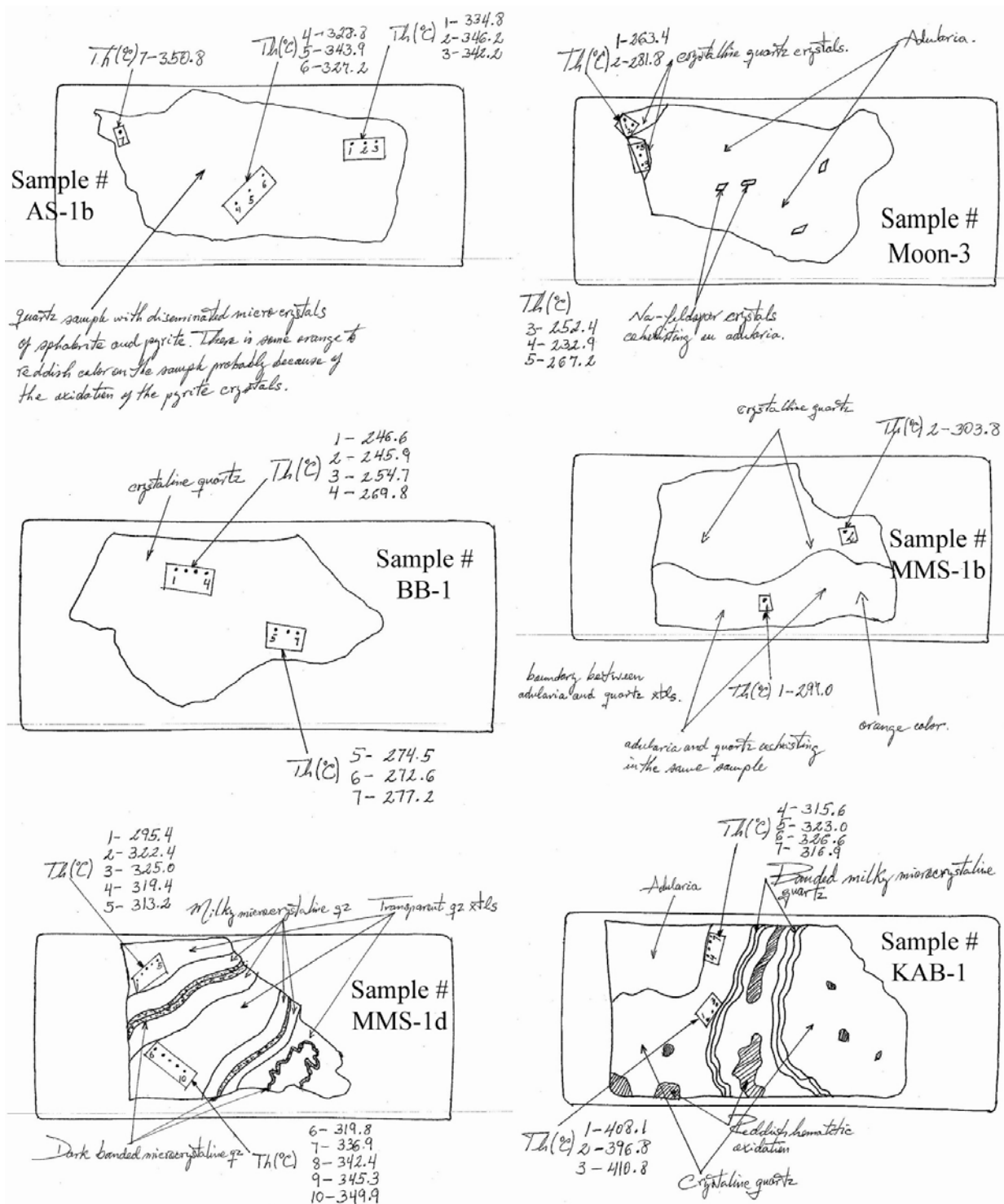


Figure 1-86. Reconnaissance of indicated thick-sections as related to fluid inclusion data interpretation.

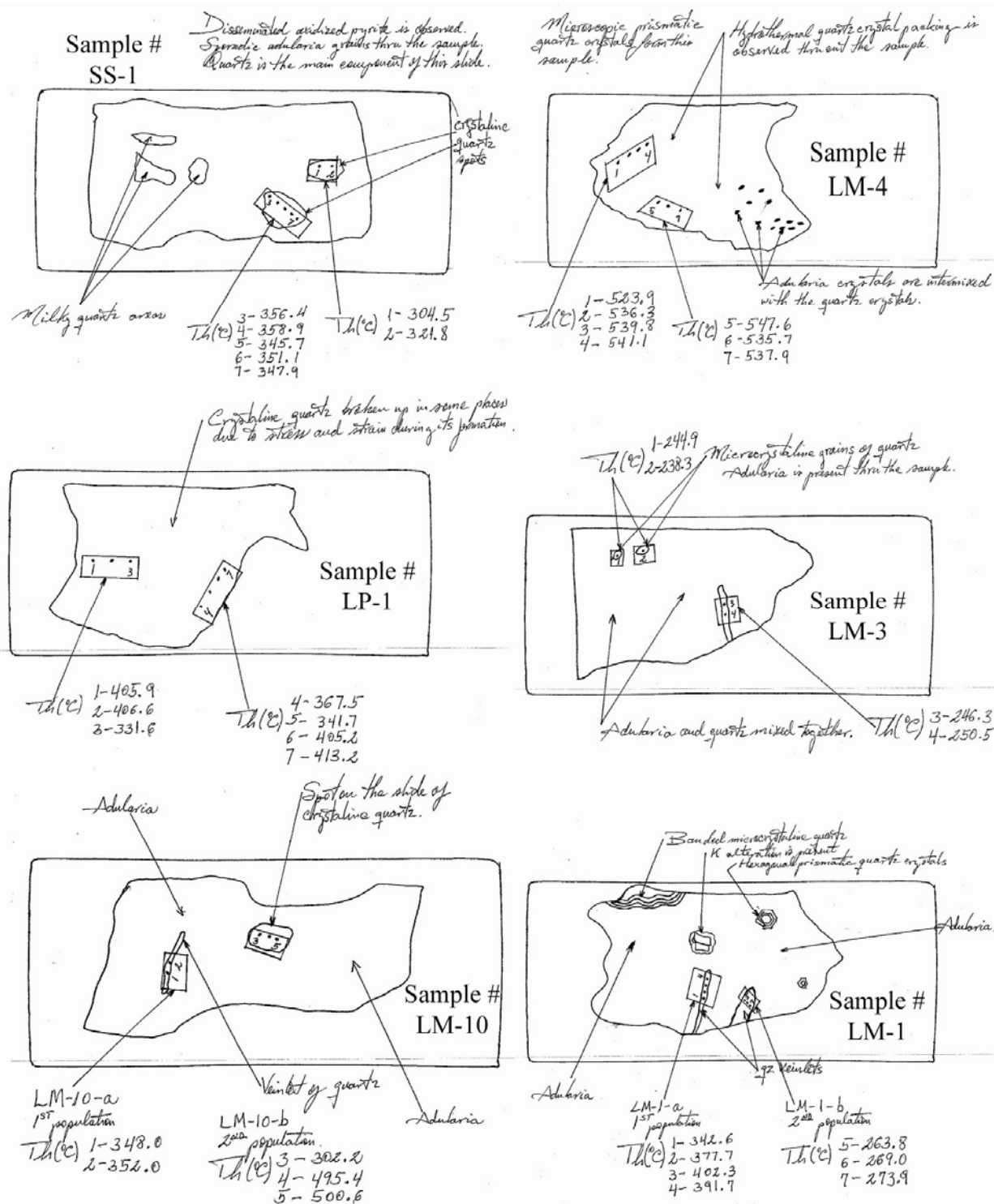


Figure 1-87. Reconnaissance of indicated thick-sections as related to fluid inclusion data interpretation.

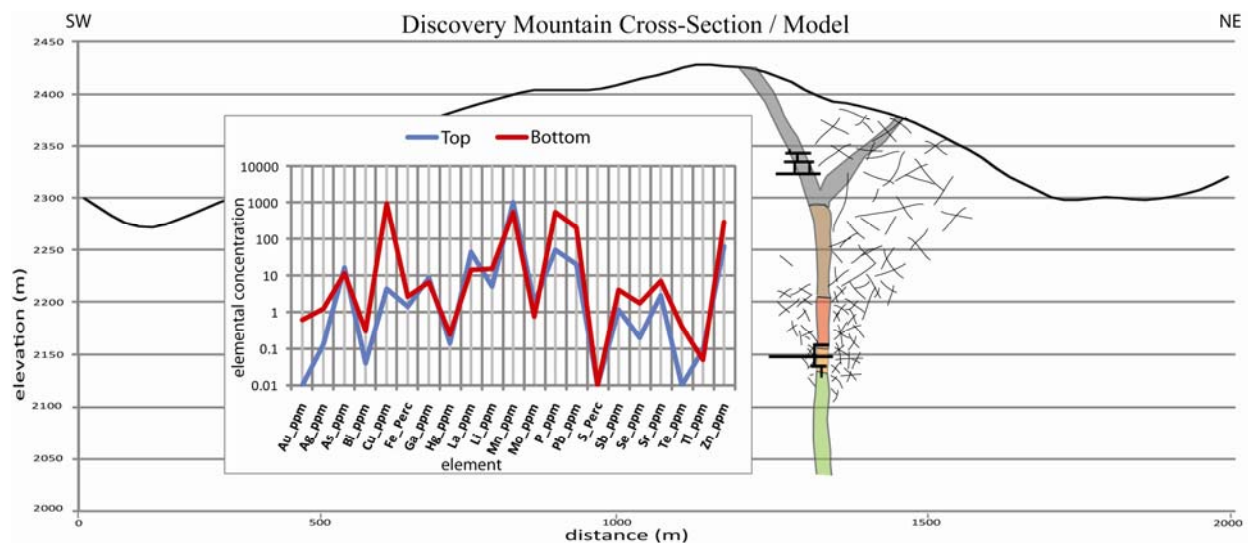


Figure 1-88. Discovery Mountain epithermal model with the active geochemistry (21 elements) observed in this portion of the study area.

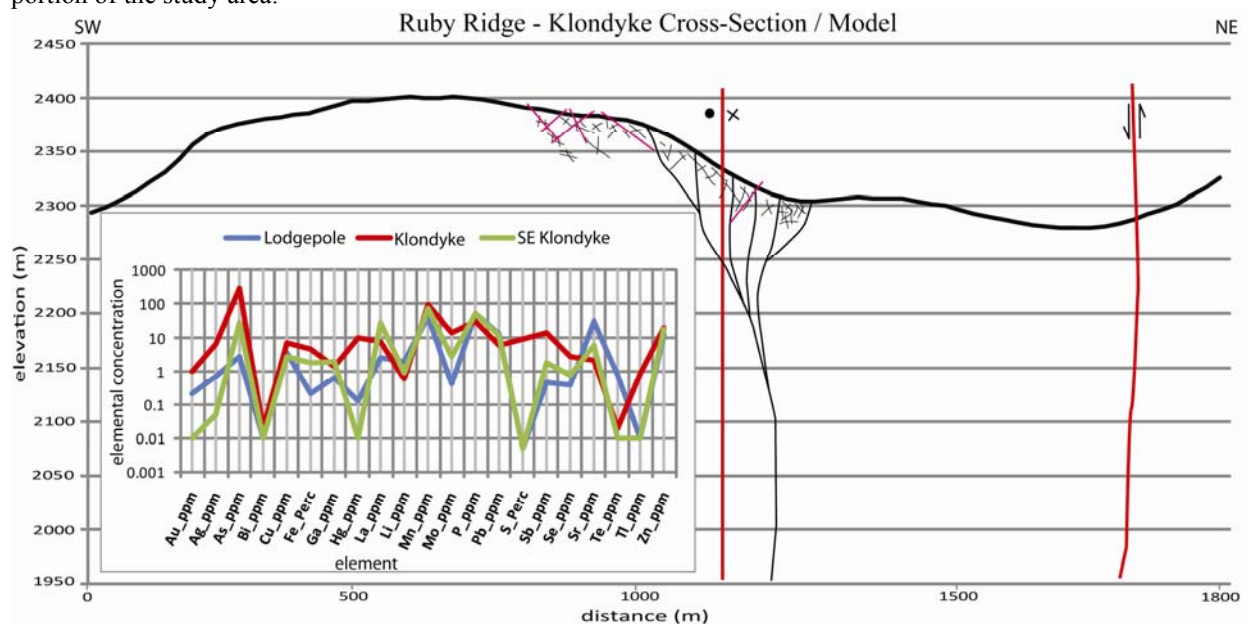


Figure 1-89. Ruby Ridge - Klondyke epithermal model with the active geochemistry (21 elements) observed in this portion of the study area.

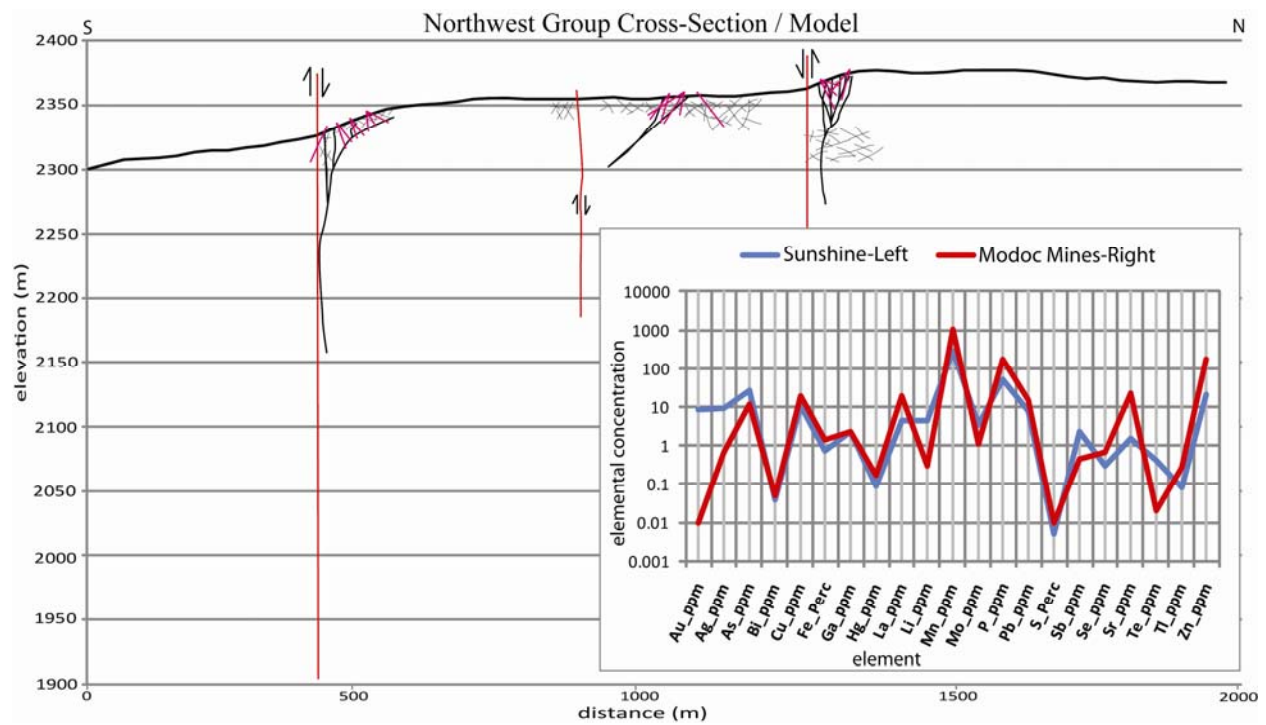


Figure 1-90. Sunshine-Modoc epithermal model with the active geochemistry (21 elements) observed in this portion of the study area.

CURRICULUM VITA

Michael Nicholas Feinstein was born on January 21st, 1982 in Houston, Texas. The only son of Richard and Carolyn Feinstein, he graduated from Cypress Creek High School, Houston, Texas, in the spring of 2000. After being introduced to the geological sciences at North Harris-Montgomery County Community College, his studies continued at the University of Houston and Sam Houston State University, in Huntsville, Texas where he received a bachelor's of science in geology in the summer of 2005. Michael entered the graduate program in Geological Sciences at the University of Texas at El Paso in the Fall of 2005, and completed a Master's Degree in 2007. Michael resides in Houston, Texas and remains involved in geologic endeavors and is an avid mineral specimen collector.

Permanent Address: 105 Angelina Cove
Georgetown, Texas 78633
mnfeinstein@gmail.com